Fabrication and Characterization of Ni-Mn-Ga Thin Films from Binder Jetting Additive Manufactured Sputtering Target

by

Christopher Yaw Bansah

Submitted in Partial Fulfillment of the Requirements

for the Degree of

Doctor of Philosophy

in the

Materials Science and Engineering

Program

YOUNGSTOWN STATE UNIVERSITY

© May 2022

Fabrication and Characterization of Ni-Mn-Ga Thin Film from Binder Jetting Additive Manufactured Sputtering Target

Christopher Yaw Bansah

I hereby release this **dissertation** to the public. I understand that this **dissertation** will be made available from the OhioLINK ETD Center and the Maag Library Circulation Desk for public access. I also authorize the University or other individuals to make copies of this thesis as needed for scholarly research.

Signature:

____

Christopher Yaw Bansah, Student Date:

Approvals:

____

Dr. C. Virgil Solomon, Thesis Advisor Date:

____

Dr. Clovis Linkous, Committee Member Date:

____

Dr. Tom Nelson Oder, Committee Member Date:

____

Dr. Donald Priour, Committee Member Date:

____

Dr. Matthew Caputo, Committee Member Date:

____

Dr. Salvatore A. Sanders, Dean of Graduate Studies Date:

ABSTRACT

Ni-Mn-Ga thin films have attracted significant attention over the past two decades due to its multifunctional properties, leveraging these characteristics in applications such as actuators, sensors, and micro-electromechanical systems (MEMS). The most favorable deposition technique for making Ni-Mn-Ga thin films is magnetron sputtering where the target used is near stoichiometric Ni_2MnGa alloy. Ni-Mn-Ga alloy target manufacturing has been challenging and costly due to design constraints, process optimization issues and inefficient target utilization resulting in compounded negative economics. To address these problems, this research aimed at investigating and demonstrating the viability of a cost-effective, modern technology known as binder jetting additive manufacturing (BJAM) technique to produce targets with excellent target consumption efficiency based on proposed target design. The additive manufactured Ni-Mn-Ga alloy target process began with ball-milled Ni-Mn-Ga powder having bimodal particle distribution to ensure an increased packing density and mechanical strength after the determination of optimized 3D printing parameters. The printed targets were post-processed through curing, de-binding and sintering. Sintering was conducted in an inert/argon atmosphere to safeguard essential material properties which were benchmarked through characterization. Backscattered electron (BSE) micrographs showed AM targets were homogenous with martensitic twin microstructures necessary for shape memory behavior. The XRD results showed that the martensitic twin microstructures were mostly tetragonal and monoclinic crystal structures. The martensitic transformation temperatures for Ni-Mn-Ga targets ranged from 79.3 to 148.1°C and possessed a maximum density of 87.18%. Using the direct current (DC) magnetron sputtering, Ni-Mn-Ga thin films were deposited on Si (100) substrates at discharge currents ranging from 0.05 to 0.15 A and substrate temperatures 20°C to 700°C. The effect of discharge current and substrate temperature on surface morphology, composition, crystal structure of Ni-Mn-Ga thin films on silicon substrates

were investigated. As the discharge current increased, the film showed increased grain size. The grain morphology, as appeared from the investigation of the film planar surface was of elongated grains. The film crystallinity also increased with increased discharge current, as proved by XRD investigations. The most important effect of maintaining the discharge current value constant and increasing the substrate temperature was the change in chemistry and crystallography of the obtained Ni-Mn-Ga thin films. The film deposited at 700^0C showed the closest chemical composition to the target composition. For the other substrate temperatures, the high oxygen contamination, due perhaps to not-so-optimum deposition conditions, drastically altered the film composition. By increasing the substrate temperature, the film crystal structure changed from Heusler $L2_I$ cubic (high temperature phase) to monoclinic (low temperature phase). It was also demonstrated that, 3D printed sputtering targets of different geometrical designs are potential for improving target utilization efficiency and film properties.

ACKNOWLEDGEMENTS

Firstly, I would like to thank our LORD JESUS CHRIST for seeing me throughout my education to this pinnacle of my academic career. May His name be praised. My sincere thanks go to my research advisor Dr. Virgil Solomon for his patience, support, and guidance throughout this academic journey without whom this Ph.D. wouldn't be possible. I would also like to thank all my committee members Dr. Clovis Linkous, Dr. Tom Oder, Dr. Donald Priour and Dr. Matthew Caputo for perfecting this work through their candid and essential critiques.

I would like to show my appreciation to the Center of Excellence in Materials Science and Engineering at YSU for providing the research assistantship scholarship for the entire duration of this work. The same goes to the Center for Innovation in Additive Manufacturing, the wide Band Gap Semiconductor laboratory in the Physics and Astronomy department at YSU for the opportunity to use their equipment and facility.

Dr. Brett Conner, I say a big thank you for providing the funds that enabled the purchase of the Ni-Mn-Ga alloy ingot. To Drs. Jeffery Dick, Timothy Wagner, Pedro Cortes and Holly Martin, I am thankful for your invaluable support by granting access to use your labs and equipment.

My indebtedness to Mr.& Mrs. Drew Hirt, and Mrs. Richel Kusnic at MRL for granting access to their facility and helping with the auger electron spectroscopy analysis is overwhelming and I am utterly grateful.

To Mr. Ray Hoff, thank you for assisting and training me on all the relevant equipment at Chemistry department which has contributed to the success of this project.

To my research colleague at South Dakota Mines & Technology, Nana Ansah Adoo, I would like to recognize your effort and contribution in this research and data analysis and I am truly grateful.

To my office and lab colleagues, Mr. Stephen Isacco and Mr. Eduardo Vega, thank you for all the help and assistance throughout my entire stay and research period at the YSU. I am going to miss you.

To my lovely wife and children, I seize this opportunity to express my sincere and profound gratitude for the borne sacrifices and encouragement through the entirety of this work. Thank you for being a part of this success story.

TABLE OF CONTENTS

Contents

Fabrication and Characterization of Ni-Mn-Ga Thin Films from Binder Jetting Additive Manufactured Sputtering Target i

Fabrication and Characterization of Ni-Mn-Ga Thin Film from Binder Jetting Additive Manufactured Sputtering Target i

ABSTRACT i

ACKNOWLEDGEMENTS iii

TABLE OF CONTENTS v

LIST OF FIGURES ix

LIST OF TABLES xiv

LIST OF ACRONYMS xv

PREFACE xvi

CHAPTER 1 1

Thin Films and Sputtering Targets 1

1.0 Introduction to thin film deposition 1

1.1 Introduction to sputtering targets 5

1.2 Metallurgical defects on sputtering target 8

1.3 Target utilization 10

1.4 Influence of deposition parameters on film properties 13

1.5 Ni-Mn-Ga targets and thin films 17

1.5.1 Background 17

1.5.2 Ni-Mn-Ga targets 19

1.5.3 Ni-Mn-Ga thin films for MEMS applications 24

1.6 Copper targets and thin film 25

1.6.1 Copper targets 25

1.6.2 Copper thin film 27

1.6.2.1 Surface morphology 28

1.6.2.2 Crystallinity and texture 29

1.6.2.3 Electrical resistivity 29

1.7 316L Stainless Steel target and thin films 30

CHAPTER 2 34

Materials and Experimental Methods 34

2.0 Introduction 34

2.1 Materials 35
2.2 Experimental method 35
2.2.1 Ni-Mn-Ga powder preparation 35
2.2.1.1 Particle size analysis 37
2.2.1.2 Heat treatment of as-milled Ni-Mn-Ga powders 39
2.2.1.3 Morphology and chemical composition 40
2.2.1.4 Crystal structure 41
2.2.1.5 Thermal analysis 43
2.2.2 3D Printing of Ni-Mn-Ga via binder jet 44
2.2.3 Post-processing of binder jet 3D printed Ni-Mn-Ga targets: curing and sintering 48
2.2.4 Target Polishing 49
2.2.5 Ni-Mn-Ga targets characterization 50
2.2.6 Synthesis of Ni-Mn-Ga thin films 51
2.2.7 Characterization of Ni-Mn-Ga thin films 54
2.3 Monte Carlo Computer Simulation using TRIM (Transport of Ions in Matter) Code 55
CHAPTER 3 57
Characterization of Ni-Mn-Ga Powder 57
3.0 Introduction 57
3.1 Particle Size Distribution Analysis 57
3.2 Particle Morphology and Chemical Composition 59
3.3 Crystal Structure 61
3.4 Thermal Analysis 63
Thermal analysis of Ni-Mn-Ga bulk and powder was performed using differential scanning calorimetry (DSC) in order to determine the martensitic phase transformation temperatures. 63
CHAPTER 4 66
Characterization of Ni-Mn-Ga Sputtering Target produced by Binder Jetting Additive Manufacturing 66
4.0 Introduction 66
4.1 Chemical composition, microstructure, phase identification, phase transformation, and shrinkage of as-printed and sintered un-polished Ni-Mn-Ga targets 66
4.2 *Microstructure, density, composition, crystal structure, and phase transformation of sintered polished Ni-Mn-Ga* 75
4.2.2 Fractography of sintered targets 81
4.2.3 Composition of targets via SEM/EDS 83
4.2.4 Crystal structure and phase transformation in polished Ni-Mn-Ga targets 86
4.3 Metallurgical properties of additive manufactured Ni-Mn-Ga targets as related to the quality of thin films 89

4.3.1 Chemical Composition ... 89
4.3.3 Density ... 92
4.4 Defects in used 3D printed Ni-Mn-Ga sputtering targets ... 92
CHAPTER 5 ... 96
Ni-Mn-Ga Thin Film Characterization ... 96
5.0 Introduction ... 96
5.1 Initial challenges of Ni-Mn-Ga thin film fabrication ... 96
5.2 Resolving oxygen contamination problem ... 102
5.3 Effect of discharge current on composition, surface morphology and microstructure of Ni-Mn-Ga thin films ... 106
5.4 Effect of substrate temperature on composition, surface morphology and structural evolution of Ni-Mn-Ga thin film ... 115
5.4.1 Compositional analysis ... 115
5.4.2 Surface and cross-sectional morphology ... 122
5.4.3 XRD analysis ... 125
5.5 Post-heat treatment of as-deposited room temperature Ni-Mn-Ga thin film ... 127
CHAPTER 6 ... 130
Binder jet 3D printing of complex geometry copper sputtering targets and characterization of obtained thin films ... 130
6.0 Introduction ... 130
6.1 Materials and Methods ... 133
6.1.1 Copper Powder ... 133
6.1.2 Justification of target designs, BJAM printing process and post-processing ... 134
6.1.3 Thin film fabrication of copper ... 135
6.1.4 Copper thin film characterization ... 136
6.1.4.1 Transmission electron microscopy (TEM) ... 136
6.1.4.2 Electrical resistivity measurement ... 137
6.2 Results and discussion ... 138
6.2.1 Powder characterization ... 138
6.2.2 Target manufacturing via binder jetting process ... 141
6.2.3 Sintering and characterization of 3D printed targets ... 141
6.2.4 Erosion and depth profile of planar and non-planar targets used in DC magnetron sputtering ... 145
6.2.5 Characterization of Copper thin films ... 148
6.2.5.1 Surface morphology of as-deposited copper thin film from TC 1 target ... 148
6.2.5.2 Microstructure of rapid thermal annealed copper thin films ... 149

6.2.5.2.1 Crystal structure 149
6.2.5.2.2 Crystallite size and microstrain 150
6.2.5.2.3 Microstructure via TEM 152
6.2.5.3 Electrical resistivity 153
6.2.5.4 Comparison between the thin films deposited by flat (TC 1) and non-flat (TC 4) targets 155
6.2.5.4.1 Surface Morphology 155
6.2.5.4.2 Crystal Structure 155
CHAPTER 7 158
316L Stainless Steel Target Made Via Binder Jetting Additive Manufacturing and Thin Film Fabrication by Magnetron Sputtering 158
7.0 Introduction 158
7.1 Materials and Methods 158
7.1.1 316L SS powder 158
7.1.2 Binder jet printing and post-processing 159
7.1.3 Thin film fabrication of 316L SS 160
7.2 Results and discussion 161
7.2.1 Powder characterization 161
7.2.2 Target characterization 163
7.2.3 Thin film characterization 166
CHAPTER 8 171
CONCLUSION AND FUTURE WORK 171
8.0 Conclusion 171
8.1 Future work 173
REFERENCE 175

LIST OF FIGURES

Figure 1.1 Energetic ions -target atom interaction [19] 2

Figure 1.2 Schematic diagram of DC diode sputtering system. 3

Figure 1.3 Schematic diagram of DC magnetron sputtering system. 4

Figure 1.4 Variation of film uniformity as a function of target grain size [23]. 7

Figure 1.5 (a) SEM image showing morphology of nodules; (b) Black nodules on ITO sputtering target; (c) Nodules on Si sputtering target [35]. 10

Figure 1.6 Target utilization : (a) Gold magnetron sputtered target showing non-uniform erosion in the shape of a racetrack [38]; (b) Schematic representation of the magnetic field distribution in a cross-sectional target and its relationship with the target erosion profile. 11

Figure 1.7 The interpoles target-hollow magnetron increases target material utilization by 60% [39]. 12

Figure 1.8 Grain size as a function of : (a) Substrate temperature; (b) Film thickness; (c) Kinetic energy of incident ions [20] 15

Figure 1.9 Optical image of cold spray deposited copper coating used as a sputtering target [128]. 26

Figure 2.1 SPEX 8000M ball milling machine used in preparing Ni-Mn-Ga powders. 36

Figure 2.2 Schematic of laser diffraction system for particle size analysis [202]. 38

Figure 2.3 Cilas 1190 particle size analyzer used in this research. 39

Figure 2.4 JEOL JIB 4500 Multi Beam System SEM/FIB equipped with EDAX apollo XV detector for morphology and chemical analysis. 41

Figure 2.5 Bruker AXS X8 Prospector single crystal diffractometer for structural analysis and phase identification. 43

Figure 2.6 Perker-Elmer Diamond DSC for investigating phase transformation. 44

Figure 2.7 ExOne innovent+ 3D printer used in this research. 45

Figure 2.8 3D CAD model design for sputtering target 3D printed using binder jetting technology. 45

Figure 2.9 Schematic diagrams of the printing process of Ni-Mn-Ga targets: (a) Initial spreading of powder-on-powder bed, (b) Projection of binder on powder bed, (c) Binder design patterned on powder bed. 47

Figure 2.10 Customized setup used for the sintering experiment of the 3D printed targets. 49

Figure 2.11 Sequence of target manufacturing process by binder jetting additive manufacturing. 50

Figure 2.12 Magnetron sputtering system at Youngstown State University (YSU) and used in this research. 53

Figure 3.1 Particle size distribution of as-milled Ni-Mn-Ga powder. 58

Figure 3.2 (a) Secondary electron (SE) micrograph of as-milled Ni-Mn-Ga powder; (b) BSE of as-milled powders indicating uniform chemical composition; (c) EDS spectra collected from an individual particle (encircled in (b)). 60

Figure 3.3 SE micrographs of annealed NiMnGa particles showing the specific morphology of twinned martensite: (a) Low magnificatio micrograph; (b) High magnification micrograph. 61

Figure 3.4 (a) Room temperature XRD patterns for Ni-Mn-Ga bulk, ball milled powder, and annealed powder, and (b) Detailed XRD pattern of annealed Ni-Mn-Ga powder. 63

Figure 3.5 DSC curves of bulk Ni-Mn-Ga ingot, ball milled powder, and annealed powder. 64

Figure 4.1(a) As-printed Ni-Mn-Ga target; (b) Ni-Mn-Ga target sintered at 1075°C for 40 hours (Target 3). 67

Figure 4.2 (a) BSE micrograph collected from the surface of as-printed Ni-Mn-Ga target, (b) EDS spectrum collected from the red square area. 68

Figure 4.3 SEM image of the surface of 3D printed Ni-Mn-Ga target sintered at 1065oC for 40 hours: (a) Morphology of the sintered target surface, (b) High magnification micrograph of the area indicated in (a), showing the presence of Mn3O4 crystals at the surface of sintered target, (c) EDS spectrum collected from the surface of sintered Ni-Mn-Ga target. 69

Figure 4.4 XRD pattern of as-sintered Ni-Mn-Ga Target 1 70

Figure 4.5 SEM micrographs of Ni-Mn-Ga samples sintered at different temperatures: (a) - (b) Target 2, (c) - (d) Target 3, (e) - (f) Target 4. 72

Figure 4.6 (a) BSE micrograph of the Target 3 surface; (b) – (f) Ni, Mn, Ga, O, and C EDS maps recorded from the area shown in (a). 73

Figure 4.7 Shrinkage of Ni-Mn-Ga targets at different sintering temperatures. 75

Figure 4.8 (a) Photo of polished Ni-Mn-Ga target named Target 1, Target 2, Target 3, and Target 4 after used, (b) Photo of Target 4 before use. 76

Figure 4.9 SEM micrographs of polished cross-section of Ni-Mn-Ga targets sintered at different temperatures: (a) Target 1, (b) Target 2, (c) Target 3, and (d) Target 4. 78

Figure 4.10 Density percentage and porosity of 3D printed Ni-Mn-Ga target sintered at different temperatures. 79

Figure 4.11 DIC image of targets: (a) Target 1, (b) Target 2, (c) Target 3. 80

Figure 4.12 BSE micrograph of targets: (a) Target 1, (b) Target 2, (c) Target 3. 81

Figure 4.13 Fractured surfaces of 3D printed Ni-Mn-Ga sintered targets: (a) Target 1, (b) Target 2, (c) Target 3, (d) Target 4. ... 82

Figure 4.14 Effect of sintering temperature on composition of 3D printed Ni-Mn-Ga targets. ... 85

Figure 4.15 (a) BSE micrograph for a cross-section area of Target 3; (b) – (d) Ni, Mn, Ga SEM/EDS maps collected from the area in (a). ... 86

Figure 4.16 XRD pattern of cross-section of 3D printed Ni-Mn-Ga targets sintered at different temperatures. ... 88

Figure 4.17 DSC curves recorded from 3D printed Ni-Mn-Ga targets sintered at different temperatures, where As - austenitic start temperature, Ap - peak temperature, Af - austenitic finish temperature, Ms - martensitic start temperature, Mp - martensitic peak temperature, and Mf - martensitic finish temperature. ... 88

Figure 4.18 (a) DIC micrograph of the target surface, before sputtering; (b) SEM image of Ni-Mn-Ga thin film, obtained from a target having the grain size and morphology, as the target in (a). ... 91

Figure 4.19 (a) Optical image of a used Ni-Mn-Ga target (Target 3); (b)SEM micrograph of the portion of racetrack area marked in (a); (c) An inset of high magnification of nodule growth in (b). ... 93

Figure 4.20 3D topography of Ni-Mn-Ga target (52.92 mm in diameter) after: (a) 10 hours, and (b) 30 hours of sputtering; (c) Erosion profile of Ni-Mn-Ga target sputtered after 10 hours and 30 hours. ... 95

Figure 5.1 Ni-Mn-Ga thin film deposited at room temperature on Si (100): (a) SEM micrograph and (b) EDS spectrum recorded from the thin film. ... 97

Figure 5.2 AES depth composition profile of Ni-Mn-Ga thin film as-deposited at room temperature on Si (100) substrate. ... 99

Figure 5.3 XRD pattern of Ni-Mn-Ga thin film as-deposited at room temperature on Si (100) substrate. ... 100

Figure 5.4 BSE micrographs of top view of Ni-Mn-Ga thin film as-deposited at room temperature on NaCl substrate: (a) Low magnification; (b) High magnification. ... 100

Figure 5.5 XRD pattern of Ni-Mn-Ga thin film as-deposited at room temperature on NaCl substrate. ... 101

Figure 5.6 SEM micrographs of plane view of Ni-Mn-Ga thin film deposited on Si (100) substrate at different argon pressures: (a) 3.2 mTorr, (b) 4.2 mTorr, (c) 5.2 mTorr, (d) 6.2mTorr. ... 103

Figure 5.7 (a) SEM micrograph of Ni-Mn-Ga thin film deposited at 500°C on Si (100), (b) EDS spectrum of selected region marked in red square. ... 104

Figure 5.8 Optical micrograph of Ni-Mn-Ga thin film deposited on NaCl substrate at 500°C substrate temperature. ... 105

Figure 5.9 XRD spectrum of Ni-Mn-Ga thin film deposited on NaCl substrate at 500°C. 105
Figure 5.10 Effect of discharge current on composition of Ni-Mn-Ga thin film. 109
Figure 5.11 Sputtering yield as function of ion energy. 109
Figure 5.12 Sputtering yield as function of incidence angle. 110
Figure 5.13 SEM micrograph of top and cross-section of Ni-Mn-Ga thin film deposited at different discharge current: S 1 (a, b), S 2 (c, d), S 3 (e, f), and S 4 (g, h). 111
Figure 5.14 Variation of film thickness and grain size with discharge current. 113
Figure 5. 15 XRD spectrum of Ni-Mn-Ga thin film deposited at different discharge current. .. 114
Figure 5.16 SEM micrographs of the thin film and the corresponding EDS spectrum collected from the film surface. 117
Figure 5.17 Effect of substrate temperature on film composition. 119
Figure 5.18 AES depth profile Ni-Mn-Ga thin film deposited at 500°C substrate temperature. 120
Figure 5.19 AES depth profile Ni-Mn-Ga thin film deposited at 600°C substrate temperature. 121
Figure 5.20 AES depth profile Ni-Mn-Ga thin film deposited at 700°C substrate temperature. 121
Figure 5.21 Secondary electron micrographs of the Ni-Mn-Ga thin films deposited on Si(100) substrate at 5000C (NMG1), 6000C (NMG2), and 7000C (NMG3). (a), (c), and (e) Morphology of thin films planar surfaces. (b), (d), and (f) Micrographs of the cross-sectioned films. 124
Figure 5. 22 Effect of substrate temperature on grain size and film thickness. 125
Figure 5. 23 X-ray diffraction spectrum of Ni-Mn-Ga thin films deposited at substrate temperatures 500°C, 600°C, and 700°C. 126
Figure 5. 24 3D Atomic force microscopy (AFM) image Ni-Mn-Ga thin films: (a) As-deposited; (b) Annealed. 128
Figure 5. 25 XRD spectrum of Ni-Mn-Ga thin film deposited at room temperature and annealed at 600°C. 129

Figure 6.1 Schematic planar magnetron sputtering with electron trapping. 131
Figure 6.2 Classification of technologies based on number of parts and parts complexity [286]. 132
Figure 6.3 (a) Target design created in SOLIDWORKS; (b) Top view of target; (c) Cross-sectional view. The dimensions are in inches. 135
Figure 6.4 Thin film lamella welded to TEM copper grid. 137
Figure 6.5 Particle size distribution of Cu powder. 139
Figure 6.6 SEM micrograph of Cu powder. 140
Figure 6.7 XRD pattern of Cu powder. 140

Figure 6.8 3D printed disc copper targets after curing (a) Planar, (b) Non-planar. 141

Figure 6.9 Photo of sputtering targets: (a) TC 1 planar target sintered at 1075°C for 3 hours; Non-planar target (b) TC 2 sintered at 1075°C for 3 hours, (c) TC 3 sintered at 1080°C for 3 hours, (d) TC 4 sintered at 1085°C for 3 hours. 143

Figure 6.10 SEM micrograph of copper target sintered at: (a) 1075oC and (b) 1085oC. 144

Figure 6. 11 Optical micrograph of cross-section of copper target. 145

Figure 6.12 Distribution of magnetic field lines near surface of proposed target design. 146

Figure 6.13 Optical image of targets after 3 hours of deposition (a) Planar (b) Non-planar. 147

Figure 6.14 Erosion depth profile of planar and non-planar target. 148

Figure 6.15 2D AFM image of copper thin film deposited at room temperature. 149

Figure 6.16 XRD pattern of as-deposited and annealed copper thin films. 150

Figure 6.17 Crystallite size and microstrain as a function of annealing temperature. 152

Figure 6.18 Bright field TEM and selected area diffraction pattern (SADP) of copper film annealed at 400°C. 153

Figure 6.19 Effect of rapid thermal annealing on electrical resistivity of copper thin films. 154

Figure 6.20 SEM micrograph of the top view of copper films sputtered from different targets: (a) Flat and (b) Non-flat. 156

Figure 6. 21 XRD pattern of copper films sputtered from different targets: (a) Flat and (b) non-flat. 157

Figure 7.1 Solidworks design for disc target. 159

Figure 7.2 Particle size analysis of 316L SS 162

Figure 7.3 316L SS powder (a) SEM micrograph (b) EDS spectrum. 162

Figure 7.4 XRD pattern of 316L SS powder 163

Figure 7.5 SEM micrographs of as-sintered target (a) Low magnification (b) High magnification. 164

Figure 7.6 Polished cross-section of 316L SS target (a) SEM (b) EDS spectrum. 165

Figure 7.7 XRD pattern of 316L SS target. 166

Figure 7.8 AFM image of as-deposited 316L SS thin film. 167

Figure 7.9 Cross-section of 316L SS thin film placed in a plastic holder embedded in epoxy: (a) SEM micrograph, (b) EDS 167

Figure 7.10 XRD pattern of as-deposited 316L SS thin film. 169

Figure 7.11 SEM micrographs of top and cross-section view of 316L SS thin films at different substrate temperatures: (a) 200°C, (b) 300°C, (c) 400°C , (d) 400°C. 170

LIST OF TABLES

Table 2.1 Process parameters for 3D printing of Ni-Mn-Ga powder in the ExOne Innovent+ machine. 46
Table 2.2 TRIM input parameters for simulation. 56

Table 3.1 Quantitative EDS analysis data for ball milled Ni-Mn-Ga powder. 61
Table 3.2 Transformation temperatures from DSC plot. 65

Table 4.1 Density of 3D printed Ni-Mn-Ga targets sintered at temperatures 1065°C, 1070°C, 1075°C, and 1080°C. 78
Table 4.2 Chemical composition of Ni-Mn-Ga powder and sintered targets. 83
Table 4.3 Phase transformation temperatures obtained from DSC sintered Ni-Mn-Ga targets. .. 89

Table 5.1 EDS quantitative analysis of as-deposited Ni-Mn-Ga thin film on Si (100). 98
Table 5.2 EDS quantitative analysis of as-deposited Ni-Mn-Ga thin film on NaCl substrate. .. 101
Table 5.3 Composition of Ni-Mn-Ga thin films deposited at different discharge current, S 1 to S 4 labeling indicates samples obtained at different discharge current. 107
Table 5.4 Film thickness measurements and uniformity calculations for Ni-Mn-Ga thin films deposited at different discharge currents 113
Table 5.5 Chemical composition of thin films deposited at different substrate temperatures.... 116

Table 6.1 Distribution percentile values of Cu powder 139
Table 6.2 Mass of fresh targets measured before and after 3 hours of sputtering. 146
Table 6. 3 Estimation of crystallite size, dislocation density, and microstrain for as-deposited and annealed copper thin films. 151
Table 6. 4 Estimation of crystallite size, dislocation density and microstrain of copper films from flat and non-flat target 157

Table 7.1 Printing parameters used for 316L SS target. 159
Table 7.2 EDS quantitative analysis of 316L SS target 165
Table 7.3 EDS quantitative analysis of cross section of 316L SS thin film. 168

LIST OF ACRONYMS

AM –Additive Manufacturing

AES – Auger Electron Spectroscopy

AFM – Atomic Force Microscopy

ALD – Atomic layer deposition

BJ – Binder Jetting

BJAM – Binder jetting Additive Manufacturing

EDS – Energy Dispersion Spectroscopy

HIP – Hot Isostatic Pressing

SEM – Scanning Electron Microscopy

FIB – Focused ion beam

TEM – Transmission Electron Microscopy

XRD – X-Ray Diffraction

DC – Direct current

AC – Alternating current

RF – Radio frequency

FESEM – Field emission scanning electron microscope

BSE – Backscattered electron

SE – Secondary electron

LM – Light microscope

DIC – Differential interference contrast

LDS – Laser diffraction spectroscopy

MEMS – Micro-electro-mechanical systems

CAD – Computer aided design

TRIM – Transport of ions in matter

SRIM – Stopping and range of ions in matter

MRL – Materials research laboratory

SS – Stainless steel

MFIS – Magnetic field induced strain

IC – Integrated circuit

RPLD – Reactive pulsed laser deposition

PSD – Particle size distribution

NM – Non-modulated

PREFACE

General Overview and Research Purpose

Additive manufacturing (AM) is a geometry-independent process of printing parts by adding materials in layers from a 3D model [1–3]. Materials processed using AM technique, undergo complex thermal processing cycles which does not guarantee a transfer of inherent properties of the enjoining elements to the manufactured parts. This phenomenon is evident in the analysis of the microstructure and post processes especially in the shape memory alloy field. Nevertheless, binder jetting (BJ), one of the prominent metallic AM techniques has been successfully used to produce system parts out of Ni-Mn-Ga, Copper, 316L stainless steel, ceramics and some novel alloys and metals lately [2, 4–13]. This is a concept farfetched and never tried in the production of sputtering targets for thin films, most importantly at a time when demand for such products is at its peak. Sputtering target is an important component in a magnetron sputtering system used as a starting material for thin film fabrication. Magnetron sputtering technique is the most common technique used in the thin film technology industry which utilizes plasma to generate energetic positive ions to eject atoms from a target material and transport the atoms by diffusion onto a substrate material. One can conclude that, the target material is an essential component of the sputtering process which requires serious attention. The quality and development of Ni-Mn-Ga thin films depend largely on the target quality which is an important and expensive component of the sputtering deposition process. Despite the advantages of binder jet additive manufacturing (BJAM), such as relative simple equipment, low production cost, and simple mount which requires no support structures the technique is also challenging in terms of creating highly dense products [14]. In effect, the relative packing density of the as-printed parts from BJAM are usually low [15]. However, there are proven solutions to address densification problems as reported by different

research groups [8], [9], [16]. These authors and others have shown that BJAM technique is a viable technique for building metal parts with complex and customized designs.

The main purpose of this research was to investigate the feasibility of employing BJAM in Ni-Mn-Ga alloy sputtering target manufacturing and to extend target life by proposing an optimized target designs capable of increasing target utilization and cost reduction. As a proof of concept, sputtering targets with various geometries obtained by 3D binder jet printing from Cu and 316L stainless steel powders have also been produced and investigated in this research. It is expected that the complex geometry target will provide a better material utilization, as compared to the flat circular targets. In addition, another purpose of this work is to fabricate thin films from 3D binder jet printing targets and to compare their morphology, crystallographic, and chemical characteristics to that of the thin films obtained from conventional targets as reported in literature. Furthermore, effect of deposition parameters such as the discharge current and substrate temperatures on the surface morphology, composition, and crystal structure of thin films obtained in this research would be investigated.

CHAPTER 1

Thin Films and Sputtering Targets

This chapter will briefly review thin film manufacturing, as well as an important component of this process, namely sputtering targets. After reviewing the sputtering targets manufacturing processes and the factors influencing the quality of these components, a general review of the targets of interest on this research will be provided. Typical target manufacturing processes such as casting and powder metallurgy techniques will be briefly discussed. The current status of thin film manufacturing using materials of interest in this research (Ni-Mn-Ga, Cu, and 316L stainless steel) will also be introduced.

1.0 Introduction to thin film deposition

There are several thin film fabrication techniques available for deposition of metals and semiconductor materials. The most common among them is sputter deposition. Sputter deposition involves ejection of atoms from a target material by energetic ions transported onto a substrate material. Several interactions occur during sputter deposition which includes ion implantation, reflection, sputtering, secondary electron emission, chemical reactions, and adsorption as schematically represented in Figure 1.1.The most important interactions during sputter deposition are sputtering and secondary electron emission [17], [18].

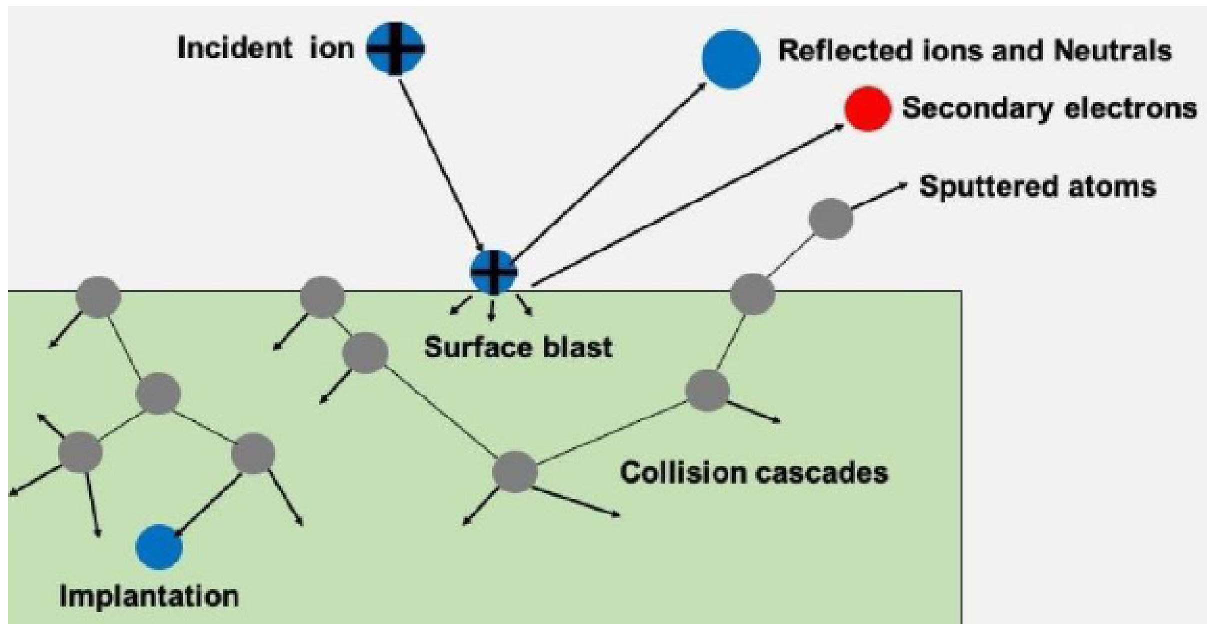

Figure 1.1 Energetic ions-target atom interaction.

Sputtering is basically achieved through the bombardment of a solid surface with high-energy particles such as argon, xenon, and etc. which are scattered backward as a result of the collision with the target surface [18]. In a case where the scattered atoms from the high-energy particle bombardment get transmitted through the material, the phenomenon is called transmission sputtering. There are different sputtering types based on design for thin-film deposition like direct current (DC) diode, radio-frequency (RF) diode, magnetron sputtering, and ion beam sputtering. DC diode sputtering system is the simplest technique and it is shown schematically in Figure 1.2. The DC diode sputtering system comprises a low pressure argon-filled chamber with a pair of planar electrodes one of which is a cold cathode bearing the target material(s) to be deposited on the surface and an anode on which the substrate is placed. At high enough potential between the electrodes, Ar^+ ions in the plasma state are generated moving at high speeds towards the target

surface. The Ar^+ ions have sufficient energy to dislodge target atoms which are transported by diffusion onto a substrate material where they accumulate building thin-film layers. Main drawback of DC diode sputtering technique is low deposition rate. DC diode sputtering technique is usually suitable for metal or alloy targets. Insulator or semiconductor targets are not suitable in the DC diode sputtering system due to build-up of electrostatic charges hindering the sustenance of the glow discharge during sputtering. The remedy for such situation is to employ alternating current (AC) or radio-frequency (RF) voltage. The sputtering system with the RF voltage is called RF diode sputtering.

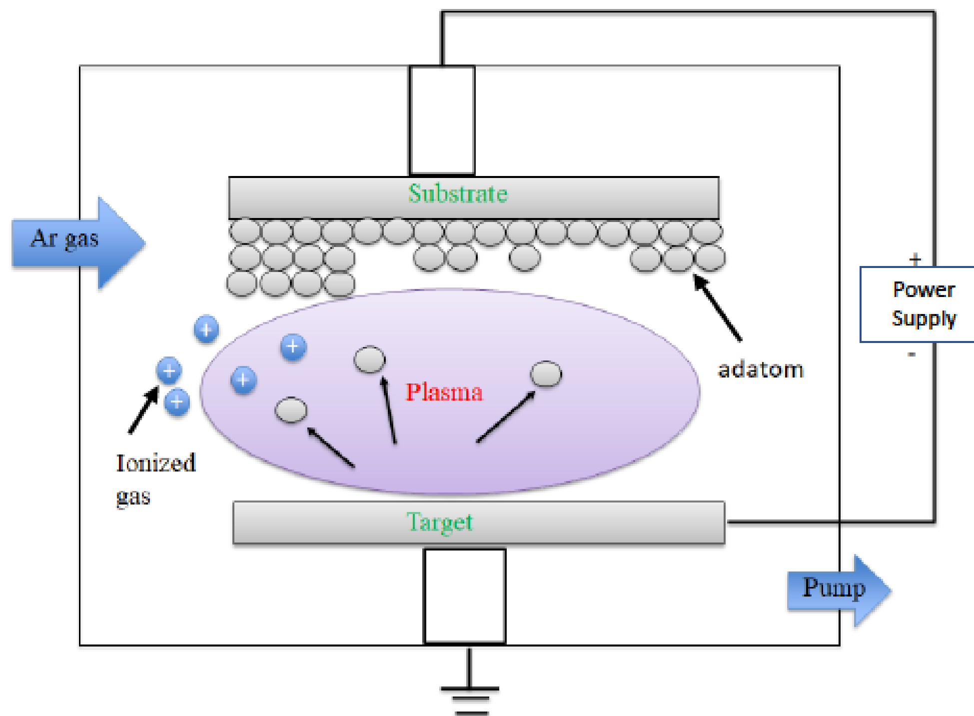

Figure 1.2 Schematic diagram of DC diode sputtering system.

In magnetron sputtering, the plasma discharge is induced by magnetic field superposed on the cathode and parallel to the cathode surface as shown in Figure 1.3. The magnetron sputtering system is design in a similar fashion like the DC diode sputtering. The only addition is a magnet (permanent or temporal) placed behind the cathode target for electron trapping. In this sputtering

system, the electrons in the plasma discharge move in a cycloidal motion in the direction of the electric (E) and magnetic (B) fields, E×B and drift velocity of E/B [19]. The electrons follow a path in the direction of the magnetic field orientation in a closed loop. This orbital restriction causes an increased collision frequency between the electrons and sputtering gas molecules in a phenomenon called electron trapping effect which allows the sputtering gas pressure to be reduced [18]. The plasma density is also controlled by the magnetic field which bears a cascading effect on the current density at the cathode target. By increasing the magnetic field, the plasma density also increases current density and ultimately the sputtering rate at the target. At low operating gas pressures, collision between sputtered particles is effectively controlled resulting in an increased deposition rate.

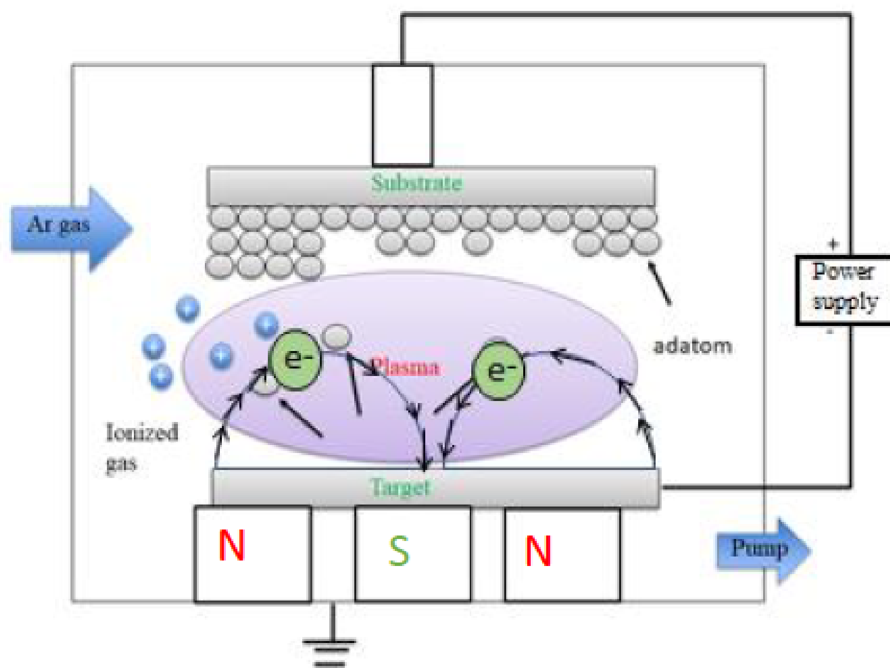

Figure 1.3 Schematic diagram of DC magnetron sputtering system.

It is important to note that the source material in all the sputtering techniques is the sputtering target. Thin film performance largely depends on sputtering target and the deposition parameters.

It is important to have the right properties in the sputtering target to get quality thin films as explained in the subchapters below.

1.1 Introduction to sputtering targets

Manufacturing of sputtering targets

Traditionally, sputtering targets are produced by casting metallurgy and powder metallurgy [20]. Casting metallurgy requires various types of furnaces such as induction melting, vacuum induction melting, electron beam melting and vacuum arc melting. Powder metallurgy involves powder processing, blending, sintering and hot pressing or hot isostatic pressing (HIP). The performance of sputtering targets depends on the following factors [20]:

- Chemical composition or purity of target
- Grain size
- Crystallographic texture
- Surface roughness
- Cleanliness of sputtering surface

Chemical Composition

The sputtering target used for thin film fabrication are of high purity. This must be also true for Ni-Mn-Ga thin film where the transformation temperatures are very sensitive to composition. Controlling target composition during manufacturing is very important. Target materials commonly used are pure metals, metallic alloys or compounds, and semiconductors. It is expected that the chemical composition of targets is transferred to the deposited film. However, in most cases it is not so, this is largely dependent on a number of factors such as the deposition conditions and the purity of the starting material. Controlling the composition of a multicomponent or a compound target is more complicated than a single or elemental target due to preferential

sputtering. co-sputtering technique which involves firing different targets simultaneously is sometimes employed to effectively tailor film composition. It is important to note that, significant deviation from target composition can affect film properties such as the crystal structure and the microstructure.

Grain size

Target grain size is another feature that plays a key role in obtaining a uniform film thickness. Target with fine grain size enables higher deposition rates than target with coarse grain size because discontinuities at the grain boundaries are more readily attacked during sputtering [21]. Bouchard *et al.* reported that fine grain size improve film uniformity whereas coarse grain size degrade film uniformity [22]. Leybovich *et al.* have shown that changing target grain size can significantly affect the stability of the plasma, deposition rate and film uniformity [23]. Dunlop *et al.* disclosed in the Pat. No.5809393 a correlation between grain size and film uniformity as shown in the Figure 1.4 [21]. A linear relationship is observed between film uniformity and target grain size in Figure 1.4 for grain size range between 100 µm to 150 µm. Michaluk *et al.* also reported that the uniformity of high-purity aluminum and titanium films is inversely proportional to the target grain size greater than 100 µm [24]. Michaluk proposed a model equation which connects the time required to consume a monolayer of a grain of a polycrystalline tantalum target and the sputtering yield of orientation for effective sputtering given by equation (1.1):

$$t_{(hkl)} = \frac{A^2_{e(hkl)}}{S_{(hkl)}} \tag{1.1}$$

Where $A^2_{e(hkl)}$ represents effective area of crystal and $S_{(hkl)}$ represents the sputtering yield of (hkl) orientation. This theoretical model connect the gain size and the crystallographic texture of the tantalum target which was used to demonstrate the erosion behavior of the target during sputtering.

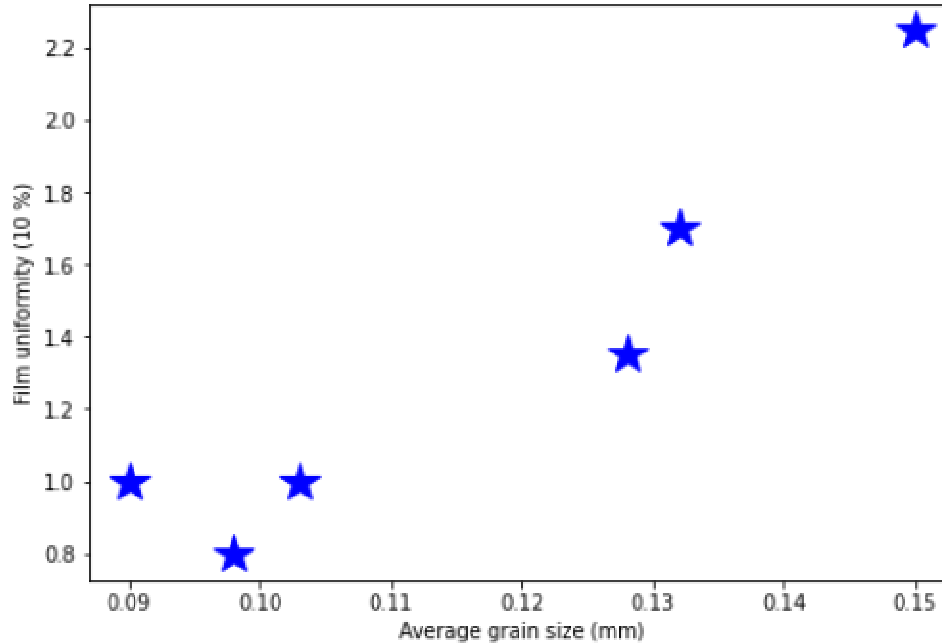

Figure 1.4 Variation of film uniformity as a function of target grain size [21].

Crystallographic texture

Crystallographic orientation of sputtering target affects the angular emission distribution and the sputtering yield of the sputtered atoms. Several researchers have reported the effect of crystallographic orientation on the ejected atoms where they showed that ejected sputtered atoms occurred preferentially along closed packed directions in the target [25]. Tsuge *et al.* have shown that heavy atoms such as Au, are preferentially ejected from closed-packed direction even at oblique incidence [26]. Zhang *et al.* have reported that changes in the target crystallographic orientation from (111) to (100) to (110) affect the sputtering yield in tantalum target [27]. Hoon Cho showed that proper control of crystallographic texture of sputtering target can produce better uniform film thickness [28].

Surface roughness

The surface finish of a sputtering target also affects the performance of the target. It has been shown that increased surface roughness results in an increased thickness of deformed layer [29].

The presence of the deformed layer results in undesirable film properties such as low film uniformity [29]. High surface roughness can also initiate nodule formation during target erosion. This can be a possible challenge for 3D printed sputtering targets, due to the inherent high roughness of the free surfaces of a 3D binder jet printed parts [30]. Notwithstanding, the surface roughness can be improved by proper selection of parameters followed by surface polishing.

Cleanliness of target surface

Surface cleaning is required in order to remove all forms of contaminations which may trickle down into the formation of film compromising thin film properties. Surface cleaning plays an essential role in obtaining a high purity thin film [31].

1.2 Metallurgical defects on sputtering target

Most target manufacturing techniques are prone to metallurgical defects. Considerable effort is required to limit metallurgical defects to the barest minimum. The following are the most common defects found in sputtering targets [20]:

- Porosity or voids
- Inclusions
- Nodules

Porosity or voids

In target manufacturing, pores can develop due to either gas entrapment or inadequate sintering or incomplete inter-diffusion of target materials [20]. Fung *et al.* have shown that voids along the grain boundaries in sputtering targets may act as particle source to lower sputtering yield [32]. It has been reported that uniformly distributed fine pores are less harmful than large, isolated pores. Narizuka *et al.* disclosed in Pat. No. 5320729 that voids in sputtering target has the tendency of

causing a localized glow discharge during sputtering creating instabilities in the electric discharge [33]. Lo and Gilman reported on the quality of W-Ti thin films deposited using targets made by powder metallurgy techniques [33]. The particles generated during the sputtering process and affecting the quality of the thin film are related to both redeposited spherical nodules located at the target voids and precipitated W-rich particles.

Inclusions

Poor processing during manufacturing of target can introduce contaminants such as inclusions. Inclusions are defects which cannot be predicted accurately and in addition vary in sizes. Inclusions of large sizes have shown to create electrical arc during sputtering. Therefore, precautionary measures are necessary to minimize inclusions formation [20].

Nodules

Nodules are defects that are generated by impurity atoms in the sputtering chamber or by redeposited target atoms. These defects are undesirable because their formation can result in low sputtering yield and deposition rate. Nodule formation is very common in indium tin oxide (ITO) with a cone-like morphology as shown in Figure 1.5 [34]. To mitigate their growth the following measures are required : routine cleaning of the sputtering chamber to minimize contaminants, proper cooling system available to cool the target during sputtering and use of power supply equip with reliable arc detecting capability [34].

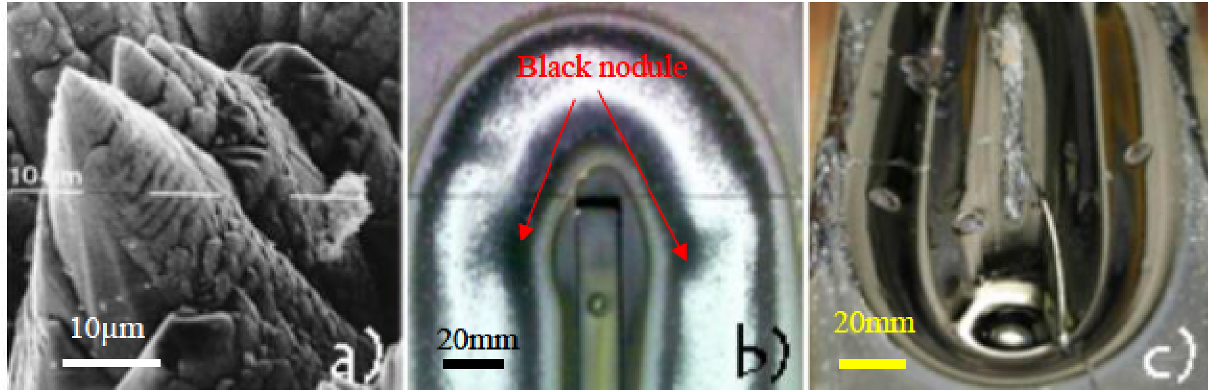

Figure 1.5 (a) SEM image showing morphology of nodules; (b) Black nodules on ITO sputtering target; (c) Nodules on Si sputtering target [34].

1.3 Target utilization

A drawback of magnetron sputtering target is the non-homogenous ion current distribution across the target surface caused by trapping of secondary electrons in the magnetic field resulting in a non-uniform erosion of the target surface in a form a racetrack as shown in Figure 1.6 (a) and (b) [37]. Due to the non-uniform etching of the target surface, material utilization is limited to about 25-30 % [36]. In the case of precious metal targets such as gold, silver, and platinum which are very expensive, makes it worse.

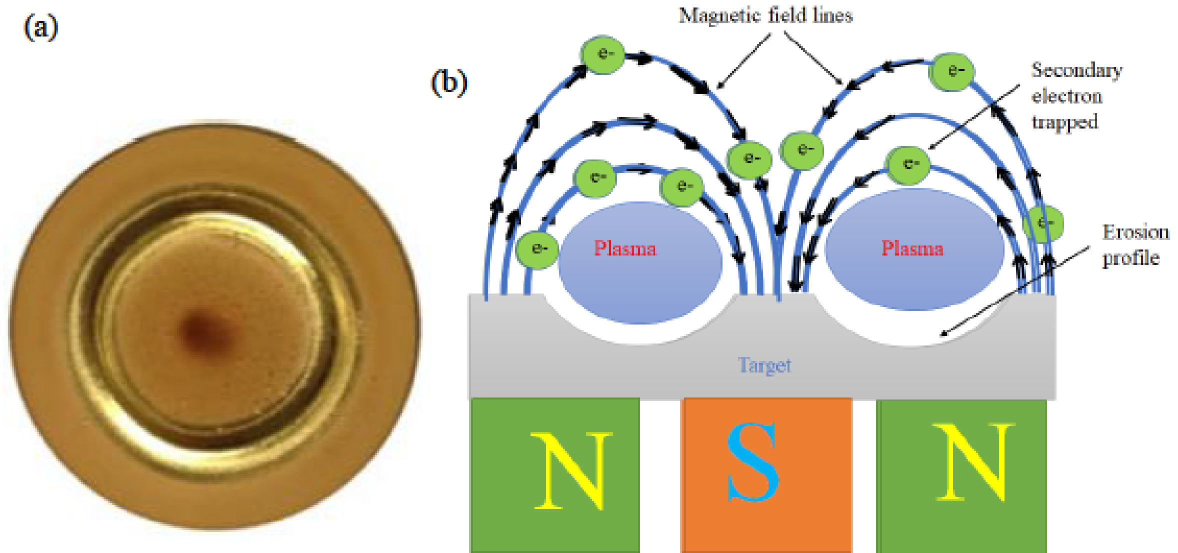

Figure 1.6 Target utilization : (a) Gold magnetron sputtered target showing non-uniform erosion in the shape of a racetrack [37], Target diameter is about 52 mm; (b) Schematic representation of the magnetic field distribution in a cross-sectional target and its relationship with the target erosion profile.

Generally, it is desirable to have a full-face target erosion to control the deposition rate and to extend the target lifetime. Several researchers have attempted to improve target utilization by focusing on the magnetic configuration of the magnetron sputtering. One of the first attempts to improve the utilization of material was the interpoles target-hollow magnetron shown in Figure 1.7 [38]. It was reported that the erosion zone was broadened with magnetic field parallel to the target which resulted in about 60% increase in material utilization [39]. Another design solution for improving the target utilization is the use of rotatable parts [37]. This option is most used with cylindrical targets. In this case the magnetron has a similar configuration to a rectangular magnetron, but the target is a hollow cylinder that rotates around the magnetron, so the erosion is uniform on the surface of the cylinder [36]. This method is usually applied for high-area rotatable substrates, but also find some use in planar magnetrons [37]. Charles Garrett reported in US Pat.

No. 4444643 that target utilization can be improved by using movable magnetic source. The magnetic source is hydraulically moved with respect to the target and substrate in such a way that the lines of magnetic flux are parallel to the target surface. Moreover, the lines of magnetic flux are swept across the target surface during sputtering process [40]. The challenge with Garrett's approach is a reliable device for providing a uniform mechanical motion. Therefore, Garrett's approach is quite complicated. Several complex magnetic field configurations have been used to optimize the magnetron sputtering but based on the literature research, so far very few researchers have considered optimizing the sputtering target itself. Lamont in the US Pat. No 4457825 disclosed the usage of an annular shaped sputtering target with inward sloping face like the frustum of a cone, in an attempt to optimize target utilization [41]. Class *et al.* also disclosed in US Pat. No. 4842703 of using a bowl-shaped concaved target as their source of sputtering material to broaden the erosion profile at the same time achieving uniform film thickness [42].

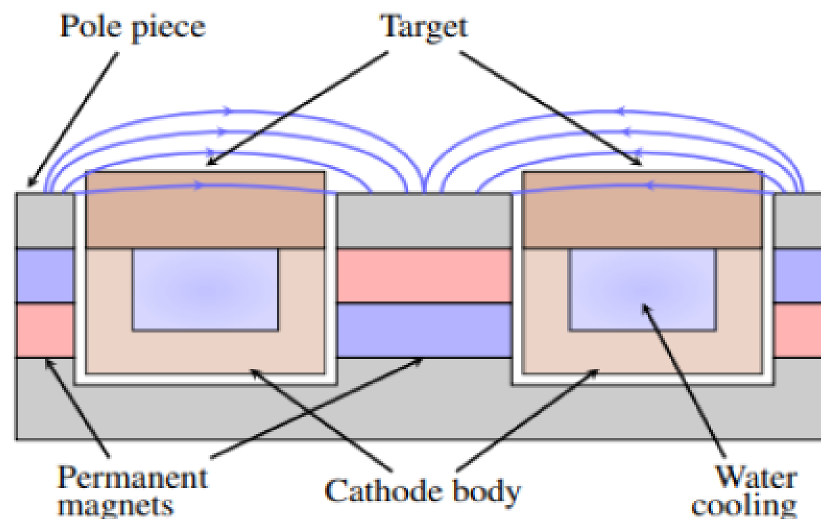

Figure 1.7 The interpoles target-hollow magnetron increases target material utilization by 60% [38].

1.4 Influence of deposition parameters on film properties

Substrate temperature

Generally, films deposited at room temperature in most cases are amorphous or partially crystalline. This happens because at low substrate temperatures, adatoms have low kinetic energy which is not sufficient enough to enhance mobility and surface diffusion. The adatoms under this condition are unable to migrate to favorable nucleation site to promote grain growth. In most cases, film deposited at room temperature show smooth and featureless morphology under certain deposition conditions [43]–[45]. However, at higher substrate temperatures, adatoms gain sufficient kinetic energy which makes them more mobile to locate favorable nucleation site for grain growth. Note that, increasing substrate temperature increases surface diffusion of adatoms which results in increasing grain size. The above assertion is supported by equations (1.2) [46] and (1.4) [47]:

$$\upsilon = \upsilon_o exp\left(\frac{-\Delta E}{K_B T}\right) \quad (1.2)$$

$$\upsilon_o = \frac{2K_B T}{h} \quad (1.3)$$

$$D^n - D_o^n = K(T)t \quad (1.4)$$

Where υ is the surface diffusion rate, υ_o is the atom frequency of vibration, K_B is Boltzmann constant, h is the Planck's constant, T is the substrate temperature, ΔE is the activation energy, D is the grain diameter, D_o is the initial grain diameter, n is the growth exponent, K(T) is the grain growth constant given by

$$K(T) = A \cdot e^{\frac{-\Delta E}{K_B T}} \quad (1.5)$$

Where A is a pre-exponential factor.

Equations (1.2) and (1.4) indeed show that the grain size and surface diffusion increase exponentially with substrate temperature. It is not surprised that, several authors have reported about the fact that, increasing substrate temperature produces large grains and high film thickness as seen in Figure 1.8 [18].

Figure 1.8 (a) show that, initially grain size increases exponentially with substrate temperature until a certain threshold is reached where a decline in grain size is observed as substrate temperature increases. It has been explained that at higher substrate temperature, kinetic energy of the incident ions increases with increasing mobility of adatoms resulting in large grain size. However, at a certain threshold kinetic energy, the mobility of adatoms decreases due to impingement of incident ions on the substrate thereby reducing grain size of adatoms as seen in Figure 1.8 (c) [18].

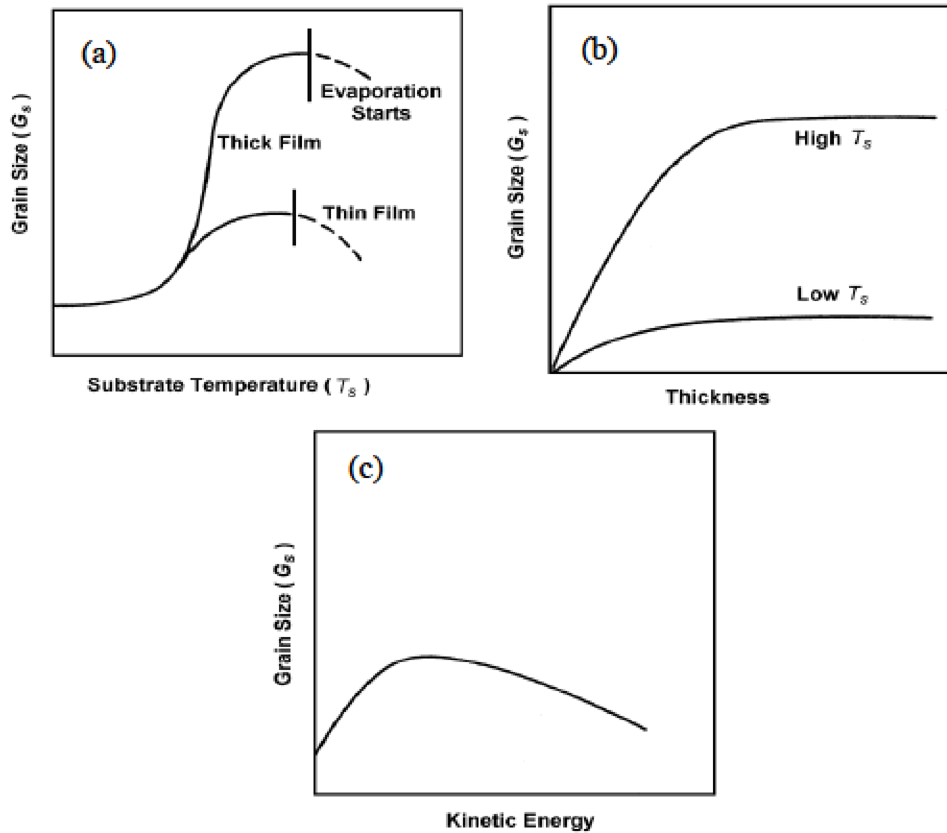

Figure 1.8 Grain size as a function of : (a) Substrate temperature; (b) Film thickness; (c) Kinetic energy of incident ions [18].

Deposition pressure

The working gas commonly used in DC magnetron sputtering is argon. Argon is used because it is inert and heavy enough to cause sputtering. The pressure of argon gas plays important role during sputtering and film formation. At low deposition pressure, few collisions occur between the argon ions and the sputtered atoms therefore less thermalization of sputtered atoms. In this way, more sputtered atoms would find their way onto the substrate increasing deposition rate. The mean free path which is the distance travelled between collisions is increased. Increasing the deposition pressure generates more argon atoms and therefore increases collision between argon

ions and the sputtered atoms due to reduced mean free path (λ). The mean free path (λ) is related to the gas pressure by the equation [48] :

$$\lambda = \frac{kT}{\sqrt{2}\, p\pi d^2} \qquad (1.6)$$

Where p is the gas pressure, d is the diameter of atom, k is the gas constant, T is the temperature. From equation (1.4), it is seen that the mean free path is inversely proportional to the gas pressure, which means increasing gas pressure corresponds to decrease mean free path which suggest that more collisions and thermalization of sputtered atoms. Deposition rate in this case would reduce because it is possible most of the sputtered atoms would be scattered away from the substrate. Also due to the thermalization, the sputtered atoms have less kinetic energy to increase deposition rate. The work by Helmer *et al.* showed that for gas pressure greater than 10 mTorr, the deposition rate varies inversely with pressure [49].

Sputtering power

In order to produce a glow discharge in the sputtering system, a certain minimum power is required so that the argon ions between the cathode and the anode can have sufficient energy greater than the binding energy of the target atoms to dislodge atoms from the target. Increasing the power, increases the glow discharge formed on the cathode (target). At higher sputtering power, argon ions gain higher kinetic energy due to momentum transfer. The current density or flux (J) is related to the DC applied voltage (V_{DC}) given by:

$$J = \frac{4\varepsilon_o}{9D^2}\sqrt{\frac{2e}{m}}\, V_{DC}^{\frac{3}{2}} \qquad (1.7)$$

Where D is the distance between the cathode and the anode, m is mass of Ar ion, e is the electronic charge, ε_o is the permittivity of free space. This equation is called the Child-Langmuir relation. Some authors have observe direct linear relationship between sputtering power and deposition rate [50], [51].It has also been shown that the sputtering power has influence on film microstructure, composition, crystallinity, and other physical properties [52]–[54].

1.5 Ni-Mn-Ga targets and thin films

1.5.1 Background

Ni-Mn-Ga Heusler alloy has been widely studied over the past two decades due to one of its unique functional property called magnetic field induced strain (MFIS) [55]. The MFIS was first achieved in 1996 by Ullakko *et al.* where a magnetic field of 8 kOe was applied to a single crystal Ni_2MnGa alloy at 265K inducing a strain of about 0.2% [55]. This was groundbreaking research and has attracted a lot more research in improving the MFIS in this material [56]. This exceptional property of Ni-Mn-Ga alloy makes it a good candidate for industrial applications such as actuators, sensors, and MEMS devises [57], [58]. Martensitic phase transformation is one of the important criteria required in Ni-Mn-Ga alloy to exhibit MFIS [59]. Martensitic phase transformation in Ni-Mn-Ga alloy is composition sensitive [60]. Chernenko *et al.* investigated the effect of composition of Ni-Mn-Ga alloy on the martensitic start transformation temperature [61]. The results from their findings showed that for a composition where Mn content is held constant, an increase in Ga content resulted in lower martensitic phase start transformation temperature (M_s). Also, for a composition whereby Ni content is held constant, an increase in Mn content shows an increase in M_s [61]. Tsuchiya *et al.* also investigated the composition dependence of martensitic transformation on polycrystalline Ni-Mn-Ga alloy. Their results showed that there is a strong correlation between the martensitic transformation temperature and the valence electron

concentration, e/a [62]. Zhou *et al.* recently demonstrated that combinatorial approach was an effective method to investigate the composition dependence on martensitic phase transformation [63]. Based on the work of several researchers in this field, it has been established that the chemical composition and electron concentration, *e/a*, of Ni-Mn-Ga alloy influence the martensitic transformation temperature. This suggest that to observe shape memory effect and magnetic field induced strain (MFIS) in Ni-Mn-Ga alloy a careful control of the chemical composition is essential.

Despite the exceptional properties of this alloy, there are some drawbacks which hinder it suitability for industrial application. For instance, single crystal Ni-Mn-Ga alloys exhibit the highest magnetic field induced strain value of 10 % and good mechanical properties. However, fabrication of single crystal Ni-Mn-Ga is very complicated, time consuming , expensive and prone to chemical segregation during crystal growth [64]–[66]. Polycrystalline Ni-Mn-Ga alloy on the other hand are cheaper and simpler to produce [67]. However, polycrystalline Ni-Mn-Ga alloy show lower MFIS (about 0.1%) due to the presence of grain boundaries which hinder twin boundary motion [68]. Another limitation of the polycrystalline Ni-Mn-Ga alloy is its intrinsic brittle nature making it difficult to plastically deform into other shapes. It has been reported that, reduced sized Ni-Mn-Ga alloy samples such as wires, ribbons and thin films have better properties and therefore have potential for practical application. Among the reduced sized samples, Ni-Mn-Ga thin films have attracted a lot of attention due to it suitability for application in miniaturized actuators, sensors, and microelectromechanical systems (MEMS) devices. Ni-Mn-Ga thin films are more ductile than the bulk polycrystalline alloy [69].

For Ni-Mn-Ga thin film to be used for practical application, two primary functional properties needed are ferromagnetic and shape memory behaviors which strongly depend on their chemical

composition and their fabrication techniques [69]. Several fabrication techniques such as pulsed laser deposition (PLD) [70]–[73], molecular beam epitaxy (MBE) [74], flash evaporation [75], ion beam sputtering [76], and magnetron sputtering [69], [77]–[81] have been used to grow Ni-Mn-Ga thin films. Among these techniques, direct current (DC) and radio frequency (RF) magnetron sputtering have been widely used. This is because it has several advantages such as high deposition rate, good adhesion to substrate, high purity films, and uniform thin film as compared to the other techniques [82]. In magnetron sputtering system, argon atoms are ionized and accelerated toward the target material by applied negative voltage to sputter Ni, Mn and Ga atoms which are deposited on the substrate to form Ni-Mn-Ga thin film. The martensitic transformation temperatures which bring about the shape memory effect are very sensitive to factors such as composition, contamination, annealing, sputtering power, gas pressure, alloy target, co-sputtering multi-targets, deposition temperature, substrate to target distance, substrate type and substrate condition. Most of the research on Ni-Mn-Ga thin film have been focused on the effects of sputtering parameters which include substrate temperature, annealing temperature, gas pressure, sputtering power, film thickness, substrate type and power source (DC or RF). However, the sputtering target being the primary material source for the deposition process, not much has been reported on the properties of Ni-Mn-Ga targets. Sputtering targets play a key role in the formation and the properties of the thin film. Therefore, the method of manufacturing, surface finish and handling of targets must be a critical concern.

1.5.2 Ni-Mn-Ga targets

The two main methods for producing Ni-Mn-Ga alloy targets reported in literature are casting and powder metallurgy [77], [83]–[86]. The casting metallurgy approach involves arc melting raw materials of high purity nickel, manganese and gallium ingots under argon atmosphere and

homogenizing to achieve uniform composition. The melt is cast into a target mold and allowed to cool, afterwards is machined to the required geometry for use in a magnetron sputtering system. Machining of the targets create waste (though the waste material can be recovered and reprocess for making new targets), which increases the production time of the entire manufacturing process. Due to the brittle nature of Ni-Mn-Ga alloy, a careful machining of the target is required to avoid cracks and defects. So far, casting technique has been widely used in Ni-Mn-Ga alloy target manufacturing. However, it has some limitations. One of which is the inability to obtain near-net shape after casting. The polycrystalline Ni-Mn-Ga alloy is inherently brittle and therefore machining to achieve sputtering targets with complex geometries would be challenging.

Several researchers have implemented the casting technique in making sputtering targets for Ni-Mn-Ga for thin film fabrication. Liu *et al.* investigated the effects of deposition pressure and sputtering power on the composition of Ni-Mn-Ga thin films using cast target [87]. Their analysis showed that Mn and Ni contents have strong dependence on the deposition pressure while Ga content barely changed. Wu *et al.* also reported on the crystallization behavior of radio frequency sputtered Ni-Mn-Ga thin films using Ni_2MnGa cast target [85]. Their results showed that as-deposited $Ni_{51.45}Mn_{25.30}Ga_{23.25}$ thin films were partially crystalline on Si (100) substrate. Complex transformation behavior of free standing epitaxial Ni-Mn-Ga films using $Ni_{46}Mn_{32}Ga_{22}$ target prepared by casting metallurgy was reported by Yeduru *et al.* [77]. They observed two stage transformation behavior in temperature ranges 40°C to 80°C and 140°C to160°C.

Powder metallurgy on the other hand, involves preparation of powders, blending and mixing of powders, compaction of powders in a target mold by hot pressing or hot isostatic pressing, sintering, machining, and polishing. Unlike casting, powder metallurgy is more efficient in material utilization and achieving near net shape. However, for very complex geometries, it

becomes a challenge to manufacture parts using powder metallurgy, though many sputtering targets of simple geometries from metals, metallic alloys, semiconductors, and ceramics have been produced. Few authors have reported using powder metallurgy to manufacture Ni-Mn-Ga sputtering targets for thin film fabrication [86], [88].

Observation from literature, shows that target properties can influence thin film properties. This implies that the quality and the method of manufacturing of sputter target have direct influence on the properties of the thin films produced. It is well established that martensitic transformation temperatures of Ni-Mn-Ga alloys are composition sensitive [60]. It is usually a challenge in controlling the composition of Ni-Mn-Ga thin film using Ni-Mn-Ga alloy target in magnetron sputtering system. Controlling the composition of the thin film is an essential part of the fabrication process. One method proposed to control the composition of Ni-Mn-Ga thin films is by employing co-sputtering method which utilizes three separate targets Ni, Mn, and Ga or by co-sputtering Ni-Mn-Ga alloy target with another Mn target. Tillier *et al.* successfully co-sputtered Ni-Mn-Ga alloy target with a manganese target to grow Ni-Mn-Ga epitaxial thin films on MgO (100) substrate [89]. Their results showed precise control of the chemical composition of the Ni-Mn-Ga epitaxial thin film during deposition at high temperature [89]. However, there are few limitations associated with co-sputtering technique, such as cross contamination of targets which may require periodic cleaning of the targets [90].

Nearly two decades ago, Takeuchi and co-workers embark on using the method of thin film compositional spread to find new compositions which will results in ferroic material having properties such as ferroelectric, ferromagnetic and ferroelastic [91]. In their work, they fired three sputtering targets Ni, Mn and Ni_2Ga_3 using both direct current and radiofrequency sputtering techniques where they deposited Ni-Mn-Ga thin film on 3-inch diameter Si (100) wafer. They

observed that regions with rich Mn content and deficient in Ga show high transition temperatures. A typical composition found in this region was $Ni_{43}Mn_{47}Ga_{10}$ [91]. They also observed large regions outside near Heusler composition showing ferromagnetic and reversible martensite. Ni-Mn-Ga targets or elemental targets are quite scarce and expensive to acquire due to the complexity involved in the manufacturing. A lot of effort is put in place to control the purity and microstructural properties of the sputter target. Several alloy target compositions of Ni-Mn-Ga targets have been reported in literature for Ni-Mn-Ga thin film fabrication as shown in Table 1.1.

Table 1.1 A table of composition of alloy target and thin film of Ni-Mn-Ga and substrate used by various authors. Reported deposition conditions are: deposition pressure (Pa, mbar, or mTorr), deposition temperature (°C), sputtering power (W), deposition rate (nm/s).

Target manufacturing	Target Composition (at%)	Film composition (at%)	Substrate	Deposition condition	Reference
Hot pressing powder	$Ni_{50}Mn_{25}Ga_{25}$	$Ni_{55}Mn_{23}Ga_{22}$	Si (100)		[86]
Vacuum arc melting	$Ni_{54}Mn_{25}Ga_{21}$	$Ni_{53.97}Mn_{25.67}Ga_{20.36}$	Si (100)	0.4 Pa, 20°C, 250 W	[87]
Hot pressing powder	$Ni_{54}Mn_{20}Ga_{26}$	$Ni_{54}Mn_{18}Ga_{28}$	Al_2O_3		[92]
Hot pressing powder	$Ni_{49.5}Mn_{28}Ga_{22.5}$	$Ni_{51.4}Mn_{28.3}Ga_{20.3}$	Al_2O_3	50 °C, 200 W	[88]
Hot pressing powder	$Ni_{52}Mn_{24}Ga_{24}$	$Ni_{53.5}Mn_{23.8}Ga_{22.7}$	Al_2O_3	50 °C, 200 W	[88]
Hot pressing powder	$Ni_{45.9}Mn_{31.4}Ga_{22.7}$	$Ni_{46.7}Mn_{30.1}Ga_{23.2}$	MgO (001)	0.026 mbar, 150 W	[93]
Casting metallurgy	$Ni_{49.3}Mn_{27.8}Ga_{22.9}$	$Ni_{52.59}Mn_{19.57}Ga_{28.05}$	MgO (100)	0.012 mbar, 420 °C	[94]
	$Ni_{46}Mn_{32}Ga_{22}$	$Ni_{50}Mn_{30}Ga_{20}$	MgO (100)		[95]
Arc-melted and cast	$Ni_{50}Mn_{25}Ga_{25}$	$Ni_{51.2}Mn_{24.6}Ga_{24.2}$	MgO (001)	350 °C	[83]
	$Ni_{49.9}Mn_{27.8}Ga_{22.3}$	$Ni_{52.2}Mn_{26.8}Ga_{21}$	MgO (001)		[96]
Cast metallurgy	$Ni_{54}Mn_{20}Ga_{26}$	$Ni_{54.1}Mn_{18.1}Ga_{28.2}$	Al_2O_3	47 °C, 200W, 0.3 nm/s	[97]
Vacuum arc melting	$Ni_{50.22}Mn_{24.77}Ga_{25.01}$	$Ni_{51.45}Mn_{25.30}Ga_{23.25}$	Si (100)		[85]
Vacuum induction melting	$Ni_{50}Mn_{30}Ga_{20}$	$Ni_{55.5}Mn_{26.5}Ga_{18}$	Si (100)	0.005 mbar, 20°C, 36 W	[69]
	$Ni_{49.9}Mn_{27.8}Ga_{22.3}$	$Ni_{52.2}Mn_{26.8}Ga_{21}$	SiNx	0.026 mbar, 500 °C, 200 W	[98]
Hot pressing powder	$Ni_{49.9}Mn_{27.8}Ga_{22.3}$	$Ni_{53.5}Mn_{23.8}Ga_{22.7}$	Mo foil	50 °C, 200 W	[99]
Casting metallurgy	$Ni_{49.5}Mn_{30.3}Ga_{20.2}$	$Ni_{51.09}Mn_{30.43}Ga_{18.48}$	SiO_2	2.58 mTorr,20 °C, 400 W	[100]
Casting metallurgy	$Ni_{46}Mn_{32}Ga_{22}$	$Ni_{47.7}Mn_{31.1}Ga_{21.2}$	MgO (100)	0.68 nms^{-1}, 400 °C	[77]
Vacuum arc melting	$Ni_{49.6}Mn_{30.6}Ga_{19.8}$	$Ni_{49.7}Mn_{30.4}Ga_{19.9}$	Si (100)	10 mTorr, 20 °C, 100 W	[101]
Induction arc melting	$Ni_{52}Mn_{24}Ga_{24}$	$Ni_{52.5}Mn_{23.8}Ga_{23.7}$	MgO (100)	400°C, 100 W, 0.74 nm/s	[102]
Induction arc melting	$Ni_{52}Mn_{24}Ga_{24}$	$Ni_{52.8}Mn_{23.6}Ga_{23.6}$	MgO (100)	500 °C, 100 W, 0.74 nm/s	[102]
Induction arc melting	$Ni_{52}Mn_{24}Ga_{24}$	$Ni_{52.8}Mn_{23.9}Ga_{23.3}$	MgO (100)	600 °C, 100 W, 0.74 nm/s	[102]
Induction arc melting	$Ni_{52}Mn_{24}Ga_{24}$	$Ni_{53.1}Mn_{23.4}Ga_{23.5}$	MgO (100)	650 °C, 100 W, 0.74 nm/s	[102]

1.5.3 Ni-Mn-Ga thin films for MEMS applications

The technology and design of MEMS is largely based on micro-electro-mechanical engineering which focuses on a fabrication technique already established in the Si based integrated circuit (IC) technology [103]. MEMS device as defined by Gardner *et al.* is a device made up of extremely small components (*ie.* microparts) [104]. Quite a significant number of MEMS devices have been developed based on Si technology for specific purposes such as micro-actuators, micro-sensors, micro-fluidic devices, energy harvester, micro-chemical reactor, micro-mirror, and etc [103]. Incorporating functionality to MEMS device where actuation and sensing is possible, improves performance efficiency [105]. The main fabrication processes of MEMS devices are thin film deposition, photolithography, and etching (wet or dry). For example, MEMS of micro-actuators are manufactured through a combination of other functional modified devices like piezoelectric ceramic cantilevers to achieve an integrated multifunctional actuator system [103]. This is achieved through thin film technology constituting ferroelectrics, piezoelectrics, magnetic shape memory alloy and several other functional materials resulting in micro-Si devices [103]. Materials such as Ni-Mn-Ga alloy with high actuation strain output would be suitable for MEMS applications [106]. Integration of Ni-Mn-Ga alloy for MEMS application is still under development. A few fabrication route for integrating Ni-Mn-Ga alloy into MEMS devices have been proposed [107]. One of such is the sacrificial layer and bond transfer technology which begins with depositing a sacrificial layer of few nanometers on a single crystal substrate, followed by epitaxial Ni-Mn-Ga thin film exhibiting martensitic structures at room temperature. Next, the sacrificial layer is selectively removed through photolithography and wet chemical etching. Finally, Ni-Mn-Ga epitaxial film is transferred and bonded to a target substrate for microsystem integration [108].

1.6 Copper targets and thin film

1.6.1 Copper targets

Few decades ago, aluminum was the main conducting material or interconnects used in integrated circuit to transfer electrical signals from one transistor to the other due to it good electrical conductivity and ability to form ohmic contact with silicon substrate [109], [110]. However, for high performance silicon chip, aluminum interconnects are limited due to their high resistivity and electromigration resistance. As miniaturization of electronic components increases power density also increases thereby increasing chances of electromigration problems. Electromigration occurs under the influence of electric field involving momentum transfer between conducting electrons and metal ions in the crystal lattice of the interconnect material. Electromigration in metal interconnects can result in void creation and hillocks formation. These defects can amount to failure in the device which poses reliability problems for the chip manufacturing industry. For these reasons, aluminum was replaced with copper as an interconnect in high performance semiconductor devices. Copper was selected as an alternative because it has better properties such as low electrical resistivity, high electromigration resistance, high melting point and thermal stability [111], [112]. Although silver has better electrical conductivity than copper, nonetheless copper is much cheaper and also in abundance than silver [113]. Copper as an interconnect material is made through thin film fabrication techniques. Copper thin films have been produced by varieties of deposition techniques including reactive pulsed laser deposition (RPLD) [114], direct current (DC) and radio frequency (RF) magnetron sputtering [115]–[122], atomic layer deposition (ALD) [123], chemical vapor deposition [124], high power impulse magnetron sputtering [125], [126], supercritical fluid deposition technique [127], electron beam evaporation [128], and ionized beam deposition [129]. DC and RF magnetron sputtering techniques appear to be the most favorable among the lots. Copper thin films made by magnetron sputtering often use

copper sputtering targets. Sputtering targets influences the quality and performance of thin films, therefore how they are manufactured is essential. Current manufacturing technique for copper targets are cold spray [130], casting metallurgy [131], [132], and powder metallurgy [133]. Most of the focus in copper target manufacturing has been channeled to improving purity level, grain size refinements, crystallographic texture control, and reduction in electrical resistivity [134]–[136]. A typical grain size of copper target is around 50 μm [131], [135], [137]. Cho *et al.* employed the technique of cold spray to manufacture copper sputtering material by depositing a large thick layer of copper on Al 6061 [130]. A typical cold spray process is a solid-state process involving the acceleration of powder particles in a stream of supersonic gas jet. In their study, they used pure copper powder of average particle size of 20 μm with nitrogen gas temperature of 600°C and spray distance of 30mm and successfully deposited 20 mm thick copper film shown in Figure 1.9.

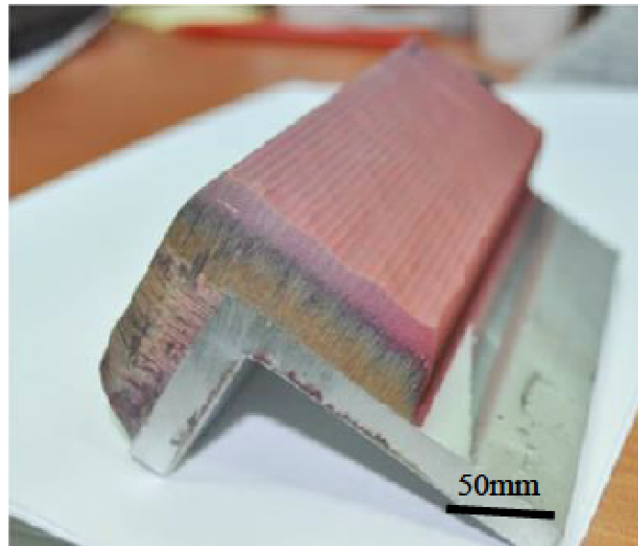

Figure 1.9 Cold spray deposited copper coating used as a sputtering target [130].

The 20 mm thick copper film was used as a target for the film deposition. Their results showed a purity level of 99.4699% which was comparable to the starting copper powder of purity 99.5%.

One advantage with cold spray process is that there is virtually no oxidation present [130]. To assess the properties of the copper thick film, post-heat treatment was conducted at temperatures 100°C, 200°C, 300°C and 400°C in argon atmosphere. Their electron backscattered diffraction (EBSD) analysis showed a non-uniform grain texture and average grain size of 1.83 μm. Though the cold spray technique has shown good target properties for copper, nonetheless, for mass production would be time consuming and expensive and may not be applicable for other target materials and substrates. Kardokus *et al.* also adopted a method which avoided melting and casting but rather machined rectangular sheet of high purity copper plate and then stacked them one on top of the other in an assembly pattern [137]. The stacked copper plate was heated at 500°C under argon atmosphere and then forged to bring down the thickness. Afterwards, further heat treatment was conducted to refined the grain size and control the grain texture. The target produced by this technique was utilized in electrodeposition to make high purity copper thin film. However, this technique may not be applicable to brittle materials like ceramics.

From the literature, it is observed that there is much quest to develop a copper sputtering target with improved properties at same time efficient and economical.

1.6.2 Copper thin film

Regarding copper thin films, much research has been conducted on the effect of sputtering parameters on film properties including surface morphology [120], [121], [123], [126], [138]–[140], microstructure [123], [141]–[143], crystal structure and texture [118], [121], [123], [144], [145], electrical resistivity [119]–[121], [125], [145]–[147], hardness and Young's modulus [115], [141], [148]–[150] and film thickness [120], [121].

1.6.2.1 Surface morphology

Film morphology has significant effect on the film quality and performance. For instance, films with micro- cracks or voided boundaries and high surface roughness can increase the resistivity of the film making it unreliable for application [151]. Deposition conditions used during film fabrication have high influence on the surface morphology of the film. Craig *et al.* investigated the influence of argon pressure and substrate temperature on the surface morphology of sputtered copper films with thicknesses 0.5 μm, 3.0 μm and 10 μm [151]. In one section of their study, the argon pressure was varied from 6.5-97.5 Pa while substrate temperature was fixed. They observed changes in film morphology from fine grains to coarse grains as the argon pressure increased. At higher argon pressures, many micro-cracks emerged with hillocks spread out on the film surface resulting in high surface roughness. In fact, the increase in the micro-cracks resulted in an increase in resistivity of the films. They concluded that the argon pressure controls the mean free path and the kinetic energy of the sputtered atoms. Yang *et al.* also reported on the impact of substrate surface and film thickness on the surface evolution of copper sputtered thin films [138]. They observed a decreasing trend in the surface roughness during the initial growth stage of the film formation in a thickness range between 130 nm and 160 nm, which they attributed to the influence of the roughness morphology of the substrate. However, as the film thickness grew past 160 nm, a uniform film morphology with a pebble-like grains and increasing surface roughness were observed. Chan *et al.* also studied the effect of sputtering power on the surface morphology of copper thin films deposited by DC magnetron sputtering [152]. Results showed smaller grains with voided boundaries dispersed on the film surface at lower sputtering power. However, at higher sputtering power coarse grains with less voided boundaries were observed. They explained that, at higher sputtering power, argon atoms are energized which is transferred to the copper atoms in

a form of kinetic energy resulting in higher surface mobility of adatoms required for continuous film formation.

1.6.2.2 Crystallinity and texture

Generally, the crystallinity and texture of most thin films are enhanced by increasing the substrate temperature and sputtering power [140], [152]–[154]. X-ray diffraction is the technique usually used for examining the crystallinity and the texture of thin films [118], [123], [140]. The reflected intensity peaks usually observed in X-ray diffraction spectrum for copper thin films are (111), (200), (220) and (311) [115], [155]. Wei *et al.* reported on the development of <110> texture in copper thin films for corrosion resistant application [144]. They demonstrated a transition of <111> texture to <110> texture as the copper film grew from thin to thicker films. Crystallographic texture influences the physical and chemical properties of copper film. For instance, <111> texture in copper thin films helps to increase the electromigration resistance [156] and oxidation resistance [123]. Chan *et al.* investigated thickness dependence on the structure and electrical properties of copper sputtered films [121]. They found that the crystallinity of the films increased as thickness increased having the (111) intensity peak as the most dominant peak.

1.6.2.3 Electrical resistivity

For copper to be suitable for interconnects, the semiconductor industry requires reduction in electrical resistivity. The deposition parameters used in sputtering can influence the electrical resistivity of copper films. The electrical resistivity of copper sputtered films has been studied to a great extent [120], [121], [127], [140], [145], [153], [157]–[160]. Le *et al.* investigated the influence of sputtering power on the electrical resistivity of copper film deposited by magnetron sputtering using four point probe [140]. They observed high resistivity value of 0.06 μΩm at a deposition power flux of 5500 Wm^{-2} which they attributed to low surface mobility of adatoms

contributing to low film crystallinity. At higher deposition power of 27400 Wm^{-2}, a lower resistivity of 0.0186 μΩm was observed due to acquisition of sufficient kinetic energy of adatoms which increased their surface mobility. They also observed that, above 100 nm film thickness, changes in the grain size as well as film thickness did not affect the resistivity. Shi *et al.* studied the electrical resistivity of copper thin films prepared by filtered cathodic vacuum arc technique [161]. Their study showed the highest resistivity value of 0.036 μΩm at a film thickness of 25 nm and lowest value of 0.018 μΩm at 150 nm film thickness. Hojabri *et al.* also reported the highest resistivity value of 0.137 μΩm with film thickness 50 nm and lowest value 0.022 μΩm with film thickness 220 nm [120]. Mukherjee *et al.* also investigated the electrical resistivity of nanocrystalline copper films deposited using anodic vacuum arc technique and reported high resistivity values for films thinner than 100 nm [158].

1.7 316L Stainless Steel target and thin films

Stainless steels (SS) are engineering materials that finds a lot of applications in the area of construction, oil and gas, aerospace, pharmaceutical and chemical process industry due to their high corrosion and oxidation resistant properties [162]–[165]. Stainless steels can be classified into five main categories based on their crystal structure [166]. They are austenitic, ferritic, duplex, martensitic and precipitation-hardening stainless steel. Among the categories of stainless steel, austenitic stainless steels are the most widely used due to their excellent corrosion resistant in harsh environment, good formability and weldability [167]–[169]. The interest to apply austenitic stainless steels as a protective coating date back in the 1970s [170]. Over the years, several techniques have been employed in fabricating austenitic stainless steel thin film which includes ion beam sputtering [168], [171], [172], magnetron sputtering [167], [173]–[177], thermal evaporation [172], [178], [179], and arc discharge [180]. Among the deposition techniques,

magnetron sputtering is the most explored due to the fact that less imperfections and defects are formed on films [181], and the capability of transporting elements of a multicomponent target with little changes in the film composition [176], [182]. It has long been observed that, sputtered austenitic stainless-steel target do not form a face centered cubic (fcc) films at room temperature but rather they form ferritic body centered cubic (bcc) films [175], [176], [183]–[186]. This is a clear deviation from the original crystal structure of the target. The ferritic bcc is known to exhibit low corrosion resistant compared to the fcc [182]. This deviation can be attributed to the different sputtering yields of the individual elements in the multicomponent target. It is important to note that, sputter target manufacturing and processing can also affect the film properties and contribute to such deviation. Most of the austenitic stainless steel targets are made by melting and casting metallurgy [175]–[177], [182], [187]. To address the deviation of the crystal structure of the sputtered austenitic stainless-steel targets, it is necessary to explore other manufacturing and processing technique to improve film properties. The most popular austenitic stainless steel thin films reported in literature are 304SS [168], [171], [173], [174], [178], [179], [187] , and 316LSS [175]–[177], [182], [186], [188]–[190]. 316L SS has comparable chemical composition to 304 SS but with additional 2%-3% molybdenum [191]. The added molybdenum content to 316L SS makes it exhibit high corrosion and oxidation resistant [176]. It has been reported that 316l SS thin films sputter deposited on substrate temperature below 375°C usually have crystal structure different from the source material [177]. Malavasi *et al.* conducted a study on the structure and crystallography texture of sputter deposited thin film on glass substrate from 316l SS target with an fcc crystal structure [193]. The structural analysis on thin film showed α-ferrite bcc crystal structure and crystallographic texture of <110> which they attributed to the change in film composition. Dahlgren also conducted phase analysis investigation of 304 SS sputter deposits on

copper substrate at different ranges of deposition temperatures [194]. Results from the analysis showed that below substrate temperature of 375°C, the film formed bcc crystal structure which agrees with previous studies, whereas between 375°C and 500°C film showed a mixture of bcc and fcc phases and at 800°C film showed fcc phase. Godbole *et al.* examined the phases and microstructure of 316l SS sputtered deposited films deposited on different substrates using X-ray diffraction (XRD) and transmission electron microscope (TEM) [175]. The substrates used in this study were microscope slides, polished oxidized and oxide-free 316l SS plates. Phase analysis results showed films deposited on microscope slides and oxidized SS contain a mixture of bcc and an ordered modified hexagonal ε-phase whereas films deposited on oxide-free SS plates contain bcc phase with <200> texture. Films containing mixture of bcc and hexagonal ε-phase transformed to purely bcc phase after annealing at 500°C and further transformed from bcc phase to fcc phase at 600°C. Films microstructure showed fine grain structure in the size range 4 - 6 nm. Recently, Schroeder *et al.* investigated the effect of changing pulsed frequency on relative stability of bcc and fcc phases in austenitic SS sputtered thin films from 316l SS target by pulse-dc magnetron sputtering [188]. The study revealed stabilization of the fcc phase which they attributed to increased average adatom energy. It is well established that nitrogen addition to austenitic stainless steel stabilizes the fcc crystal structure and enhances the mechanical properties and the corrosion resistance [169], [195]–[198]. Increasing nitrogen content in austenitic stainless steel improves the yield strength and pitting corrosion resistance [199]. Kappanthu *et al.* studied the phase evolution and morphology of sputtered deposited stainless steel thin films doped with nitrogen deposited on heated and unheated silicon substrates from austenitic 316l SS target in an argon and nitrogen atmosphere by radio-frequency (RF) magnetron sputtering [176]. The X-ray diffraction spectrum of the analysis reveal that with increasing percentage of nitrogen in the gas mixture the films

deposited at elevated temperatures transformed from a bcc α ferrite to a nitrogen stabilize austenite fcc phase and further to a distorted expanded austenite phase. Films also showed different surface morphology with fibrous growth.

CHAPTER 2

Materials and Experimental Methods

2.0 Introduction

As mentioned in the previous chapter, powders of Ni-Mn-Ga, Copper, and 316L SS were the starting materials used in this research. The steps involved in powder preparation, target manufacturing via 3D binder jet printing, and thin film fabrication by direct current (DC) magnetron sputtering will be elaborated in detailed for each material. The particle size distribution, morphology, chemical composition, crystal structure and phase transformation of powders were determined using particle size analyzer, scanning electron microscope (SEM), X-ray energy dispersion spectroscopy (EDS), X-ray diffraction (XRD) and differential scanning calorimetry (DSC). Surface morphology, chemical composition, crystal structure and phase transformation of targets were also examined using light microscopy (LM), SEM, EDS, XRD, profilometry and differential scanning calorimetry (DSC). Thin films deposition parameters were optimized especially in the case of Ni-Mn-Ga to get the film quality. Post-deposition heat treatment was performed on some thin films to improve their performance. Thin films were characterized using advanced characterization techniques such as atomic force microscopy (AFM), SEM, EDS, XRD, Auger electron spectroscopy (AES), transmission electron microscopy (TEM), and four-point probe for electrical resistivity measurement.

This chapter will focus on the experimental, analytical, and numerical methods used in fabrication and characterization of Ni-Mn-Ga targets and thin films. For the Cu and 316L SS targets and thin films the experimental methods will be presented in the individual chapters dedicated to Cu and 316L targets and thin films.

2.1 Materials

Ni-Mn-Ga powders were obtained by ball milling of Ni-Mn-Ga ingots with uniform composition obtained from two different sources. Approximately one quarter of the used Ni-Mn-Ga ingots were produced in the YSU Materials Engineering & Processing laboratory using arc melting technology. Individual ingots of approximately 15 grams have been obtained from high purity Ni (ACROS Organics, 99.97%), Mn (Alfa Aesar, 99.95%), and Ga (ACROS Organics, 99.99%) by arc melting using an Edmund Buhler MAM-1 system. The rest of the ingots have been ordered and purchased from ACI Alloys Inc.

2.2 Experimental method

2.2.1 Ni-Mn-Ga powder preparation

The powder prepared in the lab was produced from ball milling of the ingots made through arc melting of high purity nickel (99.99 at%), manganese (99.95 at%), and gallium (99.99 at%) pellets using Edmund Buhler GmbH MAM1 arc melting furnace under argon atmosphere with several re-melting to improve the homogeneity of the ingot. The chemical composition of the ball milled powder obtained in the laboratory was $Ni_{51}Mn_{30}Ga_{19}$ (at%). The second powder was ball milled from ACI Alloy Inc. Ni-Mn-Ga pellets of composition $Ni_{50}Mn_{30}Ga_{20}$ (at%). As received Ni-Mn-Ga pellets were first mechanically cleaned to remove any oxide layer from the surface to avoid contamination of the powder. The cleaned pellets were mechanically crashed and then loaded in a zirconia ceramic vial containing two ½ inch zirconia balls. The vial was placed in the SPEX sample prep mixer/mill 8000M for ball milling, as shown in Figure 2.1. The ball mass to powder mass ratio of 10:1 was chosen and was kept constant throughout the entire milling process. The milling was carried out at a rotation speed of 1425 rpm for 1 hour. The milling process was repeated for several crashed ingot with all milling parameters kept constant until Ni-Mn-Ga powder was

prepared. The Ni-Mn-Ga powder prepared in the lab was added to the ball milled powder produced from the ingots procured from ACI Alloy Inc. The mixing of the two batches of powders was performed in order to have enough powder for the operation of ExOne Innovent + binder jet printer. The building volume of the Innovent + printer (676 cm^3 [200]) requires a significant quantity of Ni-Mn-Ga powder, which was a challenge in this research, taking into account, the Ni-Mn-Ga powder is not commercially available. The slight difference in the chemical composition between the powder prepared for the homemade ingots and the one prepared for the ACI alloy Inc. ingots had no significant influence on the chemical composition of the 3D printed target, as it will be demonstrated in the following chapter.

Figure 2.1 SPEX 8000M ball milling machine used in preparing Ni-Mn-Ga powders.

After thorough mixing of two powders, sieving was performed using 75 μm standard test sieve ASTM E-11 specification with stainless steel mesh mounted on a sieve shaker with a vibratory action to separate large particles from small particles. The purpose of the sieve analysis was to obtain well distributed fine powder particles. A well distributed particle size of powder enhances flowability and packing density of additive manufactured (AM) parts.

Moreover, in binder jet 3D printing, the particle size distribution and particle morphology are key factors in determining the printing parameters needed for accurate printing of parts. For example, the layer thickness should be higher than the particle size of the powder.

2.2.1.1 Particle size analysis

Prior knowledge of particle size distribution of powders for binder jet additive manufacturing (BJAM) is essential for the optimization of printing parameters including layer thickness and binder saturation. Incorrect selection of the printing parameters can affect the build process and may introduce defects such as cracks, large pores, and non-uniformity in the built part [201], [202]. The most popular non-imaging particle size distribution technique is laser diffraction spectroscopy [203]. Laser diffraction spectroscopy (LDS) instrument is robust, easy to operate and fast to acquire data. Laser diffraction spectroscopy technique is based on the principle that light beam are scattered in the forward direction through different scattering angles by dispersed powder particles exposed to the laser beam. The scattering angle and intensity are dependent on the particle size. Small particles scatter light at large angles and large particles scatter light at small angles. The angular distribution and intensity of scattered light detected are translated by Fraunhofer model to calculate the particle size distribution. Figure 2.2 shows a schematic diagram of laser diffraction setup showing the main components of the instrument. LDS technique assumes the dispersed particles are spherical. Hence it approximates all non-spherical particles as spherical.

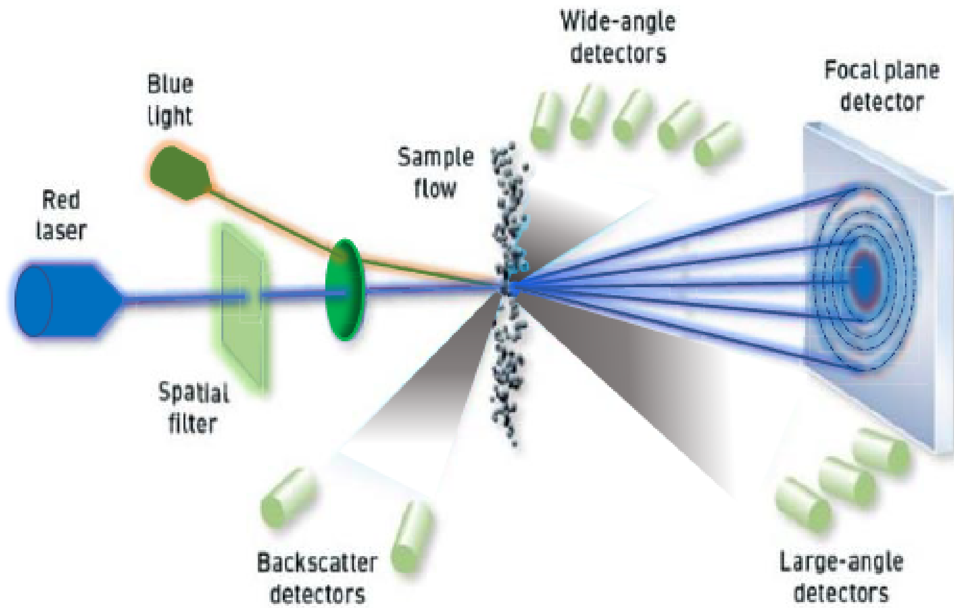

Figure 2.2 Schematic of laser diffraction system for particle size analysis [204].

The particles are dispersed either in a liquid or gas media. There are two types of media in which particles can be dispersed. They are liquid and gaseous media. In this work, the Cilas 1190, Figure 2.3, was used to determine the particle size distribution. The dispersion mode used in this work was the wet mode. First, the ultrasound water tank was cleaned with isopropanol, followed by cleaning the water supply system by draining and refilling with fresh water. A background measurement was performed to ensure quality of data acquired. The powder was introduced into the ultrasound water tank and measurement was conducted with obscuration level range of 13-20 %. This was repeated for 5 more powder samples and the average particle size determined based on Fraunhofer theory given by the equation [204]:

$$I(\theta) = \frac{I_o}{2k^2a^2}\alpha^4\left(\frac{J_1(\alpha sin\theta)}{\alpha sin\theta}\right) \quad (2.1)$$

Where $I(\theta)$ is the total scattered intensity as a function of angle θ in the forward direction, I_o represents illuminating intensity, k is the wave number, a is the distance from the scatterer to the detector, α is a dimensionless parameter. The Fraunhofer theory is usually applicable to opaque

objects whose particle size is at least 10 times greater than the wavelength of laser beam. Particle size is measured only at small scattering angle [204].

Another technique which was also employed to determine the particle size distribution was the image analysis technique. Images obtained from the scanning electron microscope (SEM) were imported into Image J software and processed to determine the particle size and particle size distribution.

Figure 2.3 Cilas 1190 particle size analyzer used in this research.

2.2.1.2 Heat treatment of as-milled Ni-Mn-Ga powders

The ball-milled Ni-Mn-Ga powders have an amorphous structure due to the high density of lattice defects induced by the high strain rate of deformation [9]. In order to be able to undergo martensitic transformation, the crystalline structure of the powder must be restored. Therefore,

small amounts of ball-milled powders were prepared for crystallographic and thermal investigations by loading the powders in quartz tubes, sealed under argon atmosphere. The quartz ampule was annealed at 1000^0C for 1 hour in a Thermolyne Type 48000 furnace.

2.2.1.3 Morphology and chemical composition

It has been reported that the morphology of powder particles has direct influence on the flowability and moisture sorption of AM parts [205], [206]. Especially powders with spherical morphology shows increasing packing density [207]. The morphology also plays a key role in optimizing the layer thickness and the density of the printed parts. In this work the powder morphology was characterized using the scanning electron microscope (SEM). The JEOL -JIB 4500 Multi Beam System SEM/FIB shown in Figure 2.4 and JEOL JSM -7600F FESEM were used to study the morphology and chemical composition of as-milled and annealed powder samples. The powder was deposited on conductive carbon tapes attached to 12.2 mm aluminum stubs mounted in a multiple stub holder. Samples introduced into the SEM sample chamber were examined at acceleration voltage of 15 kV and working distance between 10 -18 mm, using both secondary electron and backscattered electron mode for imaging. X-ray energy dispersive spectrometry (EDS) technique was used for compositional analysis. The EDS spectrometers used in this work were EDAX Octane Plus and EDAX Apollo XV.

Figure 2.4 JEOL JIB 4500 Multi Beam System SEM/FIB equipped with EDAX Apollo XV detector for chemical analysis.

2.2.1.4 Crystal structure

To determine the crystal structure or perform phase identification analysis of crystalline materials, X-ray diffraction (XRD) was used. In this research, Bruker AXS X8 Prospector single crystal diffractometer equipped with a highly sensitive Apex II charged-coupled device (CCD) detector was used for investigating the crystallinity, crystal structure and phase identification of powders, targets, and thin films (see Figure 2.5). The X-ray diffractometer uses a copper source with

wavelength 0.154178 nm operating at acceleration voltage of 45 kV. Powder samples were deposited on carbon tape affixed to the top of goniometer head and then mounted on the diffractometer. Samples were centered by viewing the instrument's mounting video camera and adjusting the X, Y, and Z directions using adjustable tool until sample were properly centered. Data for powder samples were collected between 2θ = 30° and 2θ = 90° under exposure time of 20 seconds per frame. The XRD patterns obtained were analyzed to determine the crystallinity and the phases present using DIFFRAC.EVA software from Bruker, combined with JCPS database. XRD data were also collected using D8 Advance Powder X-ray Diffractometer equipped with VANTEC-1 detector and Cu radiation source operating at 40 kV and 40 mA. The data were collected at 2θ values between 10° and 90° with a scan speed of 0.049557° per min and scan step size of 0.016519°.

Figure 2.5 Bruker AXS X8 Prospector single crystal diffractometer for structural analysis and phase identification.

2.2.1.5 Thermal analysis

In order to examine the martensitic phase transformation in Ni-Mn-Ga materials, a differential scanning calorimetry (DSC) analysis was conducted on the bulk material (initial ingot), as-milled, and annealed powder. A Perkin-Elmer Diamond differential scanning calorimetry

connected to a computer equipped with Pyris software was used for the thermal analysis, as shown in Figure 2.6. Ni-Mn-Ga samples were weighed and encapsulated in aluminum pan. Samples weights were in the range of 20 mg to 60 mg. The encapsulated Ni-Mn-Ga sample was placed on the sample side of the sample holder and an empty aluminum pan placed at the reference side of the sample holder. Samples were heated from -20°C to 300°C and cooled from 300°C to -20°C at a rate of 10°C per min and holding time of 5 minutes under argon atmosphere. This process was repeated for three cycles to a final state of 20°C.

Figure 2.6 Perker-Elmer Diamond DSC for investigating phase transformation.

2.2.2 3D Printing of Ni-Mn-Ga via binder jet

Ni-Mn-Ga sputtering targets were obtained via binder jetting additive manufacturing using ExOne Innovent+ instrument shown in Figure 2.7. Target designs were created using a 3D CAD program, SOLIDWORKS (Dassault system) prior to printing and uploaded to the printer as an STL. file. The 3D CAD model design geometry for a regular disc target is shown in Figure 2.8.

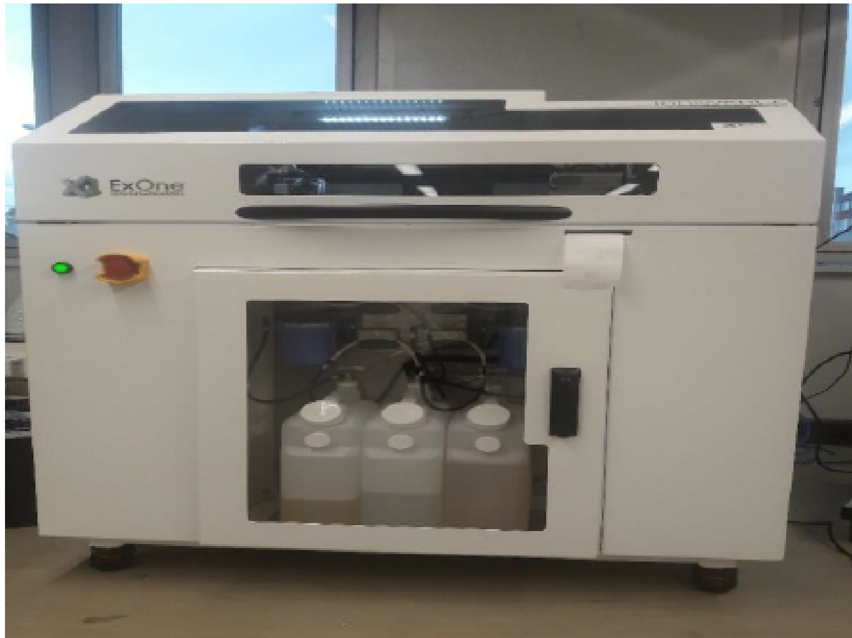

Figure 2.7 ExOne innovent+ 3D printer used in this research.

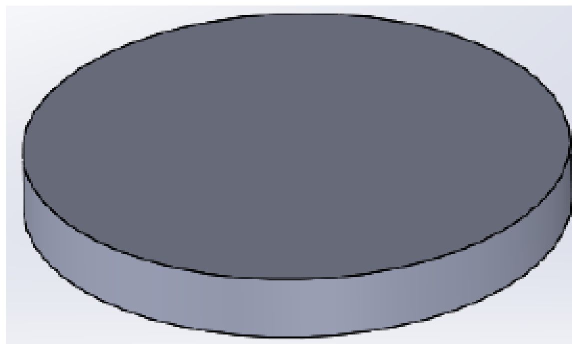

Figure 2.8 3D CAD model design for sputtering target 3D printed using binder jetting technology, diameter 63.5 mm, thickness 7.62 mm.

Next, Ni-Mn-Ga powder was introduced into the hopper of the ExOne Innovent+ binder jetting machine for printing. The CAD model design of a planar disc target was imported into the printing software of the printing machine. The ExOne Innovent+ is equipped with a hopper system having a build envelope of 160 mm x 65 mm x 65 mm. The build process starts by dispensing of powder from the hopper by ultrasonic vibrating mechanism followed by a rotating roller which spreads

and smoothens the powder at a specific layer thickness on the build platform. Afterwards, the printhead moving on both x and y axis selectively drops binder to glue the powder particles and patterns the target design onto the powder bed. The powder bed was then lowered to make way for a new layer of powder to be spread. Next, the powder bed was exposed to a heating lamp to cure the parts as the hopper moves across the powder bed to dispense and spread the next layer of powder. This process was repeated until Ni-Mn-Ga green parts were formed. Figure 2.9 shows a schematic diagram of the printing process of Ni-Mn-Ga targets. The printing parameters used for the build process are listed in Table 2.4. Once the targets were printed, post-processing steps were taking to increase the mechanical strength of the green parts.

Table 2.1 Process parameters for 3D printing of Ni-Mn-Ga powder in the ExOne Innovent+ machine.

Printing parameters	**Values**
Binder saturation	60%
Layer thickness	110 µm
Recoat speed	10 mm/s
Binder	BA005
Binder density	1.098 kgm^{-3}

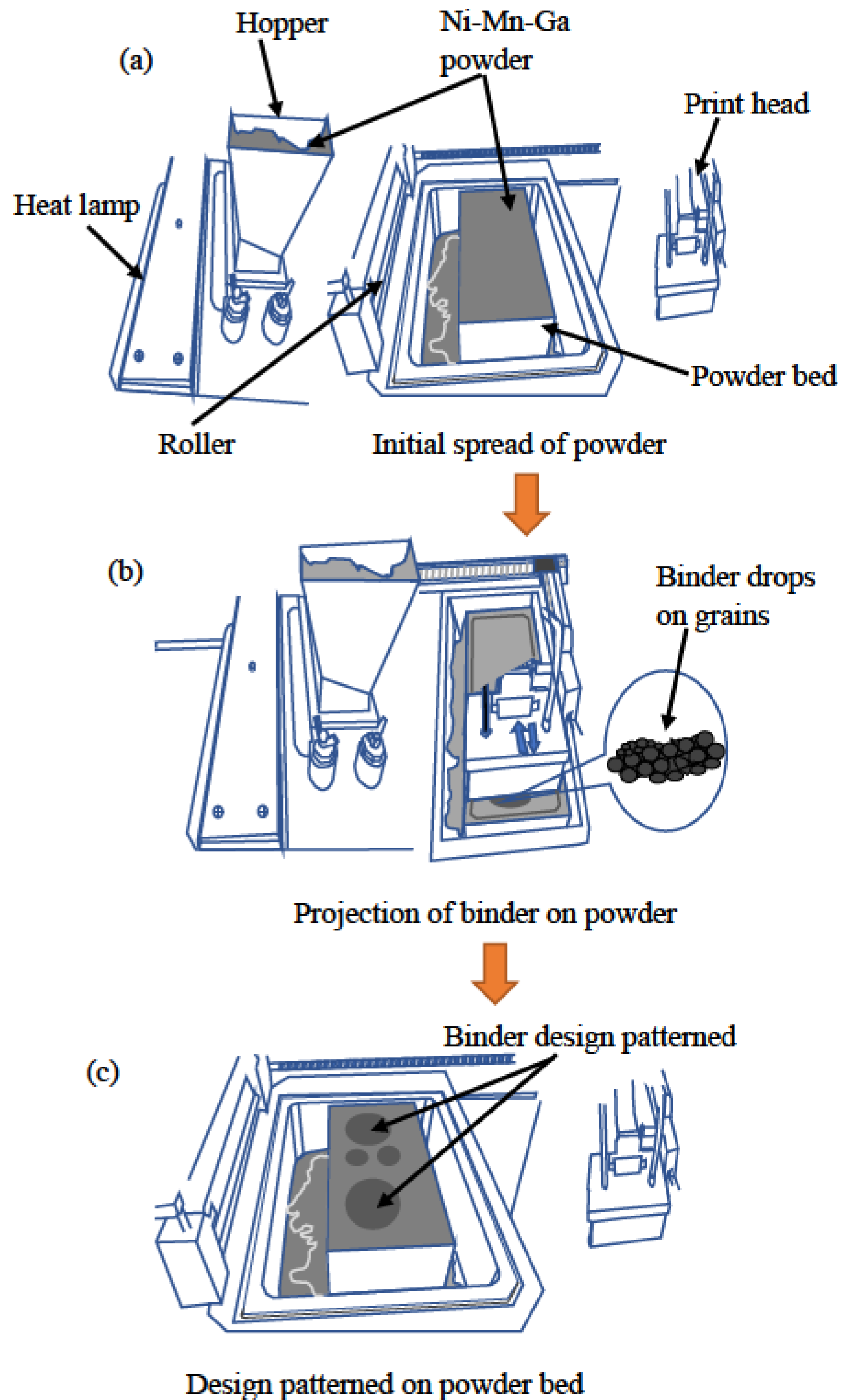

Figure 2.9 Schematic diagrams of the printing process of Ni-Mn-Ga targets: (a) Initial spreading of powder-on-powder bed; (b) Injection of binder on powder bed; (c) Binder design patterned on powder bed.

2.2.3 Post-processing of binder jet 3D printed Ni-Mn-Ga targets: curing and sintering

Curing is the first post-processing step performed right after the parts are printed. The as-printed Ni-Mn-Ga targets were placed in Yamato DX402C oven set at 180°C and holding time of 6 hours. After 6 hours had elapsed, it was allowed to cool naturally to room temperature and then removed from the oven. Loose powders on the cured targets were brushed off and then placed in a stainless steel pan for the next post-processing step.

After curing, the next post-processing step required to improve the mechanical strength of the printed parts was sintering. Sintering is a process which involves the bonding of adjacent particles by applying thermal energy. Sintering was performed to densify and eliminate as many pores as possible. The sintering step was carried out in a Carbolite tube furnace under a protective argon atmosphere. To protect samples against oxidation, flakes of Mn getters were placed around the sample. In order to achieve good vacuum for the sintering process, the empty tube furnace was first baked for six hours under vacuum. Afterwards, samples were placed inside the tube furnace and then vacuumed up to 10 mTorr by a mechanical pump, followed by backfill ultra-high purity argon gas to 300 mTorr. The above process was repeated three times to ensure protection against oxidation. Each printed target was sintered with a sacrificial sample for analysis. The 3D printed disc target was 63.5 mm in diameter and 7.6 mm in thickness. 3D printed Ni-Mn-Ga disc targets were sintered for 40 hours in the temperature range of 1065°C-1080°C. Figure 2.10 shows a schematic diagram of the sintering process of 3D printed Ni-Mn-Ga target in the tube furnace.

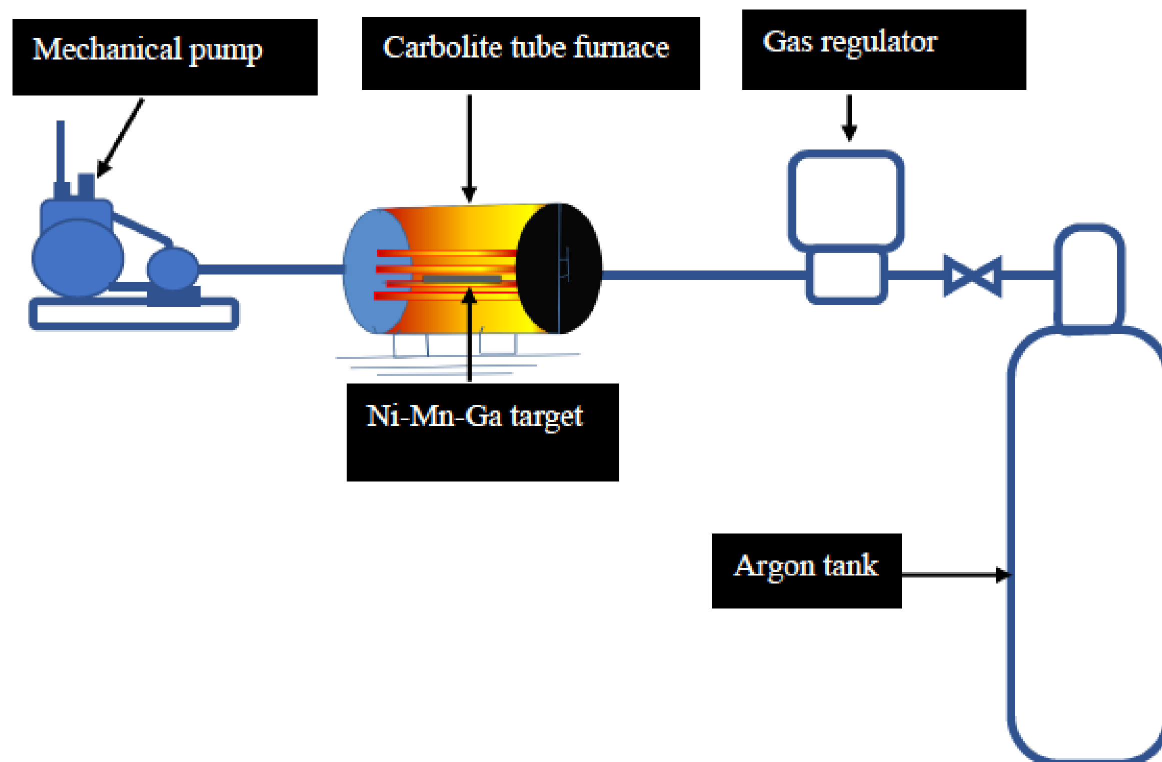

Figure 2.10 Customized setup used for the sintering experiment of the 3D printed targets.

Ni-Mn-Ga samples sintered at 1065°C, 1070°C, 1075°C, and 1080° were labelled Target 1, Target 2, Target 3, and Target 4 respectively.

2.2.4 Target Polishing

Polishing of the sputtering targets were necessary because after the sintering process, a thick oxide layer forms all over the target surface. Removal of the oxide layer will minimize contamination during sputter deposition. Polishing of the targets also smoothens the target surface and avoids electric discharge or arcing during sputtering [208].

After sintering, grinding of Ni-Mn-Ga targets was performed on silicon carbide abrasive papers wet with running water. Silicon carbide abrasive paper with grit sizes 180, 320, 600,1000, 2500 were used respectively. Cloth polishing was also carried out using colloidal silica suspension to

obtain a mirror like surface finished. Figure 2.11 shows an overall sputtering target manufacturing process by binder jetting additive manufacturing.

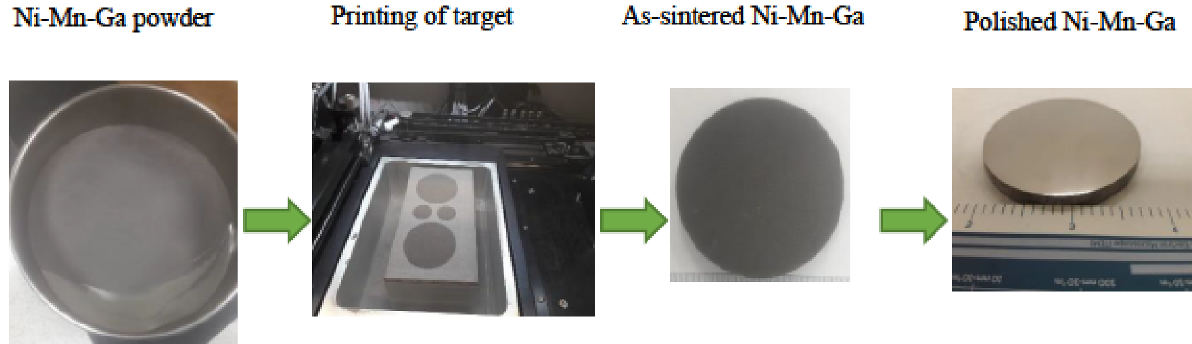

Figure 2.11 Sequence of target manufacturing process by binder jetting additive manufacturing.

2.2.5 Ni-Mn-Ga targets characterization

The sintered Ni-Mn-Ga alloy disc targets were examined using advanced characterization techniques. The crystal structure and phase identification analysis were performed using Bruker prospector CCD diffractometer equipped with Cu radiation source. The surface morphology, microstructural and chemical analysis of as-sintered and the polished cross-sections were examined by both JEOL JIB 4500 Multi-Beam scanning electron microscope (SEM) and JEOL JSM 7600F field emission scanning electron microscope (FESEM). Both SEMs were equipped with X-ray energy dispersion spectrometer (XEDS) detectors. Elemental analysis and mapping were performed using both EDAX Apollo XV and EDAX Octane Plus detector. Pieces of each Ni-Mn-Ga disc targets were cut out for differential scanning calorimetry (DSC) analysis using Perkin-Elmer Diamond DSC.

Target density was determined by volume displacement method, using the following equation:

$$Density = \frac{mass}{Volume} = \frac{M}{V_2 - V_1} \tag{2.2}$$

where M – mass, V_1 – initial de-ionized water volume, and V_2 – final water volume. Measurements were repeated 5 times for each target.

To reveal martensitic microstructures on the polished cross-section, three samples Target 1, Target 2, and Target 3 were subjected to argon ion beam etching for 15 minutes using Leica EM TIC 3X ion beam cutter system operated at 7 KV and 2.6 mA. The etched samples were examined using the LECO 300 light microscope equipped with Differential Interference Contrast (DIC) technique and SEM's backscattered electron (BSE) imaging mode to observe the crystallographic twin variants.

2.2.6 Synthesis of Ni-Mn-Ga thin films

As mentioned in the previous chapter, magnetron sputtering is the most popular technique for thin film deposition. It is the most reported technique used for Ni-Mn-Ga thin film fabrication. Thin films made with magnetron sputtering technique have good adhesion to substrate, promotes film uniformity and purity. Sputtering involves the ejecting of atoms from a target material (cathode) by bombarding with energetic argon ions and the ejected atoms are deposited onto a substrate material (anode). The magnetron sputtering system as discussed earlier is designed to trap secondary electrons closed to the target surface during sputtering. The electron trapping is as a result of magnetic configuration setup beneath the target. The electrons emitted are subjected to both electric and magnetic forces. The influence of these two forces causes the electrons to spiral along the magnetic field lines closed to the target surface. As a result of the electron trapping, high ionization plasma occurs due to rapid collision between electrons and the working gas atoms. Usually, inert gases specifically argon is used as the working gas to prevent reaction with the target. At all times the argon gas and the connecting tubes must be void of contaminants as well as leaks. In this research, direct current (DC) magnetron sputtering system was used for the

deposition of Ni-Mn-Ga thin films. A customized DC magnetron sputtering system equipped with three cathodes, a cooling system, turbomolecular Pfeiffer TC 400, and substrate heater situated at the semiconductor lab in Youngstown State University was used for the fabrication of Ni-Mn-Ga thin films. An image of the magnetron sputtering system used is shown in Figure 2.12. The substrates used in this research are silicon (Si) and sodium chloride (NaCl). Si substrate was used because it is relatively cheap and also good substrate for micro-electromechanical systems (MEMS) applications. NaCl substrate is water soluble, so it was employed to produce a freestanding Ni-Mn-Ga thin film. To initiate the deposition process, first step was to perform substrate cleaning. Si substrate was first degrease-cleaned with cotton swab soaked in acetone for few minutes and then boil in acetone for ten minutes, followed by boiling in isopropanol for ten minutes and finally rinsing in de-ionized water. Afterwards, substrate was baked for few hours and then mounted on a substrate holder. NaCl substrate was cleaned with acetone and then followed by isopropanol. De-ionized water was not used in this case because NaCl readily dissolves in water.

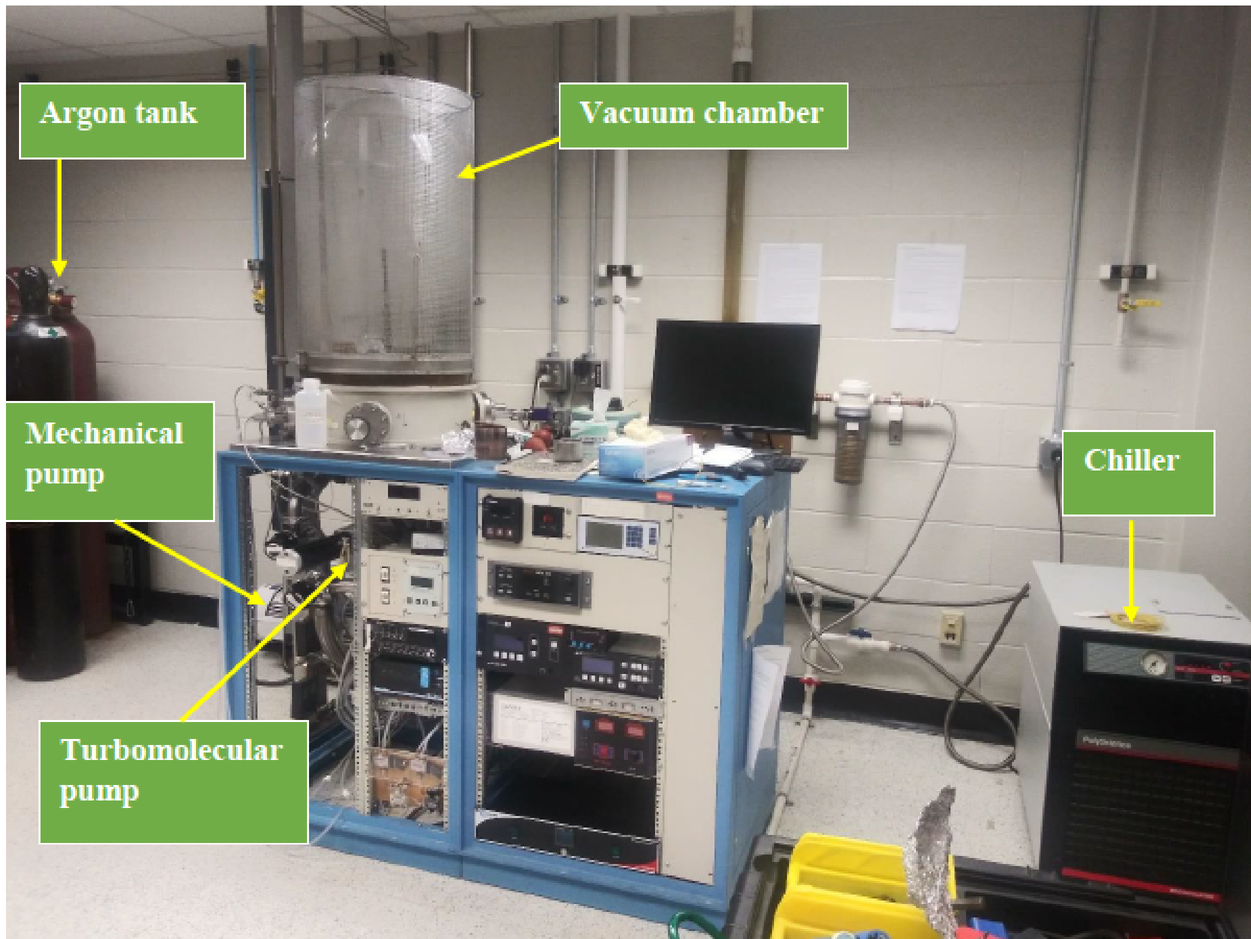

Figure 2.12 Magnetron sputtering system at Youngstown State University (YSU) used in this research.

Two sample holders have been used: one for deposition at room temperature and the other for higher substrate temperature. After installing the substrate and the AM target, the chamber was pump down for 24 hours until a base pressure of ~ 2.0 x 10^{-7} Torr was achieved. Next, the chiller was turned on to circulate the coolant needed to cool the cathode. The power supply was turned on with the gate valve to the turbomolecular pump placed in the middle. Argon gas was released into the chamber at a flow rate of 10 sccm. The gate valve was used to set the deposition pressures. The deposition pressures used in this work were in the range of 2.5 to 6.4 mTorr. Substrate

temperatures used were 20°C, 500°C, 600°C, and 700°C. Discharge currents were varied between 0.05 A to 0.15 A.

2.2.7 Characterization of Ni-Mn-Ga thin films

The crystallinity and the crystal structure of the Ni-Mn-Ga thin films were examined using Bruker Prospector diffractometer. The surface morphology and the microstructure were investigated using Agilent 5500 atomic force microscopy (AFM) system in the contact mode, Zeiss Axiophot light microscope (LM), JEOL JIB 4500 Multi-Beam System SEM/FIB and JEOL JSM 7600F FESEM. Chemical analysis of the surface of Ni-Mn-Ga thin films were carried out in FESEM using EDAX Octane plus detector calibrated with single crystal $Ni_{50.9}Mn_{29.23}Ga_{19.87}$ as a reference sample.

Composition-depth profile analysis was performed using Auger electron spectroscopy (AES) at Materials Research Laboratory (MRL. inc., Struthers, Ohio). The thin films were inserted into the analysis chamber of a Model 660 scanning Auger surface analysis system manufactured by Physical Electronics USA of Chanhassen, MN. The chamber was evacuated to a base pressure of 5×10^{-9} Torr. A cylindrical mirror electron energy analyzer was used for the electron detection. Surface spectra were collected at the surface level from most samples to illustrate elemental compositions. Concentration versus depth profiles were collected at various etching rates using a hot filament ion gun operated at 1 keV- 4 keV or a duoplasmatron ion gun operated at 5 keV-10 keV.

Ni-Mn-Ga sputtering target was also examined using the 3D Profilometer VR-5000 by Keyence in order to measure the target erosion profile. A Ni-Mn-Ga target sputtered for 10 hours was placed on the sample stage and moved to the observation position with the help of a viewer software. The data acquisition mode was selected to map the area of the sample to be analysed with lower

magnification.The selected area was scan for 10 minutes and data collected for both surface topography and depth profile. This process was repeated for target sputtered for 30 hours.

2.3 Monte Carlo Computer Simulation using TRIM (Transport of Ions in Matter) Code

A monte Carlo simulation code called TRIM (Transport of Ions in Matter) developed by J.F Ziegler and J. P. Biersack [209] was employed to calculate the sputtering yields of Ni, Mn, and Ga using Target 3 in order to understand the sputtering behavior of Ni-Mn-Ga alloy target. TRIM code is part of a software package in a SRIM 2008 program. TRIM code uses the universal potential equation to simulates the interaction between incident ions and target material [210]. The code assumes an amorphous target. The universal potential equation is given by:

$$V(r) = \frac{Z_1 Z_2 e^2}{4\pi\varepsilon_o r}\Phi_{ZBL}\left(\frac{r}{a_{ZBL}}\right) \quad (2.3)$$

Where r is the interatomic distance, Z_1 and Z_2 are atomic numbers of the incident ion and target material, e is the electronic charge, ε_o represent the permittivity of free space, a_{ZBL} is the screening length given by:

$$a_{ZBL} = 0.8853 a_o (Z_1^{0.23} + Z_2^{0.23})^{-1} \quad (2.4)$$

Where a_o is the Bohr radius given by $a_o = 0.529$ Å ,

Φ_{ZBL} is the screening function given by:

$$\Phi_{ZBL}\left(\frac{r}{a_{ZBL}}\right) = 0.1818 e^{-3.2\frac{r}{a_{ZBL}}} + 0.5099 e^{-0.9423\frac{r}{a_{ZBL}}} + 0.2802 e^{-0.4029\frac{r}{a_{ZBL}}} + 0.02817 e^{-0.2016\frac{r}{a_{ZBL}}} \quad (2.5)$$

TRIM simulation was performed in the surface sputtering mode with 50,000 Ar ions for target-ion interaction. Displacement energy, lattice binding energy, and surface binding energy were among

the input parameters used in the simulation. The values used for these parameters were chosen based on default from the TRIM code (see Table 2.5). The surface binding energy parameter plays an important role in sputtering yield calculation [209]. Since is the minimum energy required by the atoms to overcome to escape from the target surface, it is important the right value is selected to initiate the sputtering process and collision cascade evolution [210]. Two set of simulations were considered for calculating sputtering yield. The first was performed for ion energies between 100 eV – 1000 eV at a normal ion incident. For the second case, the incident angle of the ions was varied from 0° to 80° while keeping the ion energy at 1000 eV. The sputtering yield was investigated to gain insight into how the ion energy and the incident angle affect the sputtering yield of Ni, Mn, and Ga.

Table 2.2 TRIM input parameters for simulation.

Element	at%	Disp. Energy (eV)	Lattice binding energy (eV)	Surface binding energy (eV)
Ni	53	25	3	4.40
Mn	26	25	3	2.98
Ga	21	25	3	2.82

CHAPTER 3

Characterization of Ni-Mn-Ga Powder

3.0 Introduction

This chapter presents results of characterization of Ni-Mn-Ga powder obtained from ball milling. The discussion focuses on results obtained from particle size distribution analysis of powder using laser diffraction and image analysis technique, morphology and chemical composition of as-milled and annealed powder obtained using SEM/EDS techniques, crystal structure determined by XRD and phase transformation results obtained from DSC analysis. Results from particle size distribution and morphology were necessary because the particle size and its distribution for instance affect the powder's flowability and sinterability. Foreknowledge of the particle size would be helpful in the selection of the layer thickness during printing. The particle morphology on the other hand also affects both the green density and the final density of the printed parts.

3.1 Particle Size Distribution Analysis

Figure 3.1 shows the volumetric percent for as-milled Ni-Mn-Ga powder sample measured by laser diffraction technique. The particle size distribution (PSD) curve shows a bimodal distribution with peaks at 25 μm (volume percentage 0.8%) and 70 μm (volume percentage 7.8%). The bimodal distribution was achieved as a result of mixing two powders of different particle size. It can be observed that the distribution is skewed towards the large powder particles. Which suggest that the coarse particles dominate the fine particles. This way, the voids or the interstitials between the coarse particles would be occupied by the fine particles and that would enhance packing density. Bai *et al.* and other authors have shown that the use of bimodal powder mixtures improves packing density and surface finish of parts [211], [212]. According to laser diffraction technique for particle

size analysis, D_{10}, D_{50}, and D_{90} represent the percentile values whose particle diameter is below 10 %, 50 %, and 90 % respectively.

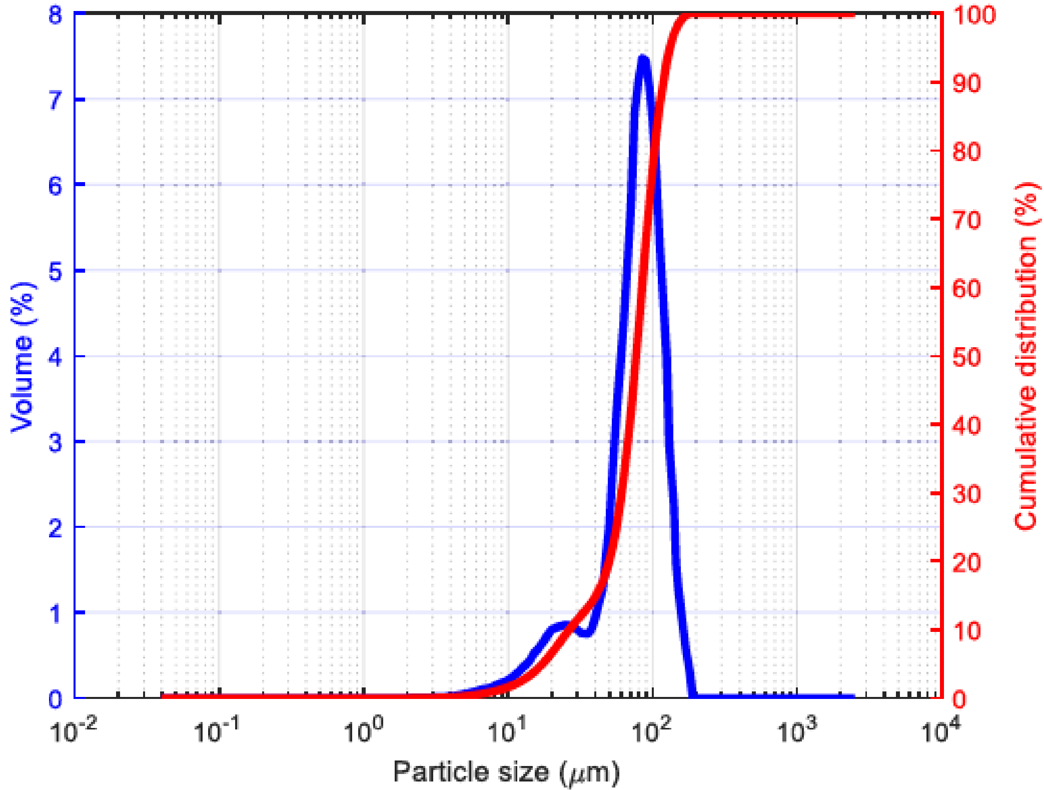

Figure 3.1 Particle size distribution of as-milled Ni-Mn-Ga powder.

The D_{10} value obtained was 23.86 μm which represents 10 % of particles diameter less than this value, D_{50} was 67.3 μm represents 50 % of particles diameter less 67.3 μm, and D_{90} was 105.2 μm represents 90% of particles diameter less than this value. The span or width of the distribution, an indication of how narrow or broad the distribution showed, it was calculated using the equation:

$$Span = \frac{D_{90} - D_{10}}{D_{50}} \tag{3.1}$$

The span of the distribution calculated from the above equation was 1.21. This value indicates a broad particle size distribution which favors particle packing density.

3.2 Particle Morphology and Chemical Composition

Powder morphology have shown to have direct influence on the printing process as well as sintering. For example, it has been reported that powders with spherical morphology demonstrate better flowability and large tap density than irregular particles due low inter-particle friction [213]. According Cima *et al.* powders with irregular morphology require higher binder saturation than spherical particle [214]. Figure 3.2 (a) - (b) shows secondary and backscattered electron micrographs of as-milled Ni-Mn-Ga powders. A typical morphology of ball milled powder is observed. The particles are irregular in shape with some showing sharp edges at the tip. The powder shows chemical homogeneity based on the backscattered electron micrograph in Figure 3.2 (b) and EDS analysis in Figure 3.2 (c).

Quantitative EDS analysis was performed on the ball milled powder to determine its chemical composition. EDS data was collected from individual particles, as indicated by the red circle in Figure 3.2 (b). Figure 3.2 (c) shows the typical EDS spectrum collected from ball milled Ni-Mn-Ga powder. Table 3.1 shows quantitative EDS analysis performed on the powder. Data was collected from 6 different points and the average and standard deviations were computed. Results show the presence of Ni, Mn, and Ga elements, which is expected. However, a weak silicon peak is also seen which might be an artifact from the detector. The atomic concentrations of the individual elements of the powder are nearly the same as the nominal composition of the Ni-Mn-Ga ingot.

As observed from Figure 3.2, there were no crystallographic twins visible on the ball milled sample, which might suggest the lack of martensitic phase in the milled powder. This might be related to the amorphous structure of the ball-milled powders [215]. For the milled Ni-Mn-Ga powders to be able to undergo martensitic transformation, the crystalline structure must be

restored. Therefore, the powders were subjected to an annealing heat treatment, as presented in Chapter 2: Materials and Experimental Methods.

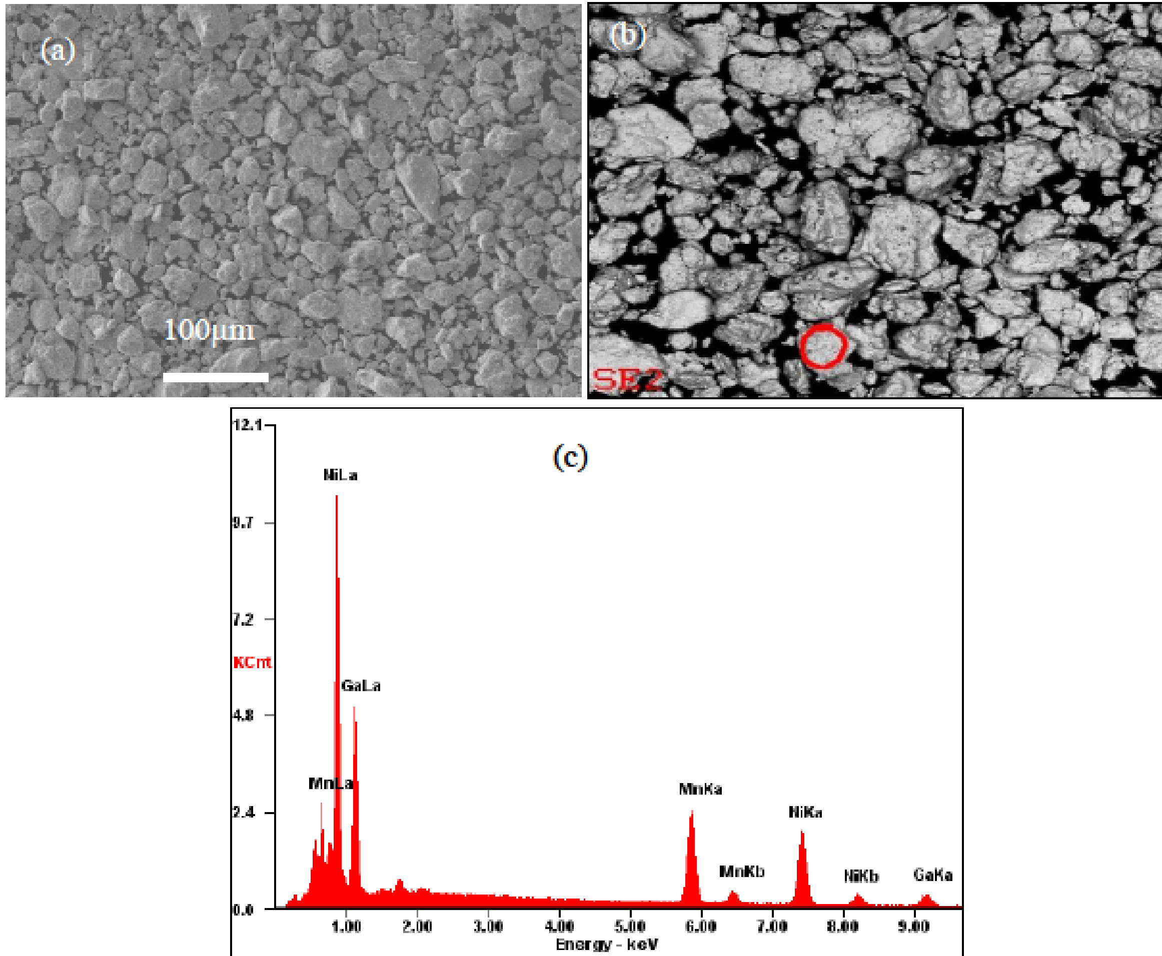

Figure 3.2 (a) Secondary electron (SE) micrograph of as-milled Ni-Mn-Ga powder; (b) BSE of as-milled powders indicating uniform chemical composition; (c) EDS spectra collected from an individual particle (encircled in (b)).

Table 3.1 Quantitative EDS analysis data for ball milled Ni-Mn-Ga powder.

Element	at%
Ni	51.13 ± 1.54
Mn	28.24 ± 1.20
Ga	20.63 ± 0.58

Post ball milling annealing treatment was performed on the milled powders to investigate the martensitic phase transformation. Figure 3.3 (a) and (b) show the SEM micrographs of annealed Ni-Mn-Ga powder revealing martensitic bands exhibiting different orientations. The martensitic twin microstructure is necessary for shape memory effect.

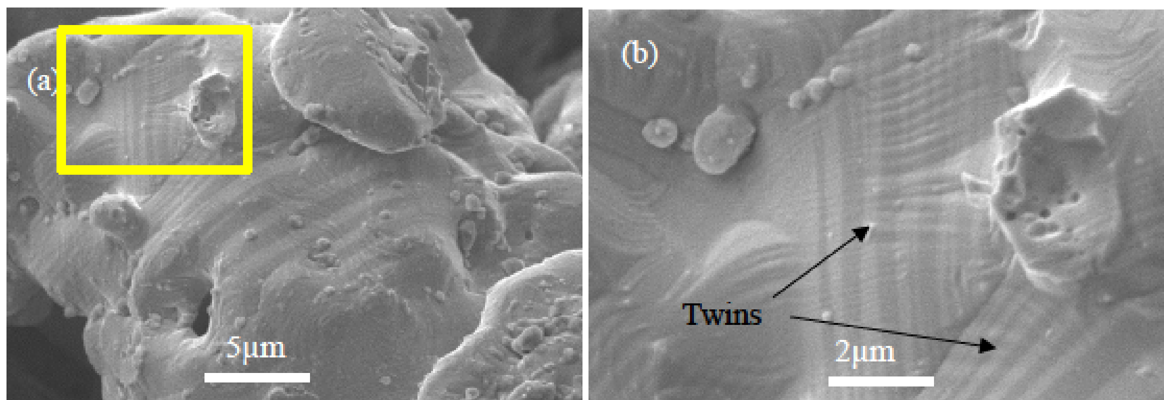

Figure 3.3 SE micrographs of annealed NiMnGa particles showing the specific morphology of twinned martensite: (a) Low magnificatio micrograph; (b) High magnification micrograph.

3.3 Crystal Structure

Figure 3.4 (a) shows XRD pattern of Ni-Mn-Ga bulk, as-milled, and annealed powder. The bulk (ingot) Ni-Mn-Ga shows a non-modulated (NM) tetragonal martensite with lattice parameters a=0.3876 nm, b=0.3876 nm, and c= 0.655 nm with space group I4/mmm [216]. The diffraction

peaks observed for the bulk sample were (110), (112), (200), (202), (220), (204), and (312). The most intense diffraction peak among them is the (112) peak and it occurs at $2\theta = 42.859°$. After ball milling for 1hour, the intensities of the diffraction peaks dropped, and some even disappeared. The peaks that remained are broader as can be seen from the XRD pattern. Similar observation was reported by Tian *et al.* [217]. Quite recently by Cavazzini *et al.* also observed same XRD pattern at room temperature after hand grinding $Ni_{49.4}Mn_{30.3}Ga_{20.3}$ ingot [218]. The broadening and disappearance of diffraction peaks is typical of ball milled metal powders. This happens as a result of collision between powder particles and milling media which causes lattice distortions and thermal stress build-up [217], [218]. Therefore, the atomic order is in disarray. In this work, the ball milling process suppressed the NM tetragonal martensite observed in the bulk ingot even though the crystal structure of the milled powder still shows a tetragonal structure. To release the internal stress induced in the ball milled powders as a result of the milling process, the powder was annealed. The XRD pattern of the annealed powder reveal incommensurate 7M martensite with a monoclinic crystal structure. The lattice parameters of the annealed sample were a = 0.42672 nm, b = 0.55074 nm, and c = 4.2228 nm, β=93.31° with superspace group I2/m [219]. This crystallographic data corresponds to a Mn-rich Ni-Mn-Ga alloy with structural formula $Ni_2Mn_{1.2}Ga_{0.8}$. Righi *et al.* were the first to show that 7M martensite exhibited incommensurate modulation using powder XRD [219]. They achieved the modulated crystal structure by refining the XRD data through Rietveld method. The XRD pattern presented in this research for the annealed Ni-Mn-Ga powder showed the same XRD pattern observed by Righi *et al.*. Recently, Cavazzini *et al.* also reported a similar XRD pattern in their investigation on the structural, morphological, and magnetic properties of as-milled and annealed milled Ni-Mn-Ga powders

[218]. Their investigation showed that after annealing milled powder for 2hours at 630°C, the 7M martensite was restored.

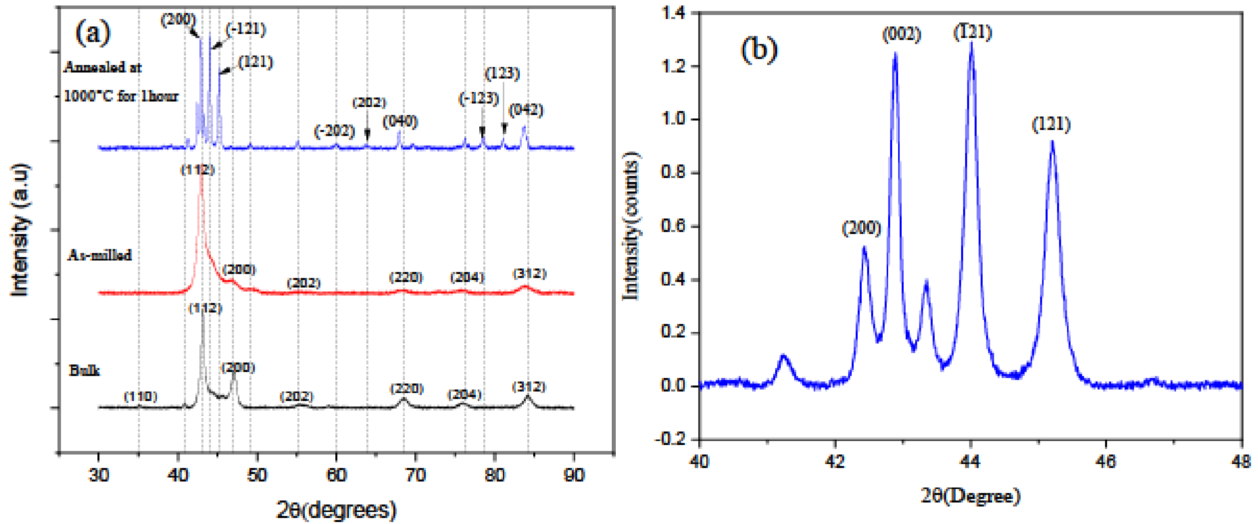

Figure 3.4 (a) Room temperature XRD patterns for Ni-Mn-Ga bulk, ball milled powder, and annealed powder, and (b) Detailed XRD pattern of annealed Ni-Mn-Ga powder.

Reflection peaks observed in the XRD pattern of annealed powder can be indexed as (200), (-121), (121), (-202), (202), (040), (-123), (123), (042). The most prominent peak (-121) is surrounded by six satellite peaks as seen in Figure 3.4 (b).

3.4 Thermal Analysis

Thermal analysis of Ni-Mn-Ga bulk and powder was performed using differential scanning calorimetry (DSC) in order to determine the martensitic phase transformation temperatures.

Figure 3.5 shows DSC curves of bulk, as-milled and annealed Ni-Mn-Ga powder. Both bulk Ni-Mn-Ga ingot and annealed powder showed strong phase transformation behaviors as seen from the plot. The endothermic and the exothermic peaks show the forward and reverse transformations between austenite and martensite phase. The transformation peaks of the bulk sample appear sharper than the annealed powder which may possibly be due to some residual internal stress

[220]. A shift towards a higher temperature was observed in the peaks of the annealed powder which can be attributed to induced microstructural changes and relaxation of internal stress from ball milling process [221]. Another possible reason for the shift in transformation temperature is due to compositional changes [61]. As was observed from the XRD pattern, a phase transformation from NM tetragonal martensite in the ball milled powder to incommensurate 7M martensite in the annealed powder was seen.

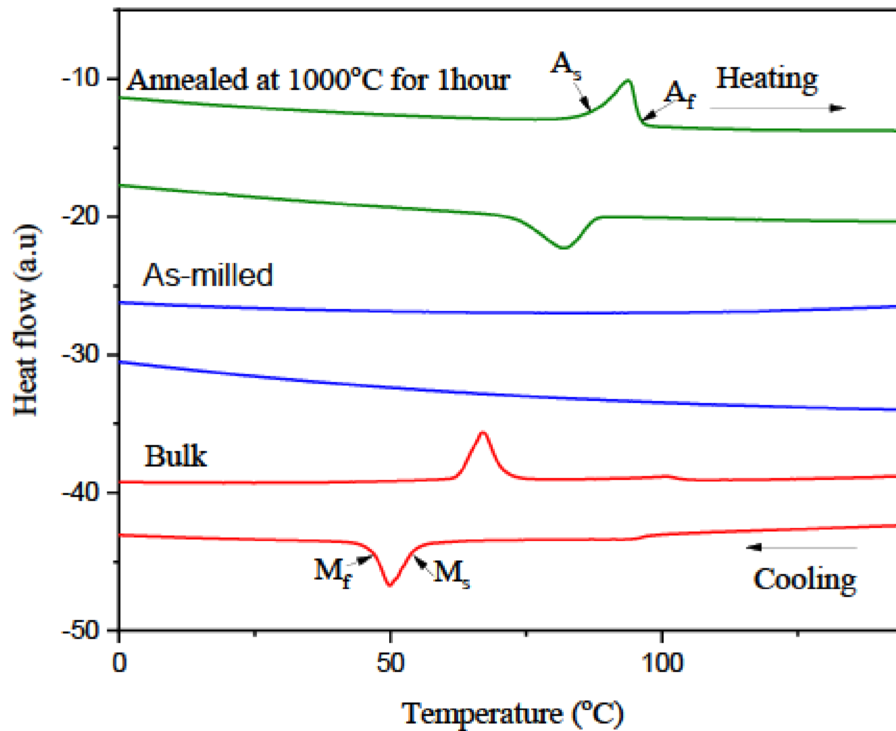

Figure 3.5 DSC curves of bulk Ni-Mn-Ga ingot, ball milled powder, and annealed powder.

The as-milled powder shows no evidence of transformation. This result is consistent with work reported by Tian *et al*. [217]. Table 3.2 shows a list of transformation temperatures for bulk, ball milled, and annealed powder.

Table 3.2 Transformation temperatures from DSC plot.

	A_s (°C)	**A_f (°C)**	**M_s (°C)**	**M_f (°C)**
Bulk	62.9	70.2	55.6	49.5
Powder	-	-	-	-
Annealed	86.69	95.95	87.74	73.29

CHAPTER 4

Characterization of Ni-Mn-Ga Sputtering Target Produced by Binder Jetting Additive Manufacturing

4.0 Introduction

This chapter presents results obtained from analytical investigation of as-printed and sintered sputtering targets. A systematic study was carried out to investigate the effects of isothermal sintering on the green targets in the temperature range 1065°C - 1080°C for 40 hours under argon atmosphere. The as-sintered and polished targets were examined with SEM/EDS to investigate the microstructural evolution and chemical composition of the samples. Results obtained from the SEM, EDS, XRD and DSC analysis on printed and sintered targets are discussed as well as the metallurgical properties of additive manufactured Ni-Mn-Ga target as related to quality of thin film.

4.1 Chemical composition, microstructure, phase identification, phase transformation, and shrinkage of as-printed and sintered un-polished Ni-Mn-Ga targets

Target characterization was initiated by investigating the surface of as-printed and sintered specimens. Figure 4.1 (a) shows an as-printed Ni-Mn-Ga target, while Figure 4.1 (b) shows the target after sintering at 1075^0C for 40 hours (Target 3).

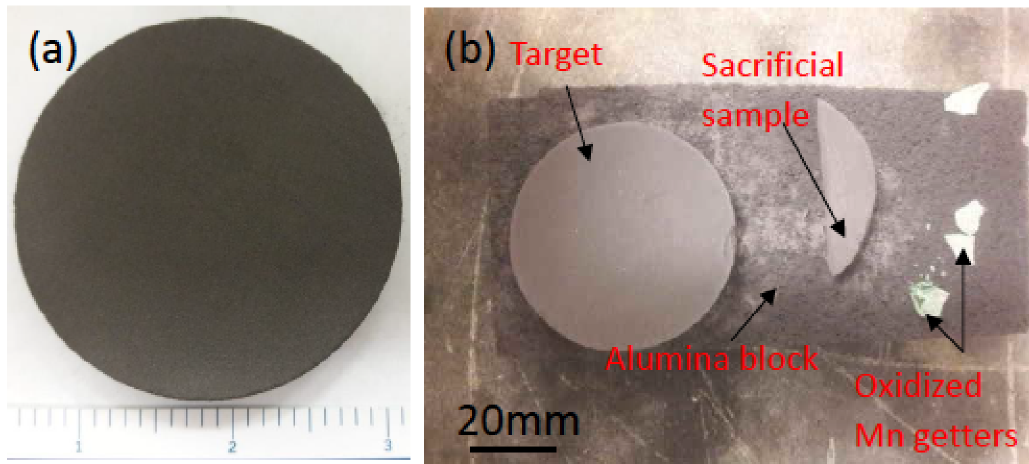

Figure 4.1(a) As-printed Ni-Mn-Ga target; (b) Ni-Mn-Ga target sintered at 1075°C for 40 hours (Target 3).

In order to assess the microscopic morphology and chemical composition of as-printed target surface, SEM and EDS investigations were performed. Figure 4.2 (a) and (b) show BSE micrograph and EDS spectrum of as-printed Ni-Mn-Ga target, respectively. EDS data was collected from the red square area in the BSE micrograph as shown in Figure 4.2 (a). The EDS spectrum shows the presence of Ni, Mn, and Ga peaks. In addition, some weak peaks were also detected which correspond to C, O, and Si.

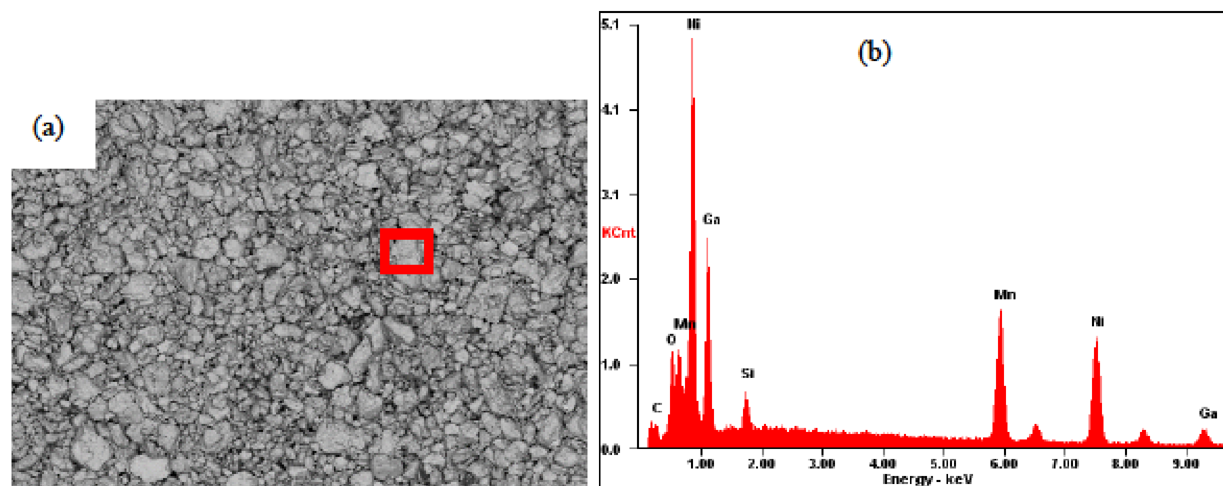

Figure 4.2 (a) BSE micrograph collected from the surface of as-printed Ni-Mn-Ga target, (b) EDS spectrum collected from the red square area.

The result indicates the apparent contamination of the as-printed sample. The C is probably due to the presence of the binder (C_4H_4O, furan-based binder used in the ExOne printers). The Si and O peaks were initially related to a possible target contamination. However, calibration of the EDS detector using known standards indicated that the presence of the Si peak is an instrument artifact of the SEM/EDS instrumentation used in this experiment.

Figure 4.3 (a) - (b) show low and high magnification SEM micrographs recorded from the surface of Ni-Mn-Ga target sintered at 1065°C for 40 hours (Target 1). As can be seen from the micrographs, particles having a cube like morphology covers the entire surface of the sintered target. In order to examine the cubic-shaped particles EDS analysis was performed on the sintered target. EDS spectrum collected from the surface of the sintered target is shown in Figure 4.3 (c). The result reveals the formation of a manganese oxide at the surface of sintered target. Further investigation on the type of manganese oxide using XRD revealed the presence of complex oxide

of manganese called hausmannite (Mn_3O_4), as shown in Figure 4.4. The high Mn concentration at the surface of sintered Target 1 might be due to high amount of Mn getters placed around the samples, combined with the residual oxygen in the furnace atmosphere. It has been reported that high Mn concentration can facilitate sublimation due to high partial vapor pressure [222]. It is also possible that due to the high vapor pressure of Mn, during the sintering process Mn will diffuse out of the sample and react with oxygen to form the manganese oxide particles.

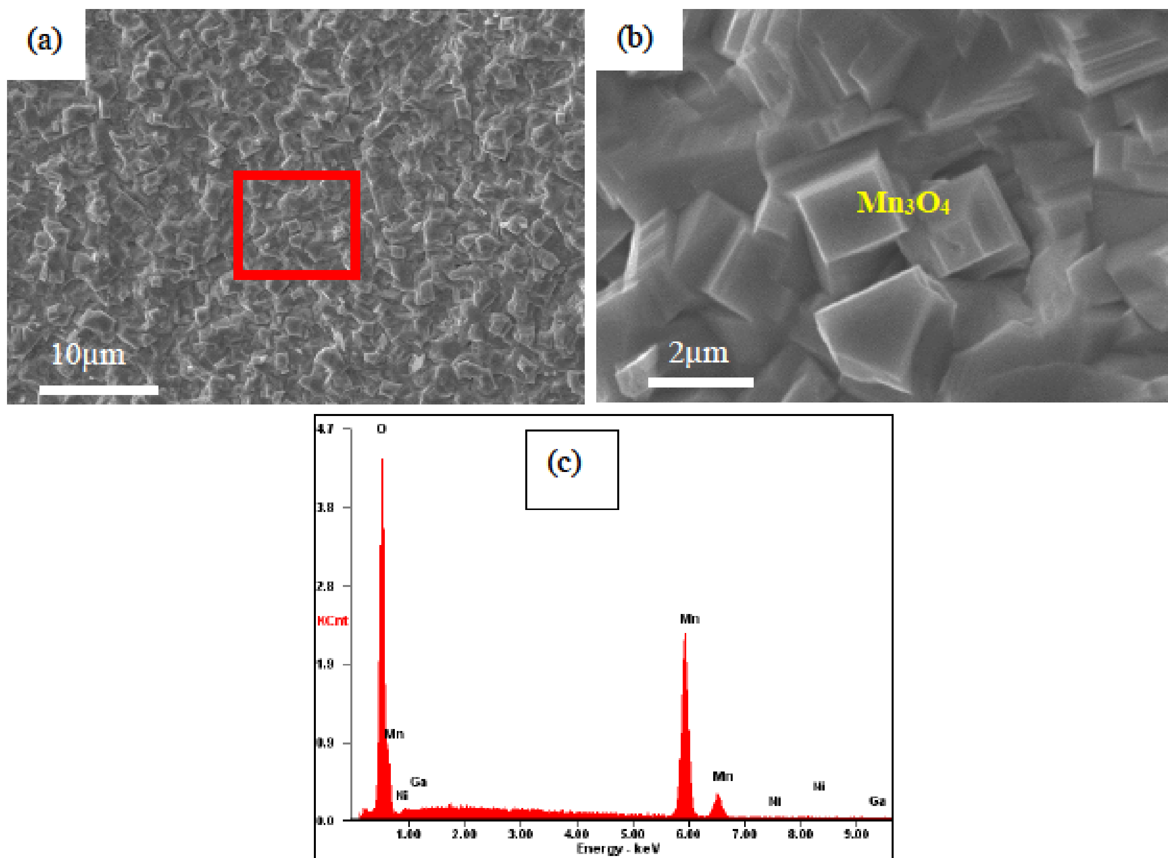

Figure 4.3 SEM image of the surface of 3D printed Ni-Mn-Ga target sintered at 1065°C for 40 hours: (a) Morphology of the sintered target surface, (b) High magnification micrograph of the

area indicated in (a), showing the presence of Mn_3O_4 crystals at the surface of sintered target, (c) EDS spectrum collected from the surface of sintered Ni-Mn-Ga target.

In order to address the oxidation problem for the subsequent sintering, the masses of Mn getters were reduced from 2.32 g (1065°C) to 1.6 g (1070°C),1.2 g (1075°C), and 0.8 g (1080°C), respectively. It was ensured the position of the getters were few millimeters away from the sample towards the direction of the mechanical pump in order to limit oxidation of Ni-Mn-Ga targets. The tube furnace was evacuated and then backfilled with ultra-high purity argon gas and process repeated three times. Sintering experiments were carried out for three additional Ni-Mn-Ga targets for temperatures 1070°C (Target 2), 1075°C (Target 3), and 1080°C (Target 4), for 40 hours.

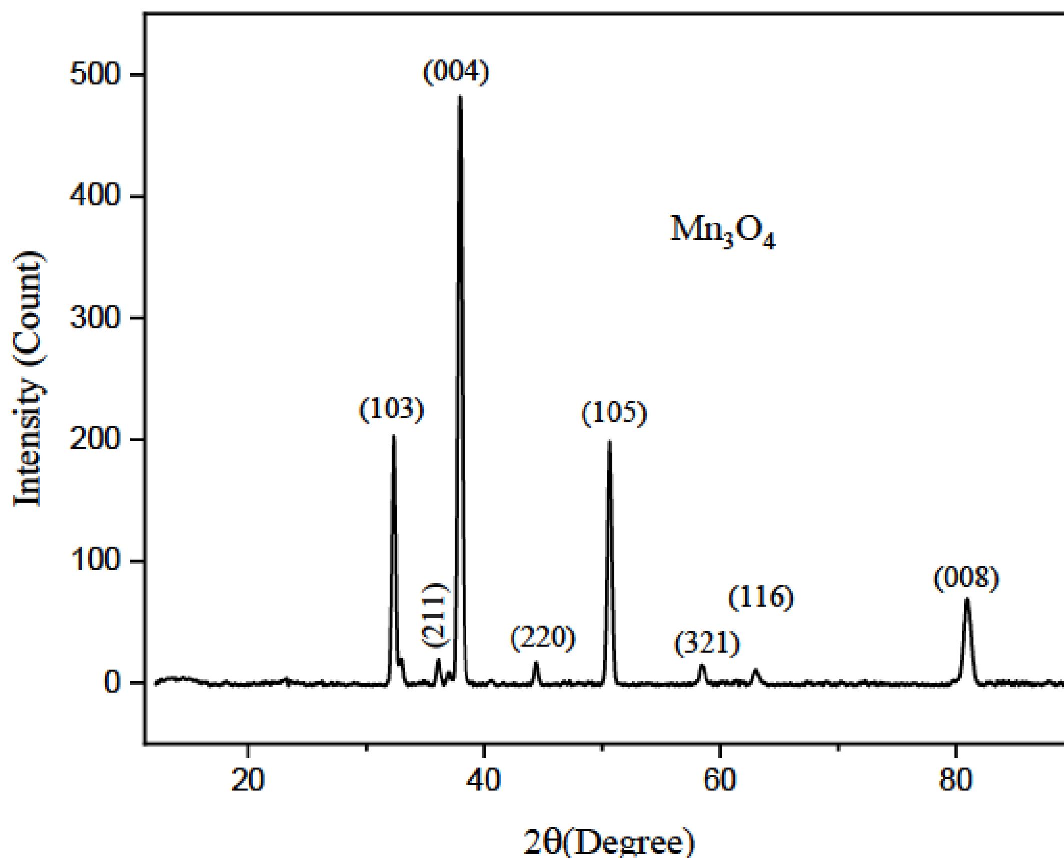

Figure 4.4 XRD pattern of as-sintered Ni-Mn-Ga Target 1.

For effective part densification, initial contact between particles was necessary to facilitate sintering and grain growth. Contacts between powder particles were achieved during the printing and the curing stages. The sintering step promotes both densification and grain growth. However, in target manufacturing densification is preferred, while grain coarsening is somehow undesirable [223]. Figure 4.5 (a) - (f) show the surface morphology of Ni-Mn-Ga targets sintered at different temperatures. Targets sintered at 1070°C (Target 2) and 1075°C (Target 3) show similar morphology, Figure 4.5 (a) - (b) and (c) - (d), respectively. Neck formation and grain boundaries were observed on the base sintered material. Similar to Target 1, manganese oxide, confirmed by EDS mapping shown in Figure 4.5, was observed at the surface of samples. It must be noted, the amount of manganese oxide formed at the surface is less in this case, compared to Target 1. This might be explained by both repositioning of the Mn getters in the sintering furnace, and to a decrease in the vapor pressure of manganese in the tube furnace during sintering due to reduction in mass of manganese getters. Yet, crystallographic twins are clearly observed going across the grain boundaries indicating the presence of a low temperature (martensitic) phase. This result is consistent with work reported by Taylor *et al.* [224]. Figure 4.5 (e) - (f) shows the surface morphology of Ni-Mn-Ga target sintered at 1080°C (Target 4). The sample shows minimal oxidation, compared to the previous three. Neck formation is observed, with particle-to-particle bonding in all four specimens. Crystallographic twins are also observed in all specimens indicating the existence of the martensitic phase, irrespective of sintering temperature.

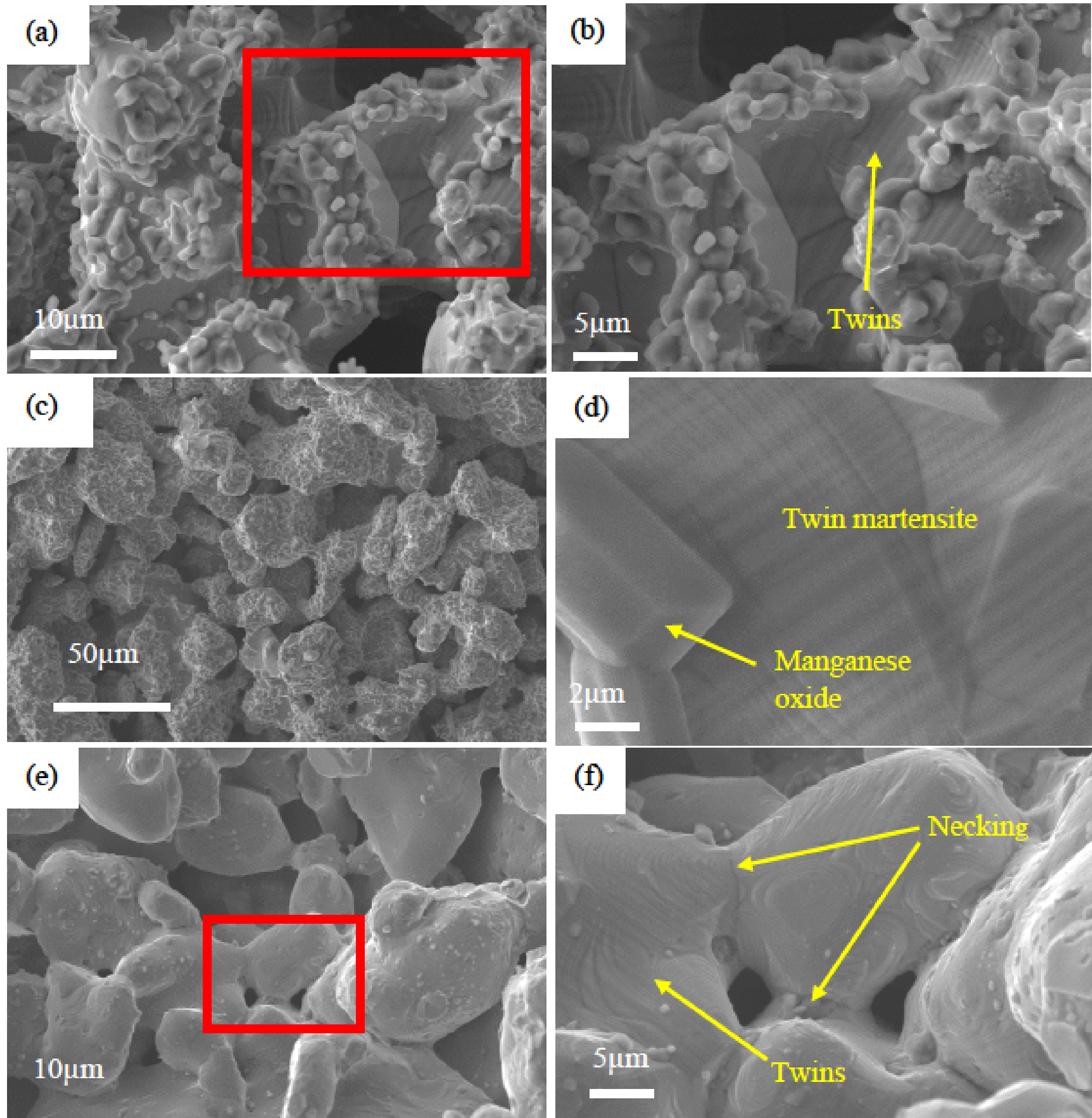

Figure 4.5 SEM micrographs of Ni-Mn-Ga samples sintered at different temperatures: (a) - (b) Target 2, (c) - (d) Target 3, (e) - (f) Target 4.

Figure 4.6 shows the EDS chemical mapping recorded from the surface of Target 3. The BSE micrograph in Figure 4.6 (a) indicates a chemical segregation at the target's surface. Based on the Ni and Mn maps (Figure 4.6 (b) and (c)) the dark-gray particles observed at the target surface in Figure 4.6 (a) are Mn-rich particles. The O map (Figure 4.6 (e)) indicates the particles are

manganese oxide. This result suggests the diffusion of Mn toward the sample's surface, indicating a reduction in Mn concentration in the target, as a result of sintering. This aspect will be further investigated in polished targets.

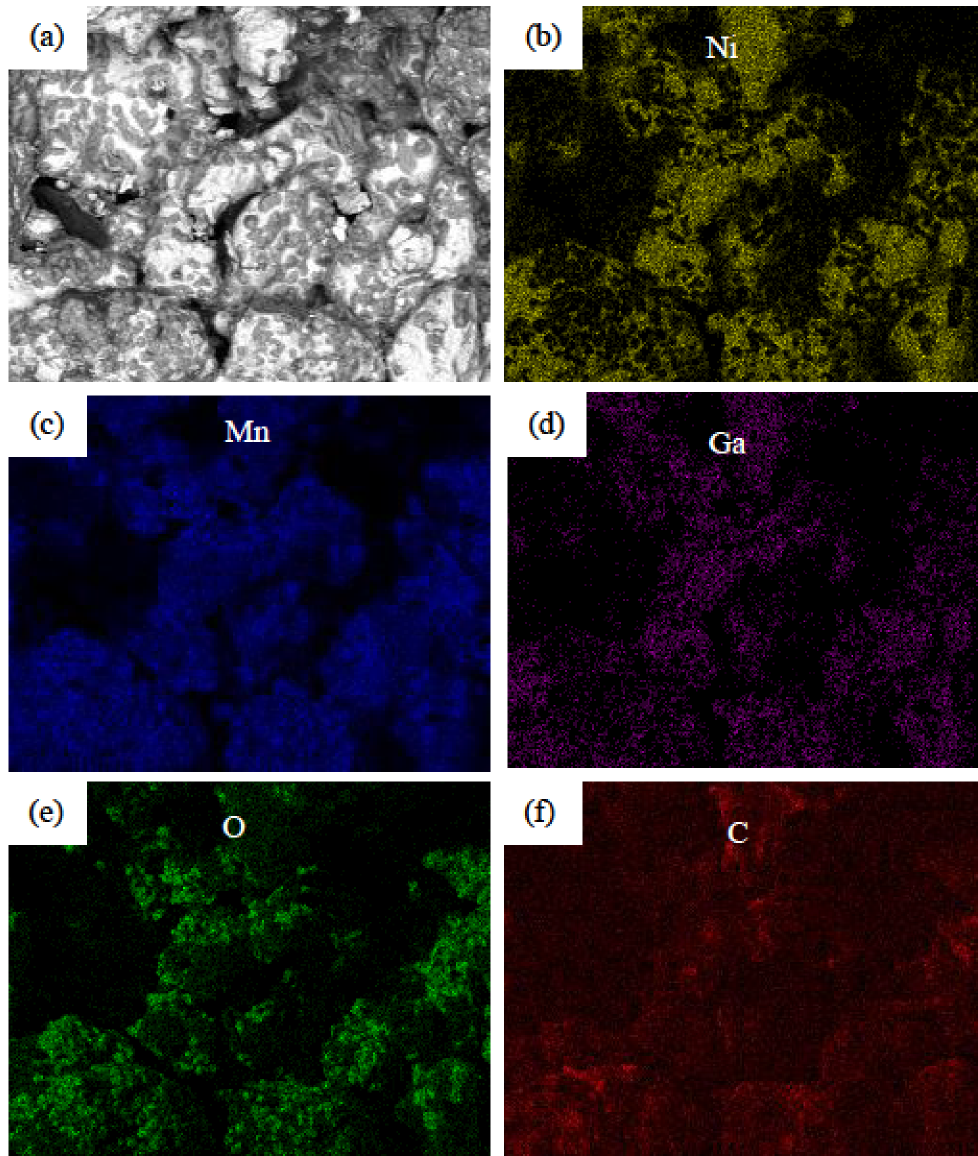

Figure 4.6 (a) BSE micrograph of the Target 3 surface; (b) – (f) Ni, Mn, Ga, O, and C EDS maps recorded from the area shown in (a).

After sintering process, linear shrinkage in diameter and thickness were calculated for all four specimens using equations (4.1) and (4.2):

$$\text{Linear Shrinkage in diameter}(\%) = \frac{D_B - D_A}{D_B} x100 \qquad (4.1)$$

$$\text{Linear Shrinkage in thickness }(\%) = \frac{t_B - t_A}{t_B} x100 \qquad (4.2)$$

Where D_B is the diameter of the target before sintering, D_A is the target diameter after sintering, t_B is the target thickness before sintering, and t_A is the target thickness after sintering. The target diameter and thickness were measured using STORM digital caliper to estimate the dimensional change after sintering. For each target, both the diameter and the thickness were measured five times, and the average values and standard deviation are plotted in Figure 4.7. Figure 4.7 shows the effect of sintering temperature on linear shrinkage of target diameter and thickness. Result shows higher shrinkage in the thickness direction whereas the radial direction experiences a lower shrinkage. As expected the dimensional shrinkage is dependent on sintering temperature. For the lowest sintering temperature (1065^0C) the dimensional shrinkage is about 6%, while for 1080^0C the shrinkage is about 16%. This information is critical for manufacturing Ni-Mn-Ga parts using 3D binder jet printing. The data from Figure 4.7 also suggests that densification was more favored in the thickness direction than the radial direction. This result is consistent with work reported by Enneti *et al.* [225]and Baojun *et al.* [226].

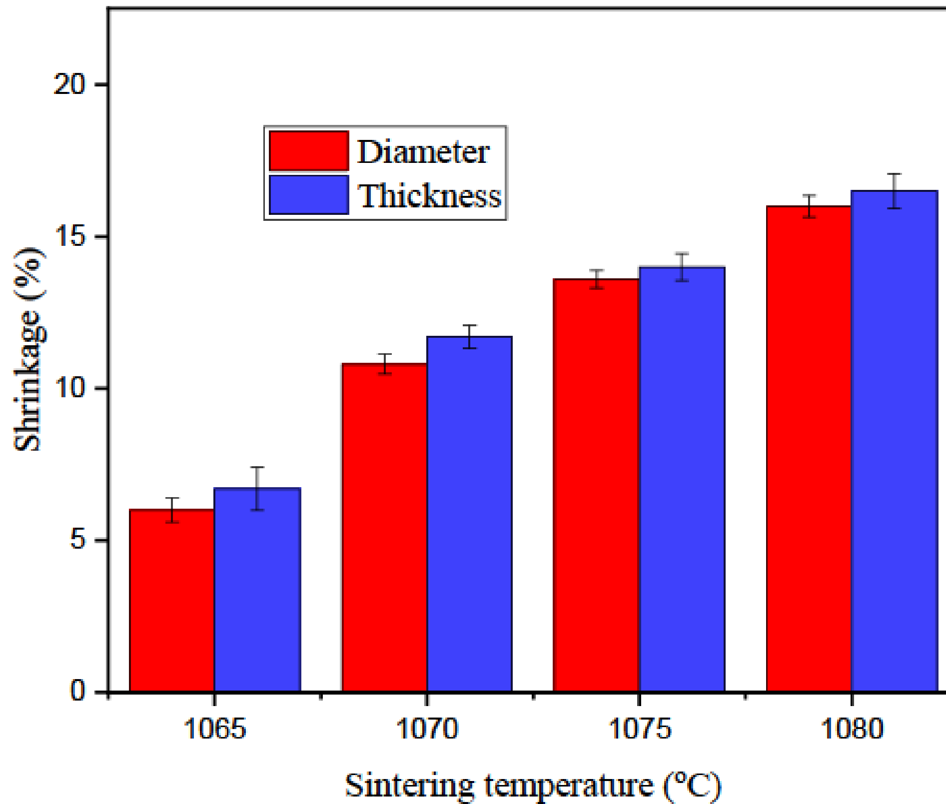

Figure 4.7 Shrinkage of Ni-Mn-Ga targets at different sintering temperatures.

4.2 *Microstructure, density, composition, crystal structure, and phase transformation of sintered polished Ni-Mn-Ga*

4.2.1 Microstructure of sintered Ni-Mn-Ga targets

The sintered targets show an irregular surface, related to the inherent surface roughness of the specimens produced by 3D binder jet printing [227], [228]. For the targets to be used in the sputtering deposition process, the target's active surface must be flat, and no manganese oxide must be present. Therefore, the sintered targets were polished using various grids silicon carbide papers, until a mirror-like surface was obtained. This sub-chapter presents the results of analytical investigation of polished Ni-Mn-Ga targets.

Figures 4.8 (a) - (b) shows images of polished 3D printed Ni-Mn-Ga disc targets prepared in this research. In Figure 4.8 (a) the second target from the left (Target 4) shows the racetrack marks (indicated by arrows) formed during target usage in the magnetron sputtering deposition process.

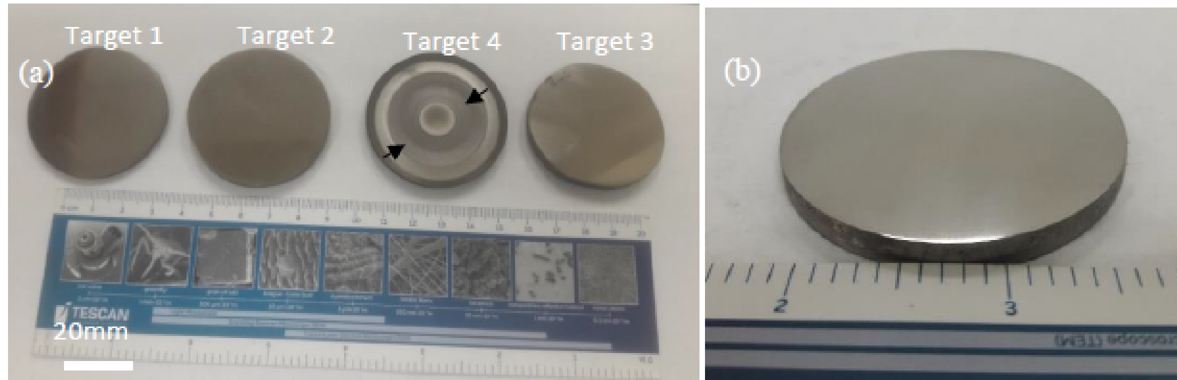

Figure 4.8 (a) Photo of polished Ni-Mn-Ga target named Target 1, Target 2, Target 3, and Target 4 after used, (b) Photo of Target 4 before use.

Figure 4.9 (a) - (d) show the microstructures of polished Ni-Mn-Ga targets sintered at temperatures 1065°C, 1070°C, 1075°C, and 1080°C, Target 1 to 4, respectively. Figure 4.9 (a) reveals large irregular pores in Target 1, of average size 5 µm, isolated from each other. The large pores observed in this target can possibly be attributed to inherent porosity of the parts made by 3D binder jet printing [229]. Increasing sintering temperature and reducing the amount of Mn getters accelerated neck formation and improved densification in samples sintered at 1070°C, 1075°C, and 1080°C, respectively, as seen in Figure 4.9 (b) - (d). At 1080°C, the number of pores and pore sizes decreased drastically, as seen in Figure 4.9 (d). The results show that increasing sintering temperature affects target microstructure and improves densification through lattice or grain boundary diffusion [230]. Similar densification process of 3D printed Ni-Mn-Ga parts have been

reported by Caputo *et al.* in their investigation of time dependency of isothermal sintering on additive manufactured Ni-Mn-Ga shape memory alloy [11]. Their investigation revealed that porous additive manufactured Ni-Mn-Ga samples showed increased density percentage from ~ 74 to ~ 83 % for samples sintered at 1080°C between 10 to 50 hours, respectively. Density percentage concept is commonly used for comparing the density of a porous materials with theoretical density of the full solid. Therefore, the density percentage is the ratio between the measured density of the porous materials and the density of the full solid, multiplied with one hundred. This work shows slight increase in the density percentage of sintered Ni-Mn-Ga material of approximately 87 % compared to the value of 82 % reported by Caputo *et al.* [11]. The density data is presented in Table 4.1. The increase in density could be attributed to an increase in green part density due to bimodal particle size distribution of starting powder. The theoretical density of the targets were calculated using equation (4.3) [231]

$$\rho_T = \frac{C_{Ni}A_{Ni}+C_{Mn}A_{Mn}+C_{Ga}A_{Ga}}{\frac{C_{Ni}A_{Ni}}{\rho_{Ni}}+\frac{C_{Mn}A_{Mn}}{\rho_{Mn}}+\frac{C_{Ga}A_{Ga}}{\rho_{Ga}}} \quad (4.3)$$

Where C_{Ni}, A_{Ni}, ρ_{Ni} represent the atomic composition, atomic weight, and density of Ni content, C_{Mn}, A_{Mn}, ρ_{Mn} represent the atomic composition, atomic weight, and density of Mn content, C_{Ga}, A_{Ga}, ρ_{Ga} represent the atomic composition, atomic weight, and density of Ga content. The theoretical density varied from one target to the other due to differences in atomic compositions, see Table 4.2. Actual density of the targets was determined from mass and volume measurements as mentioned in Chapter 2. Mass and volume measurements were repeated 5 times for each target in order to account for the random errors.

Figure 4.10 shows density percentage and porosity (obtained by subtracting density percentage from 100%) of Ni-Mn-Ga targets as a function of sintering temperature. The result shows that the density percentage increases with increasing sintering temperature whereas porosity decreases

with increasing sintering temperature. The lowest density percentage ~70 % was achieved at sintering temperature of 1065°C, however, at 1080°C, the maximum achievable density was estimated to be ~87 %.

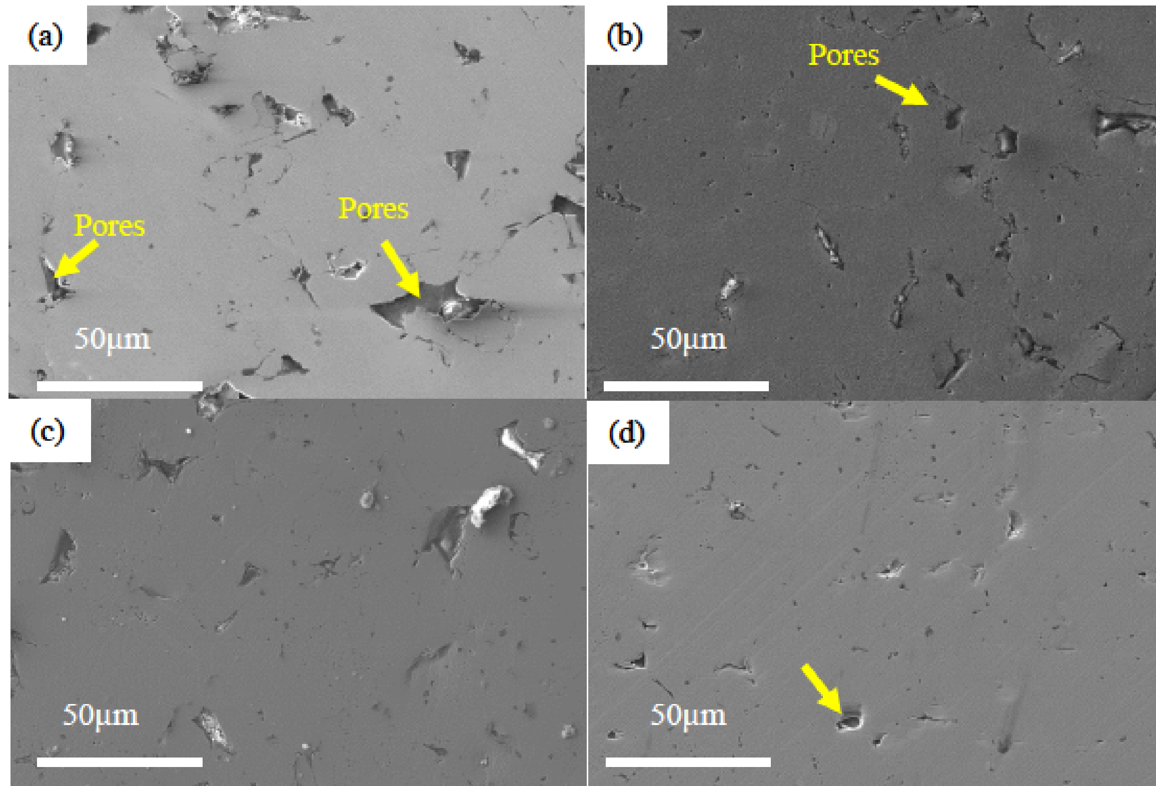

Figure 4.9 SEM micrographs of polished cross-section of Ni-Mn-Ga targets sintered at different temperatures: (a) Target 1, (b) Target 2, (c) Target 3, and (d) Target 4.

Table 4.1 Density of 3D printed Ni-Mn-Ga targets sintered at temperatures 1065°C, 1070°C, 1075°C, and 1080°C.

Sintering temperature (°C)	1065	1070	1075	1080
Measured density(gcm^{-3})	5.520±1.75	5.775±1.37	6.133±1.45	6.64±1.09
Theoretical density(gcm^{-3})	7.79±0.967	7.54±1.51	7.542±1.33	7.56±1.65
Percentage density (%)	70.86±1.79	76.60±1.82	81.32±1.29	87.81±1.98

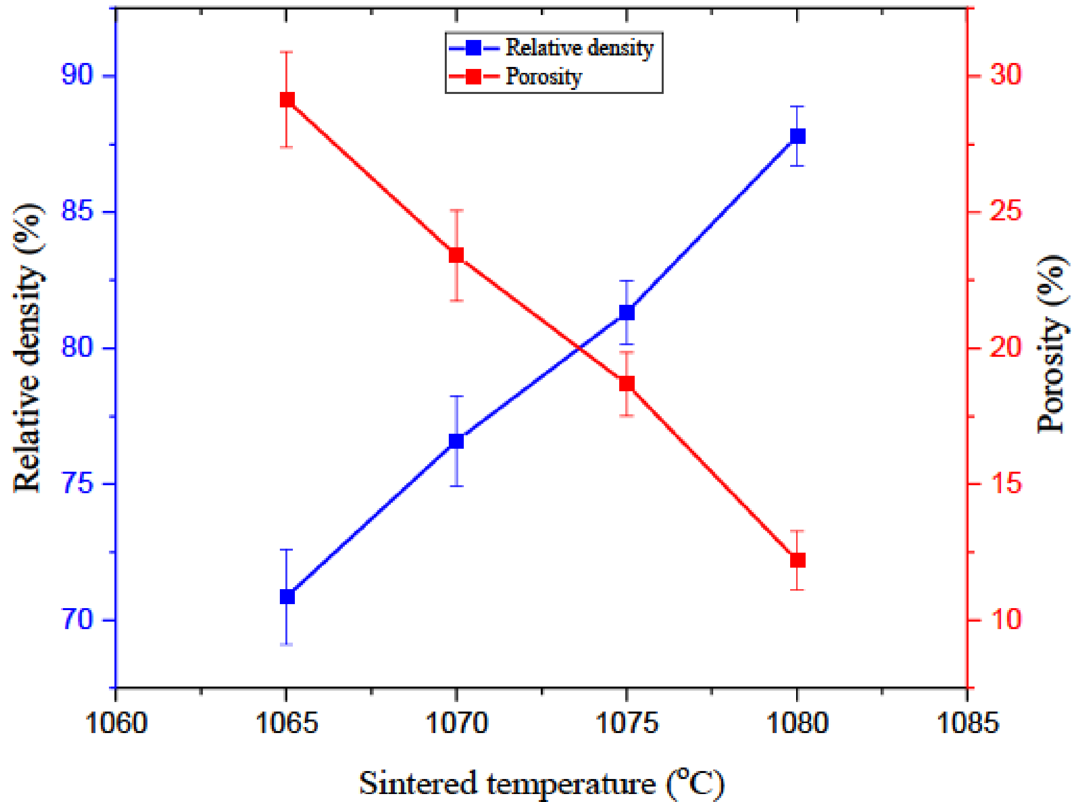

Figure 4.10 Density percentage and porosity of 3D printed Ni-Mn-Ga target sintered at different temperatures.

To reveal the microstructure of the polished targets, Target 1 to 3 were subjected to ion milling using the Leica EM TIC 3X ion beam cutter system. Figure 4.11 (a) – (c) shows the DIC micrographs of the ion milled cross-sections of Targets 1 and 3. Two observations can be made. First, the porosity decreases with increasing sintering temperature, from Target 1 to Target 3. For Target 1, large interconnecting pores can be observed. For Target 3, the pore size decreases below 10 µm and the pores seems to be no longer interconnected. Second, crystallographic twins are visible in all three samples indicating that the targets are in martensitic phase at room temperature.

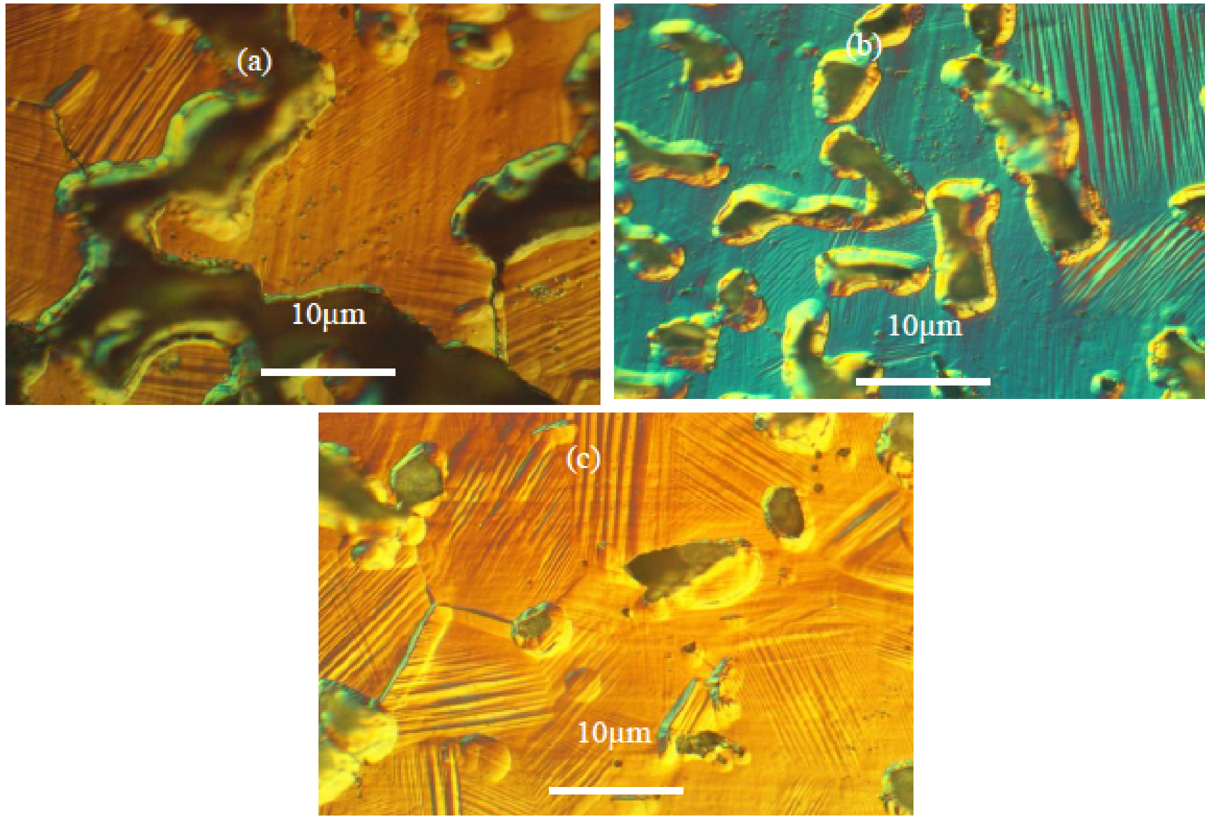

Figure 4.11 DIC image of targets: (a) Target 1, (b) Target 2, (c) Target 3.

The BSE micrographs in Figures 4.12 (a) to (c) confirm the pore distribution observed by light microscopy (Figure 4.11), as well as the presence of crystallographic twins.

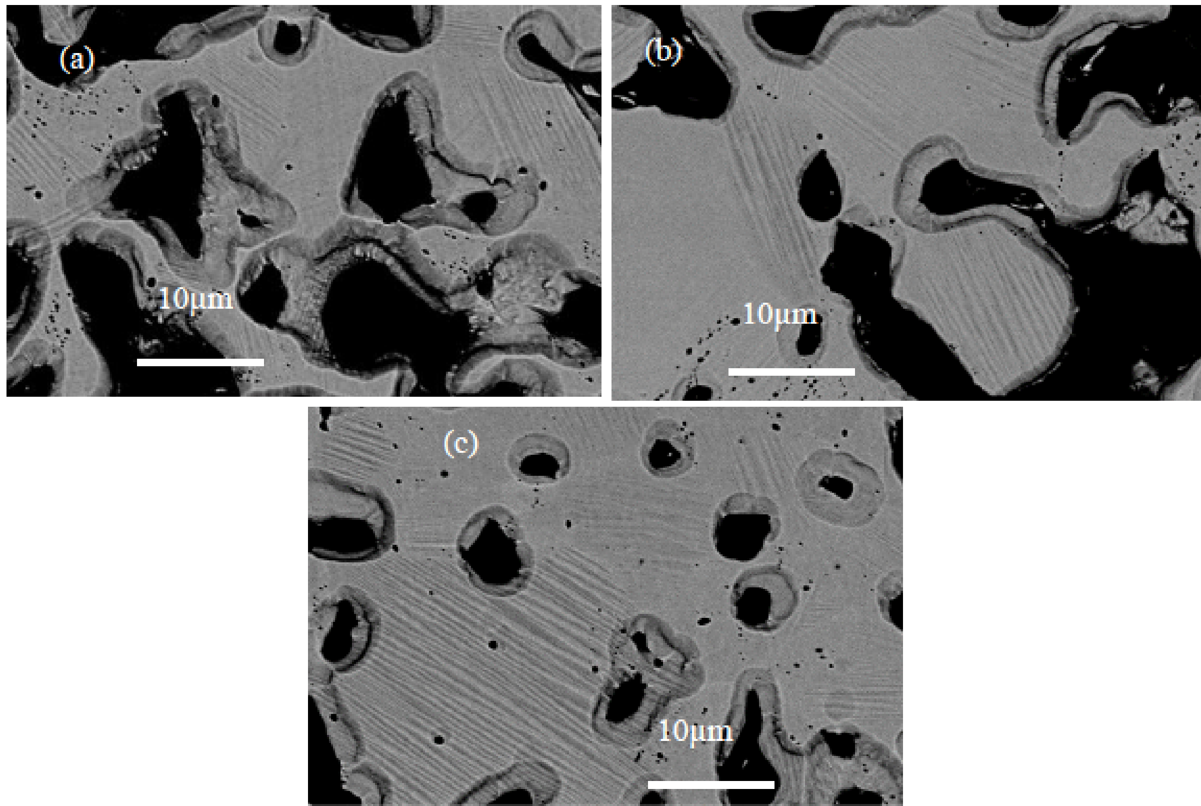

Figure 4.12 BSE micrograph of targets: (a) Target 1, (b) Target 2, (c) Target 3.

4.2.2 Fractography of sintered targets

Further examination of the sintered target microstructure was performed on the mechanically fractured surface of the target, using SEM, Figure 4.13 (a) – (d). Figure 4.13 (a) depicts the fracture surface of Target 1. It appears that the sample fractured at the sintering neck, which might be expected due to the minimal cross-section of the sintering neck. There is no sign of plastic deformation before fracture. The brittle fracture is typical for Ni-Mn-Ga materials [232]. Crystallographic twins are observed at the fractured surface, indicating the existence of room temperature martensitic phase in the sintered target. Porosity decrease with increasing sintering temperature was also confirmed by fractography investigations. The pores are reduced in size for

Target 4 (sintered at 1080^0C, Figure 4.13 (d)), while the cross-sectional area of the sintered neck seems to be larger, compared to the other specimens sintered at lower temperatures.

Crack initiation at the sintered neck, as well as pores and martensitic twins within the grains are observed in Targets 2 and 3, as indicated by the yellow arrows. Target 3 shows a blend of intergranular and cleavage fracture with crack propagation along the grain boundaries. Target 2 and 4 exhibit intergranular brittle fracture with twin martensite visible within the grains of the fractured surfaces. Overall, intergranular brittle fracture with martensitic twins is observed in all four targets, as expected in the case of brittle Ni-Mn-Ga alloy [233].

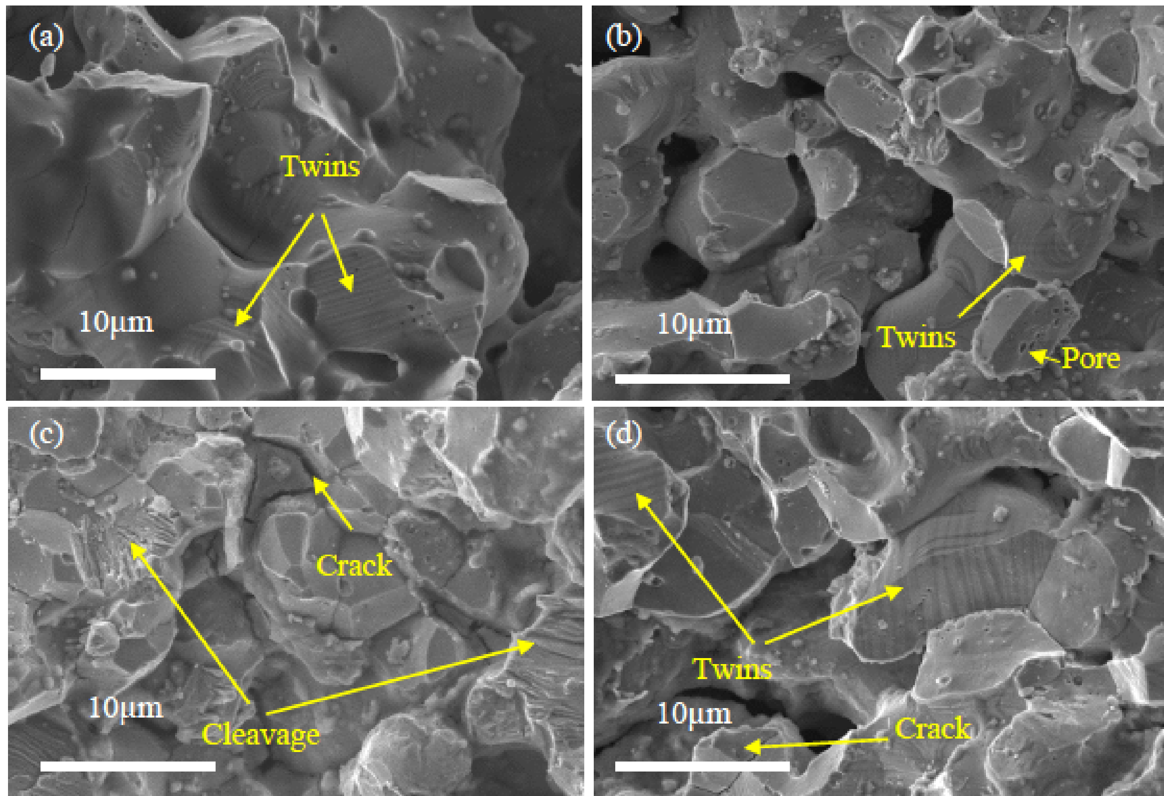

Figure 4.13 Fractured surfaces of 3D printed Ni-Mn-Ga sintered targets: (a) Target 1, (b) Target 2, (c) Target 3, (d) Target 4.

4.2.3 Composition of targets via SEM/EDS

As mentioned in the introductory chapter, in the case of Ni-Mn-Ga alloys, the martensitic transformation temperatures are strongly affected by the composition of the material. SEM/EDS analysis was carried out to assess the chemical composition of the polished sintered targets. For accurate quantitative EDS analysis, a fully dense homogeneous $Ni_{50.90}Mn_{29.23}Ga_{19.87}$ (at%) single crystal reference sample was used for EDS calibration. Table 4.2 presents the mean chemical compositions and standard deviations of EDS analysis carried out on ball milled powder and cross-sections of sintered Ni-Mn-Ga targets taken randomly from 20 selected areas from each sample.

The data from Table 4.2 was plotted in Figure 4.14 for better visualization of Ni, Mn, and Ga compositional change, as function of sintering temperature. The results show a starting powder composition of $Ni_{51}Mn_{28}Ga_{21}$. Comparing powder composition with that of the sintered targets, it is obvious some variations in the compositions can be seen. Significant loss in Ga and Mn can be seen in target sintered at 1065°C, which is due to the evaporation of Mn and Ga. Due to the volatile nature of Mn, at higher temperature, it has high propensity to evaporate which affects the composition of the alloy [234]. As a result, the atomic concentration of Ni went up by ~ 11% making the target Ni-rich.

Table 4.2 Chemical composition of Ni-Mn-Ga powder and sintered targets.

Sample	Ni at%	Mn at%	Ga at%
Powder	51.13±1.54	28.24±1.20	20.63±0.58
Target 1 (1065°C)	62.75±0.76	20.635±0.95	16.61±0.62
Target 2 (1070°C)	53.393±0.608	24.92±0.764	21.685±0.552
Target 3 (1075°C)	52.57±0.970	26.440±2.350	20.980±1.600
Target 4 (1080°C)	52.348±0.238	27.640±0.271	20.015±0.319

For target sintered at 1070°C, 1075°C and 1080°C, less deviations of atomic concentrations of Ga, Mn and Ni were observed, as seen in Table 4.2 and Figure 4.14. As expected, the sintering temperature have significant impact on target composition. The large reduction of Mn and Ga in the Target 1 could possibly be due to improper control of sintering atmosphere leading to evaporation of Mn and Ga. This might also be the case for the Target 2. For the specimens sintered at 1075°C (Target 3) and 1080°C (Target 4), Ni concentration was fairly constant and close to that of the starting powder. For those two samples, Ga concentration is almost identical with the Ga concentration of the starting powders, while Mn concentration slightly dropped, about 1.8 at% for sample sintered at 1075^{0}C and 1.6 at% for the target sintered at 1080^{0}C. This could possibly be due to proper control of sintering atmosphere minimizing the sublimation of Mn.

To better visualize the elemental distribution in the polished targets, EDS mapping was carried out on the cross-section of Target 3, Figure 4.15. The data show the presence of Ni, Mn, and Ga uniform distributed in the alloy which demonstrate chemical homogeneity of the sintered part.

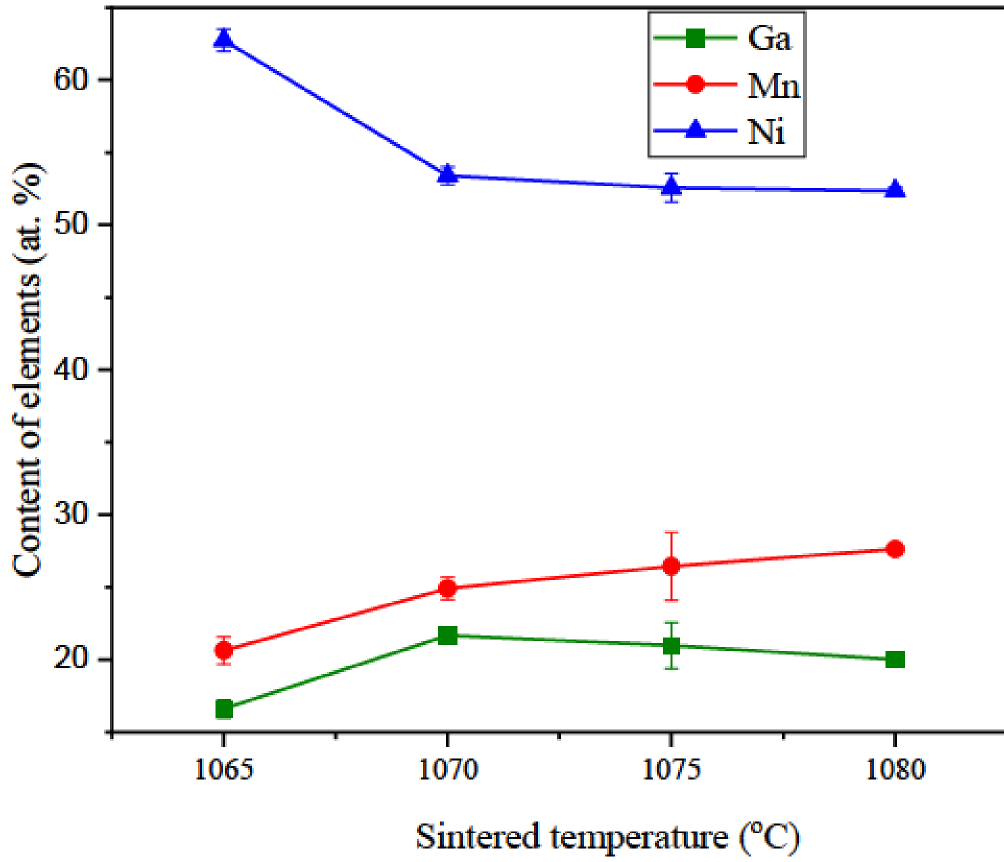

Figure 4.14 Effect of sintering temperature on composition of 3D printed Ni-Mn-Ga targets.

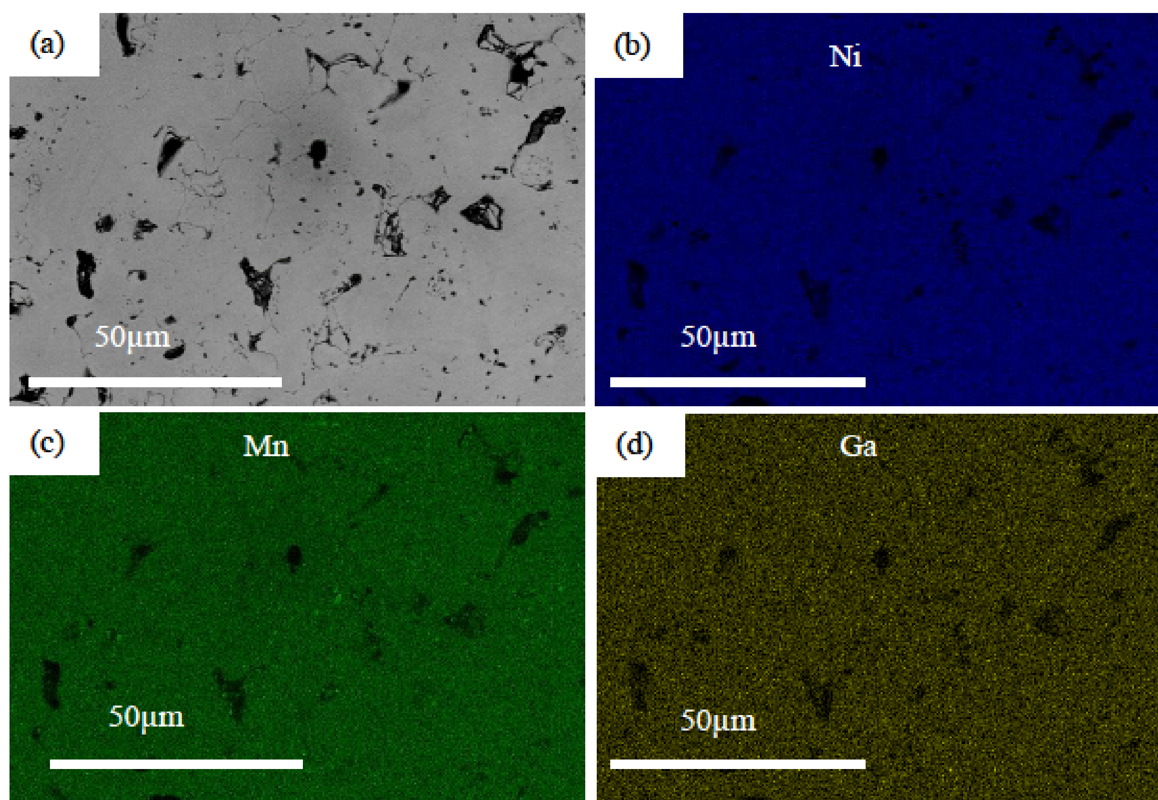

Figure 4.15 (a) BSE micrograph for a cross-section area of Target 3; (b) – (d) Ni, Mn, Ga SEM/EDS maps collected from the area in (a).

4.2.4 Crystal structure and phase transformation in polished Ni-Mn-Ga targets

Single crystal XRD pattern of polished 3D printed Ni-Mn-Ga targets at room temperature are shown in Figure 4.16. Note that, Target 1, Target 2, Target 3, and Target 4 are names given to Ni-Mn-Ga targets sintered at 1065 °C, 1070 °C, 1075 °C, and 1080 °C, respectively. The XRD pattern for Target 1 and Target 2 can be indexed by tetragonal martensitic structure but with different space group and lattice parameters. The Target 1 diffraction curve belongs to the space group F4/mmm and lattice parameters a = 0.5440 nm, c = 0.660 nm, and c/a =1.21324 [235], whereas Target 2 belongs to I4/mmm space group with lattice parameters a = 0.3865 nm, b = 0.3865 nm, c

= 0.6596 nm and c/a = 1.7066 [PDF # 04-011-7324]. The c/a ratio greater than 1 for the two targets is evidence of non-modulated (NM) martensite. In Figure 4.16, the diffraction peaks associated with non-modulated (NM) martensite are represented by the heart symbol. Identical diffraction patterns observed for Target 1 and Target 2 could be the result of increased atomic concentration of Ni, which turns out to stabilize the martensitic structure [81]. The XRD pattern for Target 3 and Target 4 exhibit splitting of peaks between $2\theta = 40°$ and $2\theta = 45°$. The splitting of peaks could be an indication of structural transition from non-modulated (NM) martensite to 7M martensite [236], [237]. The structural transition can be attributed to increase atomic concentration of Mn resulting in variation in unit cell volume [237]. The mixed phases observed are in agreement with article published by Taylor *et al.* [236]

Figure 4.17 shows DSC curves collected from samples prepared from Ni-Mn-Ga sintered targets. All targets exhibit single exothermic peak on heating and endothermic peak on cooling between 60°C and 150°C, except Target 4, which shows splitting of peak. That might be related to the structural transition from NM tetragonal to 7M orthorhombic structure, as observed by XRD investigation. The same phase transformation behavior has been observed and reported by Taylor *et al* [229]. A summary of the phase transformation temperatures of Targets 1 to 4 obtained by tangent method is shown in Table 4.3. Generally, results show a decreasing trend in martensitic transformation temperature from Target 1 to Target 4. Target 1 shows high martensitic transformation temperature (M_s) value of 148.10°C which is due to high Ni content and low Ga content [61] . Target 4 on the other hand, exhibit low martensitic transformation temperature due to low Ni content [61]. Results from this research confirms the dependency of martensitic transformation temperature on composition of off stoichiometric Ni-Mn-Ga alloys.

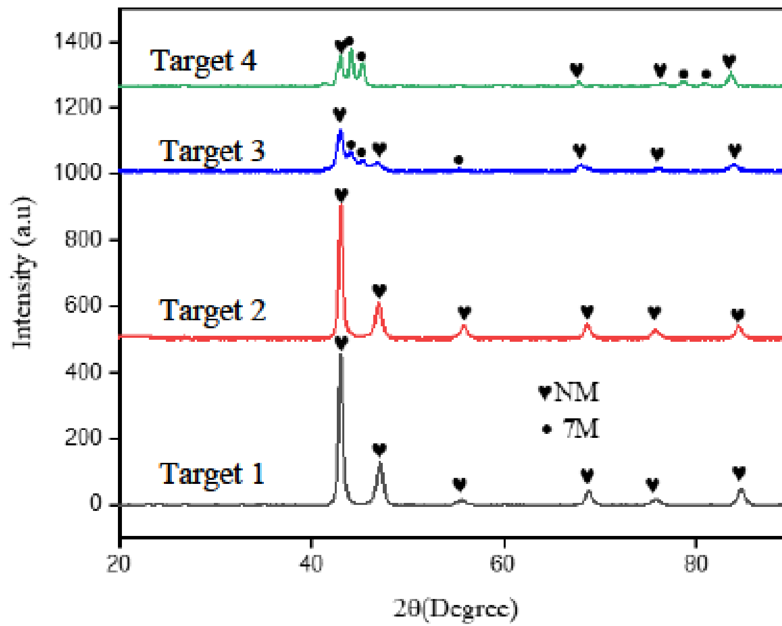

Figure 4.16 XRD pattern of cross-section of 3D printed Ni-Mn-Ga targets sintered at different temperatures.

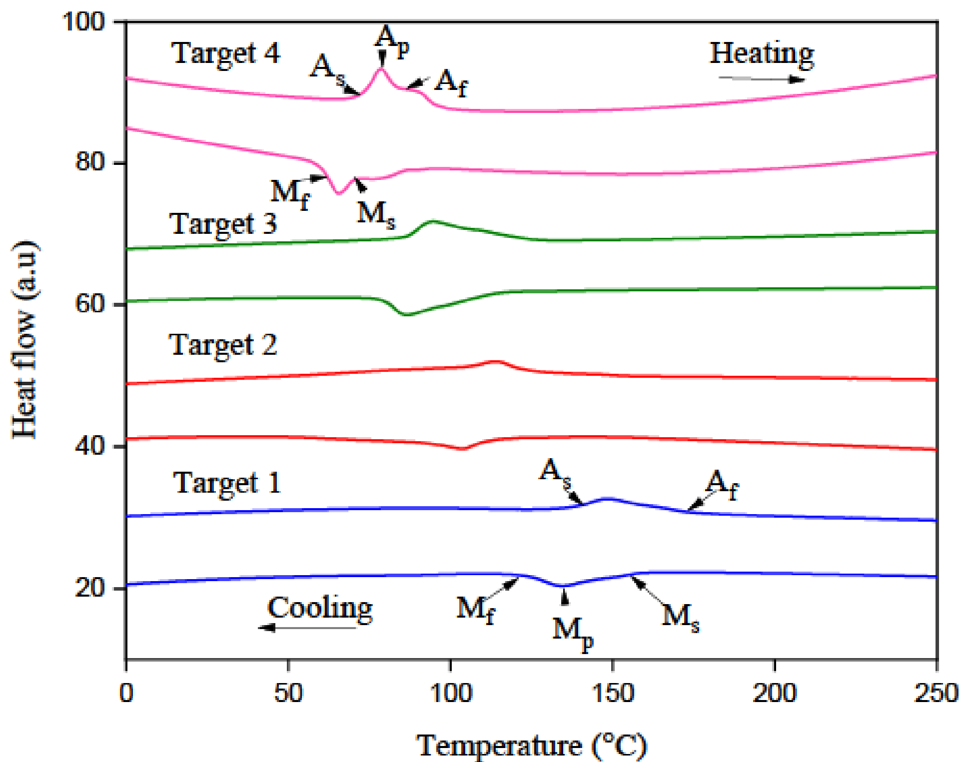

Figure 4.17 DSC curves recorded from 3D printed Ni-Mn-Ga targets sintered at different temperatures, where A_s - austenitic start temperature, A_p - peak temperature, A_f -austenitic finish

temperature, M_s - martensitic start temperature, M_p - martensitic peak temperature, and M_f - martensitic finish temperature.

Table 4.3 Phase transformation temperatures obtained from DSC sintered Ni-Mn-Ga targets.

Sample	**A_s (°C)**	**A_p (°C)**	**A_f (°C)**	**M_s (°C)**	**M_p (°C)**	**M_f (°C)**
Target 1	136.04	148.34	167.20	148.10	134.93	122.86
Target 2	104.10	113.88	125.08	111.97	103.35	90.98
Target 3	85.90	94.60	115.60	108.30	86.80	78.56
Target 4	72.57	78.65	85.91	73.90	65.55	59.34

4.3 Metallurgical properties of additive manufactured Ni-Mn-Ga targets as related to the quality of thin films

The metallurgical properties of targets, such as chemical composition, grain size, density, and porosity directly affect the quality of the thin films obtained from the sputtering targets [130], [238], [239]. This sub-chapter will investigate the chemical composition, grain size, and the density of sintered Ni-Mn-Ga targets obtained by 3D binder jet printing. As mentioned before, the sintered targets have been polished before installation in the DC magnetron sputtering machine, in order to obtain a mirror-like surface on the active surface of the target, and eliminate the surface manganese oxide formed during sintering. As demonstrated in the previous sub-chapter, the polished Ni-Mn-Ga targets have uniform chemical composition and are in the martensitic phase at room temperature.

4.3.1 Chemical Composition

It is well known that film composition in most cases deviates from the composition of a multicomponent target due to preferential sputtering. Results from this research confirm this known fact, as it will be discussed in Chapter 5. Target 3, having the chemical composition of $Ni_{53}Mn_{26}Ga_{21}$ (at%), was mostly used in this work for deposition on Ni-Mn-Ga thin films The

range of film compositions obtained from Target 3 are Ni (46-52) at%, Mn (26-30) at%, Ga (19-27) at%. It should be emphasized that especially for Ni-Mn-Ga thin film, a suitable film composition is necessary for achieving shape memory behavior. Bergstrom *et al.* investigated the origin of compositional changes in sputter deposited $T_{1-x}W_x$ diffusion barrier layers using combination of TRIM calculation and Monte Carlo gas transport simulations coupled with experimental data [240]. Their investigation showed deficiency in Ti of the sputtered film, which they attributed to preferential re-sputtering of the growing film by energetic Ar ions of the discharge. One of the key parameters that controls the sputtering process is the sputtering yield. Especially, for multicomponent target, the film composition would vary depending on the partial sputtering yields of the individual components. In this work, sputtered deposited Ni-Mn-Ga thin film showed slight deviation from the chemical composition of Target 3, which is expected. One possible reason for the deviation might be due to differences in sputtering yield of Ni, Mn, and Ga. This was confirmed by TRIM simulation results (see Chapter 5) which showed higher sputtering yield for Ni, followed by Mn, and then Ga. The sputtering yield also showed strong dependence on the ion energy and the angle of incidence of the bombarding species. It should be noted that TRIM calculations do not consider the topographical changes of the target during sputtering. However, it provides insight into the sputtering behavior of the alloy target.

4.3.2 Grain Size

Figure 4.18 (a) shows the differential interference contrast (DIC) image of the cross-section of Target 3. Figure 4.18 (b) shows SEM micrograph of top surface of Ni-Mn-Ga thin film deposited on Si (100) substrate. From Figure 4.18 (a), the grain size of the target lies in the range of 20 μm - 50 μm whereas in Figure 4.18(b) the grain size of the film lies in the range of 100 nm - 500 nm. From the results obtained, no direct relationship between target grain size and film was detected.

This results is consistent with work reported by R.S. Balley [241]. In his work, he investigated the effect of target microstructure of aluminum-based alloy on film properties and found no effect of target grain size on film properties. Reza *et al.* also found that target grain size have influence on the sputtering yield yet found no correlation between target grain size and film grain size [242]. Michaluk established that the deposition rate during sputtering of tantalum targets were influenced by target grain size [24]. It has also been found that, the sputtering rate of target with smaller grain size is faster than large grain size targets [243]. Targets with smaller grain size have more grain boundaries than targets with large grain size. Grain boundaries are more prone to ion bombardment; therefore, more grain boundaries imply faster film formation. Typical grain size of targets range from few microns to millimeters [244]. It has also been shown that, uniform grain size of sputtering targets have direct influence on film uniformity [243]. However, the target grain size has little impact on film uniformity.

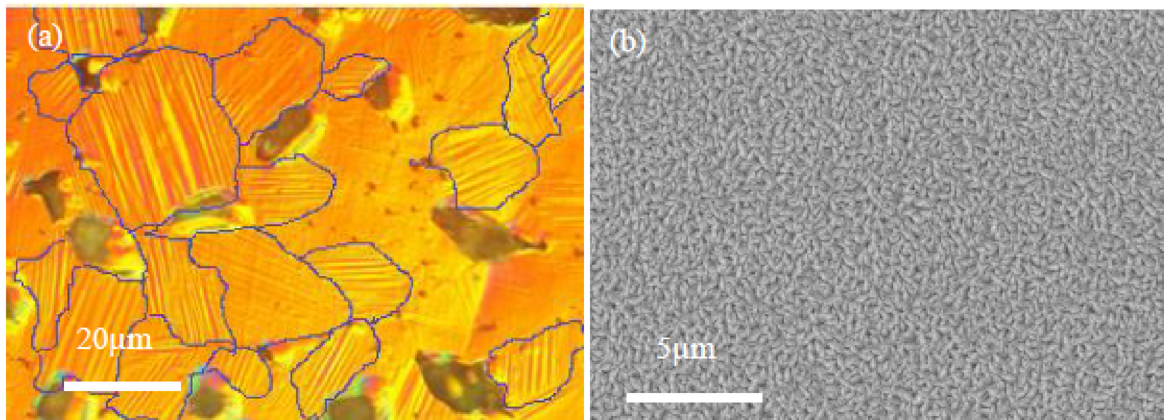

Figure 4.18 (a) DIC micrograph of the target surface, before sputtering; (b) SEM image of Ni-Mn-Ga thin film, obtained from a target having the grain size and morphology, as the target in (a).

4.3.3 Density

Even though the sputtering target used in this research is not fully dense having a density percentage maximum 88 %, yet the quality of the films was not compromised. According to industry standard, a quality thin film should possess the following characteristics: uniform film thickness [245], comparable grain size to that obtained in literature, grain size uniformity, purity, and defect free film surface. All these film qualities are seen on films deposited in this research. However, it must be stated that the density percentage of sputtering targets has an impact on film quality. Lo *et al*. study the effect of sputtering target density on film properties and found that denser sputtering target exhibit higher erosion rate and film deposition rate [246]. They also concluded that voids existing along grain boundaries are potential sources of particle generation. Voids or pores in target are not desirable because they can create electric discharges during sputtering [247]. The additive manufactured target prepared in this research, though porous, yet no electrical discharge was experienced. That notwithstanding, the density of the 3D printed target can be improved by employing various sized powders, and by optimizing the printing and sintering parameters.

4.4 Defects in used 3D printed Ni-Mn-Ga sputtering targets

During sputtering deposition process the morphology of target's active surface (the surface exposed to ion sputtering) changes. The surface modifications are considered target defects. Typical defects are the formation of a race track profile and nodule growth [248]. As presented in Chapter 1 the racetrack profile is due to non-uniform erosion of target surface caused by non-homogeneous ion current distribution across target surface. The nodules are defects generated by impurity atoms in the sputtering chamber or by redeposited target atoms. This sub-chapter presents the results of analytical investigation of the defects formed in the 3D printed Ni-Mn-Ga targets.

Figure 4.19 (a) shows an optical image of a used Ni-Mn-Ga target (Target 3). The image displays the racetrack formation after 20 hours of usage. The surface topography shows different contrast from the periphery to the center of the target. The target surface was investigated with the SEM. The dark area with red square marker is the deepest part of the trench within the racetrack. Figure 4.19 (b) shows the microstructure of the racetrack surface. The microstructure revealed a protrusion of interconnected growth of hillocks or nodules along the grain boundaries within the target. The mean size of the hillocks or nodules were estimated to be about 15 μm as seen from the inset in Figure 4.19 (c). Yet it is not clear if the nodule formation was due to the porosity in the target or contamination from the sputtering chamber. This may require further investigation to uncover the source of nodule formation.

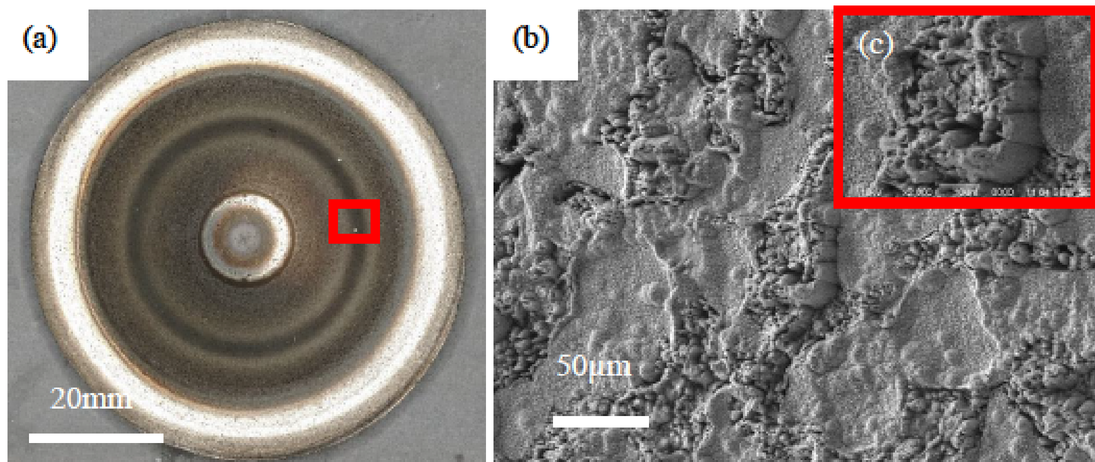

Figure 4.19 (a) Optical image of a used Ni-Mn-Ga target (Target 3); (b)SEM micrograph of the portion of racetrack area marked in (a); (c) An inset of high magnification of nodule growth in (b).

Figure 4.20 (a) and (b) shows the surface topography of Ni-Mn-Ga target sputtered for 10 hours and 30 hours, respectively. The results show evolution of racetrack or erosion groove with the sputtering time. It is observed that the erosion of the target surface was not uniform and the target was much eroded between the periphery and the center of the target. The magnetic field component parallel to the planar disc target is maximum at where the racetrack evolved. As a result, more material is consumed in the region where the race track is created, as long as the disc target is been sputtered.

The racetrack maximum depth was about 500 μm after 10 hours of sputtering, while the target used for 30 hours, shows greater erosion depth, estimated to be about 3 mm, Figure 4.20 (c). Target diameter is 52.92 mm and target thickness is about 4 mm. Based on this data, the target erosion rate can be calculated using the relation:

$$Erosion\ rate = \frac{erosion\ depth}{sputtered\ time} \tag{4.4}$$

From the equation above, the erosion rate for Ni-Mn-Ga target sputtered for 30 hours is 0.1 mm/hr. From literature, the erosion rates estimated for copper and aluminum were 0.164 mm/hr and 0.11 mm/hr, respectively [249].The erosion behavior in this work compares well with those reported in literature.

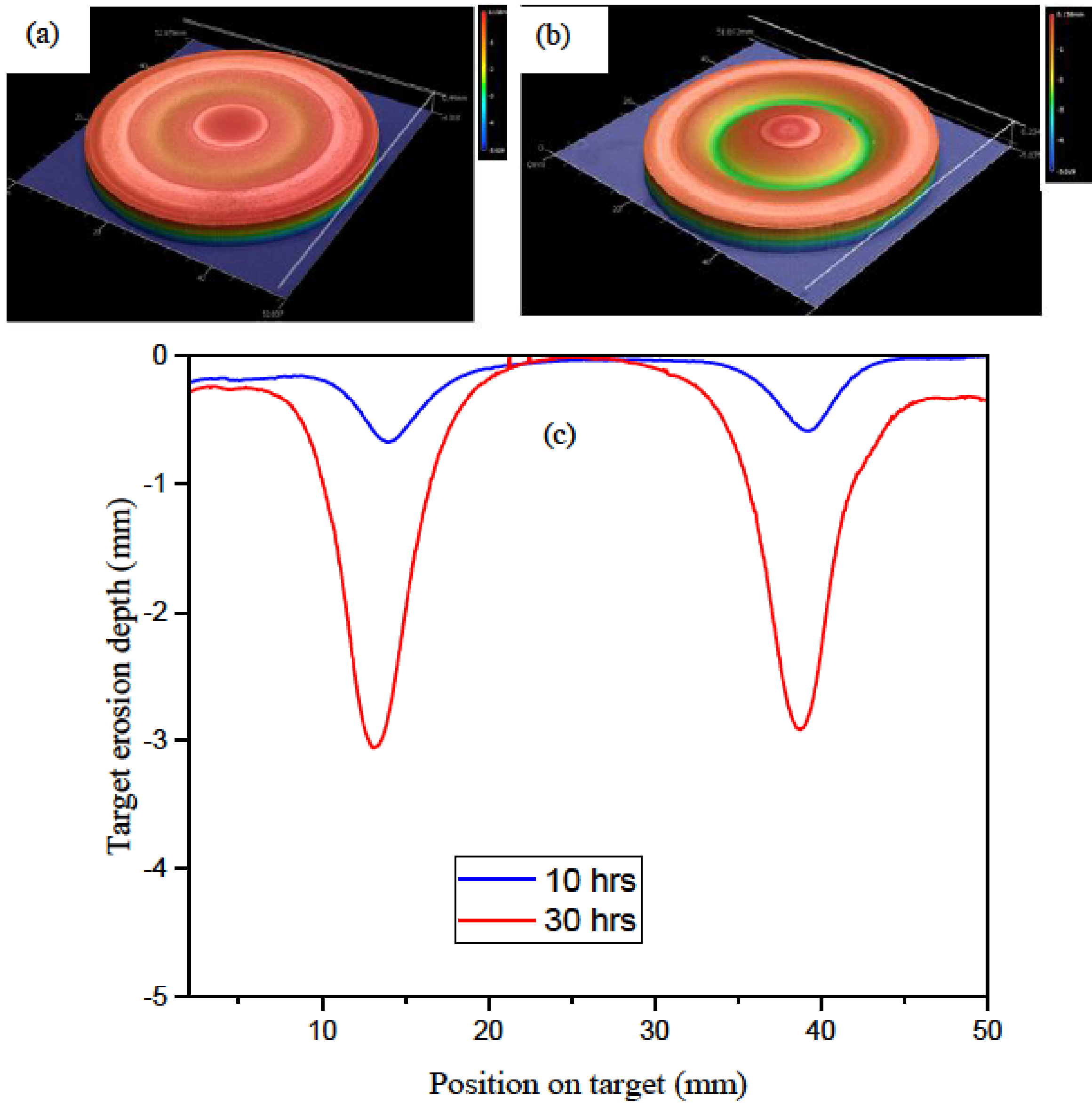

Figure 4.20 3D topography of Ni-Mn-Ga target (52.92 mm in diameter) after: (a) 10 hours, and (b) 30 hours of sputtering; (c) Erosion profile of Ni-Mn-Ga target sputtered after 10 hours and 30 hours.

CHAPTER 5

Ni-Mn-Ga Thin Film Characterization

5.0 Introduction

This chapter presents results obtained from Ni-Mn-Ga thin film deposited on Si (100) and NaCl substrates using magnetron sputtering deposition technique. Silicon substrate was selected because it is cheap and can easily be integrated into microfabrication for MEMS applications. NaCl on the other hand was selected for the purpose of obtaining free standing Ni-Mn-Ga thin films. Two targets of nominal compositions $Ni_{53}Mn_{26}Ga_{21}$ (Target 3) and $Ni_{52}Mn_{28}Ga_{20}$ (Target 4) made by additive manufacturing were employed in the magnetron sputtering deposition system for Ni-Mn-Ga thin film fabrication. Results on the Ni-Mn-Ga film morphology, microstructure, crystallinity, and composition would be discussed.

5.1 Initial challenges of Ni-Mn-Ga thin film fabrication

Initial attempt to deposit Ni-Mn-Ga thin film from additive manufactured target was met with some challenges. This is not surprising since it is a first of its kind. Ni-Mn-Ga thin films were prepared by DC magnetron sputtering using additive manufactured target of composition $Ni_{52}Mn_{28}Ga_{20}$ whose diameter and thickness were ~51 mm and ~5 mm respectively. Thin films were deposited on cleaned Si (100) and NaCl substrates at room temperature. The deposition parameters used in this first attempt were: discharge current of 0.1A, base pressure of 4.0×10^{-7} Torr, argon pressure of 6.2 mTorr, substrate to target distance of 8cm, and deposition time of 60 minutes. Visual inspection of as-deposited Ni-Mn-Ga/Si (100) appeared smooth, with mirror-like surface and that on NaCl substrate appeared yellowish-brown with a shining look. The mirror-like appearance of the as-deposited Ni-Mn-Ga thin films indicate amorphous structure [250]. At lower

substrate temperature, adatoms lack the required thermal energy to facilitate mobility and grain growth. As a result, the adatoms are not able to crystallize and therefore the structure remains amorphous. An investigation on the films morphology and chemical composition were conducted using SEM/EDS and AES techniques.

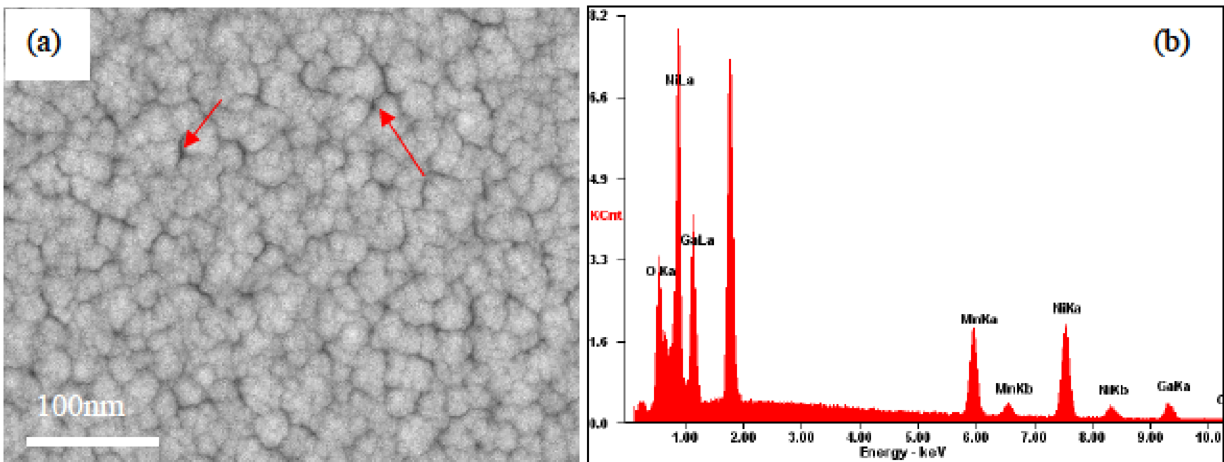

Figure 5.1 Ni-Mn-Ga thin film deposited at room temperature on Si (100): (a) SEM micrograph and (b) EDS spectrum recorded from the thin film.

Figure 5.1 (a) and (b) show backscattered electron micrograph and EDS spectrum of Ni-Mn-Ga thin film deposited on Si (100) at room temperature, respectively. Backscattered electron micrograph reveals rocky-like equiaxed grain morphology with pores in between, as indicated by the red arrows. The average grain size was about 30 nm by visual inspection of the micrograph. The EDS spectrum revealed high oxygen contamination with reduction in Mn, Ga, and Ni content. A quantitative EDS analysis on the as-deposited Ni-Mn-Ga thin film on Si (100) is shown in Table 5.1.

Table 5.1 EDS quantitative analysis of as-deposited Ni-Mn-Ga thin film on Si (100).

Element	wt%	at%
O	10.32	30.22
Ga	23.01	15.46
Mn	20.26	17.28
Ni	46.41	37.04

High oxygen contamination found in Ni-Mn-Ga thin film would affect martensitic phase transformation and affect the shape memory behavior [251]. A further assessment of the film composition was performed by collecting depth composition profiles at various etching rates using AES. Results depicted in Figure 5.2 reveal AES depth composition profile of Ni-Mn-Ga thin film deposited on Si (100). It can be observed that the concentrations of Ga, Mn, and Ni in the film were about 19 - 22 at%, 17-19 at%, and 30 - 35 at% in addition to oxygen contamination with atomic concentration of about 25 - 43 at%. The high oxygen contamination observed in Figure 5.3 confirms result from the EDS analysis. To identify the phases present in the as-deposited Ni-Mn-Ga thin film, XRD analysis was carried out at room temperature. Figure 5.3 depicts XRD pattern of film deposited at room temperature exhibiting broad diffraction peak at 43.3°. The broad diffraction peak indicates disordered structure [81], [252]. The result is consistent with work reported by Wuttig *et al.* [252]. Only austenitic phase with a diffraction peak (220) at $2\theta = 43.3°$ was identified whereas the oxide phase expected was missing because it could not be detected by the diffractometer. The SEM analysis on Ni-Mn-Ga thin film deposited on NaCl substrate, illustrated in Figure 5.4 revealed a triangular pyramid-like grain morphology of the thin film, and uniform composition. The grain size varied from approximately 60 nm to 120 nm. A quantitative EDS analysis on the thin film deposited on NaCl also showed high oxygen contamination of about ~ 20 at% as seen in Table 5.2. Further XRD analysis revealed a disordered structure, as indicated by the broad diffraction peak of (220) representing austenitic phase, Figure 5.5. High oxygen

contamination was a hindrance in obtaining Ni-Mn-Ga thin film exhibiting martensitic phase transformation. Therefore, it became necessary to take steps to reduce or eliminate oxygen contamination.

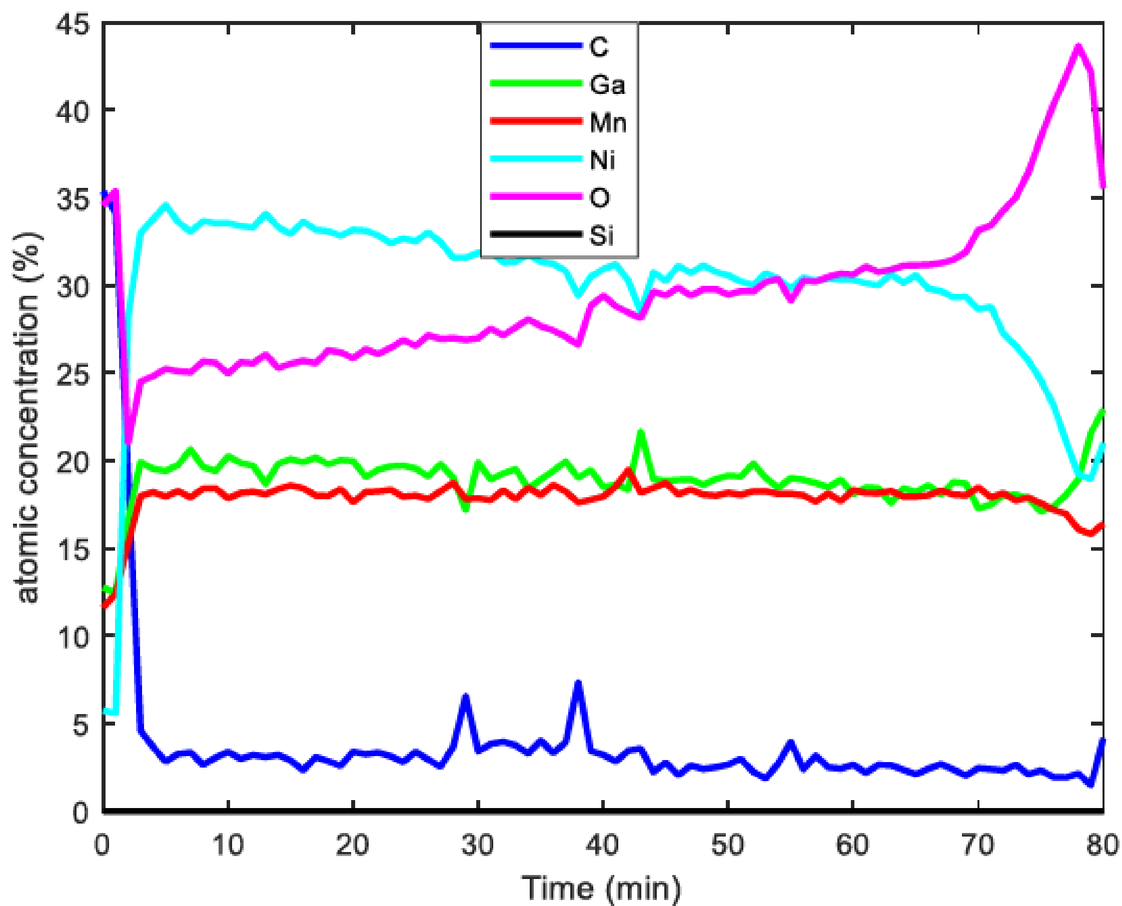

Figure 5.2 AES depth composition profile of Ni-Mn-Ga thin film as-deposited at room temperature on Si (100) substrate.

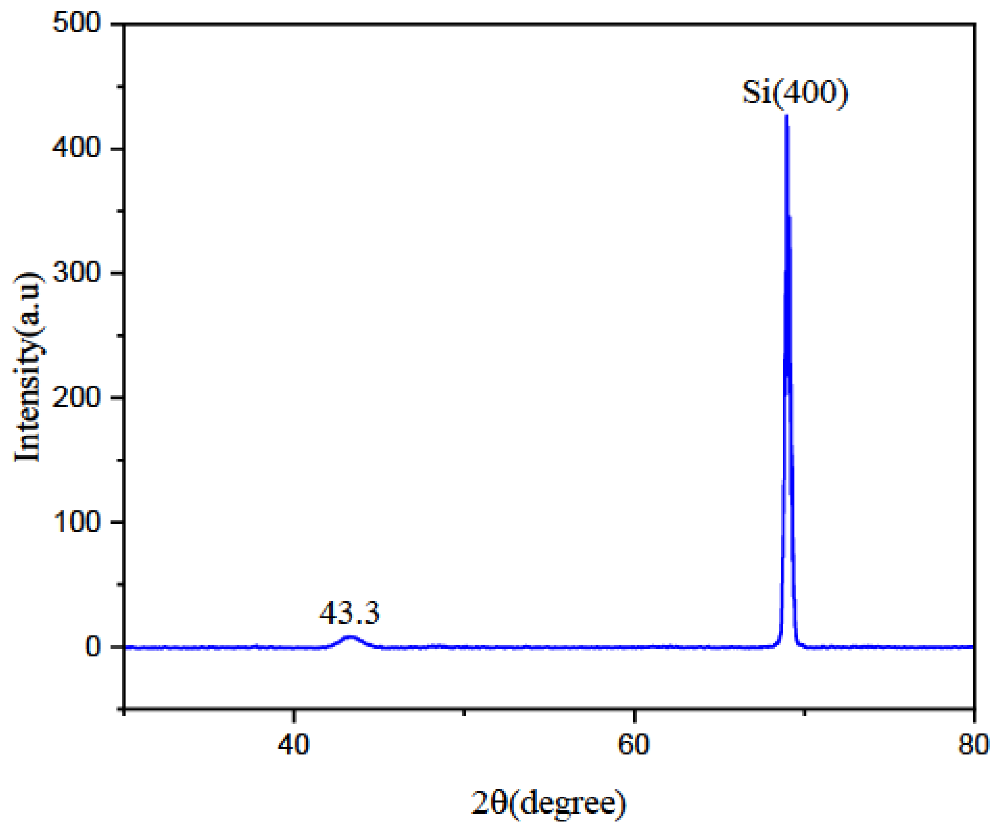

Figure 5.3 XRD pattern of Ni-Mn-Ga thin film as-deposited at room temperature on Si (100) substrate.

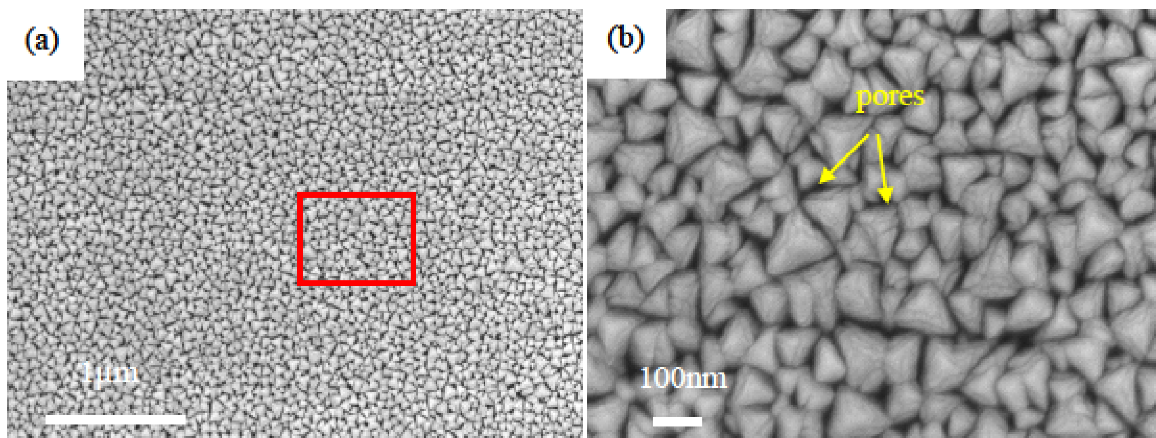

Figure 5.4 BSE micrographs of top view of Ni-Mn-Ga thin film as-deposited at room temperature on NaCl substrate: (a) Low magnification; (b) High magnification.

Table 5.2 EDS quantitative analysis of as-deposited Ni-Mn-Ga thin film on NaCl substrate.

Element	wt%	at%
O	6.44	20.49
Ga	22.16	16.18
Mn	23.25	21.55
Ni	48.15	41.77

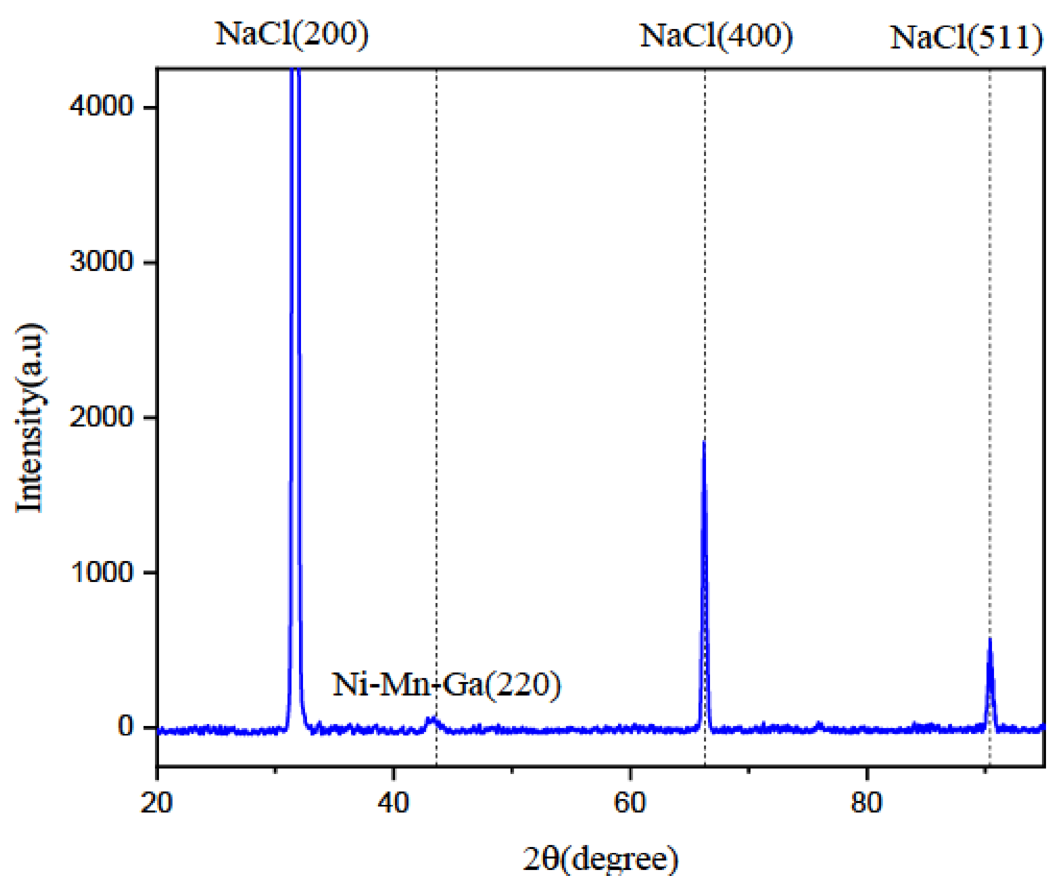

Figure 5.5 XRD pattern of Ni-Mn-Ga thin film as-deposited at room temperature on NaCl substrate.

5.2 Resolving oxygen contamination problem

To minimize oxygen contamination in Ni-Mn-Ga thin films, a cleaned piece of Mn getter flake was employed and positioned on substrate holder while substrate material was in place. The magnetron sputtering chamber was pumped down until a base pressure on the order of 10^{-7} Torr was attained. It was ensured that the connecting tube between argon tank and the sputtering chamber was well evacuated alongside with the chamber to remove any residual oxygen trapped in the tube. Substrate heating was carried out in order to activate the Mn getter to reduce oxidation of thin film during sputtering. The sputtering deposition was conducted under ultra-high purity argon gas (99.9999 %) atmosphere with a flow rate of 10 sccm. The deposition pressure was varied from 3.2 mTorr to 6.2 mTorr. Target composition of $Ni_{53}Mn_{26}Ga_{21}$ (Target 3) was used for the deposition. Target to substrate distance was about 4 cm. Prior to the deposition, Ni-Mn-Ga target was pre-sputtered for 20 minutes to remove any surface contamination. Ni-Mn-Ga thin films were deposited on single crystal silicon and sodium chloride substrates at substrate temperature of 500°C and a discharge current of 0.1 A, for 60 minutes. Substrate temperature and discharge current were constant while varying the argon pressure. This was done in order to get the optimum gas pressure necessary to tailor film composition. Figure 5.6 (a) - (d) depicts SEM micrographs of Ni-Mn-Ga thin films deposited on silicon substrate at different argon pressures 3.2 mTorr, 4.2 mTorr, 5.2 mTorr, and 6.2 mTorr respectively. Results show the surface morphology of films exhibiting increasing grain size from low to high deposition pressure contrary to what has been reported in literature. The possible explanation is that, at 3.2 mTorr the kinetic energy of the adatoms is not sufficient enough to produce large grains, but at 6.2 mTorr the adatoms acquire sufficient energy to form large grains, which means certain minimum deposition pressure is required in order to realize large grains [253], [254]. It is also seen that film prepared at 6.2 mTorr exhibits pyramidal-

like morphology with densely packed grains. The thin film appears to be homogeneous, irrespective of the deposition pressure. It has been shown that martensitic transformation temperature is dependent on grain size of ferromagnetic shape memory alloys [59], [255]. A certain critical grain size is required for martensitic transformation to occur [255], [256]. Micrometer-sized grains are desirable for achieving martensitic transformation in Ni-Mn-Ga thin films. Hence, it was concluded that the optimum deposition pressure was 6.2 mTorr.

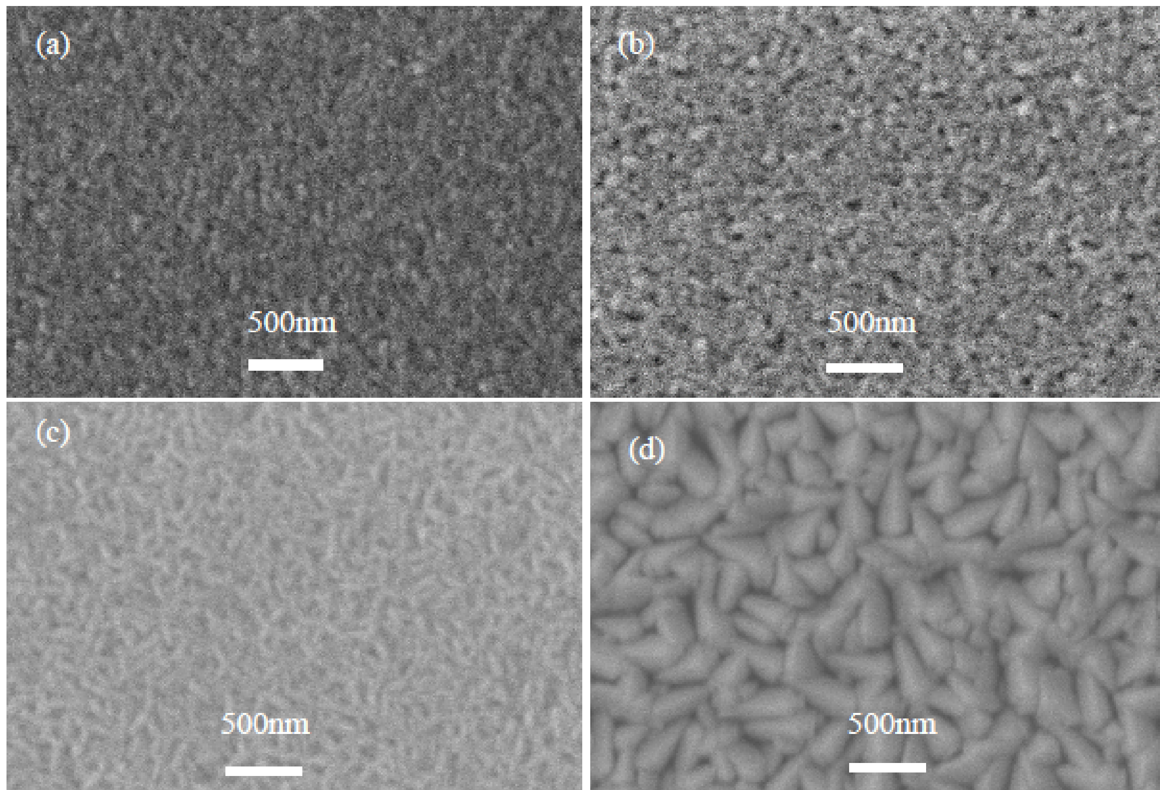

Figure 5.6 SEM micrographs of plane view of Ni-Mn-Ga thin film deposited on Si (100) substrate at different argon pressures: (a) 3.2 mTorr, (b) 4.2 mTorr, (c) 5.2 mTorr, (d) 6.2mTorr.

EDS analysis was used to verify the chemical composition of the film, Figure 5.7. The analysis showed reduced oxygen contamination, as seen in Figure 5.7 (b), compared to the previous samples.

Figure 5.8 depicts optical micrograph of top view of Ni-Mn-Ga thin film deposited on NaCl substrate. The film appeared crumpled upon cooling with connected bumps and valleys. This behavior could be attributed to differences in thermal expansion coefficient of Ni-Mn-Ga and NaCl inducing thermal stresses [70], [257]. The crumpling behavior of the film deposited on NaCl makes it unsuitable for application. XRD analysis was also carried out to assess the thin film crystallinity. Result from XRD spectrum shows austenitic cubic structure with (220) diffraction peak which occurred at 43.72°, Figure 5.9. Three other additional peaks were detected which are associated with NaCl indexed as (200), (400) and (511). The most prominent among the peaks is (200). Based on these results, it was decided to use silicon substrate for the following Ni-Mn-Ga thin film depositions.

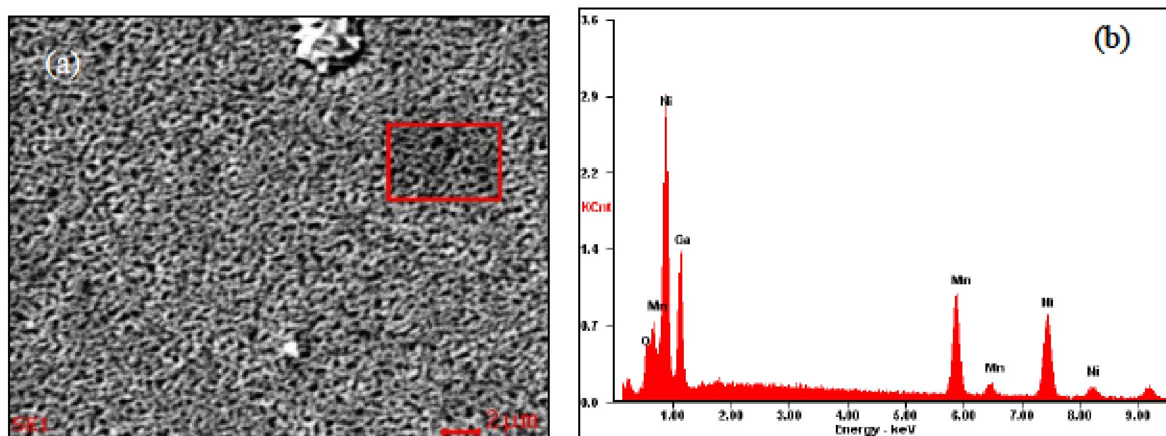

Figure 5.7 (a) SEM micrograph of Ni-Mn-Ga thin film deposited at 500°C on Si (100), (b) EDS spectrum of selected region marked in red square.

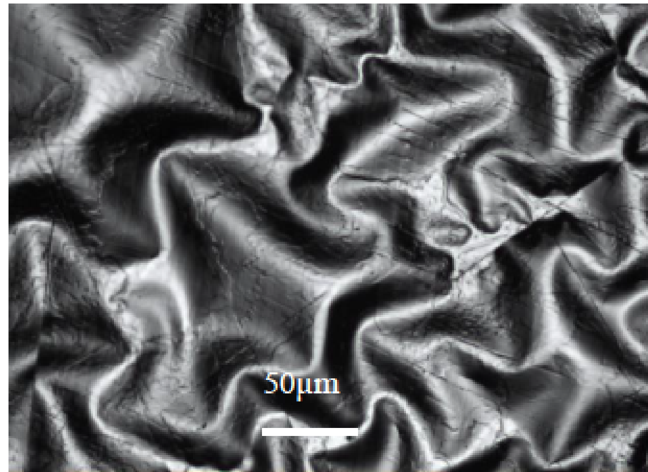

Figure 5.8 Optical micrograph of Ni-Mn-Ga thin film deposited on NaCl substrate at 500°C substrate temperature.

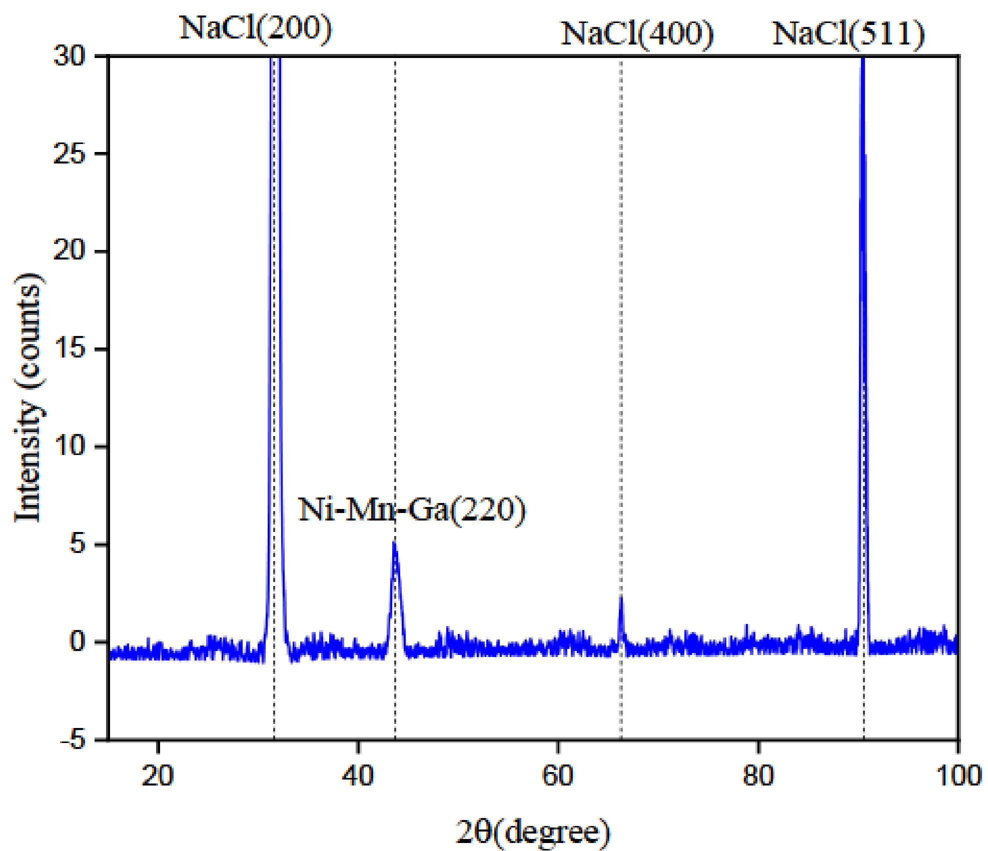

Figure 5.9 XRD spectrum of Ni-Mn-Ga thin film deposited on NaCl substrate at 500°C.

5.3 Effect of discharge current on composition, surface morphology and microstructure of Ni-Mn-Ga thin films

One of the important deposition parameters in magnetron sputtering that has not been explored in the fabrication of Ni-Mn-Ga thin film is the discharge current. Even though other deposition parameters such as sputtering power [87], [258], [259], substrate temperature [81], deposition pressure [87], [259], post-heat treatment [99], [260], target to substrate distance [259], and deposition time [260] have been reported yet no study has been carried out on the influence of discharge current on Ni-Mn-Ga thin film. The discharge current and discharge voltage were read directly from the meter reading of the sputtering machine. It made it easier to vary the discharge current while keeping other deposition conditions constant.

In this section, the influence of discharge current on the surface morphology and the microstructure of the Ni-Mn-Ga thin films will be reported. The target used for this investigation was Target 3 ($Ni_{53}Mn_{26}Ga_{21}$ at%). Target to substrate distance was 4 cm. Substrate heating was conducted at a rate of 15°C/min until 500°C temperature was reached. Sputtering was conducted with an argon pressure of 6.2 mTorr for 60 minutes. Several depositions were conducted by varying the discharge current from 0.05 A to 0.15 A in steps of 0.02 *ie*. (0.05 A, 0.07 A, 0.09 A, 0.11 A, 0.13 A, and 0.15 A). The first two (0.05 A and 0.07 A) and the last two (0.13 A and 0.15 A) discharge currents were selected for analysis because the two samples 0.09 A and 0.11 A got damage while transporting it for analysis. The composition of Ni-Mn-Ga thin films with varying discharge current, as obtained by EDS investigation, is presented in Table 5.3.

Table 5.3 Composition of Ni-Mn-Ga thin films deposited at different discharge current, S 1 to S 4 labeling indicates samples obtained at different discharge current.

Sample	Discharge current (A)	Ni (at%)	Mn (at%)	Ga (at%)
S 1	0.05	46.19	26.73	27.09
S 2	0.07	51.38	29.24	19.38
S 3	0.13	47.55	26.69	25.76
S 4	0.15	49.81	26.09	24.15

The samples deposited at discharge currents 0.05 A, 0.07 A, 0.13 A and 0.15 A were named S 1, S 2, S 3, and S 4, respectively. Figure 5.10 presents the results on the relationship between discharge current and film composition. It can be seen that Ni and Mn content show similar trend initially as the discharge current increases up to 0.13 A. For the highest value of the discharge current Ni content showed an increase whereas Mn content showed a slight decrease, which may be due to different sputtering yields. Ga content on the other hand didn't show any definite trend. Comparing target composition $Ni_{53}Mn_{26}Ga_{21}$ to thin films composition, a slight deviation from target composition is observed. It is seen that Ni content in thin films are generally lower than that of the target whereas Mn and Ga contents are higher than that of the target. The differences could be attributed to differences in sputtering yields of Ni, Mn, and Ga [79]. It also appears that sample S 4 of composition $Ni_{49.81}Mn_{26.09}Ga_{24.15}$ is the closest to the target composition $Ni_{53}Mn_{26}Ga_{21}$. The result suggest that the discharge current have direct influence on the film composition and therefore could be varied to adjust the chemical composition of the films.

In an attempt to understand the compositional changes in Ni-Mn-Ga thin film with respect to the target composition a computer simulation was performed using a Monte Carlo code called TRIM program [209]. The effect of ion energy and angle of incidence on the sputtering yield of Ni-Mn-

Ga alloy were investigated. The sputtering yield is defined as the average number of sputtered target atoms per incident ion. Results from TRIM simulation show that the sputtering yield of Ni, Mn, and Ga increases with ion energy from 100 eV to 1000 eV (see Figure 5.11). Ni content showed the highest sputtering yield and Ga showed the lowest sputtering yield. All three curves show similar behavior. The differences in the sputtering yield of Ni, Mn, and Ga observed in Figure 5.11 confirms the compositional changes in the thin film. Ni is preferentially sputtered from the alloy target compared to Mn and Ga. Similar trend has been reported by Sharma *et al*. in their investigation of the effect of sputtering power on the composition of Ni-Mn-Ga thin film [79]. They found that the differences in sputtering yield of Ni, Mn, and Ga increases with sputtering power. They concluded that the film composition is strongly dependent on the sputtering power.
Figure 5.12 shows the sputtering yield of Ni-Mn-Ga alloy bombarded by 1000 eV of Ar^+ ions at incident angles from 0° to 80°. Between 20° and 60° angle of incidence, it is observed that sputtering yield increases exponentially. Above 60° incidence angle, a decline in the sputtering yield is seen. Again, all three curves show similar behavior. Observation from both plots show strong dependency of sputtering yield on ion energy and incident angle.

Based on the modeling results, it is expected that the Ni content of the thin film will increase, while Mn and Ga content will decrease. However, this is not the case for the Ni-Mn-Ga thin films deposited in this work (see Table 5.3 and Figure 5.10). More experimental and modeling work is necessary, in order to understand the influence of discharge current on the chemistry of Ni-Mn-Ga thin films.

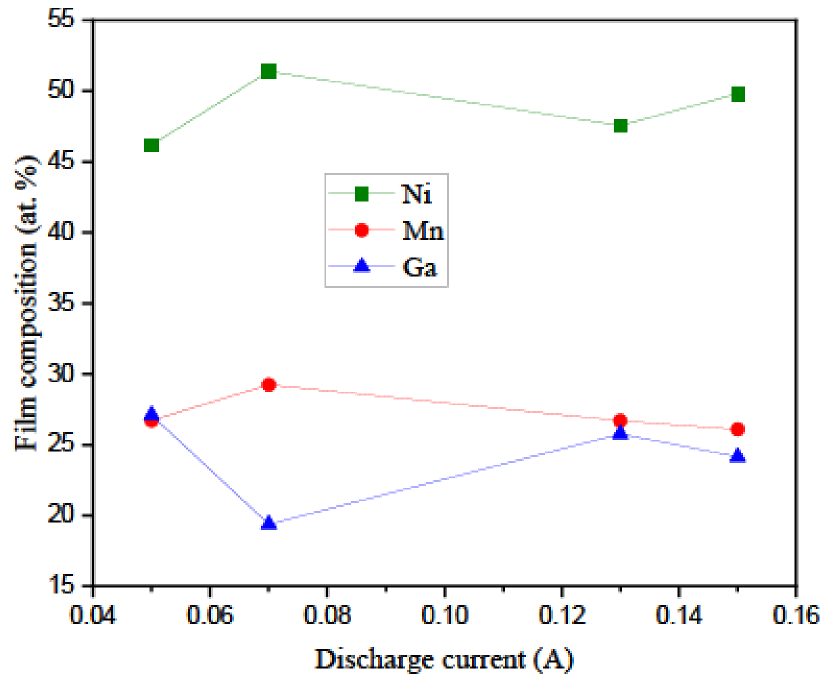

Figure 5.10 Effect of discharge current on composition of Ni-Mn-Ga thin film.

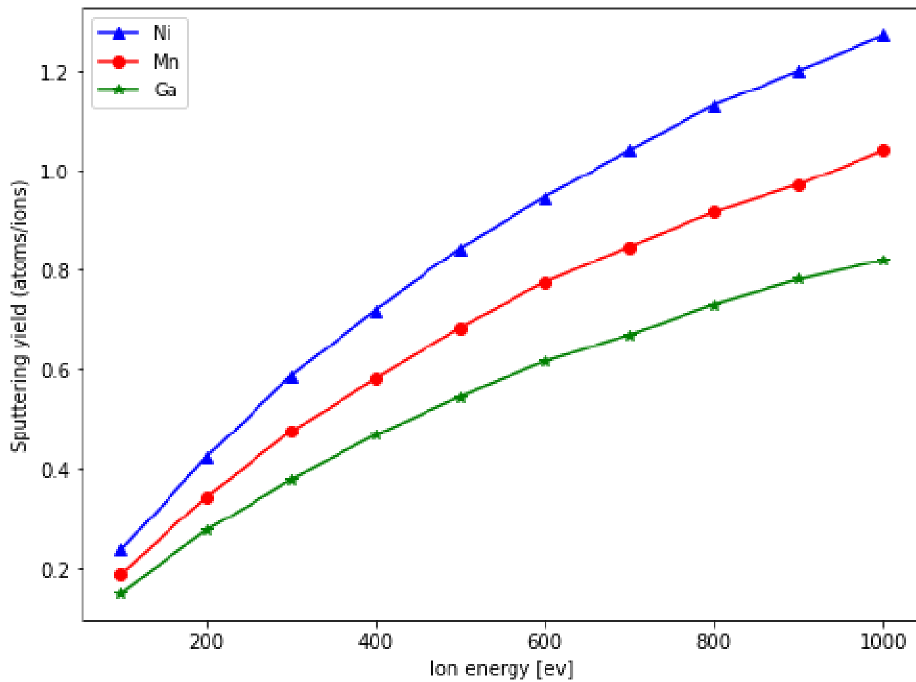

Figure 5.11 Sputtering yield as function of ion energy.

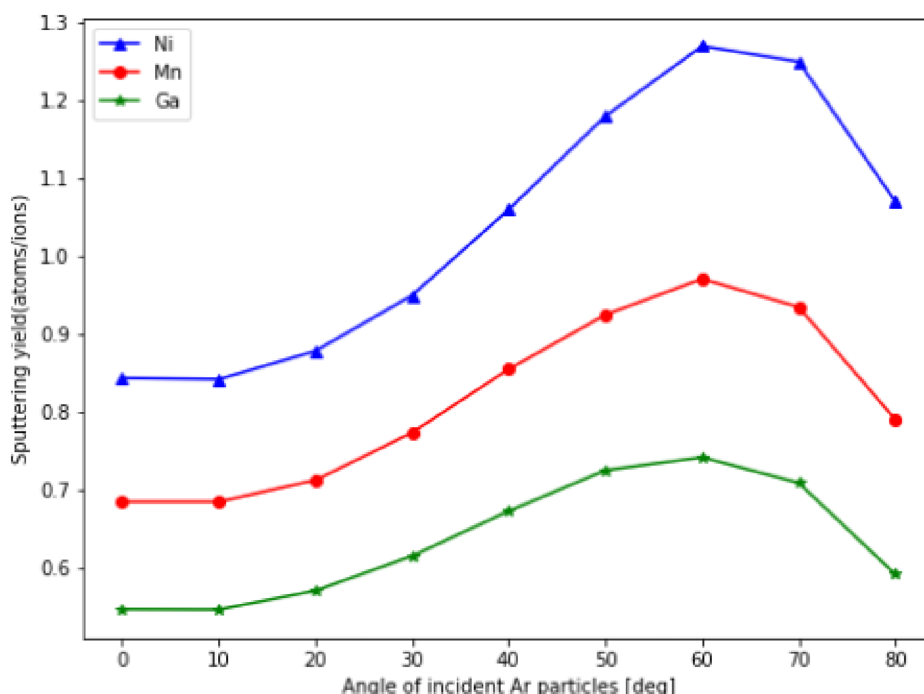

Figure 5.12 Sputtering yield as function of incidence angle.

Figure 5.13 (a) – (h) show the SEM micrographs of the plane view and cross-sections of the Ni-Mn-Ga thin films deposited on the Si (100) substrate at a discharge currents of 0.05 A, 0.07 A, 0.13 A, and 0.15 A for 60 minutes, samples S 1 to S 4, respectively. The plane view images show uniform grain size and morphology, which indicates a stable deposition process. The influence of the discharge current on the film morphology showed significant change in the grain size as the discharge current increased from 0.05 A to 0.07 A. This is an indication that during the deposition process an increase in discharge current increases the deposition rate which enables increase in adatoms mobility and enhances surface diffusion of the of the adatoms. Fewer voids are observed due to increase in adatom mobility and surface diffusion during the growth process because of increase discharge current. All samples show elongated grain morphology with a rice-like shape. The width of the elongated grains is in the range of 60 nm to 100 nm and the length in the range of 200 nm to 450 nm. The cross-sectional micrographs of the S 1, S 2, S 3, and S 4 samples show

uniform film thickness and columnar microstructure. It is evident that the discharge current affect film thickness. As the discharge current increases, film thickness increases with no pores in sight.

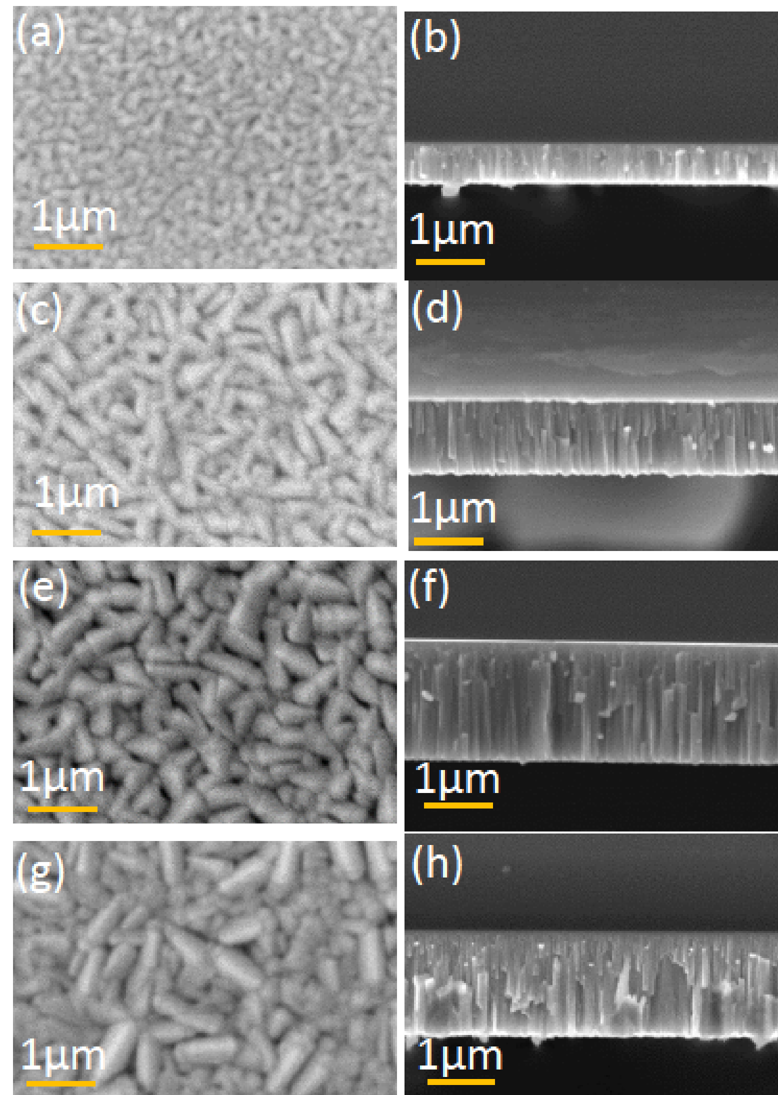

Figure 5.13 SEM micrograph of top and cross-section of Ni-Mn-Ga thin film deposited at different discharge current: S 1 (a, b), S 2 (c, d), S 3 (e, f), and S 4 (g, h).

Grain size measurement was carried out by processing the plane view SEM micrographs of samples in ImageJ software. The average grain size and standard deviations for each sample were calculated.

Film thickness for each sample was measured from cross-section SEM images. The average grain size was determined using the main linear intercept method, as described in the ASTM standard E112 [261]. Five measurements were taken for each sample and the average, and the standard deviations were computed. It can be observed from Figure 5.14 that, both grain size and film thickness increase with discharge current. Except for sample S 4, 0.15 A discharge current where a drop in both grain size and film thickness was observed which may be due to shorter deposition time. The deposition time was about 50 minutes.

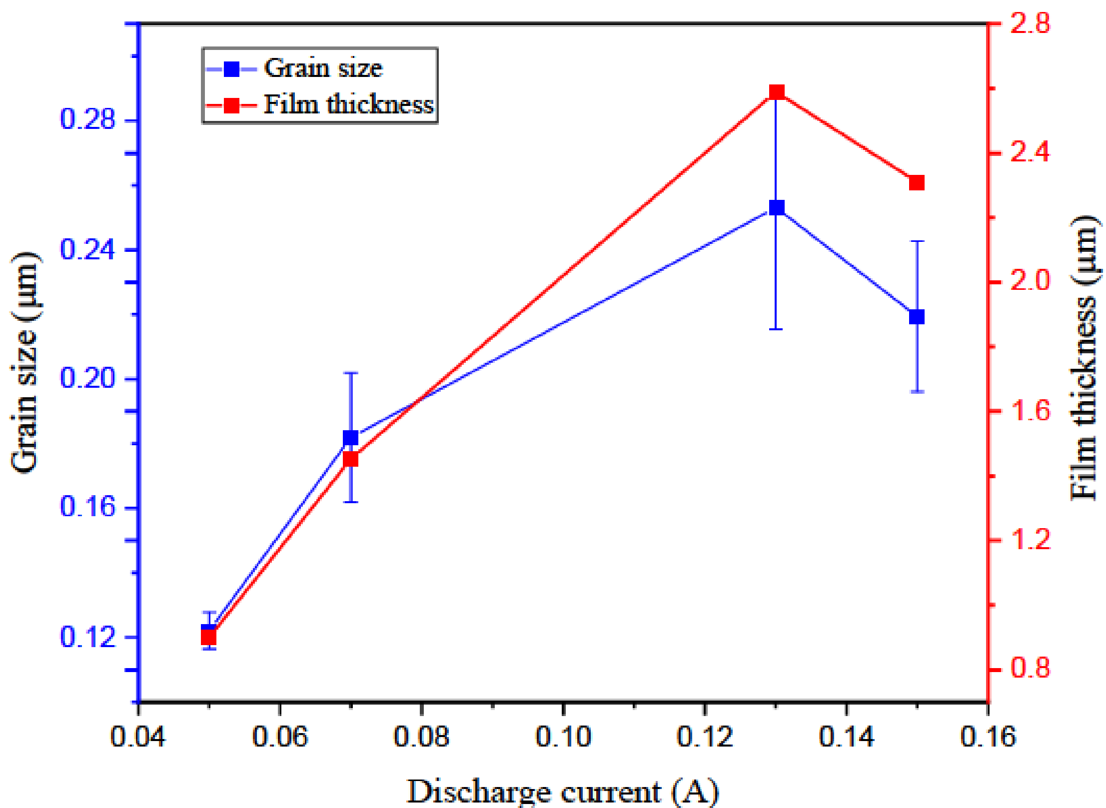

Figure 5.14 Variation of film thickness and grain size with discharge current.

Film uniformity was also calculated using the relation below [262]:

$$\% \, Non\ uniformity = \frac{Max\ film\ thickness - Minimum\ film\ thickness}{Average\ film\ thickness} x100 \qquad (5.1)$$

Results from the film uniformity calculation as observed from Table 5.4 show that, the film thickness range for the 4 samples varied between 0.022 µm to 0.07 µm. Sample S 4 showed the lowest film non-uniformity value of 0.949 % and S 1 showed the highest film non-uniformity of 2.682 % which suggest Sample S4 exhibited the highest degree of film uniformity.

Table 5.4 Film thickness measurements and uniformity calculations for Ni-Mn-Ga thin films deposited at different discharge currents

	Film thickness (µm)			
Location	S 1	S 2	S 3	S 4
1	0.9	1.452	2.59	2.31
2	0.893	1.475	2.64	2.33
3	0.896	1.467	2.66	2.308
4	0.905	1.459	2.6	2.326
5	0.881	1.446	2.6	2.315
Average (µm)	0.895	1.4598	2.622	2.3178
Standard deviation	0.009028	0.01156	0.0286	0.009757
Range (µm)	0.024	0.029	0.07	0.022
Non-uniformity (%)	2.682	1.987	2.670	0.949

Figure 5.15 shows the X-ray diffraction pattern of Ni-Mn-Ga thin films deposited at different discharge current. For sample deposited at discharge current of 0.05 A (S 1), the data shows a broad diffraction peak at 2θ = 44.2° which indicates a disordered structure [81], [258]. At low discharge current, adatoms have less kinetic energy and therefore have reduced surface mobility which affect the crystallinity of the films. However, by increasing the discharge current, adatoms would have sufficient kinetic energy to enhance surface diffusion for atomic ordering [81]. At a

discharge current of 0.07A (S 2), a sharp diffraction peak begins to emerge at 2θ = 44.2°. Samples S3 and S4 exhibit sharper diffraction peak with increasing intensity which corresponds to better crystallinity. The diffraction peak at 2θ = 44.2° is indexed as austenitic cubic structure (220) with lattice parameters a = b = c = 0.5786 nm belonging to the *Fm-3m* space group [PDF 04-015-2460]. Result obtained is consistent with work reported by Kumar *et al.* [101].

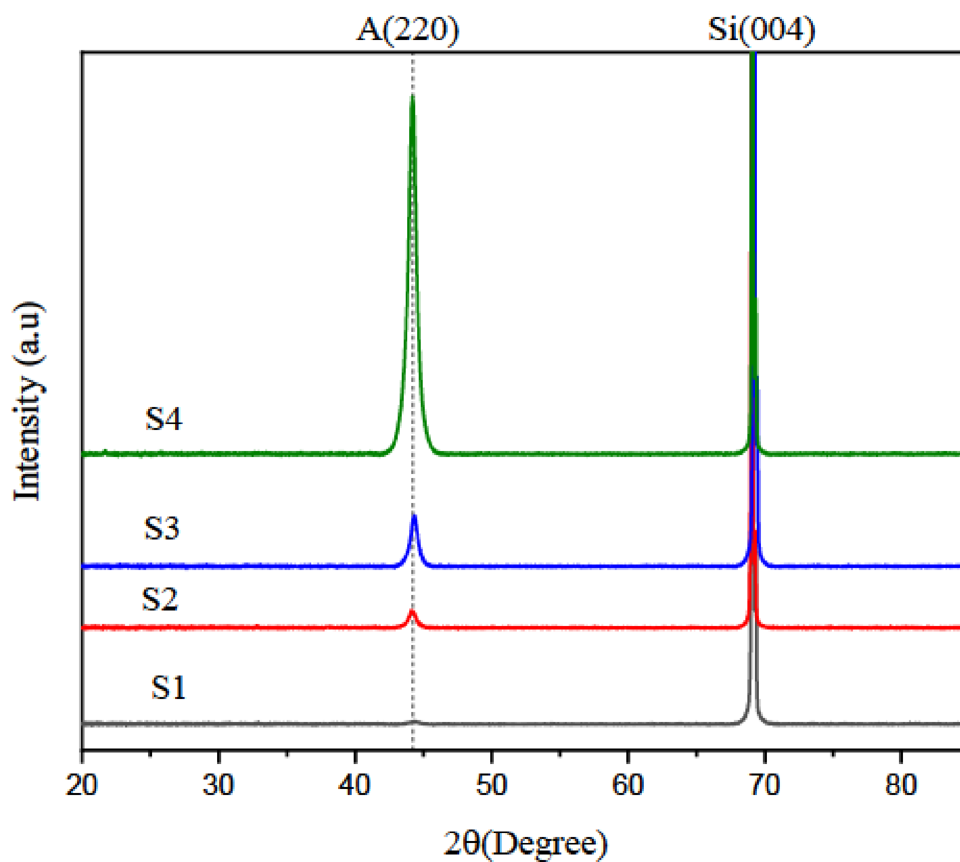

Figure 5. 15 XRD spectrum of Ni-Mn-Ga thin film deposited at different discharge current.

5.4 Effect of substrate temperature on composition, surface morphology and structural evolution of Ni-Mn-Ga thin film

Ni-Mn-Ga thin films have been obtained by DC magnetron sputtering of Ni-Mn-Ga targets manufactured by 3D binder jet printing of pre-alloyed Ni-Mn-Ga powders. The thin films have been grown on Si(100) substrate heated up to 500^0C, 600^0C, and 700^0C for 1 hours. The following sputtering parameters were used in the sputtering process: discharge current 0.11 A, target to substrate distance 4 cm, and the argon pressure was 6.2 mTorr. For simplification, the Ni-Mn-Ga thin films obtained by deposition at 500^0C, 600^0C, and 700^0C for 1 hour, and reported in this subchapter, are labeled as NMG1, NMG2, and NMG3, respectively.

5.4.1 Compositional analysis

Chemical composition analysis of the Ni-Mn-Ga thin films deposited at 500^0C, 600^0C, and 700^0C was investigated using the EDS and AES techniques. The film composition obtained using EDS spectroscopy for the various deposition temperatures are shown in Table 5.5. Figure 5. 16 shows the SEM micrographs recorded form the top surface of the films and the corresponding EDS spectra collected from the films. The EDS spectra show the presence of Ni, Mn, Ga peaks and a weak oxygen peak. The presence of the oxygen peak might be due to exposure of the thin films to the atmospheric environment resulting in surface oxides. Observation from Table 5.5 shows decreasing atomic concentration of oxygen contaminants with increasing substrate temperature which suggest the substrate temperature has significant influence on thin film composition.

Table 5.5 Chemical composition of thin films deposited at different substrate temperatures

Sample	Ni (at%)	Mn (at%)	Ga (at%)	O (at%)
NMG1	46.67	27.91	19.05	06.37
NMG2	47.45	28.34	18.92	05.29
NMG3	47.49	28.41	19.73	04.37

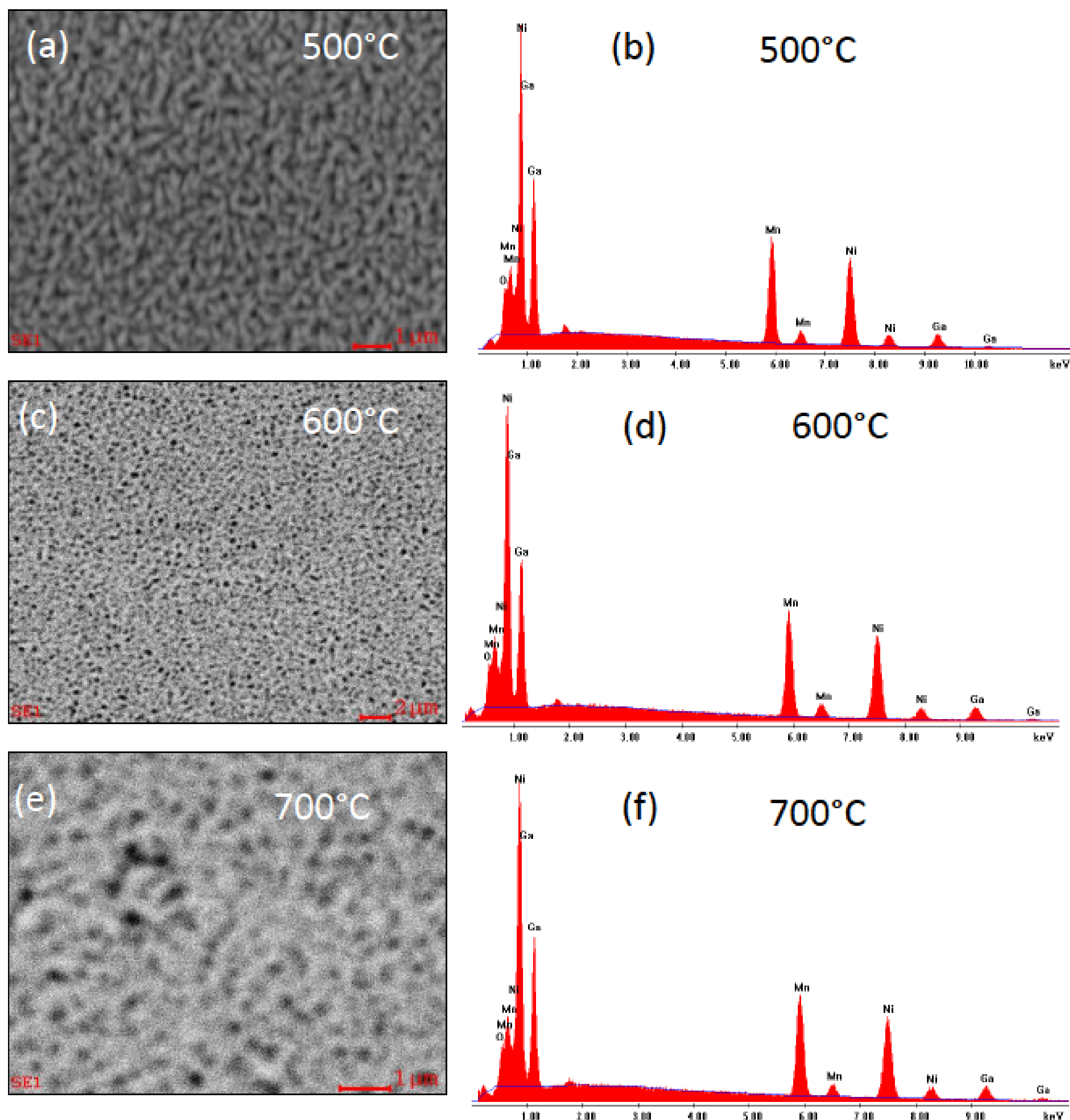

Figure 5.16 SEM micrographs of the thin film and the corresponding EDS spectrum collected from the film surface.

Figure 5.17 shows film composition as a function of substrate temperature obtained based on the results from EDS analysis. Result reveals the presence of Ni, Mn, and Ga in all the films with no

significant change in film composition with substrate temperature. However, from the target composition ($Ni_{53}Mn_{26}Ga_{21}$) standpoint, Ni content showed a decrease in atomic concentration whereas Mn content showed an increase which could be due to three reasons. The Ga content in the thin film is very closed to the target's Ga content. One reason is that, Mn with lower atomic weight would be easier to sputter from the target surface and due to lower target to substrate distance Mn would be deposited faster without been scattered by reflected Ar atoms during the transport [263]. Another reason may be due to differences in sputtering yields of Mn, Ga and Ni [69]. As mentioned in the previous section, the film composition can be affected by differences in sputtering yield of individual components. The TRIM calculations show that Mn exhibit higher sputtering yield than Ga, hence the increase atomic concentration of Mn. Finally, resputtering of the deposited film by Ar ion bombardment can be a possible reason for the compositional changes in the thin film [264].

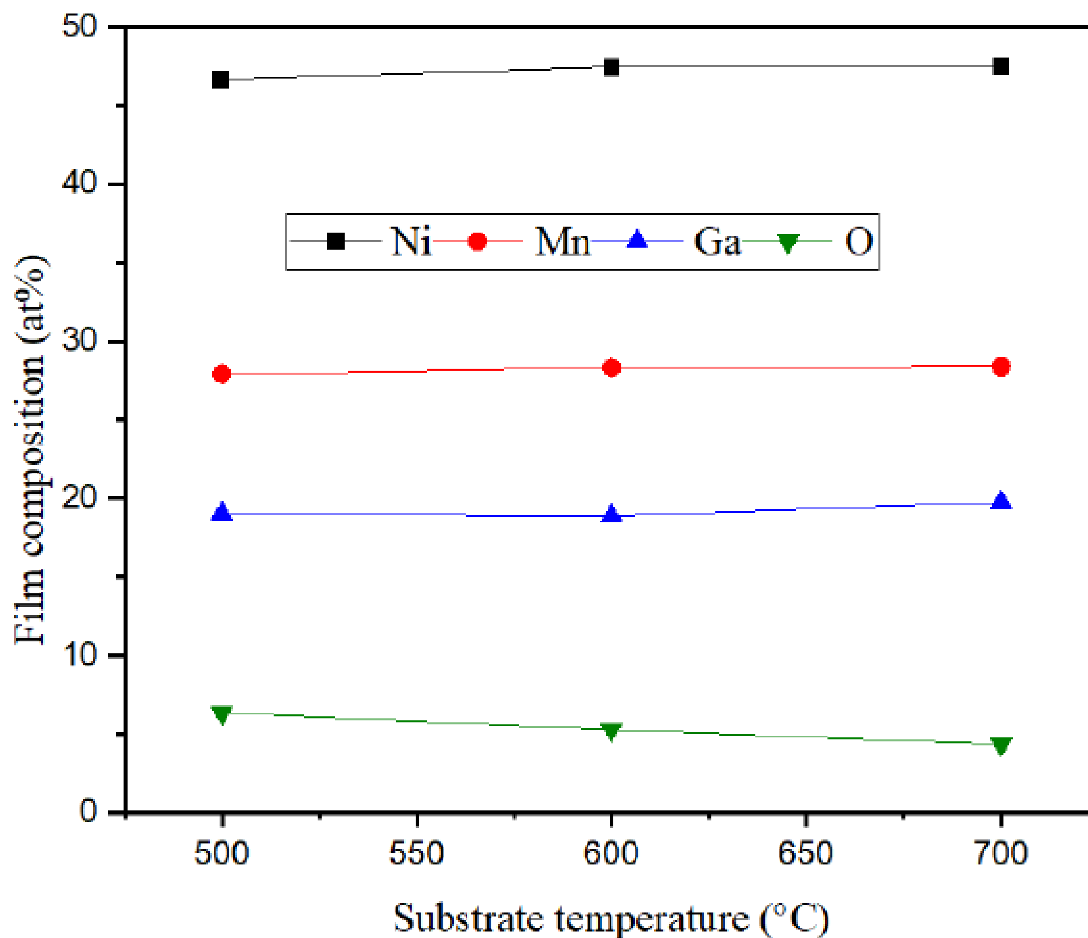

Figure 5.17 Effect of substrate temperature on film composition.

Further assessment of the film composition was carried out using Auger electron spectroscopy (AES) to measure the depth profiles of NMG1, NMG2, and NMG3 samples. AES depth profile of Ni-Mn-Ga film deposited at 500°C is shown in Figure 5.18. The AES result shows a loss in Ni and Mn content while Ga content remained constant. The film composition is different compared to the target composition, one reason being the oxygen contamination. Result also show the presence of oxygen contamination of about 11% atomic concentration. At 600°C as seen in Figure 5.19, Ni, Mn, and Ga content showed a constant depth profile from the surface to substrate interface. However, a loss in Ni and Mn content were observed due to the presence of oxygen contamination.

Finally, at 700°C, a significant drop in oxygen contamination is observed in Figure 5.20. Ni content in the film was about same as that in the target but Mn and Ga content showed a drop in atomic concentration.

Comparing the EDS results to the AES data, Mn content was quite low in the AES results for all the samples, Ni content in 500°C and 600°C from the AES data were lower than results from the EDS data. Ni content in the 700°C sample from the AES were close to the EDS data. Ga content in both analyses were close. Though there is some disparity in the results from both analyses, yet both analyses showed decreasing oxygen contamination as the substrate temperature increases.

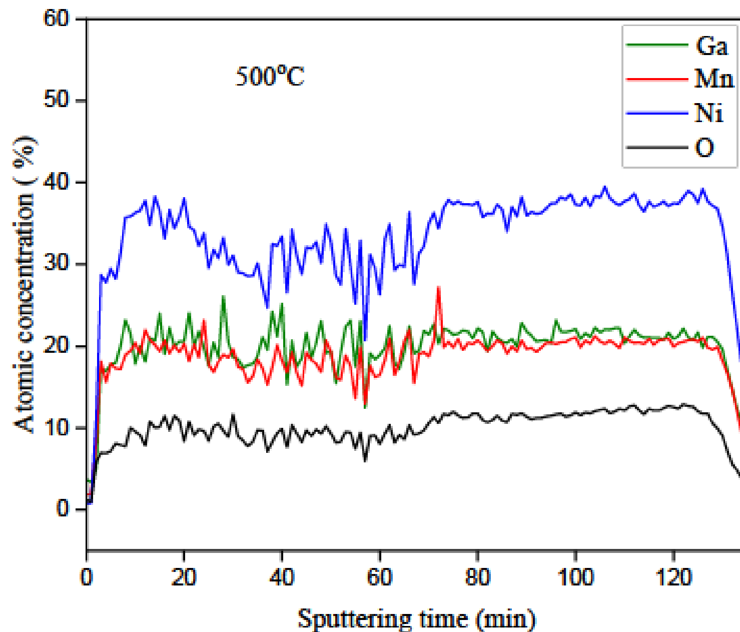

Figure 5.18 AES depth profile Ni-Mn-Ga thin film deposited at 500°C substrate temperature.

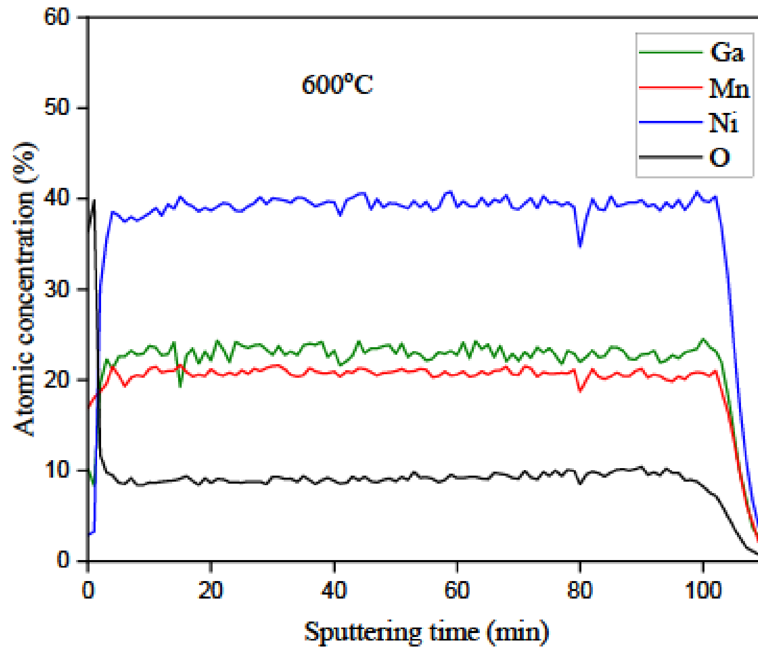

Figure 5.19 AES depth profile Ni-Mn-Ga thin film deposited at 600°C substrate temperature.

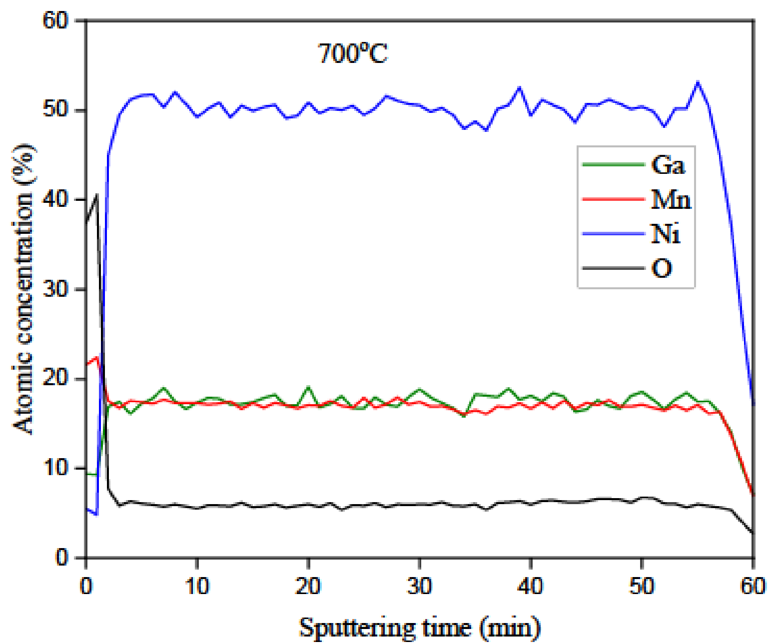

Figure 5.20 AES depth profile Ni-Mn-Ga thin film deposited at 700°C substrate temperature.

5.4.2 Surface and cross-sectional morphology

The morphology of the film planar surface and the appearance of the cross-sectioned NMG1, NMG2, and NMG 3 thin films are shown in Figure 5.21. Figure 5.21 (a), (c), and (e) shows the secondary electron micrographs of the NMG1, NMG2, and NMG3 films planar surface. The three micrographs have been recorded at the same magnification for easy comparison of both film morphology and grain size. All three films show the same morphology, consisting of slightly elongated grains, which seem to form an irregular surface. The grain size analysis was performed, and it is reported in Figure 5.22. Figure 5.21 (b), (d), and (f) shows the secondary electron micrographs of the cross-sectioned NMG1, NMG2, and NMG3 films. Columnar grains, oriented perpendicular to the substrate surface, are clearly visible in all thin films. For NMG1 and NMG2 the film thickness is almost identical, while the NMG3 is thinner. Reduced film thickness at higher substrate temperature might be due to re-evaporation of the film after sputter deposition. Similar observation have been reported by some authors of which they attributed to the re-evaporation phenomenon [265], [266]. *Jaber et al.* deposited Cadmium Sulfide (CdS) thin film by thermal evaporation at different substrate temperatures and observed decreasing film thickness as the substrate temperature increases [265]. This they attributed to enhancement of re-evaporation coefficient of the adsorbed thin film material which resulted in decrease in surface concentration of the film material. *Bilgin et al.* also observed decreasing film thickness as the substrate temperature increases in the deposition of CdS thin film by ultrasonic spray pyrolysis technique [266]. When the substrate temperature is too high, the adatoms kinetic energy increases with collisions with each other and consequently results in re-evaporation of the film material [267].

The grain size analysis was performed using the micrographs of the film planar surface, Figure 5.21 (a), (c), and (e), and the ImageJ software [268]. The average grain size was determined using the mean linear intercept method, as described in the ASTM standard E112 [261]. The

measurement of the average grain size and obtaining grain size distribution from electron micrographs of thin films by using the mean linear intercept method was reported by several authors [269]–[271]. The grain size average and its standard deviation for each thin film is plotted in Figure 5.22, as function of substrate temperature. The film thickness variation is also plotted in Figure 5.22.

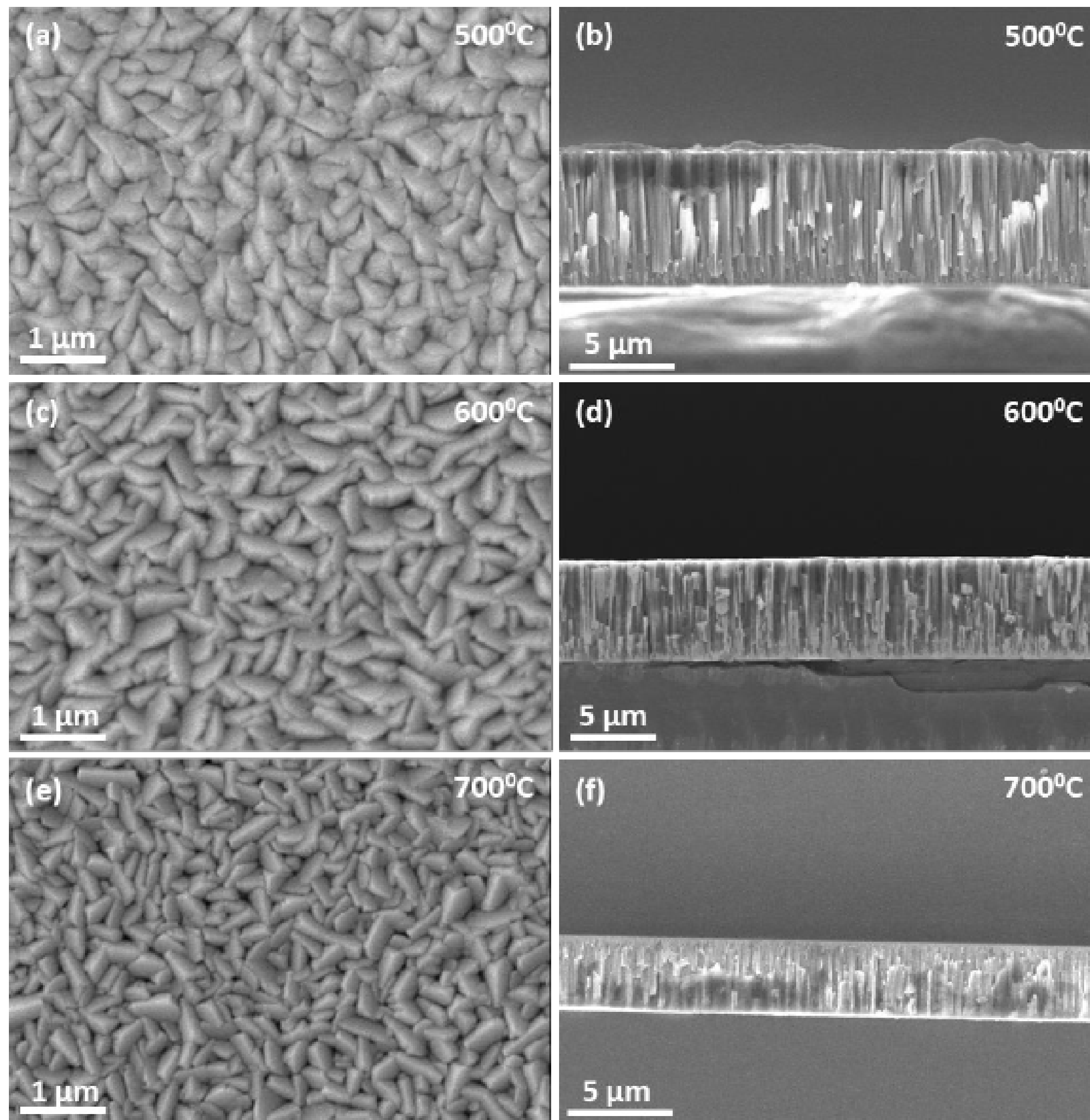

Figure 5.21 Secondary electron micrographs of the Ni-Mn-Ga thin films deposited on Si(100) substrate at 500^0C (NMG1), 600^0C (NMG2), and 700^0C (NMG3). (a), (c), and (e) Morphology of thin films planar surfaces. (b), (d), and (f) Micrographs of the cross-sectioned films.

Figure 5.22 shows the effect of substrate temperature on grain size and film thickness. Both, the average grain size and film thickness decrease with increasing substrate temperature. The average grain size slightly decreases from 258 nm of the NMG1 thin film (deposited at 500^0C), to 227 nm for the NMG3 thin film (deposited at 700^0C). The decrease in grain size with increasing substrate

temperature contradict what is largely reported. The explanation to this behavior can be associated to two possible reasons: the first reason is that, at higher substrate temperatures, adatoms gain higher kinetic energy which increases their collision with each other and consequently result in re-evaporation of the thin film material [267]. As a result, a reduction in grain size and film thickness are observed. The second reason might be due to variation in the chemical composition of the three samples as confirmed by both EDS and AES data. The oxygen contamination might also be a contributing factor to the variation in grain size as reported by Vergara *et al* [272].

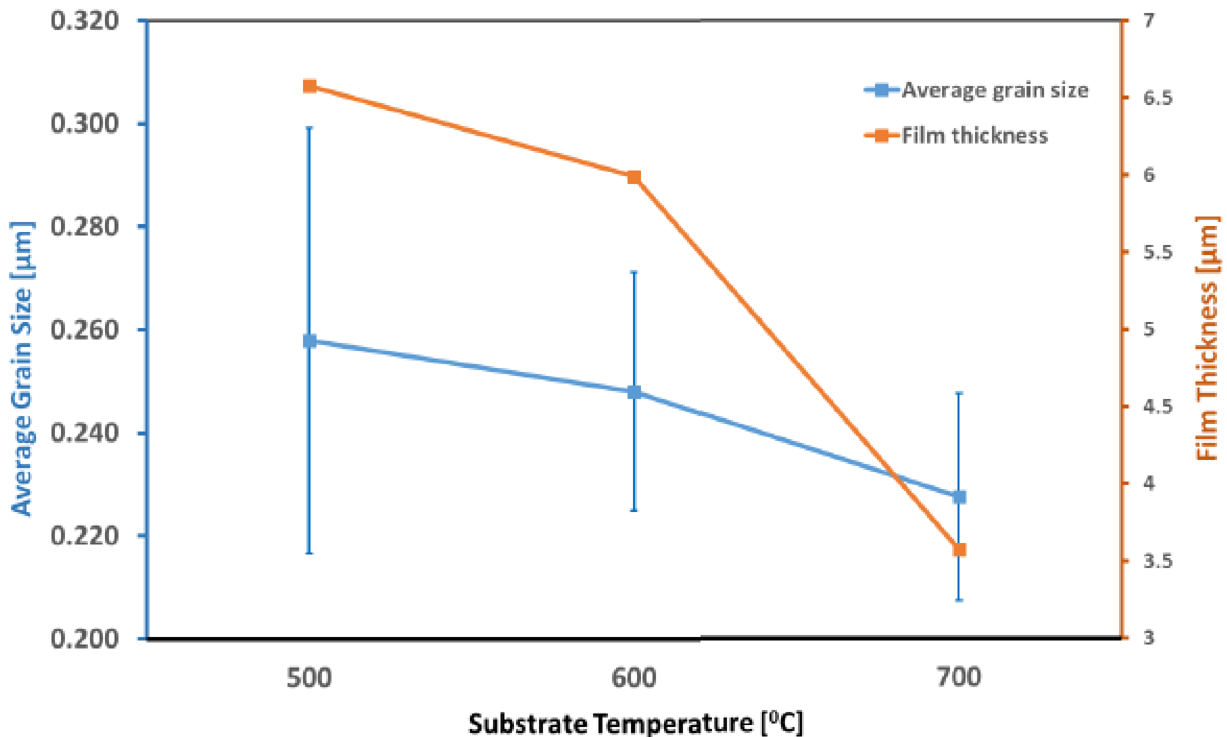

Figure 5. 22 Effect of substrate temperature on grain size and film thickness.

5.4.3 XRD analysis

Figure 5.23 illustrates the XRD patterns of Ni-Mn-Ga thin films deposited at 500°C, 600°C, and 700°C respectively. Film deposited at 500°C has the Heusler $L2_1$ cubic structure having the space group $Fm\bar{3}m$ and lattice parameter a = 0.5820 nm . The dominant austenitic peak occurred at 2θ

= 44.02°. Increasing the substrate temperature to 600°C, resulted in the splitting of the austenitic peak (220) into three diffraction peaks at 2θ = 41.94°, 42.93°, 44.31°. Peak splitting has been reported as an indication of martensitic transformation [77]. The diffraction peaks observed are associated with the monoclinic martensitic structure belonging to the I2/m space group having lattice parameters a = 0.422830 nm, b = 0.55752 nm, c = 2.1001 nm, β = 90.325° [273].

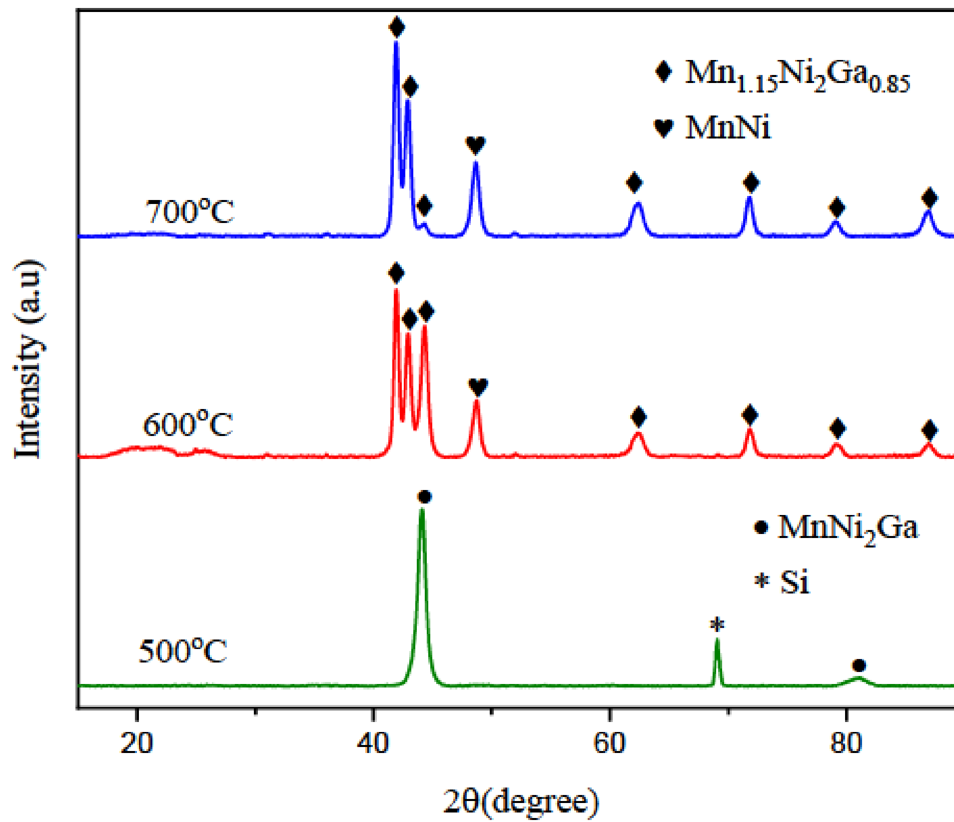

Figure 5. 23 X-ray diffraction spectrum of Ni-Mn-Ga thin films deposited at substrate temperatures 500°C, 600°C, and 700°C.

In addition, a diffraction peak at 2θ = 48.66° which belongs to MnNi phase was seen which may be due to chemical segregation as a result of preferential sputtering. Further increase in substrate

temperature to 700°C, showed similar diffraction pattern except that the intensity of the diffraction peak at $2\theta = 44.31°$ is reduced.

5.5 Post-heat treatment of as-deposited room temperature Ni-Mn-Ga thin film

Ni-Mn-Ga thin film deposited at room temperature was subjected to post-annealing treatment to investigate annealing effect on the surface morphology and the crystal structure. The heat-treatment was carried out in the Carbolite tube furnace used for the target sintering. Thin film was place in alumina crucible sample holder and gently transferred into the tube furnace. The tube was evacuated using a mechanical pump until a base pressure of 5 mTorr was attained and then ultra-high purity argon gas was introduced into the tube at a pressure of 300 mTorr. The tube furnace was subsequently purged three times with argon gas. Thin film was annealed at 600°C for 1 hour at heating rate of 15°C/min. Figure 5.24 (a) - (b) shows 3D atomic force microscopy (AFM) micrographs of Ni-Mn-Ga thin films deposited at room temperature and annealed. The as-deposited film seen in Figure 5.24 (a) revealed a smooth surface morphology with some noticeable spherical grains of about 90 nm size. The annealed film on the other hand showed a morphology whose grain structure is quite rocky and rough as seen in Figure 5.24 (b). The film experienced grain growth with an average grain size of about 200 nm. Figure 5.25 shows XRD spectrum of Ni-Mn-Ga thin films deposited at room temperature and annealed at 600°C.

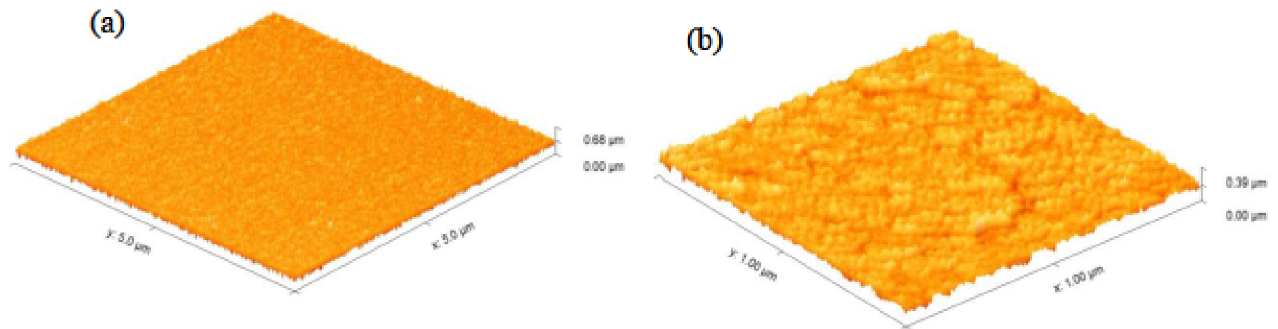

Figure 5. 24 3D Atomic force microscopy (AFM) image Ni-Mn-Ga thin films: (a) As-deposited; (b) Annealed.

The XRD spectrum for the room temperature film shows a typical austenitic phase with a (220) diffraction peak associated with the stoichiometric Ni_2MnGa. The annealed film on the other hand showed much higher (220) diffraction peak assoicated with the austenitic phase and additional peaks matched with $Ni_{0.85}Mn_{0.15}$ and $Ga_{0.25}Mn_{0.75}$ and an extra peak without a match. The result showed that the annealed film is more crystalline than the as-deposited film, however, it also experienced chemical segregation resulting in chemical inhomogenieties.

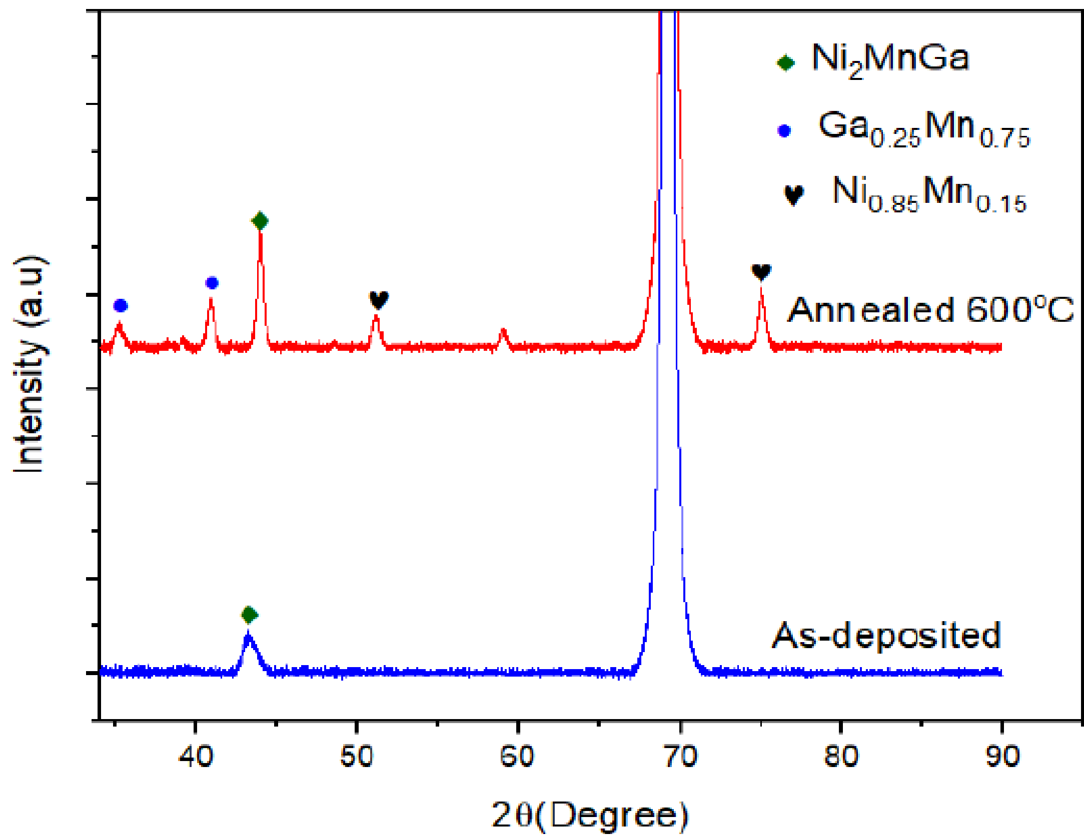

Figure 5. 25 XRD spectrum of Ni-Mn-Ga thin film deposited at room temperature and annealed at 600°C.

CHAPTER 6

Binder jet 3D printing of complex geometry copper sputtering targets and characterization of obtained thin films

6.0 Introduction

Magnetron sputtering technique is among the most widely used technique for thin film fabrication due to its high deposition rate, formation of high purity films, high rate of film uniformity and good adhesion to substrate [36]. This technique employs magnetrons to effectively trap secondary electrons closed to the target surface to enhance ionization efficiency at low gas pressure [274]. The secondary electrons trapping is achieved by the interaction of both electric and magnetic fields [275]. This interaction is governed by the Lorentz force equation given by equation (6.1).

$$F = q\boldsymbol{E} + q\boldsymbol{v} \times \boldsymbol{B} \qquad (6.1)$$

Where q is the electric charge on electron, E is the electric field vector, v is the velocity of electron, and B is the magnetic field vector. The cross product between the velocity vector and the magnetic field vector observed in the second term on the right-hand side of equation (6.1) is an indication that the magnetic force is perpendicular to the direction of the moving electron and the magnetic field [276]. As a result, the electron traverses along the magnetic field lines following a curve path near the target surface creating more ionization of argon gas [276], [277]. Thus, the positive charge argon ions are attracted at high speed towards the cathode (target) inducing sputtering of the target material. The high ionization of the argon gas due to the electron trapping confined the plasma locally in the vicinity of strong magnetic field parallel to the target [278]. The plasma generated is intense at regions where the electric and magnetic fields are mutually perpendicular [279]. This leads to non-uniform erosion profile of the target which subsequently affect the efficiency of the target (see Figure 6.1) [280].

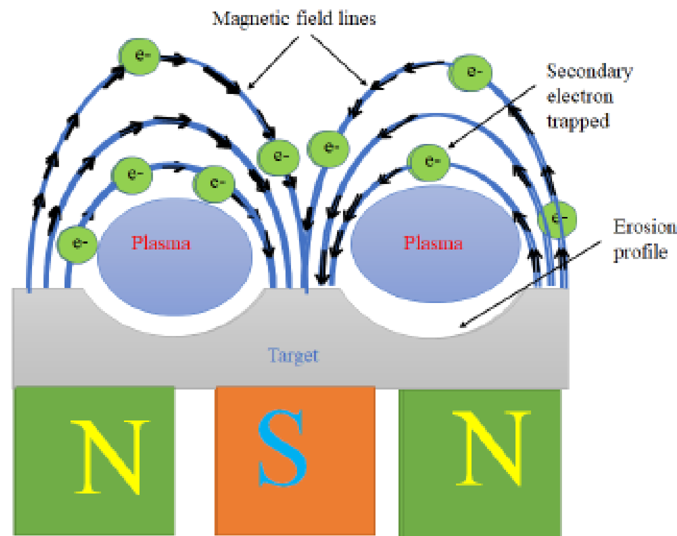

Figure 6.1 Schematic planar magnetron sputtering with electron trapping.

In a typical planar magnetron sputtering system, target utilization reported in literature is about 20-30 % [281]. The poor target utilization of the planar magnetron sputtering makes the process inefficient and uneconomical [282] especially for high cost target materials like gold, indium tin oxide (ITO) [283] and Ni-Mn-Ga alloy. Many attempts have been made to improve the target utilization by employing techniques such as interpoles target-hollow magnetron [39], a rotatable cylindrical magnetron [284], and rotating tilted unbalanced yoke magnet [285]. Most of these techniques are complicated and may be difficult to implement on the industrial scale. A simplified approach to improve the target utilization efficiency have been proposed by Arakelova *et al.* [279]. They proposed a non-planar target with a conical protrusion at the erosion region based on the ballistic transport model. The idea was to create a target profile such that the magnetic field generated would be directed parallel to the target surface for uniform erosion during sputtering. Results from their work showed improvement in target utilization efficiency and better film properties in the case of ZnO [279]. Bulk polycrystalline Ni-Mn-Ga alloy is very brittle and

difficult to machine into complex parts. To produce Ni-Mn-Ga targets with complex geometries, using the existing target manufacturing techniques, it would be challenging due to the brittleness of the material. However, binder jet additive manufacturing (BJAM) could be the game changer due to the design freedom of making complex parts, Figure 6.2. This is evident in the work of Caputo *et al.* and Mostafaei *et al.* of making complex parts of Ni-Mn-Ga alloy through BJAM.

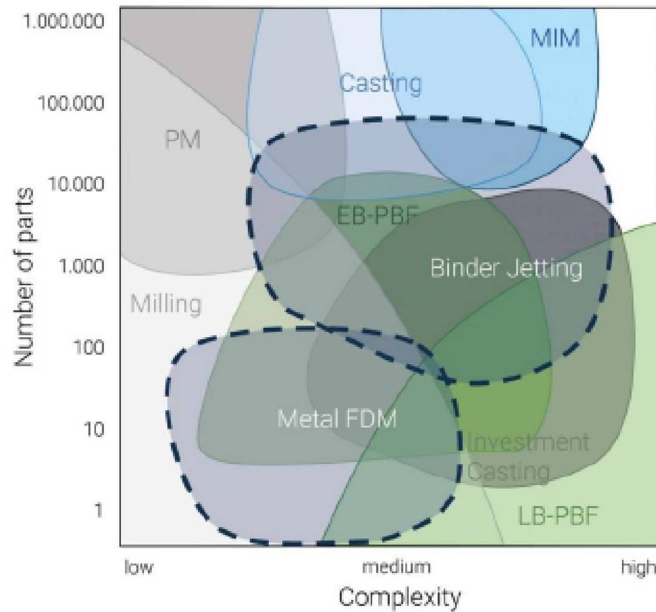

Figure 6.2 Classification of technologies based on number of parts and parts complexity [286].

In this work, there was limited quantity of Ni-Mn-Ga powder available to explore complex sputtering target geometries. However, 155A copper and 316L SS gas atomized powders were available in large quantities. Therefore, in order to demonstrate that non-planar targets having an increased life time usage can be easily manufactured from various materials (including brittle ones, such as ceramics and Ni-Mn-Ga alloys) using BJAM, copper powder was selected, due to its availability in the Youngstown State University laboratory. Copper targets of different designs were proposed in this work for target utilization enhancements. Comparison between flat and non-

flat targets erosion assessment were carried out to estimate target life or utilization using the following equation:

$$\text{Target Utilization } (U_L) = \frac{M_I - M_F}{M_I} \times 100 \qquad (6.2)$$

Where M_I is the initial mass of target and M_F is the final mass after target erosion.

This chapter will present the results on binder jetting 3D printing of Cu targets with planar and non-planar geometries, the results of analytical investigations of Cu thin films deposited using the 3D printed targets, and the evaluation of target utilization for both planar and non-planar targets. The Si(100) substrate have been used for Cu thin film depositions. The printed targets and the thin films have been investigated using scanning and transmission electron microscopy, atomic force microscopy, X-ray diffraction, profilometry, and four-point probe electrical resistivity measurement.

6.1 Materials and Methods

6.1.1 Copper Powder

Copper atomized powder purchased from ACuPowder International; LLC was used in this research with composition shown in Table 6.1. Sieving was performed using 75 µm mesh size of sieve. Particle size distribution and particle morphology analysis were carried out using particle size analyzer Cilas 1190 and JEOL JIB-4500 Multi Beam System SEM/FIB.

Table 6. 1 Chemical composition of 155A Cu powder.

Element	**Cu**	**Fe**
Composition (wt%)	98.5	1.5

6.1.2 Justification of target designs, BJAM printing process and post-processing

The conventional planar target in a magnetron sputtering system erode non-uniformly due to the interaction between the electric field and the magnetic field. As a result, a racetrack of about 30 mm in diameter is created which affects the target utilization. It becomes even more problematic for high purity and expensive materials since it limits the usage of the material. This research is proposing new target designs such as toroidal, conical, and trapezoidal protrusions at the target surface in order to address target wastage. The protrusions are situated where the racetrack of the planar target is formed. During sputtering the protrusion area is exposed to the magnetic field to enable uniform erosion of the target and the surface parallel to the horizontal component of the magnetic flux density. In this way, material utilization will be enhanced, and material wastage minimized. Figure 6.3 (a) – (c) shows one of the proposed target designs with the top and cross-sectional views.

Initial attempt to print copper target failed because the size of the mesh beneath the hopper (150 µm) of the ExOne Innovent+ was too large to hold the copper powder in the hopper. In order to print the copper target, an extra mesh of 75 µm was embedded inside the hopper in order to hold the powder in place for the printing process. Copper targets were successfully printed with binder saturation ranging 50% - 60% and layer thickness of 90 µm. 3D printed targets were then cured at 180°C for six hours using Yamato DX402C oven. Cured targets were sintered at temperature range 1075 -1085°C for 3 hours under argon atmosphere using Carbolite VST 12/300 tube furnace. Sintered copper targets were characterized for their microstructure using both optical microscopy and SEM.

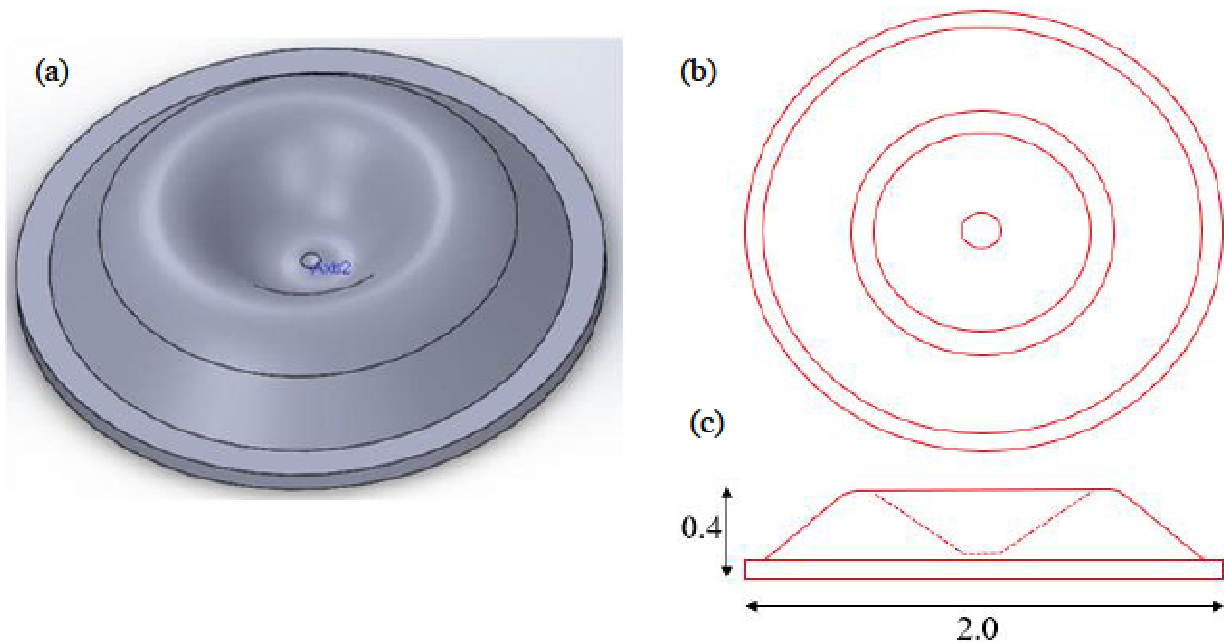

Figure 6.3 (a) Target design created in SOLIDWORKS; (b) Top view of target; (c) Cross-sectional view. The dimensions are in inches.

6.1.3 Thin film fabrication of copper

Copper targets prepared by 3D printing were employed in the DC magnetron sputtering system for film deposition. Prior to the deposition, Si (100) substrate was prepared by following standard cleaning procedure set out in the sample preparation: cleaning in acetone, followed by isopropanol, and then rinsing in deionized water. Copper thin films were prepared using the following sputtering conditions: 0.1 A discharge current, 4.5 mTorr argon pressure, 4×10^{-7} Torr base pressure, two to three hours deposition time, 20°C substrate temperature, and 8 cm target to substrate distance. Copper films deposited at room temperature were further subjected to post-heat treatment (annealing) in argon atmosphere using rapid processor (RTP-300). The annealing process was carried out at temperatures 150°C, 200°C, 250°C, 300°C, and 400°C respectively for

120 seconds. Thin films were characterized for their morphology, microstructure and cystal structure. Sputtered targets with erosion groove were also examined using 3D profilometer VR-5000 Keyence to estimate the depth profiles.

6.1.4 Copper thin film characterization

6.1.4.1 Transmission electron microscopy (TEM)

Prior to TEM investigation, electron transparent copper thin film samples of about 100 nm or less were prepared using the JEOL JIB-4500 Multi-Beam (SEM-FIB) system equipped with gas injection system and a nano-manipulator. The FIB generates a beam of gallium (Ga^+) ions which are accelerated toward a target area for milling or etching. First of all, the area of interest on the sample was viewed with the SEM and then tilted and viewed with the FIB, until the eucentric height was achieved. This was followed by deposition of carbon at the area of interest as a protective layer against surface damage by Ga^+ ions. Two trenches were cut out on both side of the target area by ion beam milling, followed by lift-out in which the thin film lamella was welded to the tip of a tungsten needle and transferred to the TEM grid. The thin film lamella was welded to the TEM copper grid support by depositing platinum (see Figure 6.4). Further thinning and polishing of the lamella was performed until electron transparent sample was obtained.

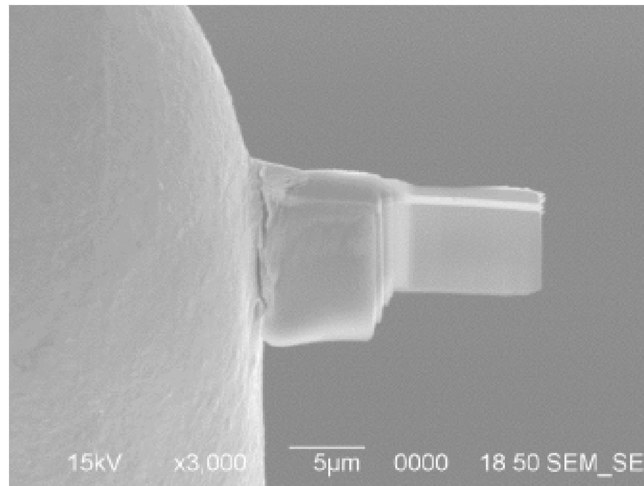

Figure 6.4 Thin film lamella welded to TEM copper grid.

TEM studies were performed using JOEL 2100 scanning transmission electron microscopy (STEM) at acceleration voltage of 200 KV. Bright and dark field imaging modes were used to examine the microstructure of the cross-sectioned samples, while the selected area diffraction (SAD) mode was used for crystallographic investigation.

6.1.4.2 Electrical resistivity measurement

The electrical resistivity of the films was determined at room temperature by the four-point probe technique where two outer probes were used for the current source and two inner probes for voltage measurement. The probes were positioned on the film at equal spacing of 200 µm from each other in a linearly manner. The Instruments used for the electrical resistance measurements were Keithley precision current source and Keithley nanovoltmeter 2400 model. Ten electrical resistance measurements were performed for each sample.

A differential electrical resistance for test sample is given by:

$$dR = \rho \frac{dx}{A} \tag{6.3}$$

Where dx is an infinitesimal length of test sample, ρ represents the resistivity of test sample, and A represents the cross-sectional area of the test sample. For the copper thin film, the cross-sectional area is given by $A = 2\pi \cdot x \cdot t$, where t represents film thickness. Integrating equation (6.3) becomes

$$\int dR = \int_{S}^{2S} \rho \frac{dx}{2\pi xt} \tag{6.4}$$

Where S is the probe spacing.

$$R = \frac{\rho}{2\pi t}[ln(x)]_{S}^{2S} \tag{6.5}$$

$$R = \frac{\rho}{2\pi t}\left(ln(2S) - ln(S)\right) \tag{6.6}$$

$$R = \frac{\rho}{2\pi t} ln2 \tag{6.7}$$

$$\rho = \frac{2\pi tR}{ln2} \tag{6.8}$$

Electrical resistance R is given by:

$R = \frac{V}{2I}$, where v represents voltage across the inner probes, and I is the current flowing through the outer probes.

$$\rho = \frac{\pi t}{ln2}\left(\frac{V}{I}\right) \tag{6.9}$$

The film thickness was used for the resistivity calculations instead of the probe spacing because the film thickness was far below the probe spacing.

6.2 Results and discussion

6.2.1 Powder characterization

As-received Cu powder was examined for its particle size distribution and particle morphology using laser diffraction particle size analysis method and SEM. Results from laser diffraction method are shown in Table 6.1 and Figure 6.5. The D_{10}, D_{50}, and D_{90} are typical statistical

parameters used in describing size distribution of powder particles which were found to be 25.66 μm, 36.88 μm, and 53.30 μm respectively as shown in Table 6.2. Result shown in Figure 6.5 depicts monomodal size distribution with average particle size around 37 μm.

Table 6.2 Distribution percentile values of Cu powder

Powder	D_{10} (μm)	D_{50} (μm)	D_{90} (μm)
155A Cu	25.66	36.88	53.30

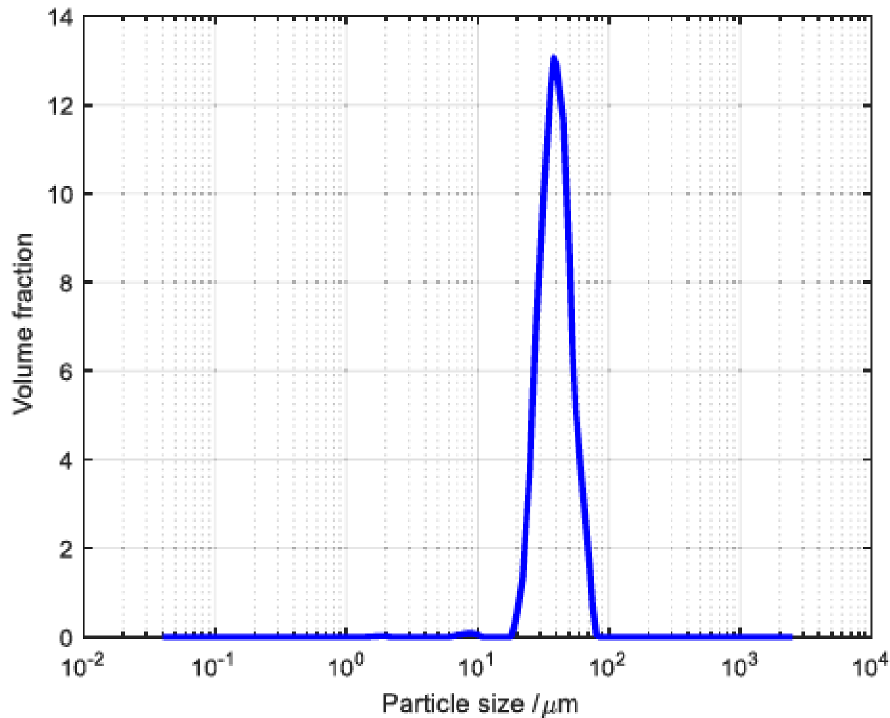

Figure 6.5 Particle size distribution of Cu powder.

Figure 6.6 shows SEM micrograph of Cu powder. The micrograph shows the spherical morphology of powder particles. No agglomerations of powder particles are observed which indicates good flowability. XRD analysis was also performed on the Cu powder to determine its crystal structure.

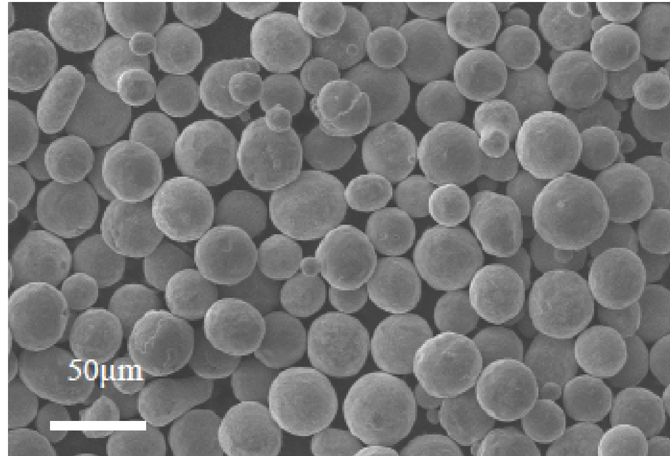

Figure 6.6 SEM micrograph of Cu powder.

Figure 6.7 shows XRD pattern of 155A Cu powder indicating diffraction peaks at 2θ values 43.35°, 50.49°, 74.19°, and 90.03° correspond to the crystallographic planes (111), (200), (220), and (311) respectively. The result shows a typical XRD pattern of copper with face centered cubic structure in $Fm\bar{3}m$ space group having lattice parameter a = 0.36122 nm [PDF no. 04-001-2746].

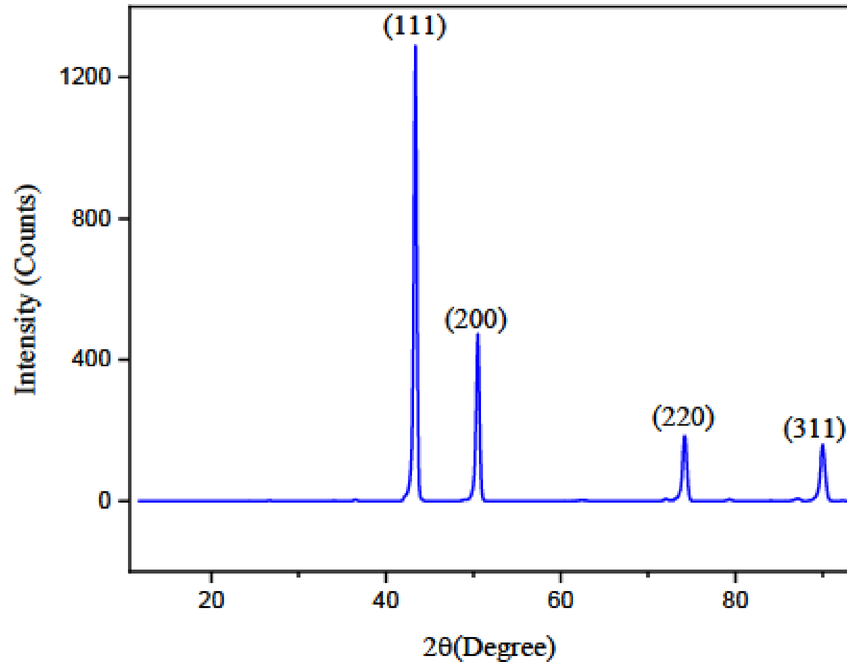

Figure 6.7 XRD pattern of Cu powder.

6.2.2 Target manufacturing via binder jetting process

Figure 6.8 shows 3D printed planar and non-planar disc targets after curing. A dark grey color of the cured 3D printed copper target is observed which may be due to the binder responding to changes in temperature as a result of the heat from the oven. The diameter and thickness of the disc target measured were 58.80 mm and 4.3 mm, respectively.

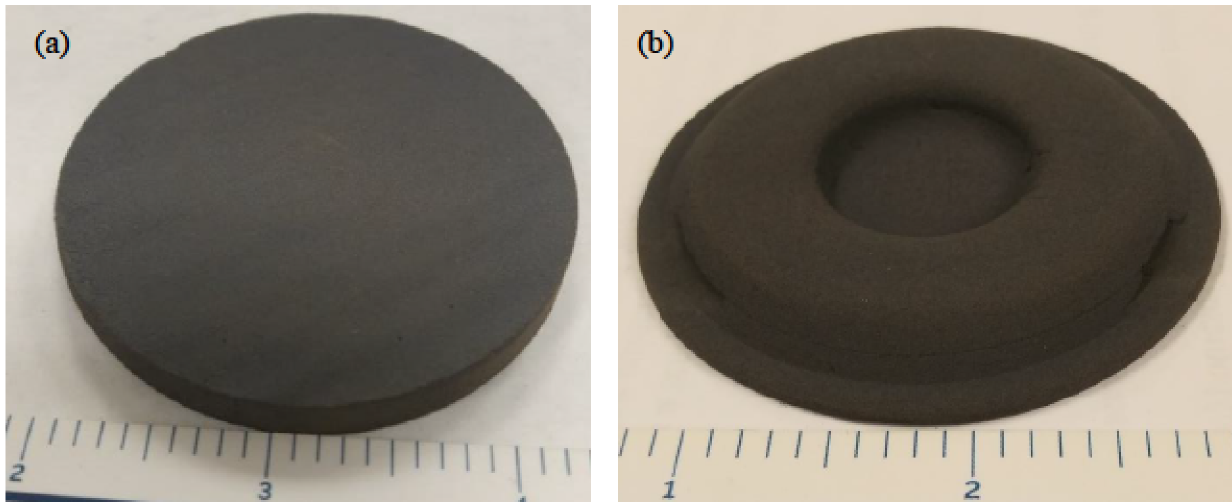

Figure 6.8 3D printed disc copper targets after curing (a) Planar, (b) Non-planar.

6.2.3 Sintering and characterization of 3D printed targets

To further increase target strength and burn out the binder, target sintering was carried out in a Carbolite furnace equipped with a vacuum system, under argon atmosphere.

Figure 6.9 (a)-(d) show photos of as-sintered targets labeled TC 1, TC 2, TC 3, and TC 4. By visual inspection of the targets, it is seen that the sintering process had significant influence on the appearance of the target. A complete color change from dark grey (cured targets) to orange red (sintered targets) is observed which is due to pyrolysis of the binder at higher temperature [287]. At higher temperature, liquid binder undergoes decomposition which may results in the formation

of combustion products. After a complete burnout of the binder, densification is initiated by fusion of powder particle which results in neck formation. The structural integrity of sintered targets remained intact since no geometrical defects or warping was seen. However, a considerable linear shrinkage was observed in the sintered targets. The linear shrinkage was determined from the disc diameter and thickness of as-printed and sintered targets. Ten measurements were recorded for both diameter and thickness in order to estimate the mean value and standard deviation using a STORM digital caliper. The linear shrinkage was calculated by subtracting the diameter or thickness of the sintered disc from the diameter or thickness of the as-printed disc target divided by diameter or thickness of as-printed disc target expressed as a percentage. The disc target sintered at 1075°C for 3 hours exhibited a linear shrinkage of 16.34% ± 1.93 whereas targets sintered at 1085°C for 3 hours showed a linear shrinkage of 20.80% ± 2.16. Results showed dependency of linear shrinkage on sintering temperature. Increasing sintering temperature amount to increasing linear shrinkage due to decreasing pore volume in the target. Results obtained is consistent with work reported by Richmawi *et al.* [287].

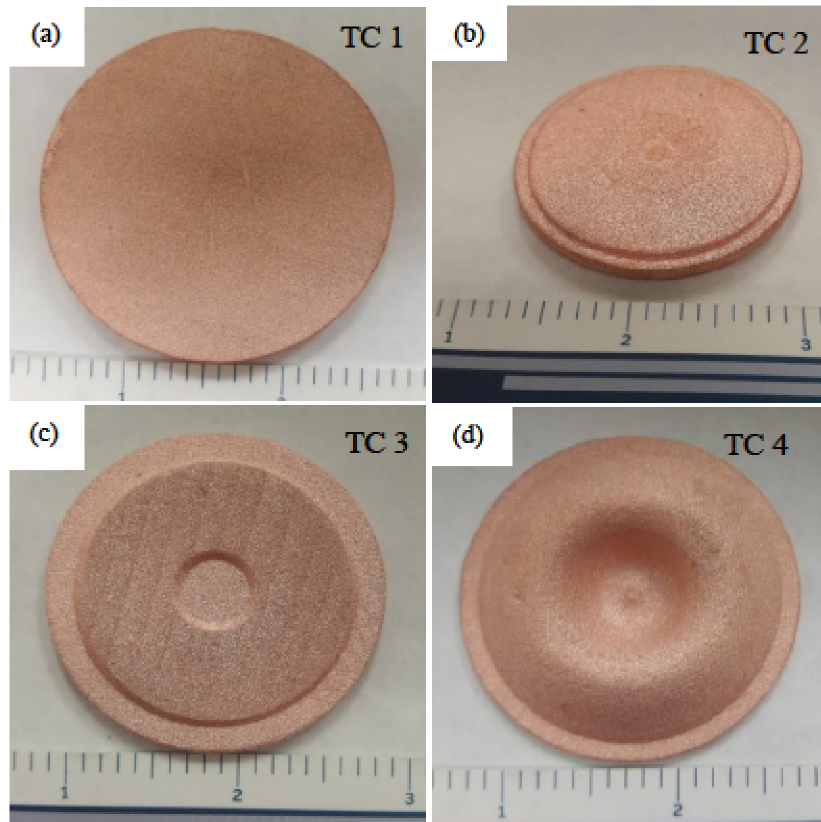

Figure 6.9 Photo of sputtering targets: (a) TC 1 planar target sintered at 1075°C for 3 hours; Non-planar target (b) TC 2 sintered at 1075°C for 3 hours, (c) TC 3 sintered at 1080°C for 3 hours, (d) TC 4 sintered at 1085°C for 3 hours.

Figure 6.10 (a) and (b) show SEM micrographs of copper targets sintered at 1075°C and 1085°C for 3 hours. In Figure 6.10 (a), some areas of the target show particle to particle contact indicating onset of necking whereas other areas display sintered necks with varying neck lengths. A complete neck formation seen in the inset is evidence of densification. During the period of sintering, mass transport occurs by atomic diffusion causing particles to fuse or bond together and evolves into sintered necks. Rapid growth of sintered necks increases densification and minimizes pore volume. For the specimen sintered at 1085°C, the target exhibits high grain growth with the elimination of necks and reduced pore volume, Figure 6.10 (b).

Figure 6.11 shows optical micrograph of cross-section of copper target sintered at 1085°C revealing its microstructure after etching with the following reagent: 2.0 g potassium dichromate dissolve in 100 mL of distilled water and mixed with 8 mL of sulfuric acid.

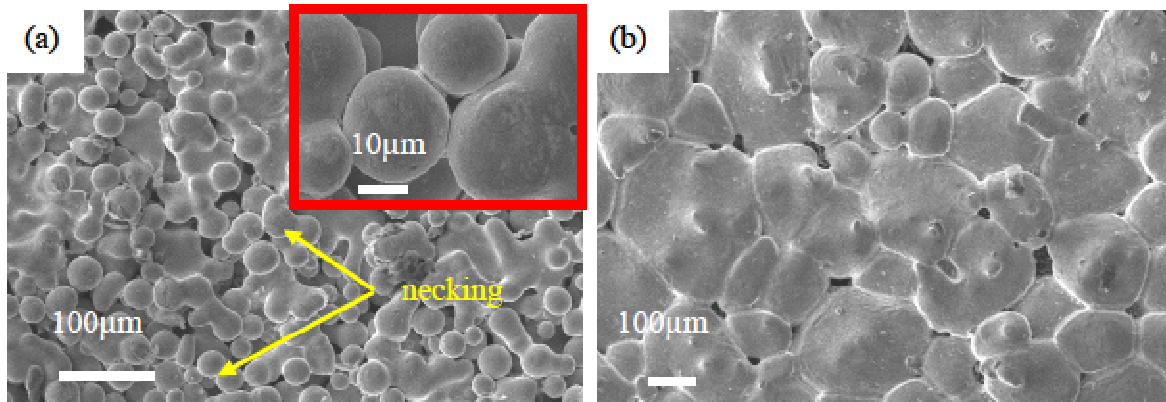

Figure 6.10 SEM micrograph of copper target sintered at: (a) 1075°C and (b) 1085°C.

The polycrystalline target consists of equiaxed grains and uniform distributed pores. The pores are largely circular in shape and are seen along the grain boundaries. Annealing twins are visible in several grains. Annealing twins usually occur after recrystallization and grain growth in face centered cubic (FCC) metals with low stacking fault energy [288]. Grain boundary migration by curvature reduction is another mechanism for the occurrence of annealing twins [289].

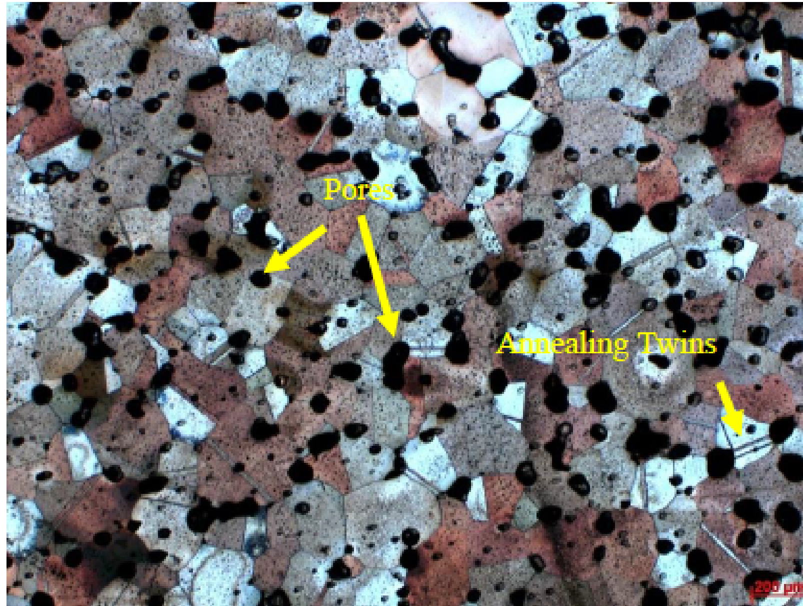

Figure 6. 11 Optical micrograph of cross-section of copper target.

6.2.4 Erosion and depth profile of planar and non-planar targets used in DC magnetron sputtering

A subtle way to improve the target life in this research was to increase the amount of material in the target region where maximum erosion occurs or where the horizontal component of the magnetic field (B_H) is maximum and reduce material at regions where erosion is low. A distribution of magnetic field lines can be observed near the surface of the proposed target design in Figure 6.12. It is anticipated that, the proposed target would have longer target life than the regular flat target due to more material at erosion region. A comparative study was carried out between flat (TC 1) and non-flat (TC 4) target to estimate the rate of mass sputtered and depth profile. Target mass was measured before and after each deposition to determine amount of material sputtered as seen in Table 6.2. Each target was sputtered for 3 hours at a discharge current of 0.13 A. The results showed that within 3 hours of sputtering, the flat target losses 1.28% of material whereas the non-flat target losses 0.733%. Results suggest that less material is sputtered

from the non-flat target than the flat target which implies non-flat target would last much longer than the flat target. In order words, target utilization is improved using the non-flat target.

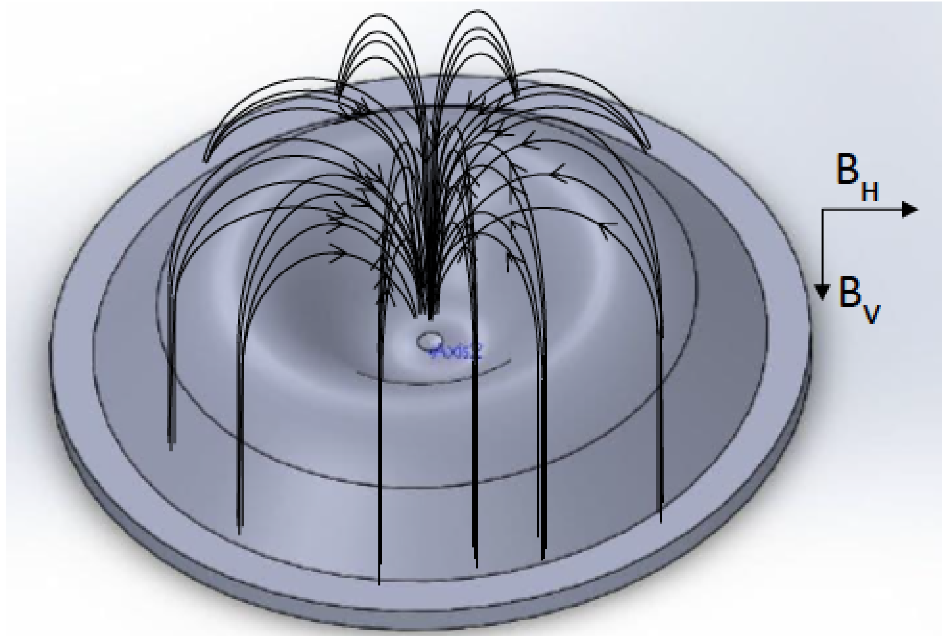

Figure 6.12 Distribution of magnetic field lines near surface of proposed target design.

Table 6.3 Mass of fresh targets measured before and after 3 hours of sputtering.

Target	Flat (TC 1)	Non-Flat (TC 4)
Initial mass (g)	70.378	80.535
Final mass (g)	69.474	79.9445
Mass loss (g)	0.904	0.5905
Target utilized (%)	1.28	0.733

In order to examine the surface evolution of racetrack and the depth profile, a 3D profilometer VR-5000 Keyence was employed. Figure 6.13 (a) and (b) show optical images of targets sputtered after 3 hours. Results show how the racetrack pattern evolved between the center and the periphery of the targets. The racetrack region confirms where the ion current density was high. Figure 6.14

shows the depth profile of both flat and non-flat targets. It can be seen that for the flat target the erosion mostly occurred between the target radius whereas for the non-flat target the erosion occurred on the side walls of the cavity. Observation of the surface erosion of the non-flat target is very interesting and may require more depositions to estimate target efficiency. The preliminary result in this research has laid the foundation for further investigation into improving target utilization using different target geometries.

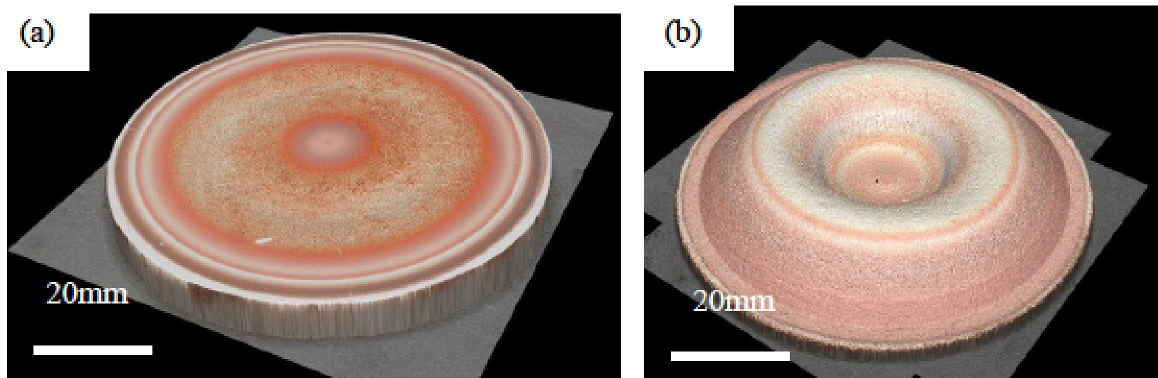

Figure 6.13 Optical image of targets after 3 hours of deposition (a) Planar (b) Non-planar.

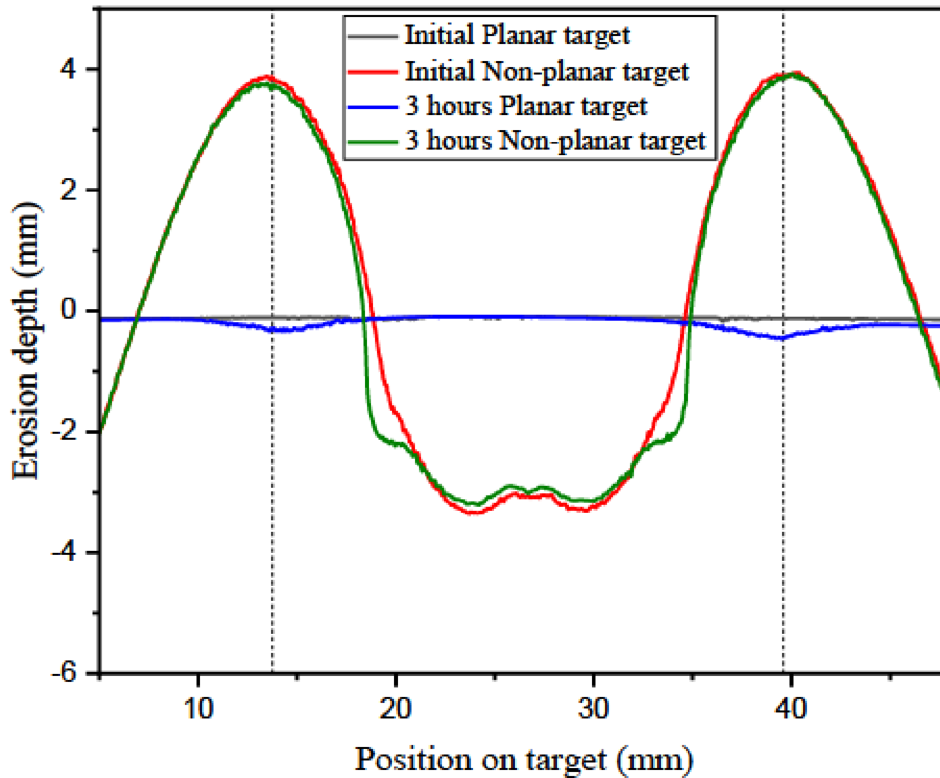

Figure 6.14 Erosion depth profile of planar and non-planar target.

6.2.5 Characterization of Copper thin films

6.2.5.1 Surface morphology of as-deposited copper thin film from TC 1 target

The surface morphology of the copper film was examined using Agilent 5500 atomic force microscopy (AFM) with a scan area of 5 µm x 5 µm at a scan rate of 0.2 in/s in the contact mode. Figure 6.15 shows 2D AFM image of as-deposited copper thin film. The result depicts a surface morphology with equiaxed grain structure with no visible crack. The average grain size was found to be about 30 nm.

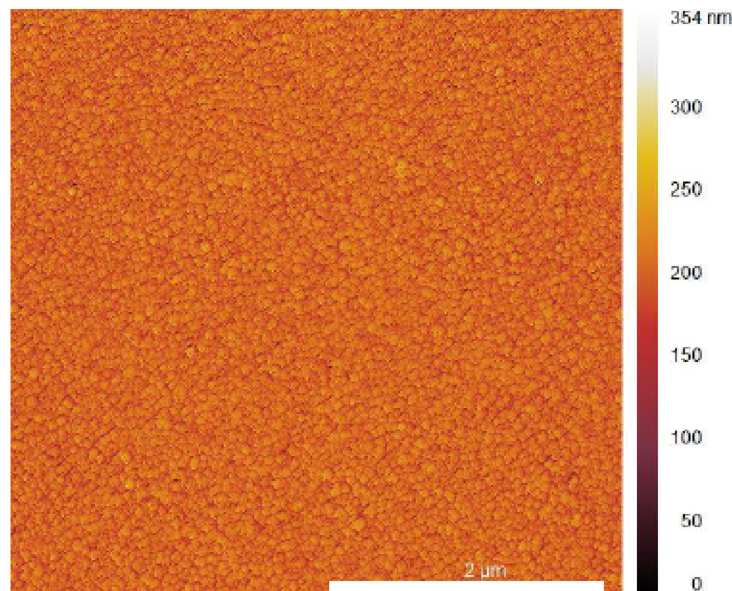

Figure 6.15 2D AFM image of copper thin film deposited at room temperature.

6.2.5.2 Microstructure of rapid thermal annealed copper thin films

Copper thin films deposited at room temperature were further subjected to post-heat treatment using rapid thermal annealing and their crystallinity and microstructure was investigated using XRD and TEM respectively.

6.2.5.2.1 Crystal structure

XRD pattern of as-deposited and annealed copper thin films are illustrated in Figure 6.16. The XRD pattern reveal that the Cu thin films are polycrystalline and have cubic structure. The as-deposited and annealed films showed strong diffraction peak along the (111) plane observed at $2\theta = 43.34°$ and smaller diffraction peaks (200), (220), and (311) at $2\theta = 50.54°$, 74.10°, and 90.02° respectively, which is expected since Cu has a face centered cubic (FCC) structure. This suggests that the Cu thin films have a preferred orientation in [111] direction. No significant difference was found in the intensity peaks for films annealed from 150°C to 250°C which may be attributed to less thermal energy necessary to recrystallize the films. At 300°C and beyond, a sharp increase in

(111) diffraction peak is observed with reduced peak broadening which suggest that enough thermal energy was acquired by virtue of increased temperature for recrystallization of the films.

6.2.5.2.2 Crystallite size and microstrain

To gain more insight into the microstructure of the Cu thin films, the crystallite size and microstructural parameters such as microstrain and dislocation density were calculated from the XRD data. The dominant X-ray diffraction peak (111) for each film was fitted using the Gaussian shape in a fitting software called OriginPro 2021b (student version).

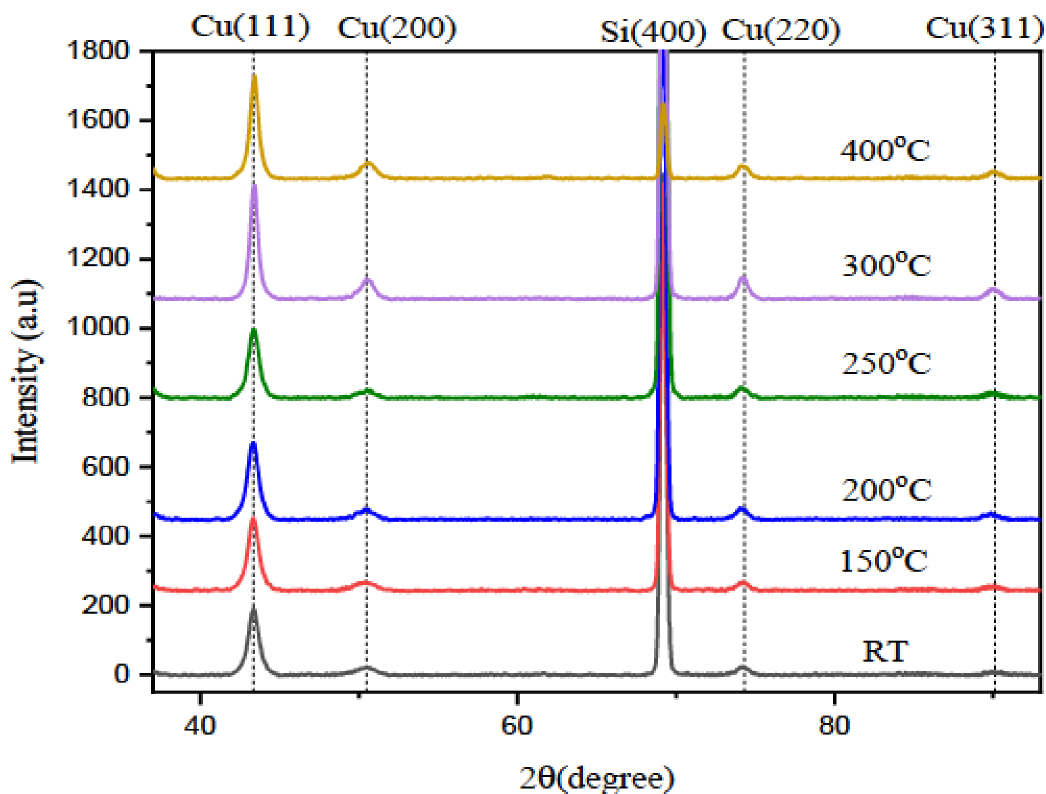

Figure 6.16 XRD pattern of as-deposited and annealed copper thin films.

The fitting analysis was used to calculate the full width at half maximum (FWHM). The FWHM values were converted into radians and then used in the Scherrer equation below, to determine the crystallite size.

$$D = \frac{K\lambda}{\beta cos\theta} \tag{6.10}$$

Where D is the crystallite size, λ is the X-ray wavelength (0.15406 nm), β is the width of the peak (FWHM) after correcting for instrumental peak broadening (β expressed in radians), θ is the Bragg angle and K is a dimensionless number of the order of unity known as the Scherrer constant [290]. The Scherrer constant (K) used in this work is 0.94. The dislocation density and the microstrain were also determined using the equations (6.11) and (6.12) respectively.

$$\delta = \frac{1}{D^2} \tag{6.11}$$

$$\varepsilon = \frac{\beta}{4tan\theta} \tag{6.12}$$

Where δ = dislocation density, ε = microstrain. Table 6.3 presents calculated values for crystallite size, dislocation density and microstrain. The highest crystallite size of 14 nm occurred at 300°C with corresponding microstrain of 0.007001.

Table 6. 4 Estimation of crystallite size, dislocation density, and microstrain for as-deposited and annealed copper thin films.

Sample	2θ	Crystallite size (nm)	Dislocation density (nm^{-2})	Microstrain
RT	43.34	10.25	0.0095	0.009561
150°C	43.33	10.05	0.0099	0.009759
200°C	43.30	10.00	0.01	0.009812
250°C	43.35	10.60	0.0089	0.009245
300°C	43.37	14.00	0.0051	0.007001
400°C	43.38	12.78	0.0061	0.007667

Figure 6.17 shows a plot of crystallite size and microstrain as a function of annealing temperature. The crystallite size was relatively constant from 20°C to 200°C but at 250°C a sharp rise in the crystallite size is observed. An opposite trend occurred in the case of the microstrain. Increase in annealing temperature promotes recrystallization and grain growth thereby increasing the average crystallite size of the films. Higher crystallite size might be attributed to decrease in defects such as grain boundaries, lattice distortions, dislocations, faults, and inhomogeneities.

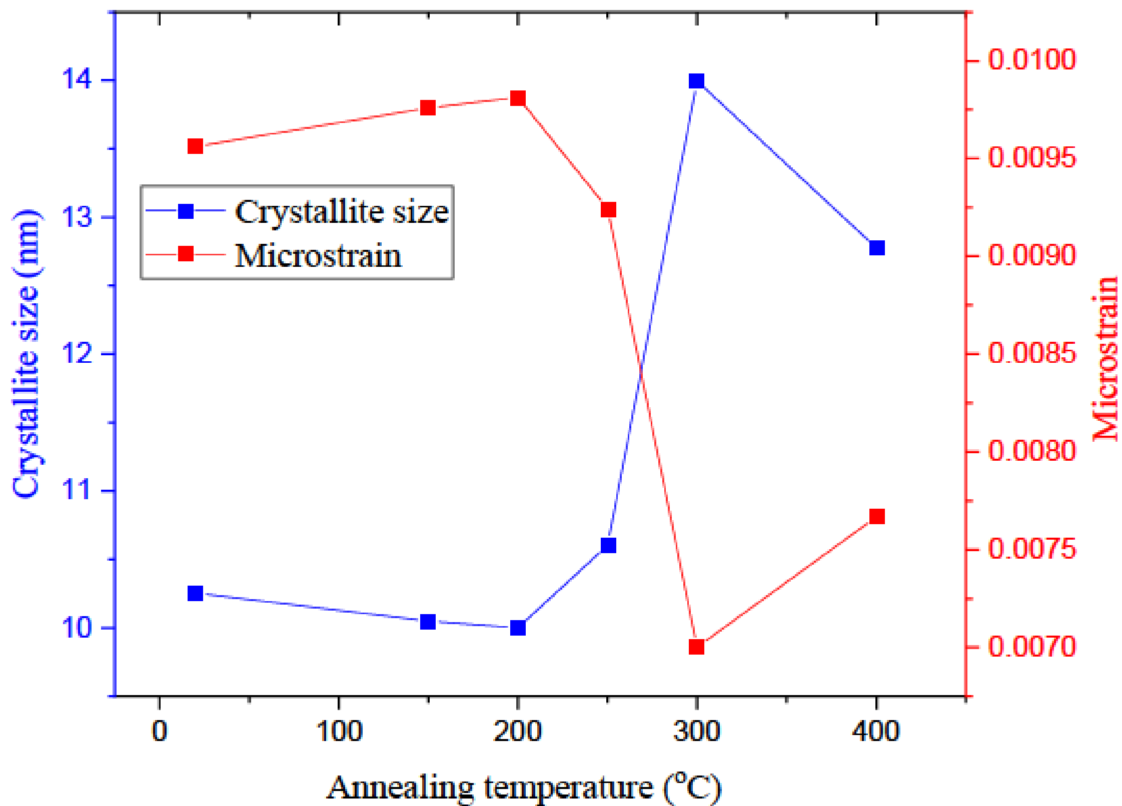

Figure 6.17 Crystallite size and microstrain as a function of annealing temperature.

6.2.5.2.3 Microstructure via TEM

From the XRD results, it was shown that samples annealed at 300°C and 400°C exhibited higher crystallite size, therefore, a further microstructural assessment was carried out using transmission electron microscopy (TEM). Figures 6.18 shows bright field TEM image and selected area

diffraction patterns (SADP) of copper thin films annealed at 400°C. Both films reveal columnar grains, oriented with the longer axis perpendicular to the substrate. Nanotwins are visible within some grains, as indicated by the yellow arrow in Figure 6.18. Few visible pores are observed between the columnar grains. The film thickness for 300°C and 400°C samples are 500 nm and 400 nm respectively. The selected area diffraction pattern (SADP) shows diffraction rings corresponding to (111), (200), (220), and (311) planes which confirms results obtained from the XRD.

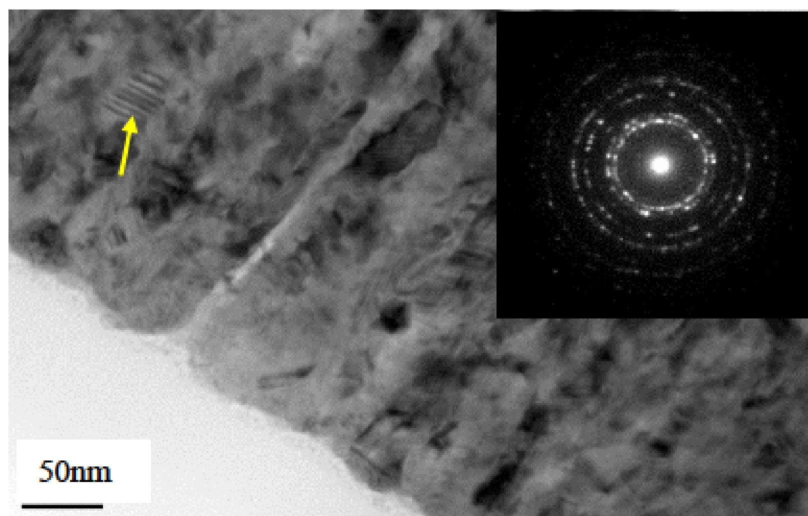

Figure 6.18 Bright field TEM and selected area diffraction pattern (SADP) of copper film annealed at 400°C.

6.2.5.3 Electrical resistivity

The electrical property of copper thin film deposited at room temperature and rapid annealed were investigated using four-point probe. The electrical property of interest in this work is the electrical resistivity. Results obtained from the electrical resistivity measurements are shown in Figure 6.19. The results show that film deposited at room temperature exhibits an average resistivity value of

6 μohm-cm which is higher than the bulk resistivity of 1.68 μohm-cm [291]. However, the room temperature sample have lower resistivity than 300°C and 400°C samples. A possible reason may be due to oxygen contamination which might have occurred during the annealing process of the two samples. The average resistivity of samples annealed at 300°C and 400°C are about 13.5 μohm-cm and 19 μohm-cm respectively. This is because the 300°C sample exhibits good crystallinity and higher crystallite size than sample annealed at 400°C. In addition, the XRD results showed that the 300°C sample exhibits lower lattice strain or microstrain than the 400°C sample which suggest that the 300°C sample has less impurities and defects than the 400°C, hence lower resistivity.

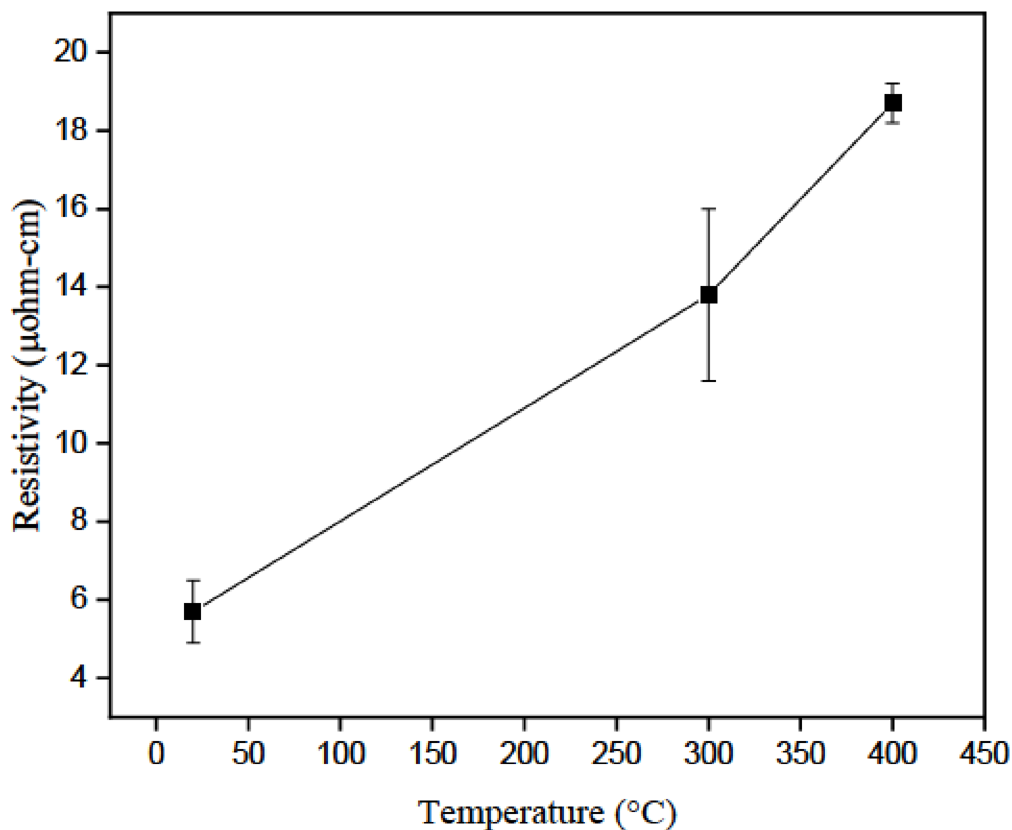

Figure 6.19 Effect of rapid thermal annealing on electrical resistivity of copper thin films.

6.2.5.4 Comparison between the thin films deposited by flat (TC 1) and non-flat (TC 4) targets

6.2.5.4.1 Surface Morphology

The surface morphology of films sputtered from both TC 1 and TC 4 targets have been investigated. Figure 6.20 (a) and (b) illustrate the SEM of the top view of copper films deposited at room temperature by planar and non-planar targets, respectively. Result for the film deposited by the planar (flat) target shows open cracks within the film. During deposition at room temperature, due to limited thermal energy, it is possible the adatoms lack sufficient kinetic energy to nucleate and migrate to other adatoms for coalescence of islands for the formation of continuous films. As a result, micro-cracks are generated and that would affect film properties. This crack-like microstructure in Cu thin film was first reported by Joh *et al.* when they were investigating the effects of the deposition pressure on the microstructure of Cu thin film [292]. They attributed the open boundary microstructures to shadowing effect which occurred at high deposition pressure. However, film deposited by non-flat target show different surface morphology as can be seen in Figure 6.21 (b). The surface morphology appears grainier and no microcracks. Due to the protrusion of the target, during deposition, the Cu atoms are sputtered from different angles of the protruded area creating uniform distribution of adatoms on the surface of the substrate [279]. In addition, the sputtered atoms from the non-flat target acquired higher thermal energy by virtue of its geometry (protrusion region closer to the substrate), promote surface diffusion and adatom mobility.

6.2.5.4.2 Crystal Structure

Figure 6.22 shows XRD pattern of copper thin films sputtered from TC 1 and TC 4 targets. Result from Figure 6.22 shows that film sputtered from TC 4 show higher intensity peak at (111), (200), (220), and (311) than film sputtered from TC 1. Hence, TC 4 film show better crystallinity than

TC 1 film. In addition, Table 6.4 shows values of crystallite size, dislocation density, and microstrain for films sputtered from both flat and non-flat targets. Results show higher crystallite size and lower microstrain for the film obtained from the non-flat target which may be due to decrease in lattice defects [293].

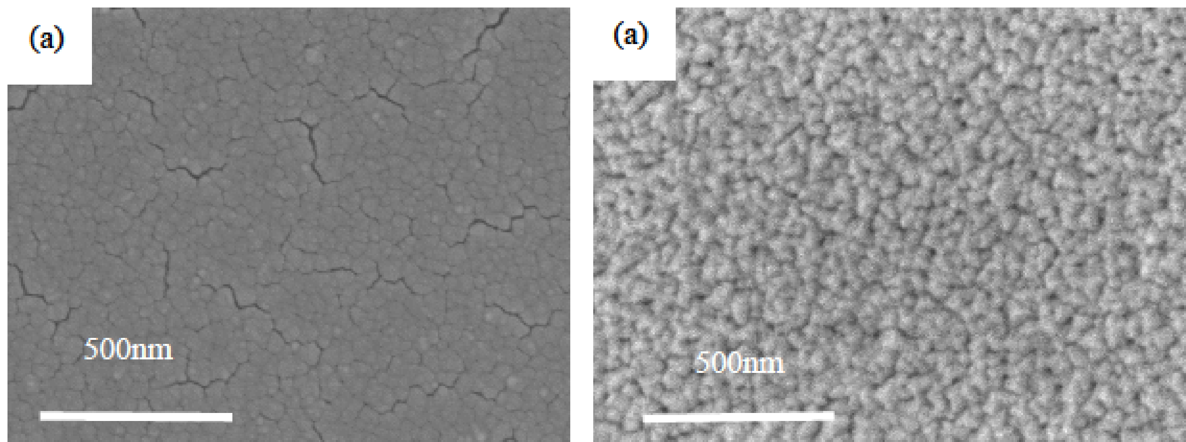

Figure 6.20 SEM micrograph of the top view of copper films sputtered from different targets: (a) Flat and (b) Non-flat.

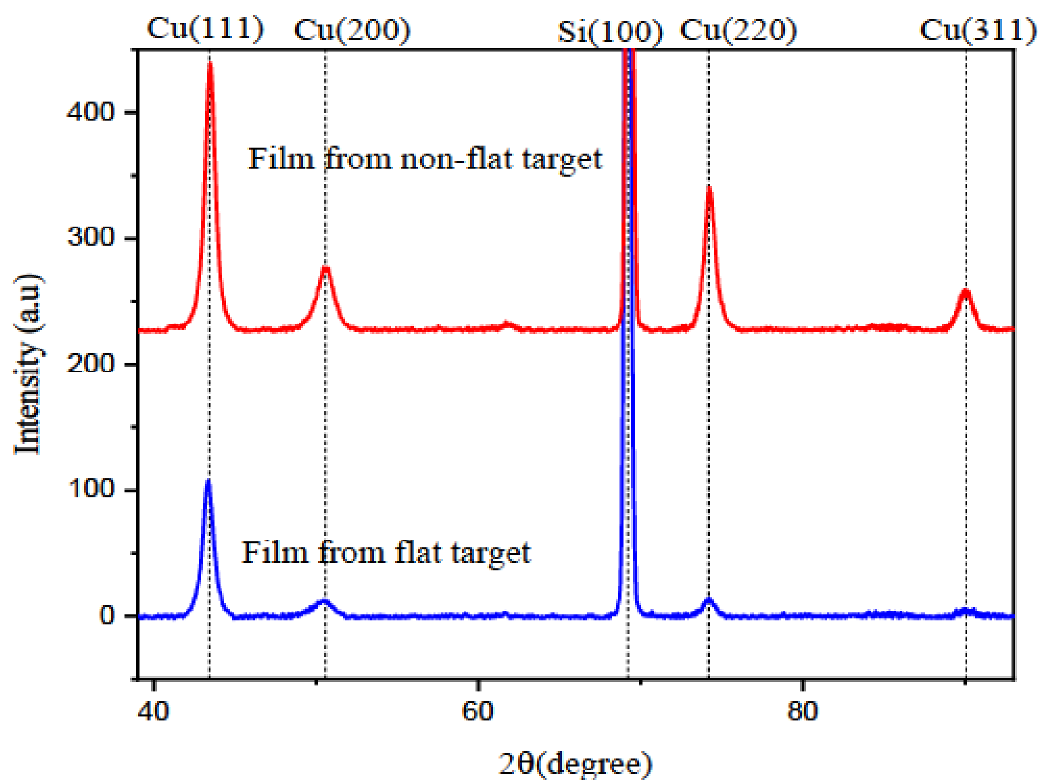

Figure 6. 21 XRD pattern of copper films sputtered from different targets: (a) Flat and (b) non-flat.

Table 6. 5 Estimation of crystallite size, dislocation density and microstrain of copper films from flat and non-flat target.

Films	2θ	Crystallite size (nm)	Dislocation density (nm^{-2})	Microstrain
Flat target	43.34	10.25495256	0.009509	0.009561
Non-flat target	43.46	10.89279682	0.008428	0.008977

CHAPTER 7

316L Stainless Steel Target Made Via Binder Jetting Additive Manufacturing and Thin Film Fabrication by Magnetron Sputtering

7.0 Introduction

It was mentioned at the beginning of the previous chapter, in order to investigate the possibility of manufacturing complex geometry sputtering targets via 3D binder jet techniques, two readily available powders have been used: copper powders and 316L stainless steel (SS) powders. This chapter will present the results of investigating the 3D printing of sputtering targets from 316L SS powders. Also, the preliminary results on the characterization of thin films obtained from the stainless-steel targets will be introduced.

7.1 Materials and Methods

7.1.1 316L SS powder

Gas atomized 316L SS powder purchased from ExOne was used as the starting material for proof of concept. The composition of the 316L SS used in this research is shown in Table 7.1. Sieving was performed using a 45 µm mesh size of sieve. Particle size distribution and particle morphology analysis were carried out using particle size analyzer Cilas 1190 and JEOL JIB-4500 Multi Beam System SEM/FIB. Phase structure analysis was conducted using Bruker-Nonius D8 Advanced Powder X-ray Diffractometer equipped with Cu kα radiation source.

Table 7.1 Chemical composition of 316L SS powder (procured from ExOne).

Element	Fe	Cr	Ni	Mo	Mn	Si	C
Composition (wt%)	Bal	16-18	10-14	2-3	2	1	0.03

7.1.2 Binder jet printing and post-processing

A disc of diameter 55.88 mm (2.2 inches) and thickness 6.35mm (0.25 inches) was created in Solidworks (see Figure 7.1(a)) and imported to the printing software of the printer. The target was printed using Exone Innovent + binder jetting 3D printer with printing parameters shown in Table 7.2.

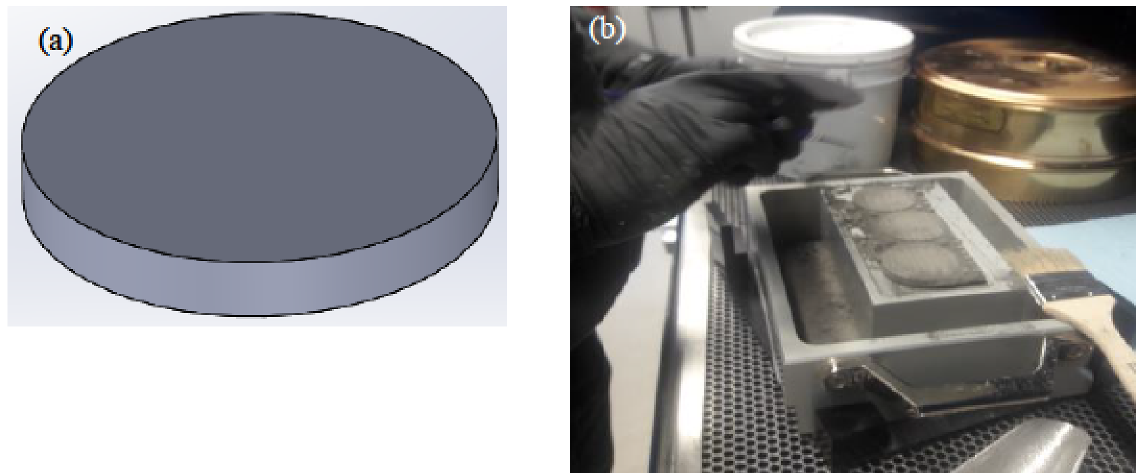

Figure 7.1 (a) Solidworks design for disc target, diameter 55.88 mm, thickness 6.35 mm, (b) 3D printed 316L SS sputtering targets.

Table 7.2 Printing parameters used for 316L SS target.

Printing parameters	Values
Binder saturation	50 %
Layer thickness	50 µm
Recoat speed	150 mms^{-1}
Roller rotation speed	250 rpm
Roller traverse speed	3 mms^{-1}

Afterwards target was cured at 180°C for six hours using Yamato DX402C oven. After curing, the green part was sintered at 1200°C for 12 hours with a ramp rate of 10°C/min under argon atmosphere for densification, using a TevTech vacuum furnace. In order to obtain a smooth surfaced target, sintered target was ground and polished to obtain a mirror like surface. As-sintered and cross-section of 316L SS target were examined for their morphology and chemical composition using SEM/EDS. The crystal structure investigation was performed using Bruker-Nonius D8 Advanced Powder X-ray Diffractometer with a Cu kα radiation source. The density of the target was determined using Archimedes method. Equation (7.1) was employed to calculate the density.

$$\text{Density} = \frac{M_T}{V_T} \quad (7.1)$$

Where M_T is the mass of target and V_T the volume of target. The volume of the target was measured by immersing the target in a graduated cylinder filled with de-ionized water and recording volume of water displaced. Image analysis software ImageJ was also used to estimate the porosity and the density.

7.1.3 Thin film fabrication of 316L SS

Si (100) substrate was prepared by cleaning using acetone, alcohol, and de-ionized water. 3D printed target together with the Si (100) substrate were loaded in the vacuum chamber and pumped down to 5.0×10^{-7} Torr. 316l SS thin films were prepared under argon atmosphere using direct current (DC) magnetron sputtering system. Several deposition trial experiments were conducted in order to optimize the deposition parameters for better film quality. The deposition conditions used for the sputtering process were as follows: argon pressure = 4 mTorr, flow rate = 10 sccm, discharge current = 0.1 A, substrate temperatures = 20°C, 200°C, 300°C, 400°C, and deposition

time = 10 minutes. The surface morphology, chemical composition, and crystal structure of the thin films were investigated using advanced characterization techniques such as Agilent Technologies 5500 AFM, SEM/EDS JEOL instrument, and Bruker-Nonius D8 advanced powder X-ray diffractometer.

7.2 Results and discussion

7.2.1 Powder characterization

Figure 7.2 shows a bimodal size distribution plot for 316L SS powder where a small fraction of fine particles with a distribution ranging from 0.1 μm to 0.5 μm corresponds to 8% volume fraction. A large fraction of the powder is distributed in range of 1 μm to 20 μm corresponding to about 92% volume fraction. The mean diameter of the powder is about 9 μm. The statistical distribution parameters D_{10}, D_{50}(median), and D_{90} obtained for the powder are 4.75 μm, 11.02 μm, and 19.66 μm respectively.

Figure 7.3 (a) shows secondary electron image recorded from the 316L SS powder. Result shows both fine and coarse particles having spherical morphology and some few irregular particles. The fine particles form agglomerates, and the coarse particles show attachment of satellite particles. Yusuf *et al.* reported similar powder morphology of agglomerates of satellite particles attached to the coarse particles [294]. Figure 7.3 (b) shows EDS spectrum collected from the 316L SS powder, red square region in Figure 7.3 (a). Result shows the presence of Fe, Cr, Ni, Mn, and Mo same as the nominal composition of 316L SS powder specified by the supplier.

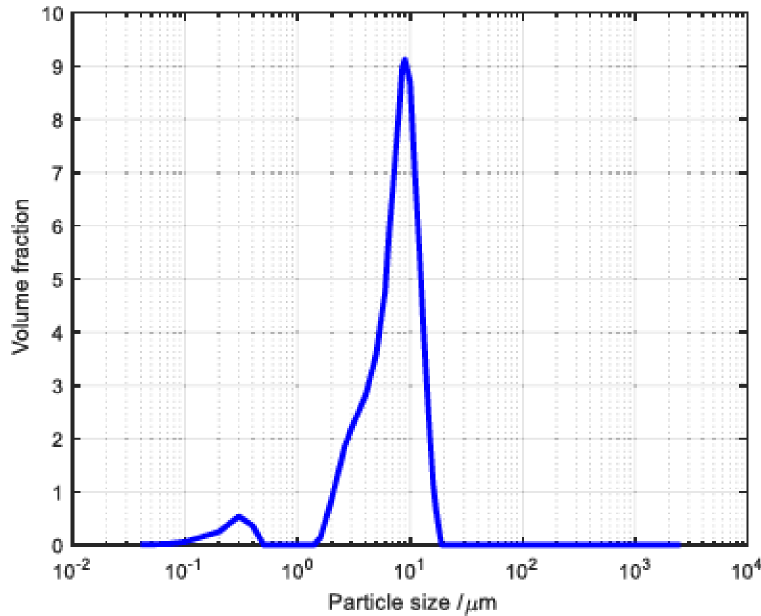

Figure 7.2 Particle size analysis of 316L SS.

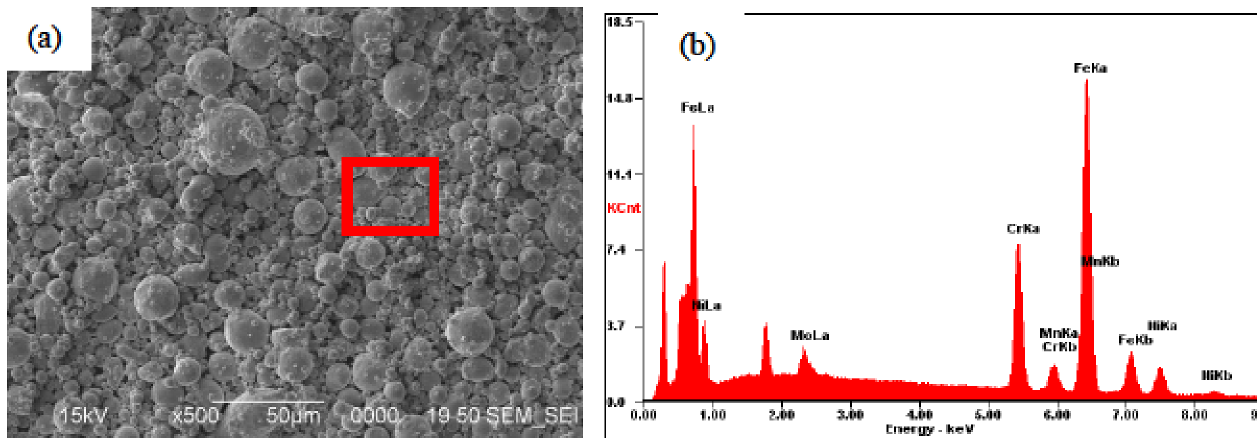

Figure 7.3 316L SS powder: (a) SEM micrograph and (b) EDS spectrum.

Figure 7.4 shows XRD pattern of 316L SS powder containing a mixture of austenite (γ-Fe) and delta ferrite (δ-Fe) phases. The delta ferrite phase constitutes a small fraction of the mixture evident by the weak diffraction peak. The small fraction of the delta ferrite prevents hot cracking during weld solidification [295]. The austenite phase dominates with high intensity peaks which correspond to (111), (200), and (220).

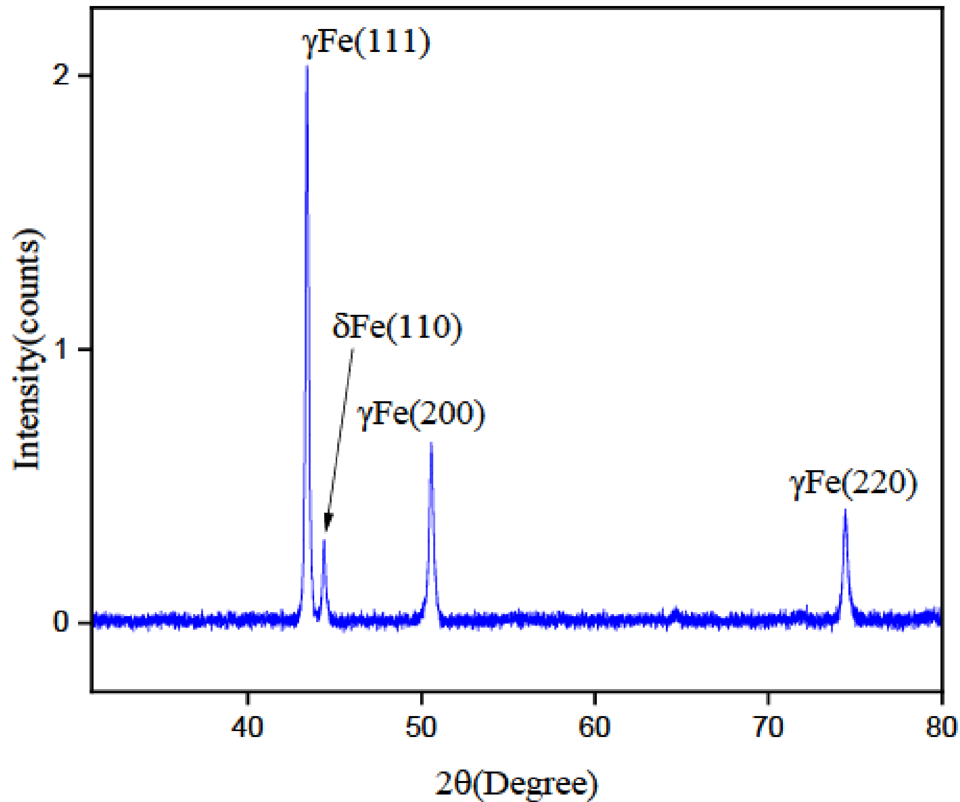

Figure 7.4 XRD pattern of 316L SS powder.

7.2.2 Target characterization

The microstructure and crystal structure of the sintered target was investigated using SEM/EDS and XRD techniques. Figure 7.5 show SEM micrographs of 316L SS target sintered at 1100°C for 12 hours under argon atmosphere. Neck formation is observed as the particles bond together with reduced pore volume. This apparent good densification is the result of bimodal size distribution of the starting powders. The fine particles filled well the space between the large ones. Similar observation was reported by Shan *et al.* in their investigation of fast densification mechanism of AlON powder with a bimodal particle size distribution under pressureless sintering condition [296]. Shan *et al.* achieved a relative density of 96.33% under sintering held at 1700°C for 30 min. The fast densification and grain growth were attributed to the re-arrangement of near-spherical

particles in the bimodal particle size distribution. The density of the 316L SS target was found to be 7.769 gcm^{-3} which is 97.11% of the theoretical density. The linear shrinkage following the sintering was estimated to be 13.64%.

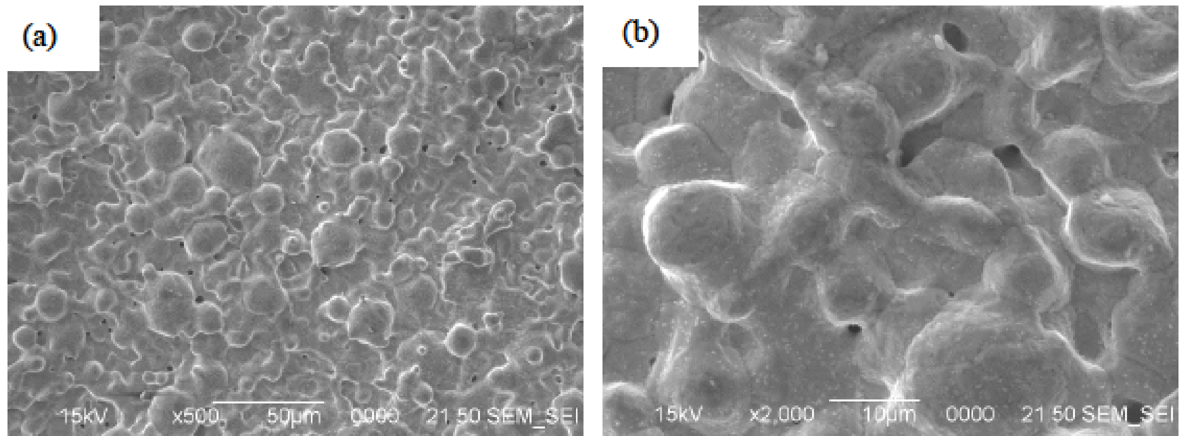

Figure 7.5 SEM micrographs of as-sintered target: (a) Low magnification and (b) High magnification.

Figure 7.6 (a) and (b) show SEM micrograph and EDS spectrum of polished cross-section of 316L SS target. The SEM micrograph shows small open pores randomly distributed. The porosity determined by ImageJ was found to be 2.388%. EDS spectrum collected from a section in Figure 7.6 (a) shows the presence of Fe, Cr, Ni, Mn, and Mo as seen in Figure 7.6 (b). Table 7.3 shows atomic concentrations of element present in 316L SS target obtained from the EDS quantitative analysis. Result agrees with composition of starting powder indicating less contamination during sintering process.

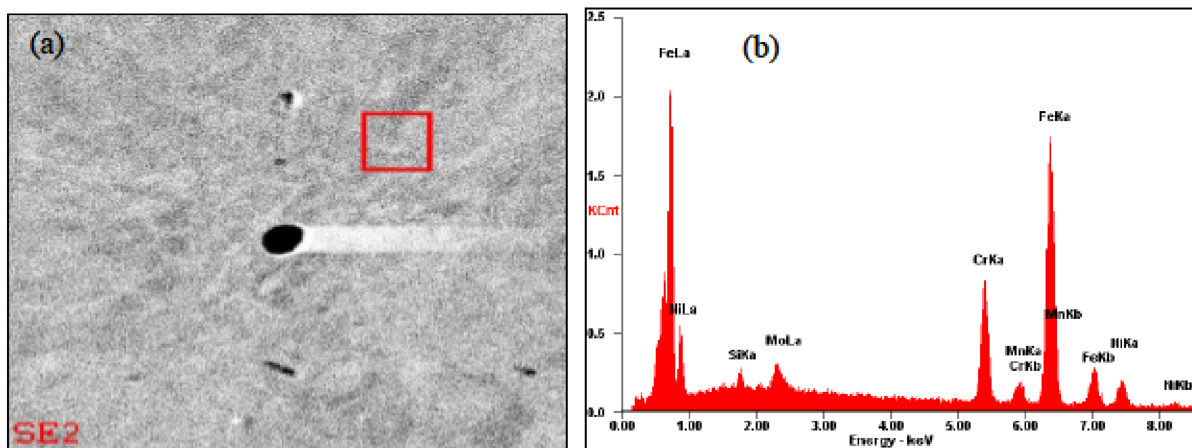

Figure 7.6 Polished cross-section of 316L SS target: (a) SEM and (b) EDS spectrum collected from the red square area in (a).

Table 7.3 EDS quantitative analysis of 316L SS target.

Element	at%
Mo	1.90
Mn	1.34
Ni	10.63
Cr	18.86
Fe	67.27

Figure 7.7 shows XRD pattern of 316L SS target with diffraction peaks corresponding to the austenitic phase. There are no secondary phases present. No evidence of oxidation was seen due to the inert atmosphere used during the sintering process.

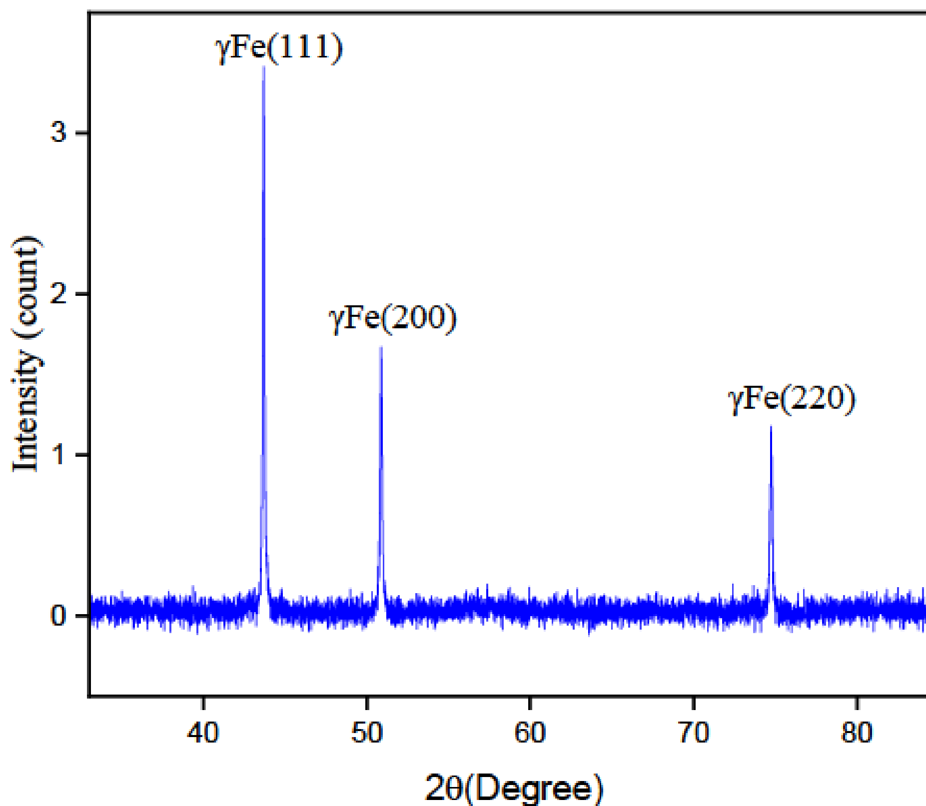

Figure 7.7 XRD pattern of 316L SS target.

7.2.3 Thin film characterization

Figure 7.8 shows AFM image of 316L SS thin film deposited at room temperature. The film surface shows few pores with no visible cracks. The grains show spherical morphology with uniform composition. The average grain size is about 15 nm. Figure 7.9 (a) and (b) show SEM micrograph and EDS spectrum of cross-section of 316L SS thin film sandwich in a plastic holder embedded in epoxy. Due to improper cutting of the film section, the SEM micrograph displays broken pieces of film cross-section. The EDS analysis of the thin film shows the presence of all expected elements as seen in Figure 7.9 (b). Table 7.4 shows atomic concentrations of individual element present in the film cross-section. Other peaks such C, O, and Si were detected by the EDS detector which possibly may be coming from the epoxy and substrate. Comparing the composition of the powder, target, and the film, no significant variation can be seen which is an indication of less contamination throughout the process.

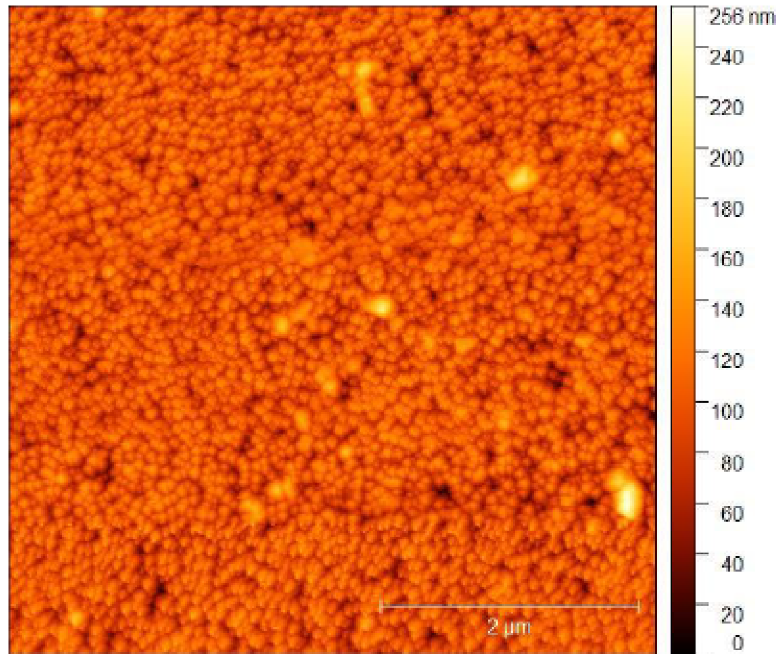

Figure 7.8 AFM image of as-deposited 316L SS thin film.

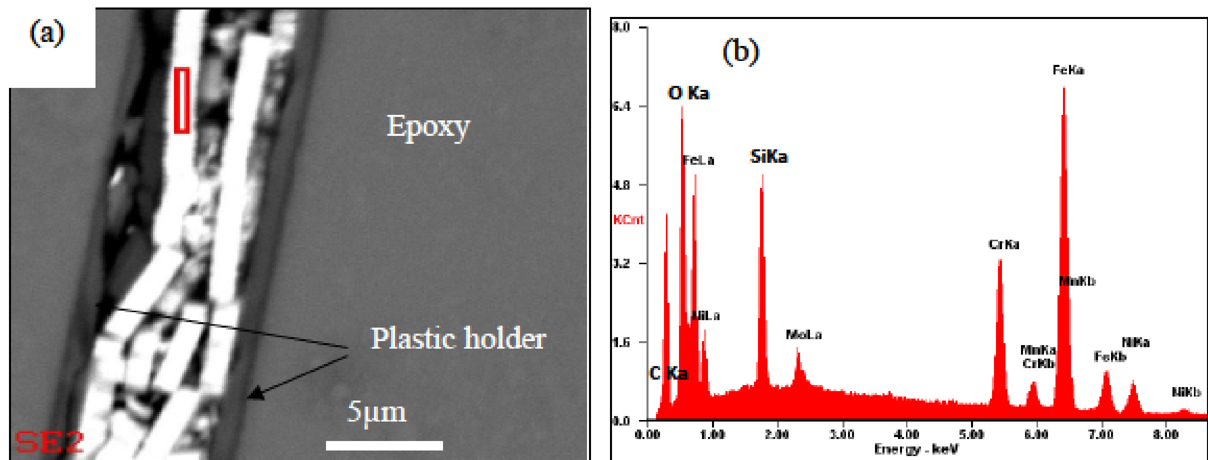

Figure 7.9 (a) Cross-section of 316L SS thin film placed in a plastic holder embedded in epoxy and corresponding EDS spectrum (b).

Table 7.4 EDS quantitative analysis of cross section of 316L SS thin film.

Element	at%
Mo	2.33
Mn	1.39
Ni	11.01
Cr	18.80
Fe	66.47

Figure 7.10 shows XRD pattern of as-deposited 316L SS thin film on Si (100) substrate. Two diffraction peaks are observed, one corresponds to the film and the other to the substrate. The diffraction peak for the film was indexed as (111) which corresponds to the austenitic phase. No secondary phase or precipitates were detected. Result show consistency with XRD pattern obtained for the target.

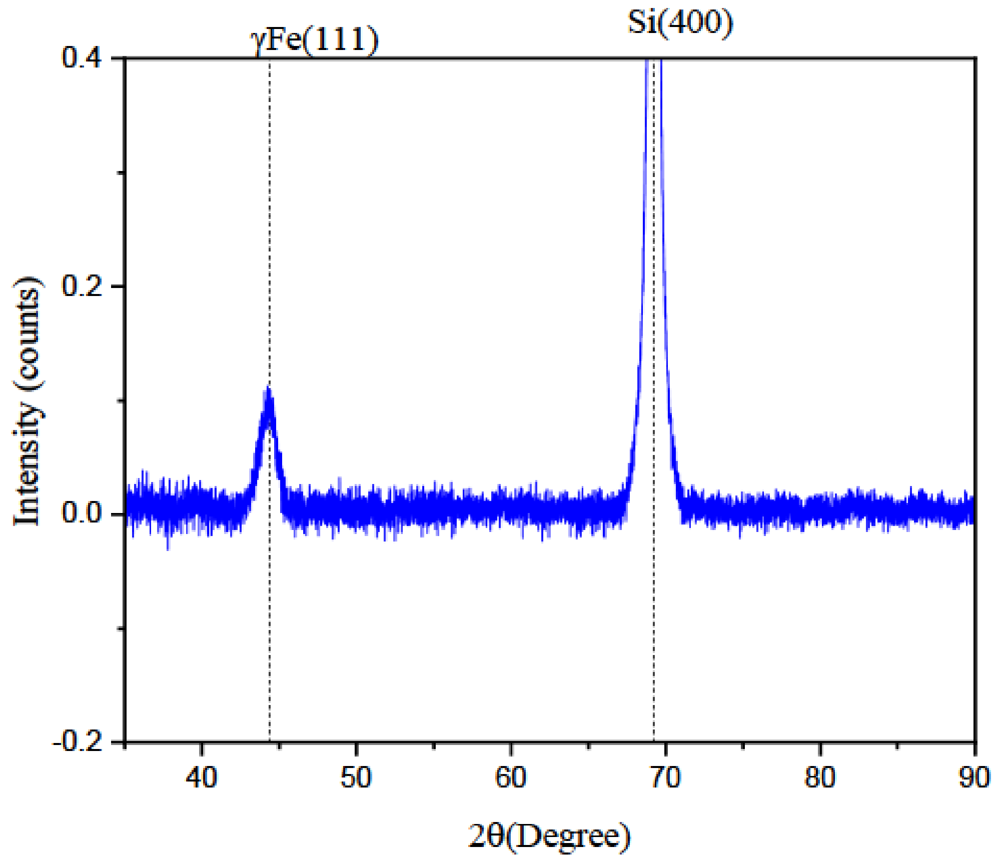

Figure 7.10 XRD pattern of as-deposited 316L SS thin film.

Figure 7.11 (a)-(c) show top view SEM micrographs of 316L SS thin film deposited at substrate temperatures 200°C, 300°C, and 400°C. The SEM micrograph of film deposited at 200°C shows nano-size grains with spherical morphology. At 300°C substrate temperature, a shift from spherical to triangular-pyramidal morphology is observed with increased grain size of about 30 nm. At much higher substrate temperature, the grain morphology remained unchanged but with increased grain size as seen in Figure 7.11(c). Figure 7.11 (d) shows cross-section view of 316L SS thin film deposited at 400°C. The thickness of the film was measured and found to be 70 nm.

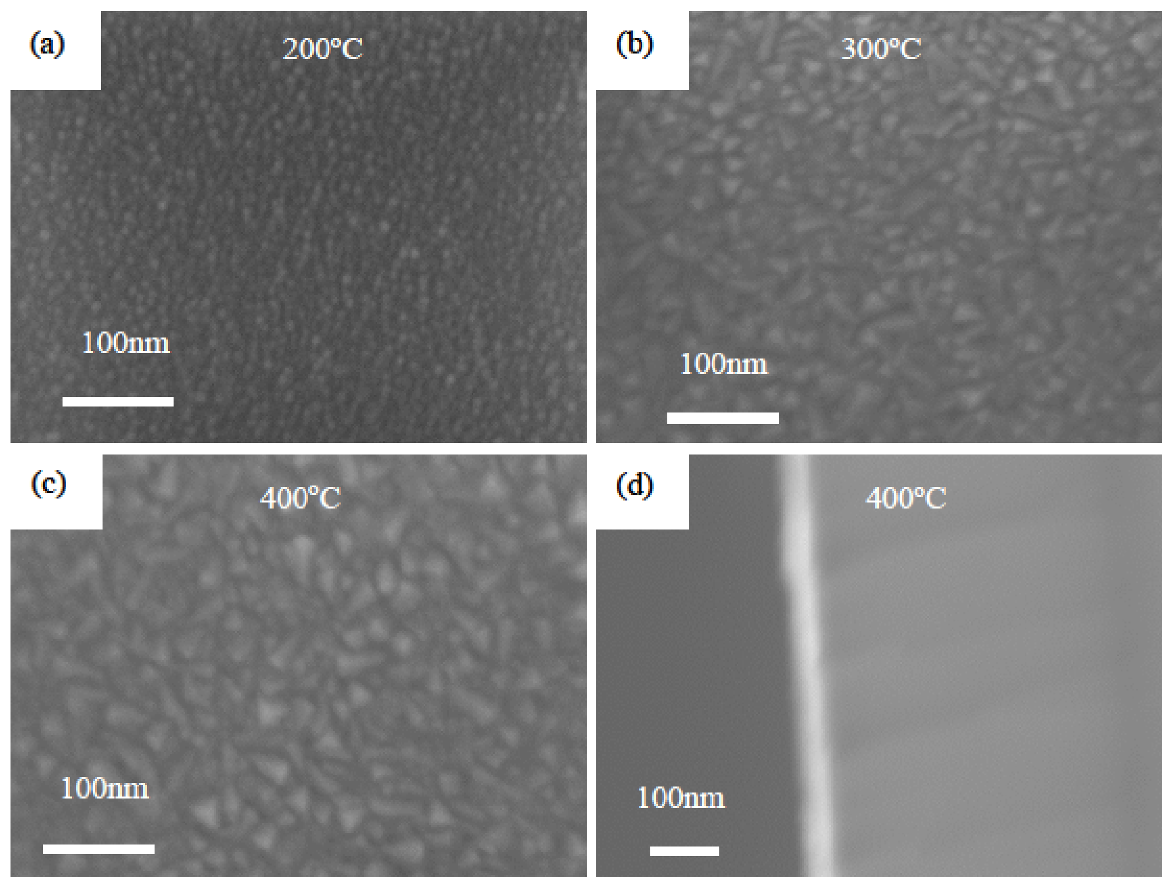

Figure 7.11 SEM micrographs of top and cross-section view of 316L SS thin films at different substrate temperatures: (a) 200°C, (b) 300°C, (c) 400°C, and (d) 400°C.

CHAPTER 8

CONCLUSION AND FUTURE WORK

8.0 Conclusion

The conclusion drawn from this research are summarized as follows:

Chapter 3 presented results obtained from powder characterization of ball milled Ni-Mn-Ga powder. Particle size analysis result showed a bimodal particle size distribution characterized by the statistical parameter values D_{10} = 23.86 µm, D_{50} = 67.3 µm, and D_{90} = 105.2 µm. The powder showed an irregular powder morphology with homogenous composition. The thermal analysis performed on the as-milled powder showed no martensitic transformation due to induced stress coming from mechanical collisions between powder particles. To relieve the induce stress and to restore the martensitic transformation, annealing experiment was carried out on the powder. SEM result showed the presence of martensitic twin microstructure. DSC result of the annealed powder showed martensitic transformation at 87.7°C.

Chapter 4 presented results obtained from the characterization of printed and sintered target of Ni-Mn-Ga alloy. Ni-Mn-Ga targets were successfully printed using BJAM. Observation from the as-printed target showed better green density estimated to be ~ 57% which is an improvement of what was reported in literature. The improvement of the green density of the as-printed target was due to the bimodal particle size distribution of the starting powder. Ni-Mn-Ga targets were sintered for densification and mechanical strengthening. It was found that the microstructural evolution of the martensitic twin structures was influenced by the sintering conditions whereby a transformation from tetragonal (Target 1 and Target 2) for low sintering temperatures to orthorhombic structure (Target 3 and Target 4) for high sintering temperatures were observed. Oxidation of the targets were reduced by employing flakes of manganese getters.

Linear shrinkage of targets sintered at different temperatures were also examined in both radial and axial direction. It was found that as the sintering temperature increases shrinkage in the axial (thickness) direction was higher than in the radial (diameter) direction which suggest that particles packed in the printing direction (vertical) fuse faster than the radial direction.

Porosity of the targets decreased as the sintering temperature increased. The maximum achieved density percentage of the target was about 88% which occurred at a sintering temperature of 1080°C. The composition of Target 2, Target 3, and Target 4 were closed to the powder composition with variation within a 3% limit with the exception of Target 1. Target 1 showed significant variation in both Ni and Mn contents, a result of high manganese evaporation during sintering. XRD results showed that Target 1 and Target 2 have tetragonal martensitic structure but different space group and lattice parameters, which could be attributed to variation in chemical composition. Target 3 and Target 4 showed mixed phases of 7M martensite and non-modulated martensite structures. The martensitic transformation temperatures of the targets were observed to be composition dependent, that is, it was seen that as the atomic concentration of Ni content decreased the martensitic transformation temperature also decreased. Target 1 exhibited the highest martensitic transformation temperature at ~148°C and the lowest martensitic transformation temperature at ~74°C was seen in Target 4.

In Chapter 5, the effect of discharge current and substrate temperature on the surface morphology, composition and crystal structure of Ni-Mn-Ga thin films deposited on Si (100) substrate was investigated. As the discharge current increased, the film showed increased grain size. The grain morphology, as appeared from the investigation of the film planar surface was of elongated grains. The film crystallinity also increase with increased discharge current, as proved by XRD investigations.

The most important effect of maintaining the discharge current value constant and increasing the substrate temperature was the change in chemistry and crystallography of the obtained Ni-Mn-Ga thin films. The film deposited at 700^0C showed the closest chemical composition to the target composition. For the other substrate temperatures, the high oxygen contamination, due perhaps to not-so-optimum deposition conditions, drastically altered the film composition. By increasing the substrate temperature, the film crystal structure changed from Heusler $L2_I$ cubic (high temperature phase) to monoclinic (low temperature phase).

In Chapters 6 and 7, it was demonstrated, using sputtering targets 3D printed from Cu and 316L SS powders, that sputtering targets of different design geometries such as trapezoidal, conical protrusions could be manufactured by BJAM with improved target utilization efficiency compared to regular disc target. It was also shown that thin films sputtered from these 3D printed targets have similar morphological, chemical, and crystallographic characteristics to the films made using classical manufacturing techniques, such as casting, machining, and HIP.

Moreover, thin films sputtered from binder jet 3D printed non-planar targets exhibited less micro-cracks as compared to films produced from flat targets. Higher crystallite size and lower micro-strain was observed for films sputtered from non-planar targets, which is an indication of improved crystallinity.

8.1 Future work

This research has demonstrated that Ni-Mn-Ga alloy sputtering targets can be manufactured by binder jetting additive manufacturing technique. In addition, Ni-Mn-Ga thin films have been fabricated from the binder jetting additive manufactured targets with film properties comparable to those reported in literature. Yet there is still more work to be done. For future work the following are recommended:

- To achieve full target density, much finer particle size powder is recommended as a starting material for the 3D printing. In addition, sintering conditions should be optimized to enhance densification and reduce porosity.
- The target designs proposed in this work should be implemented to make more targets of Ni-Mn-Ga alloy with different geometries to realize higher target utilization efficiency.
- Further investigation should be carried out on Ni-Mn-Ga thin films deposited at substrate temperatures of 600°C and 700°C using high resolution SEM or TEM to confirm martensitic microstructures observed from the XRD spectra.
- Target manufacturing by BJAM should be extended to ceramic and semiconductor materials.

REFERENCE

[1] D. M. Solis, A. V. Silva, N. Volpato, and L. F. Berti, "Reaction-bonding of aluminum oxide processed by binder jetting," *J. Manuf. Process.*, vol. 41, pp. 267–272, May 2019, doi: 10.1016/j.jmapro.2019.04.008.

[2] B. Utela, D. Storti, R. Anderson, and M. Ganter, "A review of process development steps for new material systems in three dimensional printing (3DP)," *J. Manuf. Process.*, vol. 10, no. 2, pp. 96–104, Jul. 2008, doi: 10.1016/j.jmapro.2009.03.002.

[3] Y. Bai and C. B. Williams, "Binder jetting additive manufacturing with a particle-free metal ink as a binder precursor," *Mater. Des.*, vol. 147, pp. 146–156, Jun. 2018, doi: 10.1016/j.matdes.2018.03.027.

[4] M. Ziaee and N. B. Crane, "Binder jetting: A review of process, materials, and methods," *Addit. Manuf.*, vol. 28, pp. 781–801, Aug. 2019, doi: 10.1016/j.addma.2019.05.031.

[5] Y. Bai and C. B. Williams, "An exploration of binder jetting of copper," *Rapid Prototyp. J.*, vol. 21, no. 2, pp. 177–185, Jan. 2015, doi: 10.1108/RPJ-12-2014-0180.

[6] Y. Tang, Y. Zhou, T. Hoff, M. Garon, and Y. F. Zhao, "Elastic modulus of 316 stainless steel lattice structure fabricated via binder jetting process," *Mater. Sci. Technol.*, vol. 32, no. 7, pp. 648–656, May 2016, doi: 10.1179/1743284715Y.0000000084.

[7] A. Mostafaei, P. Rodriguez De Vecchis, E. L. Stevens, and M. Chmielus, "Sintering regimes and resulting microstructure and properties of binder jet 3D printed Ni-Mn-Ga magnetic shape memory alloys," *Acta Mater.*, vol. 154, pp. 355–364, Aug. 2018, doi: 10.1016/j.actamat.2018.05.047.

[8] M. P. Caputo, A. E. Berkowitz, A. Armstrong, P. Müllner, and C. V. Solomon, "4D printing of net shape parts made from Ni-Mn-Ga magnetic shape-memory alloys," *Addit. Manuf.*, vol. 21, pp. 579–588, May 2018, doi: 10.1016/j.addma.2018.03.028.

[9] M. P. Caputo and C. V. Solomon, "A facile method for producing porous parts with complex geometries from ferromagnetic Ni-Mn-Ga shape memory alloys," *Mater. Lett.*, vol. 200, pp. 87–89, Aug. 2017, doi: 10.1016/j.matlet.2017.04.112.

[10] M. Caputo, M. Krizner, and C. Solomon, *INVESTIGATION OF 3D PRINTING PARAMETERS OF SHAPE MEMORY ALLOY POWDERS*. 2015.

[11] M. P. Caputo, D. R. Waryoba, and C. V. Solomon, "Sintering effects on additive manufactured Ni–Mn–Ga shape memory alloys: a microstructure and thermal analysis," *J. Mater. Sci.*, vol. 55, no. 12, pp. 5311–5321, Apr. 2020, doi: 10.1007/s10853-020-04352-9.

[12] A. Mostafaei, K.A. Kimes, E.L. Stevens, J. Toman, Y.L. Krimer, K. Ullako, M. Chmielus, "Microstructural evolution and magnetic properties of binder jet additive manufactured Ni-Mn-Ga magnetic shape memory alloy foam," *Acta Mater.*, vol. 131, pp. 482–490, Jun. 2017, doi: 10.1016/j.actamat.2017.04.010.

[13] Y. Mao, J. Li, W. Li, D. Cai, and Q. Wei, "Binder jetting additive manufacturing of 316L stainless-steel green parts with high strength and low binder content: Binder preparation and process optimization," *J. Mater. Process. Technol.*, vol. 291, p. 117020, May 2021, doi: 10.1016/j.jmatprotec.2020.117020.

[14] "Metal Binder Jetting Additive Manufacturing: A Literature Review | J. Manuf. Sci. Eng. | ASME Digital Collection." https://asmedigitalcollection.asme.org/manufacturingscience/article/142/9/090801/1084395?casa_token=ZfztJQcbY1QAAAAA:iIYBcDAgAqv3b0Hv9l9l1hjwvPwa_FhH8Sg8u5kBBEDhhTqTz0XqgyRm1FUus92y1KSZ (accessed Nov. 17, 2021).

[15] W. Du, X. Ren, Y. Chen, C. Ma, M. Radovic, and Z. Pei, "Model Guided Mixing of Ceramic Powders With Graded Particle Sizes in Binder Jetting Additive Manufacturing," in *Volume 1: Additive Manufacturing; Bio and Sustainable Manufacturing*, College Station, Texas, USA, Jun. 2018, p. V001T01A014. doi: 10.1115/MSEC2018-6651.
[16] Y. Bai and C. B. Williams, "Binderless Jetting: Additive Manufacturing of metal parts via jetting nanoparticles," p. 12.
[17] *Comprehensive Materials Processing*. Newnes, 2014.
[18] K. Wasa, M. Kitabatake, and H. Adachi, *Thin film materials technology: sputtering of control compound materials*. Springer Science & Business Media, 2004.
[19] J. A. Thornton, "Magnetron sputtering: basic physics and application to cylindrical magnetrons," *J. Vac. Sci. Technol.*, vol. 15, no. 2, pp. 171–177, Mar. 1978, doi: 10.1116/1.569448.
[20] J. Sarkar, *Sputtering Materials for VLSI and Thin Film Devices*. William Andrew, 2010.
[21] J. A. Dunlop, J. Yuan, J. K. Kardokus, and R. A. Emigh, "Sputtering target with ultra-fine, oriented grains and method of making same," EP0746436A4, May 07, 1997 Accessed: Apr. 22, 2020. [Online]. Available: https://patents.google.com/patent/EP0746436A4/en
[22] F. Bouchard, M. B. Dittmar, and B. Manring, "Monte Carlo simulations of textured planar magnetron targets," *J. Vac. Sci. Technol. Vac. Surf. Films*, vol. 11, no. 5, pp. 2765–2770, Sep. 1993, doi: 10.1116/1.578639.
[23] A. Leybovich, T. Kuniya, P. C. Smith, M. B. Hendricks, and D. N. Ruzic, "Effects of target polycrystalline structure and surface gas coverage on magnetron $I-V$ characteristics," *J. Vac. Sci. Technol. Vac. Surf. Films*, vol. 12, no. 4, pp. 1618–1622, Jul. 1994, doi: 10.1116/1.579024.
[24] C. A. Michaluk, "Correlating discrete orientation and grain size to the sputter deposition properties of tantalum," *J. Electron. Mater.*, vol. 31, no. 1, pp. 2–9, Jan. 2002, doi: 10.1007/s11664-002-0165-9.
[25] C. E. Wickersham, "Crystallographic target effects in magnetron sputtering," *J. Vac. Sci. Technol. Vac. Surf. Films*, vol. 5, no. 4, pp. 1755–1758, Jul. 1987, doi: 10.1116/1.574531.
[26] H. Tsuge and S. Esho, "Angular distribution of sputtered atoms from polycrystalline metal targets," *J. Appl. Phys.*, vol. 52, no. 7, pp. 4391–4395, Jul. 1981, doi: 10.1063/1.329365.
[27] Z. Zhang, L. Kho, and C. E. Wickersham, "Effect of grain orientation on tantalum magnetron sputtering yield," *J. Vac. Sci. Technol. Vac. Surf. Films*, vol. 24, no. 4, pp. 1107–1111, Jul. 2006, doi: 10.1116/1.2212436.
[28] H. Cho, "DEVELOPMENT OF COPPER SPUTTERING TARGET WITH SUPERIOR SPUTTER YIELD VIA CRYSTALLOGRAPHIC TEXTURE CONTROL ANNEALING," *Mod. Phys. Lett. B*, vol. 23, no. 31n32, pp. 3893–3896, Dec. 2009, doi: 10.1142/S021798490902196X.
[29] Y. Yamakoshi, H. Miyashita, and K. Seki, "Sputtering target and method for manufacturing thereof," US6153315A, Nov. 28, 2000 Accessed: Sep. 20, 2020. [Online]. Available: https://patents.google.com/patent/US6153315A/en
[30] A. Lores, N. Azurmendi, I. Agote, E. Espinosa, and M. B. García-Blanco, "A study of parameter and post-processing effects on surface quality improvement of Binder Jet 3D-printed Invar36 alloy parts," *Prog. Addit. Manuf.*, Feb. 2022, doi: 10.1007/s40964-022-00267-w.

[31] "(3) (PDF) On the target surface cleanness during magnetron sputtering," *ResearchGate*. https://www.researchgate.net/publication/282629411_On_the_target_surface_cleanness_during_magnetron_sputtering (accessed Sep. 27, 2020).
[32] C.-F. Lo and P. Gilman, "Particle generation in W–Ti deposition," *J. Vac. Sci. Technol. A*, vol. 17, no. 2, pp. 608–610, Mar. 1999, doi: 10.1116/1.581625.
[33] Y. Narizuka, M. Ishino, A. Kenmotsu, Y. Chiba, and A. Hiraki, "Sputtering target," US5320729A, Jun. 14, 1994 Accessed: Sep. 25, 2020. [Online]. Available: https://patents.google.com/patent/US5320729A/en
[34] "Nodule Formation on Magnetron Sputtering Targets – Vacuum Coating .info – VCi." /nodule-formation-on-magnetron-sputtering-targets (accessed Sep. 20, 2020).
[35] "Gas-Phase Synthesis of Nanoparticles: present status and perspectives. - Abstract - Europe PMC." https://europepmc.org/article/PMC/6173303 (accessed Dec. 19, 2019).
[36] G. Bräuer, B. Szyszka, M. Vergöhl, and R. Bandorf, "Magnetron sputtering – Milestones of 30 years," *Vacuum*, vol. 84, no. 12, pp. 1354–1359, Jun. 2010, doi: 10.1016/j.vacuum.2009.12.014.
[37] T. Iseki, "Completely flat erosion magnetron sputtering using a rotating asymmetrical yoke magnet," *Vacuum*, vol. 84, no. 12, pp. 1372–1376, Jun. 2010, doi: 10.1016/j.vacuum.2010.01.008.
[38] V. Gorshanov, "Modeling of magnetic field distribution and optimization of a magnetron for magnetron sputtering technology," 2019, Accessed: Dec. 11, 2019. [Online]. Available: https://lutpub.lut.fi/handle/10024/159597
[39] R. Kukla, T. Krug, R. Ludwig, and K. Wilmes, "A highest rate self-sputtering magnetron source," *Vacuum*, vol. 41, no. 7, pp. 1968–1970, Jan. 1990, doi: 10.1016/0042-207X(90)94147-I.
[40] C. B. Garrett, "Planar magnetron sputtering device," US4444643A, Apr. 24, 1984 Accessed: Sep. 20, 2020. [Online]. Available: https://patents.google.com/patent/US4444643A/en
[41] L. T. L. Jr, "Sputter target for use in a sputter coating source," US4457825A, Jul. 03, 1984 Accessed: Sep. 20, 2020. [Online]. Available: https://patents.google.com/patent/US4457825A/en
[42] W. H. Class and J. F. Smith, "Magnetron cathode and method for sputter coating," US4842703A, Jun. 27, 1989 Accessed: Oct. 10, 2020. [Online]. Available: https://patents.google.com/patent/US4842703A/en
[43] H. B. Wang, C. Liu, Y. C. Lei, and W. Cai, "Characterization of Ni55.6Mn11.4Fe7.4Ga25.6 high temperature shape memory alloy thin film," *J. Alloys Compd.*, vol. 465, no. 1, pp. 458–461, Oct. 2008, doi: 10.1016/j.jallcom.2007.10.136.
[44] T. W. Scharf, A. Rajendran, R. Banerjee, and F. Sequeda, "Growth, structure and friction behavior of titanium doped tungsten disulphide (Ti-WS2) nanocomposite thin films," *Thin Solid Films*, vol. 517, no. 19, pp. 5666–5675, Aug. 2009, doi: 10.1016/j.tsf.2009.02.103.
[45] J.-A. Jeong and H.-K. Kim, "Transparent Ga and Zn co-doped In2O3 electrode prepared by co-sputtering of Ga:In2O3 and Zn:In2O3 targets at room temperature," *Thin Solid Films*, vol. 519, no. 10, pp. 3276–3282, Mar. 2011, doi: 10.1016/j.tsf.2010.12.034.
[46] P. Zhang, X. Zheng, S. Wu, J. Liu, and D. He, "Kinetic Monte Carlo simulation of Cu thin film growth," *Vacum*, vol. 72, no. 4, pp. 405–410, Jan. 2004, doi: 10.1016/j.vacuum.2003.08.013.

[47] R. Dannenberg, E. Stach, J. R. Groza, and B. J. Dresser, “TEM annealing study of normal grain growth in silver thin films,” *Thin Solid Films*, vol. 379, no. 1, pp. 133–138, Dec. 2000, doi: 10.1016/S0040-6090(00)01570-4.
[48] “Mean Free Path, Molecular Collisions.” http://hyperphysics.phy-astr.gsu.edu/hbase/Kinetic/menfre.html (accessed Feb. 22, 2022).
[49] J. C. Helmer and C. E. Wickersham, “Pressure effects in planar magnetron sputter deposition,” *J. Vac. Sci. Technol. Vac. Surf. Films*, vol. 4, no. 3, pp. 408–412, May 1986, doi: 10.1116/1.573892.
[50] F. X. Cheng, C. H. Jiang, and J. S. Wu, “Effect of sputtering input powers on CoSi2 thin films prepared by magnetron sputtering,” *Mater. Des.*, vol. 26, no. 4, pp. 369–372, Jun. 2005, doi: 10.1016/j.matdes.2004.06.004.
[51] H. Mahdhi, Z. Ben Ayadi, J. L. Gauffier, K. Djessas, and S. Alaya, “Effect of sputtering power on the electrical and optical properties of Ca-doped ZnO thin films sputtered from nanopowders compacted target,” *Opt. Mater.*, vol. 45, pp. 97–103, Jul. 2015, doi: 10.1016/j.optmat.2015.03.015.
[52] S.-H. Kim, Y.-L. Choi, Y.-S. Song, D. Y. Lee, and S.-J. Lee, “Influence of sputtering parameters on microstructure and morphology of TiO2 thin films,” *Mater. Lett.*, vol. 57, no. 2, pp. 343–348, Dec. 2002, doi: 10.1016/S0167-577X(02)00788-7.
[53] C. Zhou, T. Li, X. Wei, and B. Yan, “Effect of the Sputtering Power on the Structure, Morphology and Magnetic Properties of Fe Films,” *Metals*, vol. 10, no. 7, Art. no. 7, Jul. 2020, doi: 10.3390/met10070896.
[54] S. Yu, W. Xu, H. Zhu, W. Qiu, Q. Fu, and L. Kong, “Effect of sputtering power on structure and properties of ZTO films,” *J. Alloys Compd.*, vol. 883, p. 160622, Nov. 2021, doi: 10.1016/j.jallcom.2021.160622.
[55] K. Ullakko, J. K. Huang, C. Kantner, R. C. O’Handley, and V. V. Kokorin, “Large magnetic-field-induced strains in Ni2MnGa single crystals,” *Appl. Phys. Lett.*, vol. 69, no. 13, pp. 1966–1968, Sep. 1996, doi: 10.1063/1.117637.
[56] A. Sozinov, N. Lanska, A. Soroka, and W. Zou, “12% magnetic field-induced strain in Ni-Mn-Ga-based non-modulated martensite,” *Appl. Phys. Lett.*, vol. 102, no. 2, p. 021902, Jan. 2013, doi: 10.1063/1.4775677.
[57] A. Hobza, C. L. Patrick, K. Ullakko, N. Rafla, P. Lindquist, and P. Müllner, “Sensing strain with Ni-Mn-Ga,” *Sens. Actuators Phys.*, vol. 269, pp. 137–144, Jan. 2018, doi: 10.1016/j.sna.2017.11.002.
[58] A. R. Smith, J. Tellinen, and K. Ullakko, “Rapid actuation and response of Ni–Mn–Ga to magnetic-field-induced stress,” *Acta Mater.*, vol. 80, pp. 373–379, Nov. 2014, doi: 10.1016/j.actamat.2014.06.054.
[59] X. H. Tian, J. H. Sui, X. Zhang, X. Feng, and W. Cai, “Martensitic transformation, mechanical property and magnetic-field-induced strain of Ni–Mn–Ga alloy fabricated by spark plasma sintering,” *J. Alloys Compd.*, vol. 509, no. 10, pp. 4081–4083, Mar. 2011, doi: 10.1016/j.jallcom.2011.01.001.
[60] X. Jin, M. Marioni, D. Bono, S. M. Allen, R. C. O’Handley, and T. Y. Hsu, “Empirical mapping of Ni–Mn–Ga properties with composition and valence electron concentration,” *J. Appl. Phys.*, vol. 91, no. 10, pp. 8222–8224, May 2002, doi: 10.1063/1.1453943.
[61] V. Chernenko, E. Cesari, V. V. Kokorin, and I. N. Vitenko, “The Development of New Ferromagnetic Shape Memory Alloys in Ni-Mn-Ga System,” *Scr. Metall. Mater.*, vol. 33, pp. 1239–1244, Oct. 1995, doi: 10.1016/0956-716X(95)00370-B.

[62] K. Tsuchiya, A. Ohashi, D. Ohtoyo, H. Nakayama, M. Umemoto, and P. G. McCormick, "Phase Transformations and Magnetostriction in Ni–Mn–Ga Ferromagnetic Shape Memory Alloys," *Mater. Trans. JIM*, vol. 41, no. 8, pp. 938–942, 2000, doi: 10.2320/matertrans1989.41.938.
[63] L. Zhou, M. M. Schneider, A. Giri, K. Cho, and Y. Sohn, "Microstructural and crystallographic characteristics of modulated martensite, non-modulated martensite, and pre-martensitic tweed austenite in Ni-Mn-Ga alloys," *Acta Mater.*, vol. 134, pp. 93–103, Aug. 2017, doi: 10.1016/j.actamat.2017.05.050.
[64] Y. Zhang, M. Li, Y.D. Wang, J.P. Lin, K.A. Dahmen, Z.L. Wang, and P.K. Liaw, "Superelasticity and Serration Behavior in Small-Sized NiMnGa Alloys," *Adv. Eng. Mater.*, vol. 16, no. 8, pp. 955–960, 2014, doi: https://doi.org/10.1002/adem.201300518.
[65] A. K. Panda, M. Ghosh, A. Kumar, and A. Mitra, "Magnetic transitions and structure of a NiMnGa ferromagnetic shape memory alloy prepared by melt spinning technique," *J. Magn. Magn. Mater.*, vol. 320, no. 17, pp. L116–L120, Sep. 2008, doi: 10.1016/j.jmmm.2008.03.055.
[66] U. Gaitzsch, C. Hurrich, M. Potschke, F. Thoss, A. Bohm, S. Roth, B. Rellinghaus, and L. Schultz, *Properties of polycrystalline NiMnGa alloys for application as magneto-mechanic actuator*. 2008.
[67] Z. Li, B. Yang, N. Zou, Y. Zhang, C. Esling, W. Gan, X. Zhao, and L. Zou "Crystallographic Characterization on Polycrystalline Ni-Mn-Ga Alloys with Strong Preferred Orientation," *Materials*, vol. 10, no. 5, p. 463, May 2017, doi: 10.3390/ma10050463.
[68] P. Sratong-on, V. A. Chernenko, J. Feuchtwanger, and H. Hosoda, "Magnetic field-induced rubber-like behavior in Ni-Mn-Ga particles/polymer composite," *Sci. Rep.*, vol. 9, no. 1, Art. no. 1, Mar. 2019, doi: 10.1038/s41598-019-40189-2.
[69] A. Annadurai, A.K. Nandakumar, S. Jayakumar, M.D. Kannan, M.M. Raja, S. Bysak, R. Gopalan, and V. Chandrasekaran "Composition, structure and magnetic properties of sputter deposited Ni–Mn–Ga ferromagnetic shape memory thin films," *J. Magn. Magn. Mater.*, vol. 321, no. 6, pp. 630–634, Mar. 2009, doi: 10.1016/j.jmmm.2008.10.015.
[70] A. Hakola, O. Heczko, A. Jaakkola, T. Kajava, and K. Ullakko, "Pulsed laser deposition of NiMnGa thin films on silicon," *Appl. Phys. A*, vol. 79, no. 4, pp. 1505–1508, Sep. 2004, doi: 10.1007/s00339-004-2831-7.
[71] P. G. Tello, F.J. Castano, R.C. O'Handley, and S.M. Allen "Ni–Mn–Ga thin films produced by pulsed laser deposition," *J. Appl. Phys.*, vol. 91, no. 10, pp. 8234–8236, May 2002, doi: 10.1063/1.1452222.
[72] B. Nelson-Cheeseman, R. O'Handley, C. Ross, C. Redondo, and F. Castano, "Structure and Thermomagnetic Properties of Polycrystalline Ni–Mn–Ga Thin Films," *J. Appl. Phys.*, vol. 93, pp. 8492–8494, May 2003, doi: 10.1063/1.1555976.
[73] T. J. Zhu, L. Lu, M. O. Lai, and J. Ding, "Growth and magnetic properties of NiMnGa thin films prepared by pulsed laser ablation," *Smart Mater. Struct.*, vol. 14, no. 5, pp. S293–S296, Oct. 2005, doi: 10.1088/0964-1726/14/5/018.
[74] J. W. Dong, L. C. Chen, C. J. Palmstro/m, R. D. James, and S. McKernan, "Molecular beam epitaxy growth of ferromagnetic single crystal (001) Ni2MnGa on (001) GaAs," *Appl. Phys. Lett.*, vol. 75, no. 10, pp. 1443–1445, Aug. 1999, doi: 10.1063/1.125009.

[75] J. Dubowik, I. Gościańska, Y. V. Kudryavtsev, Y. P. Lee, P. Sovák, and M. Konĉ, "Magnetic properties of Ni-Mn-Ga Heusler alloy films," *Phys. Status Solidi C*, vol. 3, no. 1, pp. 143–146, 2006, doi: 10.1002/pssc.200562465.

[76] Jae-Pyoung Ahn, Ning Cheng, T. Lograsso, and K. M. Krishnan, "Magnetic properties, structure and shape-memory transitions in Ni-Mn-Ga thin films grown by ion-beam sputtering," *IEEE Trans. Magn.*, vol. 37, no. 4, pp. 2141–2143, Jul. 2001, doi: 10.1109/20.951103.

[77] S. R. Yeduru, A. Backen, S. Fähler, L. Schultz, and M. Kohl, "Transformation behaviour of freestanding epitaxial Ni–Mn–Ga films," *J. Alloys Compd.*, vol. 577, pp. S353–S357, Nov. 2013, doi: 10.1016/j.jallcom.2012.02.151.

[78] A. Backen, S.R. Yeduru, M. Kohl, S. Baunack, A. Diestel, B. Holzapfel, L. Schultz, and S. Fähler ,"Comparing properties of substrate-constrained and freestanding epitaxial Ni–Mn–Ga films," *Acta Mater.*, vol. 58, no. 9, pp. 3415–3421, May 2010, doi: 10.1016/j.actamat.2010.02.016.

[79] A. Sharma, S. Mohan, and S. Suwas, "The effect of the deposition rate on the crystallographic texture, microstructure evolution and magnetic properties in sputter deposited Ni-Mn-Ga thin films," *Thin Solid Films*, vol. 616, pp. 530–542, Oct. 2016, doi: 10.1016/j.tsf.2016.08.033.

[80] B. Yang, Y. Zhang, Z. Li, G. Qin, X. Zhao, C. Esling, and L. Zuo, "Insight into variant selection of seven-layer modulated martensite in Ni–Mn–Ga thin films grown on MgO(001) substrate," *Acta Mater.*, vol. 93, pp. 205–217, Jul. 2015, doi: 10.1016/j.actamat.2015.04.024.

[81] S. Vinodh Kumar, M. Mahendran, M. Manivel Raja, V. L. Niranjani, and P. K. Mukhopadhyay, "Phase structure evolution on Ni-Mn-Ga/Si (100) thin films: Effect of substrate temperature," *Intermetallics*, vol. 101, pp. 18–26, Oct. 2018, doi: 10.1016/j.intermet.2018.07.006.

[82] D. H. Zhang, T. L. Yang, J. Ma, Q. P. Wang, R. W. Gao, and H. L. Ma, "Preparation of transparent conducting ZnO:Al films on polymer substrates by r. f. magnetron sputtering," *Appl. Surf. Sci.*, vol. 158, no. 1, pp. 43–48, May 2000, doi: 10.1016/S0169-4332(99)00591-7.

[83] J. Buschbeck, R. Niemann, O. Heczko, M. Thomas, L. Schultz, and S. Fähler, "In situ studies of the martensitic transformation in epitaxial Ni–Mn–Ga films," *Acta Mater.*, vol. 57, no. 8, pp. 2516–2526, May 2009, doi: 10.1016/j.actamat.2009.02.008.

[84] M. Schmitt, M. Ohtsuka, and M. Kohl, "Electron beam lithography of Free-Standing Ni–Mn–Ga films," *Phys. Procedia*, vol. 10, pp. 174–181, Jan. 2010, doi: 10.1016/j.phpro.2010.11.095.

[85] S. K. Wu, K. H. Tseng, and J. Y. Wang, "Crystallization behavior of r.f.-sputtered near stoichiometric Ni2MnGa thin films," *Thin Solid Films*, vol. 408, no. 1, pp. 316–320, Apr. 2002, doi: 10.1016/S0040-6090(02)00134-7.

[86] F. Bernard, P. Delobelle, C. Rousselot, and L. Hirsinger, "Microstructural, mechanical and magnetic properties of shape memory alloy Ni55Mn23Ga22 thin films deposited by radio-frequency magnetron sputtering," *Thin Solid Films*, vol. 518, no. 1, pp. 399–412, Nov. 2009, doi: 10.1016/j.tsf.2009.06.037.

[87] C. Liu, W. Cai, X. An, L. X. Gao, Z. Y. Gao, and L. C. Zhao, "Preparation and characterization of Ni–Mn–Ga high temperature shape memory alloy thin films using rf

magnetron sputtering method," *Mater. Sci. Eng. A*, vol. 438–440, pp. 986–989, Nov. 2006, doi: 10.1016/j.msea.2006.01.115.

[88] V. A. Chernenko, M. Ohtsuka, M. Kohl, V. V. Khovailo, and T. Takagi, "Transformation behavior of Ni–Mn–Ga thin films," *Smart Mater. Struct.*, vol. 14, no. 5, pp. S245–S252, Aug. 2005, doi: 10.1088/0964-1726/14/5/012.

[89] J. Tillier, D. Bourgault, S. Pairis, L. Ortega, N. Caillault, and L. Carbone, "Martensite structures and twinning in substrate-constrained epitaxial Ni–Mn–Ga films deposited by a magnetron co-sputtering process," *Phys. Procedia*, vol. 10, pp. 168–173, Jan. 2010, doi: 10.1016/j.phpro.2010.11.094.

[90] A. Belkind, J. Felts, and M. McBride, "Sputtering and Co-sputtering of Optical Coatings using a C-MAG^{TM} Rotatable Cylindrical Cathode," p. 5.

[91] I. Takeuchi, O.O. Famodu, J.C. Read, M.A. Aronova, K.S. Chang, C. Cracuinescu, S.E. Lofland, M. Wuttig, F.C. Wellstood, L. Knauss, and A. Orozco, "Identification of novel compositions of ferromagnetic shape-memory alloys using composition spreads," *Nat. Mater.*, vol. 2, no. 3, pp. 180–184, Mar. 2003, doi: 10.1038/nmat829.

[92] S. Shevyrtalov, H. Miki, M. Ohtsuka, V. Khovaylo, and V. Rodionova, "The evolution of martensitic transformation in Ni-Mn-Ga/Al2O3 polycrystalline 100-nm – 2-μm films with Ni- and Ga-excess," *J. Alloys Compd.*, vol. 767, pp. 538–543, Oct. 2018, doi: 10.1016/j.jallcom.2018.07.144.

[93] I. R. Aseguinolaza, V. Golub, O.Y. salyuk, B. Muntifering, W.B. Knowlton, P. Mullner, J.M. Barandiarán, and V. A. Chernenko, "Self-patterning of epitaxial Ni–Mn–Ga/MgO(001) thin films," *Acta Mater.*, vol. 111, pp. 194–201, Jun. 2016, doi: 10.1016/j.actamat.2016.03.065.

[94] P. Ranzieri, S. Fabbrici, L. Nasi, L. Righi, F. Casoli, V. A. Chernenko, E. Villa, and F. Albertini, "Epitaxial Ni–Mn–Ga/MgO(100) thin films ranging in thickness from 10 to 100nm," *Acta Mater.*, vol. 61, no. 1, pp. 263–272, Jan. 2013, doi: 10.1016/j.actamat.2012.09.056.

[95] B. Yang, Z.B. Li, Y.D. Zhang, G.W. Qin, X. Zhao, O. Perroud, C. Esling, and L. Zuo, "Microstructural features and orientation correlations of non-modulated martensite in Ni–Mn–Ga epitaxial thin films," *Acta Mater.*, vol. 61, no. 18, pp. 6809–6820, Oct. 2013, doi: 10.1016/j.actamat.2013.07.055.

[96] I. R. Aseguinolaza, I. Orue, A. V. Svalov, V. A. Chernenko, S. Besseghini, and J. M. Barandiarán, "Fabrication conditions and transformation behavior of epitaxial Ni–Mn–Ga thin films," *J. Mater. Sci.*, vol. 47, no. 8, pp. 3658–3662, Apr. 2012, doi: 10.1007/s10853-011-6212-2.

[97] S. Shevyrtalov, H. Miki, M. Ohtsuka, A. Grunin, I. Lyatun, A. Mashirov, M. Seredina, V. Khovaylo, and V. Rodionova, "Martensitic transformation in polycrystalline substrate-constrained and freestanding Ni-Mn-Ga films with Ni and Ga excess," *J. Alloys Compd.*, vol. 741, pp. 1098–1104, Apr. 2018, doi: 10.1016/j.jallcom.2018.01.255.

[98] I. R. Aseguinolaza, I. Reyes-Salazar, A. V. Svalov, K. Wilson, E. Villa, W.B. Knowlton, P. Mullner, J.M. Barandiarán, and V. A. Chernenko, "Transformation volume strain in Ni-Mn-Ga thin films," *Appl. Phys. Lett.*, vol. 101, no. 24, p. 241912, Dec. 2012, doi: 10.1063/1.4772005.

[99] S. Doyle, V. A. Chernenko, S. Besseghini, A. Gambardella, M. Kohl, P. Müllner, and M. Ohtsuka, "Residual stress in Ni-Mn-Ga thin films deposited on different substrates," *Eur.

Phys. J. Spec. Top., vol. 158, no. 1, pp. 99–105, May 2008, doi: 10.1140/epjst/e2008-00660-8.

[100] N. Jetta, N. Ozdemir, S. Rios, D. Bufford, I. Karaman, and X. Zhang, "Phase transformations in sputtered Ni–Mn–Ga magnetic shape memory alloy thin films," *Thin Solid Films*, vol. 520, no. 9, pp. 3433–3439, Feb. 2012, doi: 10.1016/j.tsf.2011.12.029.

[101] S. V. Kumar, R. K. Singh, M. M. Raja, A. Kumar, S. Bysakh, and M. Mahendran, "Microstructure and nanomechanical properties of Mn-rich Ni–Mn–Ga thin films," *Intermetallics*, vol. C, no. 71, pp. 57–64, 2016, doi: 10.1016/j.intermet.2015.12.012.

[102] R. Xie, S.-L. Tang, Y.-M. Tang, X.-C. Liu, T. Tang, and Y.-W. Du, "Transformation behaviors, structural and magnetic characteristics of Ni—Mn—Ga films on MgO (001)," *Chin. Phys. B*, vol. 22, no. 10, p. 107502, Oct. 2013, doi: 10.1088/1674-1056/22/10/107502.

[103] K. Wasa, *Handbook of Sputter Deposition Technology: Fundamentals and Applications for Functional Thin Films, Nano-Materials and MEMS*. William Andrew, 2012.

[104] J. W. Gardner, V. K. Varadan, and O. O. Awadelkarim, *Microsensors, MEMS, and Smart Devices*, 1st ed. Wiley, 2001. doi: 10.1002/9780470846087.

[105] M. R. J. Gibbs, E. W. Hill, and P. J. Wright, "Magnetic materials for MEMS applications," *J. Phys. D: Appl. Phys.*, vol. 37, no. 22, pp. R237–R244, Oct. 2004, doi: 10.1088/0022-3727/37/22/R01.

[106] D. C. Lagoudas, Ed., *Shape Memory Alloys: Modeling and Engineering Applications*, 2008th Edition. New York, NY: Springer, 2008.

[107] M. Kohl, S. R. Yeduru, F. Khelfaoui, B. Krevet, T. Eichhorn, A. Backen, S. Fähler, G. Jakob, and A. Mecklenburg,"Recent Progress in FSMA Microactuator Developments," *Mater. Sci. Forum*, vol. 635, pp. 145–154, Dec. 2009, doi: 10.4028/www.scientific.net/MSF.635.145.

[108] M. Kohl, M. Gueltig, V. Pinneker, R. Yin, F. Wendler, and B. Krevet, "Magnetic Shape Memory Microactuators," *Micromachines*, vol. 5, no. 4, Art. no. 4, Dec. 2014, doi: 10.3390/mi5041135.

[109] D. S. Gardner, J. D. Meindl, and K. C. Saraswat, "Interconnection and electromigration scaling theory," *IEEE Trans. Electron Devices*, vol. 34, no. 3, pp. 633–643, Mar. 1987, doi: 10.1109/T-ED.1987.22974.

[110] P. B. Ghate, "Electromigration-Induced Failures in VLSI Interconnects," in *20th International Reliability Physics Symposium*, San Diego, NV, USa, Mar. 1982, pp. 292–299. doi: 10.1109/IRPS.1982.361948.

[111] D. C. Edelstein, G. A. Sai-Halasz, and Y.-J. Mii, "VLSI on-chip interconnection performance simulations and measurements," *IBM J. Res. Dev.*, vol. 39, no. 4, pp. 383–401, Jul. 1995, doi: 10.1147/rd.394.0383.

[112] P.-L. Pai and C. H. Ting, "Copper as the future interconnection material," in *Proceedings., Sixth International IEEE VLSI Multilevel Interconnection Conference*, Jun. 1989, pp. 258–264. doi: 10.1109/VMIC.1989.78029.

[113] C. C. Patterson, "Native Copper, Silver, and Gold Accessible to Early Metallurgists," *Am. Antiq.*, vol. 36, no. 3, pp. 286–321, 1971, doi: 10.2307/277716.

[114] B. Ramamoorthy, "An Investigation into the Adhesion Strength of Diamond Like Carbon Multilayer Coating (DLC/TiN/Ti/Cu/Ni)," *Intell. Inf. Manag.*, vol. 01, no. 03, pp. 179–194, 2009, doi: 10.4236/iim.2009.13027.

[115] I.-L. Velicu, V. Tiron, B.-G. Rusu, and G. Popa, “Copper thin films deposited under different power delivery modes and magnetron configurations: A comparative study,” *Surf. Coat. Technol.*, vol. 327, pp. 192–199, Oct. 2017, doi: 10.1016/j.surfcoat.2016.11.001.

[116] D. Desideri, T. Cavallin, A. Maschio, and M. Natali, “Characterisation of copper thin films deposited on machinable glass–ceramic and glass by DC magnetron sputtering,” *IET Sci. Meas. Technol.*, vol. 8, no. 1, pp. 1–8, 2014, doi: 10.1049/iet-smt.2012.0049.

[117] A. Arman, Ş. Ţălu, C. Luna, A. Ahmadpourian, M. Naseri, and M. Molamohammadi, “Micromorphology characterization of copper thin films by AFM and fractal analysis,” *J. Mater. Sci. Mater. Electron.*, vol. 26, no. 12, pp. 9630–9639, Dec. 2015, doi: 10.1007/s10854-015-3628-5.

[118] H. Huang, H. L. Wei, C. H. Woo, and X. X. Zhang, “Copper thin film of alternating textures,” *Appl. Phys. Lett.*, vol. 82, no. 24, pp. 4265–4267, Jun. 2003, doi: 10.1063/1.1583866.

[119] W. L. Prater, E.L. Allen, W.Y. Lee, M.F. Toney, A. Kellock, J.S. Daniels, J.A. Hedstrom, and T. Harrell, “Microstructural comparisons of ultrathin Cu films deposited by ion-beam and dc-magnetron sputtering,” *J. Appl. Phys.*, vol. 97, no. 9, p. 093301, May 2005, doi: 10.1063/1.1886275.

[120] A. Hojabri, F. Hajakbari, M. A. Moghri Moazzen, and S. Kadkhodaei, “Effect of Thickness on Properties of Copper Thin Films Growth on Glass by DC Planar Magnetron Sputtering,” *J. Nanostructures*, vol. 2, no. 1, pp. 107–112, Mar. 2012, doi: 10.7508/jns.2012.01.013.

[121] K.-Y. Chan, T.-Y. Tou, and B.-S. Teo, “Thickness dependence of the structural and electrical properties of copper films deposited by dc magnetron sputtering technique,” *Microelectron. J.*, vol. 37, no. 7, pp. 608–612, Jul. 2006, doi: 10.1016/j.mejo.2005.09.016.

[122] J.-H. Boo, M. J. Jung, H. K. Park, K. H. Nam, and J. G. Han, “High-rate deposition of copper thin films using newly designed high-power magnetron sputtering source,” *Surf. Coat. Technol.*, vol. 188–189, pp. 721–727, Nov. 2004, doi: 10.1016/j.surfcoat.2004.07.005.

[123] A. U. Mane and S. A. Shivashankar, “Growth of (111)-textured copper thin films by atomic layer deposition,” *J. Cryst. Growth*, vol. 275, no. 1, pp. e1253–e1257, Feb. 2005, doi: 10.1016/j.jcrysgro.2004.11.143.

[124] I. A. Rauf, R. Siemsen, M. Grunwell, R. F. Egerton, and M. Sayer, “Gas-phase nucleation during chemical vapor deposition of copper films and its effect on the resistivity of deposited films,” *J. Mater. Res.*, vol. 14, no. 11, pp. 4345–4350, Nov. 1999, doi: 10.1557/JMR.1999.0588.

[125] A. A. Solovyev, V. A. Semenov, V. O. Oskirko, K. V. Oskomov, A. N. Zakharov, and S. V. Rabotkin, “Properties of ultra-thin Cu films grown by high power pulsed magnetron sputtering,” *Thin Solid Films*, vol. 631, pp. 72–79, Jun. 2017, doi: 10.1016/j.tsf.2017.04.005.

[126] F. Cemin, D. Lundin, D. Cammilleri, T. Maroutian, P. Lecoeur, and T. Minea, “Low electrical resistivity in thin and ultrathin copper layers grown by high power impulse magnetron sputtering,” *J. Vac. Sci. Technol. A*, vol. 34, no. 5, p. 051506, Sep. 2016, doi: 10.1116/1.4959555.

[127] B. Giroire, M.A. Ahmad, G. Aubert, L. Teule-Gay, D. Michau, J.J. Watkins, C. Aymonier, and A. Poulon-Quintin, “A comparative study of copper thin films deposited using

magnetron sputtering and supercritical fluid deposition techniques," *Thin Solid Films*, vol. 643, pp. 53–59, Dec. 2017, doi: 10.1016/j.tsf.2017.09.002.

[128] J. T. Wetzel, D. A. Smith, and G. Appleby-Mougham, "The Microstructure of Copper Films Deposited by E-Beam Evaporation onto Thin Polyimide Films," *MRS Proc.*, vol. 40, p. 271, 1984, doi: 10.1557/PROC-40-271.

[129] R. A. Roy, J. J. Cuomo, and D. S. Yee, "Control of microstructure and properties of copper films using ion-assisted deposition," *J. Vac. Sci. Technol. A*, vol. 6, no. 3, pp. 1621–1626, May 1988, doi: 10.1116/1.575339.

[130] J.-H. Cho, Y.-M. Jin, D.-Y. Park, H.-J. Kim, I.-H. Oh, and K.-A. Lee, "Manufacture and properties of cold spray deposited large thickness Cu coating material for sputtering target," *Met. Mater. Int.*, vol. 17, no. 1, pp. 157–166, Feb. 2011, doi: 10.1007/s12540-011-0222-0.

[131] V. Pavate, S. Ramaswami, M. Abburi, and M. Narasimhan, "Copper target for sputter deposition," 6139701, Oct. 31, 2000 Accessed: May 02, 2021. [Online]. Available: https://www.freepatentsonline.com/6139701.html

[132] A. Fukushima and S. Tsukamoto, "Deep-pot-shaped copper sputtering target and process for producing the same," EP2123790A1, Nov. 25, 2009 Accessed: May 02, 2021. [Online]. Available: https://patents.google.com/patent/EP2123790A1/en

[133] C. A. Michaluk, S. Yuan, and J. D. M. Jr, "Powder metallurgy sputtering targets and methods of producing same," US8168118B2, May 01, 2012 Accessed: May 02, 2021. [Online]. Available: https://patents.google.com/patent/US8168118B2/en

[134] A. Perry and P. Gilman, "Ultrafine-grain-copper-base sputter targets," US20050133125A1, Jun. 23, 2005 Accessed: May 03, 2021. [Online]. Available: https://patents.google.com/patent/US20050133125/en

[135] V. Segal, W. Yi, S. Ferrasse, C. Wu, S. Strothers, F. Alford, and W. Willett, "Copper sputtering targets and methods of forming copper sputtering targets," WO2004011691A1, Feb. 05, 2004 Accessed: May 02, 2021. [Online]. Available: https://patents.google.com/patent/WO2004011691A1/en

[136] J. K. Kardokus, "Method of making high purity copper sputtering targets," US5803342A, Sep. 08, 1998 Accessed: Nov. 23, 2021. [Online]. Available: https://patents.google.com/patent/US5803342A/en

[137] A. Fukushima and S. Tsukamoto, "Pot-shaped copper sputtering target and manufacturing method thereof," US8728255B2, May 20, 2014 Accessed: May 02, 2021. [Online]. Available: https://patents.google.com/patent/US8728255B2/en

[138] J. Yang, Y. Huang, and K. Xu, "Effect of substrate on surface morphology evolution of Cu thin films deposited by magnetron sputtering," *Surf. Coat. Technol.*, vol. 201, no. 9, pp. 5574–5577, Feb. 2007, doi: 10.1016/j.surfcoat.2006.07.227.

[139] N. Promros, P. Sittimart, N. Patanoo, S. Kongnithichalerm, M. Horprathum, W. Bhathumnavin, and B. Paosawatyanyong, "Physical Properties of Copper Films Deposited by Compact-Size Magnetron Sputtering Source with Changing Magnetic Field Strength," *Key Eng. Mater.*, vol. 675–676, pp. 193–196, Jan. 2016, doi: 10.4028/www.scientific.net/KEM.675-676.193.

[140] M.-T. Le, Y.-U. Sohn, J.-W. Lim, and G.-S. Choi, "Effect of Sputtering Power on the Nucleation and Growth of Cu Films Deposited by Magnetron Sputtering," *Mater. Trans.*, vol. 51, no. 1, pp. 116–120, 2010, doi: 10.2320/matertrans.M2009183.

[141] O. Anderoglu, A. Misra, H. Wang, and X. Zhang, "Thermal stability of sputtered Cu films with nanoscale growth twins," *J. Appl. Phys.*, vol. 103, no. 9, p. 094322, May 2008, doi: 10.1063/1.2913322.

[142] S. Simões, R. Calinas, M. T. Vieira, M. F. Vieira, and P. J. Ferreira, "In situTEM study of grain growth in nanocrystalline copper thin films," *Nanotechnology*, vol. 21, no. 14, p. 145701, Mar. 2010, doi: 10.1088/0957-4484/21/14/145701.

[143] E. M. Zielinski, R. P. Vinci, and J. C. Bravman, "The Influence of Strain Energy Minimization on Abnormal Grain Growth in Copper Thin Films," *MRS Online Proc. Libr. OPL*, vol. 391, ed 1995, doi: 10.1557/PROC-391-103.

[144] H. L. Wei, H. Huang, C. H. Woo, R. K. Zheng, G. H. Wen, and X. X. Zhang, "Development of 〈110〉 texture in copper thin films," *Appl. Phys. Lett.*, vol. 80, no. 13, pp. 2290–2292, Mar. 2002, doi: 10.1063/1.1466518.

[145] K. Mech, R. Kowalik, and P. Żabiński, "Cu thin films deposited by DC Magnetron sputtering for contact surfaces on electronic components," *Arch. Metall. Mater.*, no. Vol. 56, iss. 4, pp. 903–908, 2011.

[146] A. Hojabri, N. Haghighian, K. Yasserian, and M. Ghoranneviss, "The effect of nitrogen plasma on copper thin film deposited by DC magnetron sputtering," *IOP Conf. Ser. Mater. Sci. Eng.*, vol. 12, p. 012004, Jun. 2010, doi: 10.1088/1757-899X/12/1/012004.

[147] K.-Y. Chan, P.-Q. Luo, Z.-B. Zhou, T.-Y. Tou, and B.-S. Teo, "Influence of direct current plasma magnetron sputtering parameters on the material characteristics of polycrystalline copper films," *Appl. Surf. Sci.*, vol. 255, no. 10, pp. 5186–5190, Mar. 2009, doi: 10.1016/j.apsusc.2008.09.072.

[148] Y.-S. Lee, S. Ha, J.-H. Park, and S.-B. Lee, "Structure-dependent mechanical behavior of copper thin films," *Mater. Charact.*, vol. 128, pp. 68–74, Jun. 2017, doi: 10.1016/j.matchar.2017.03.036.

[149] D. Beegan, S. Chowdhury, and M. T. Laugier, "Comparison between nanoindentation and scratch test hardness (scratch hardness) values of copper thin films on oxidised silicon substrates," *Surf. Coat. Technol.*, vol. 201, no. 12, pp. 5804–5808, Mar. 2007, doi: 10.1016/j.surfcoat.2006.10.031.

[150] T.-H. Fang and W.-J. Chang, "Nanomechanical properties of copper thin films on different substrates using the nanoindentation technique," *Microelectron. Eng.*, vol. 65, no. 1, pp. 231–238, Jan. 2003, doi: 10.1016/S0167-9317(02)00885-7.

[151] S. Craig and G. L. Harding, "Effects of argon pressure and substrate temperature on the structure and properties of sputtered copper films," *J. Vac. Sci. Technol.*, vol. 19, no. 2, pp. 205–215, Jul. 1981, doi: 10.1116/1.571105.

[152] K.-Y. Chan and B.-S. Teo, "Atomic force microscopy (AFM) and X-ray diffraction (XRD) investigations of copper thin films prepared by dc magnetron sputtering technique," *Microelectron. J.*, vol. 37, no. 10, pp. 1064–1071, Oct. 2006, doi: 10.1016/j.mejo.2006.04.008.

[153] J. Musil, A. J. Bell, and M. Čepera, "Deposition of copper films by unbalanced d.c. magnetron sputtering," *Czechoslov. J. Phys.*, vol. 45, no. 3, pp. 249–261, Mar. 1995, doi: 10.1007/BF01700266.

[154] K.-Y. Chan and B.-S. Teo, "Investigation into the influence of direct current (DC) power in the magnetron sputtering process on the copper crystallite size," *Microelectron. J.*, vol. 38, no. 1, pp. 60–62, Jan. 2007, doi: 10.1016/j.mejo.2006.09.011.

[155] G. A. Bleykher, A.O. Borduleva, A.V. Yuryeva, V.P. Krivobokov, , J. Lančok, J. Bulíř, J. Drahokoupil, L. Klimša, J. Kopeček, L. Fekete, R. Čtvrtlik, J. Tomaštik, "Features of copper coatings growth at high-rate deposition using magnetron sputtering systems with a liquid metal target," *Surf. Coat. Technol.*, vol. 324, pp. 111–120, Sep. 2017, doi: 10.1016/j.surfcoat.2017.05.065.

[156] S. Vaidya and A. K. Sinha, "Effect of texture and grain structure on electromigration in Al-0.5%Cu thin films," *Thin Solid Films*, vol. 75, no. 3, pp. 253–259, Jan. 1981, doi: 10.1016/0040-6090(81)90404-1.

[157] C. Cabral, J. M. E. Harper, K. Holloway, D. A. Smith, and R. G. Schad, "Preparation of low resistivity Cu–1 at. %Cr thin films by magnetron sputtering," *J. Vac. Sci. Technol. A*, vol. 10, no. 4, pp. 1706–1712, Jul. 1992, doi: 10.1116/1.577774.

[158] S. K. Mukherjee, L. Joshi, and P. K. Barhai, "A comparative study of nanocrystalline Cu film deposited using anodic vacuum arc and dc magnetron sputtering," *Surf. Coat. Technol.*, vol. 205, no. 19, pp. 4582–4595, Jun. 2011, doi: 10.1016/j.surfcoat.2011.03.119.

[159] A. F. Burnett and J. M. Cech, "Relationship of crystallographic orientation and impurities to stress, resistivity, and morphology for sputtered copper films," *J. Vac. Sci. Technol. A*, vol. 11, no. 6, pp. 2970–2974, Nov. 1993, doi: 10.1116/1.578677.

[160] J. W. Bae, J.-W. Lim, K. Mimura, and M. Isshiki, "Agglomeration of Copper Thin Film in Cu/Ta/Si Structure," *Mater. Trans.*, vol. 45, no. 3, pp. 877–879, 2004, doi: 10.2320/matertrans.45.877.

[161] J. R. Shi, S. P. Lau, Z. Sun, X. Shi, B. K. Tay, and H. S. Tan, "Structural and electrical properties of copper thin films prepared by filtered cathodic vacuum arc technique," *Surf. Coat. Technol.*, vol. 138, no. 2, pp. 250–255, Apr. 2001, doi: 10.1016/S0257-8972(00)01159-2.

[162] N. R. Baddoo, "Stainless steel in construction: A review of research, applications, challenges and opportunities," *J. Constr. Steel Res.*, vol. 64, no. 11, pp. 1199–1206, Nov. 2008, doi: 10.1016/j.jcsr.2008.07.011.

[163] L. Coudreuse, V. Ligier, J. P. Audouard, and P. Soulignac, "Lean Duplex Stainless Steel for Oil and Gas Applications," presented at the CORROSION 2003, Mar. 2003. Accessed: May 13, 2021. [Online]. Available: https://onepetro.org/NACECORR/proceedings/CORR03/All-CORR03/NACE-03529/114400

[164] Z. Liu, W. Gao, and Y. He, "Oxidation behaviour of nanocrystalline Fe–Ni–Cr–Al alloy coatings," *Mater. Sci. Technol.*, vol. 15, no. 12, pp. 1447–1450, Dec. 1999, doi: 10.1179/026708399101505446.

[165] J. Baranowska, S. Fryska, J. Przekop, and T. Suszko, "THE PROPERTIES OF HARD COATING COMPOSED OF s-PHASE OBTAINED BY PVD METHOD," p. 11.

[166] Z. Tao, X.-Q. Wang, M. K. Hassan, T.-Y. Song, and L.-A. Xie, "Behaviour of three types of stainless steel after exposure to elevated temperatures," *J. Constr. Steel Res.*, vol. 152, pp. 296–311, Jan. 2019, doi: 10.1016/j.jcsr.2018.02.020.

[167] T. Li, L. Liu, B. Zhang, Y. Li, X. Wang, and F. Wang, "Direct observation of thin membrane passive film over the growing pit on sputtered nanocrystalline austenitic stainless steel film," *Electrochem. Commun.*, vol. 52, pp. 80–84, Mar. 2015, doi: 10.1016/j.elecom.2015.01.013.

[168] M. Idiri, B. Boubeker, R. Sabot, P. Goudeau, J.-F. Dinhut, and J.-L. Grosseau-Poussard, "Structure and related corrosion behaviour in 1M H2SO4 of b.c.c. 304L films prepared by

ion beam sputtering," *Surf. Coat. Technol.*, vol. 122, no. 2, pp. 230–234, Dec. 1999, doi: 10.1016/S0257-8972(99)00303-5.
[169] I. Machado, P. Carvalho, and A. Padilha, "Austenite instability and precipitation behavior of high nitrogen stainless steels," 2015, pp. 1–36.
[170] P. J. Grundy and J. M. Marsh, "Amorphous thin films of stainless steel," *J. Mater. Sci.*, vol. 13, no. 3, pp. 677–681, Mar. 1978, doi: 10.1007/BF00541820.
[171] S. Fujimoto, H. Hayashida, and T. Shibata, "Extremely high corrosion resistance of thin film stainless steels deposited by ion beam sputtering," *Mater. Sci. Eng. A*, vol. 267, no. 2, pp. 314–318, Jul. 1999, doi: 10.1016/S0921-5093(99)00108-2.
[172] G. P, M. N, E. P, F. D, B. B, and B. B, "Structural and mechanical properties of stainless steel thin films elaborated by thermal evaporation and ion beam sputtering," *Mater. Sci. Forum*, vol. 426–4, pp. 3451–3456, 2003.
[173] R. B. Inturi and Z. Szklarska-Smialowska, "Localized Corrosion of Nanocrystalline 304 Type Stainless Steel Films," *CORROSION*, vol. 48, no. 5, pp. 398–403, May 1992, doi: 10.5006/1.3315951.
[174] M. P. Ryan, N. J. Laycock, H. S. Isaacs, and R. C. Newman, "Corrosion Pits in Thin Films of Stainless Steel," *J. Electrochem. Soc.*, vol. 146, no. 1, p. 91, Jan. 1999, doi: 10.1149/1.1391569.
[175] M. J. Godbole, A. J. Pedraza, L. F. Allard, and G. Geesey, "Characterization of sputter-deposited 316L stainless steel films," *J. Mater. Sci.*, vol. 27, no. 20, pp. 5585–5590, Oct. 1992, doi: 10.1007/BF00541627.
[176] S. R. Kappaganthu and Y. Sun, "Studies of structure and morphology of sputter-deposited stainless steel–nitrogen films," *Appl. Phys. A*, vol. 81, no. 4, pp. 737–744, Sep. 2005, doi: 10.1007/s00339-004-3144-6.
[177] M. J. Godbole, A. J. Pedraza, J. W. Park, and G. Geesey, "The crystal structures of stainless steel films sputter-deposited on austenitic stainless steel substrates," *Scr. Metall. Mater. U. S.*, vol. 28:10, May 1993, doi: 10.1016/0956-716X(93)90454-Z.
[178] J.-P. Eymery, N. Merakeb, Ph. Goudeau, A. Fnidiki, and B. Bouzabata, "A Mössbauer comparative study of the local environment in metastable 304 stainless steel films depending on the preparation mode," *J. Magn. Magn. Mater.*, vol. 256, no. 1, pp. 227–236, Jan. 2003, doi: 10.1016/S0304-8853(02)00487-0.
[179] N. Merakeb, A. Messai, and A. I. Ayesh, "Investigation of phase transformation for ferrite–austenite structure in stainless steel thin films," *Thin Solid Films*, vol. 606, pp. 120–126, May 2016, doi: 10.1016/j.tsf.2016.03.038.
[180] J. Koskinen, P. Torri, J.-P. Hirvonen, A. Mahiout, and A. Stanishevsky, "Arc discharge deposition of stainless steel coatings at different nitrogen pressures," *Surf. Coat. Technol.*, vol. 80, no. 1, pp. 57–60, Mar. 1996, doi: 10.1016/0257-8972(95)02685-1.
[181] K. Leinartas, M. Samulevičien≐, A. Bagdonas, R. Juškenas, and E. Juzeliūnas, "Structural and anticorrosive properties of magnetron-sputtered Fe–Cr–Ni and Fe–Cr–Ni–Ta alloy films," *Surf. Coat. Technol.*, vol. 168, no. 1, pp. 70–77, May 2003, doi: 10.1016/S0257-8972(03)00003-3.
[182] O.-H. Kwon, S.-H. Ahn, J.-G. Kim, and J.-G. Han, "An optimized condition for corrosion protection of type 316L films prepared by unbalanced magnetron sputtering in 3.5% NaCl solution," *J. Mater. Sci. Lett.*, vol. 21, no. 1, pp. 41–44, Jan. 2002, doi: 10.1023/A:1014286426768.

[183] S. Inoue, T. Saeki, H. Uchida, K. Koterazawa, and M. Iwasa, "Effects of ion flux on the properties of dc magnetron-sputtered stainless steel films," *Vacuum*, vol. 66, no. 3, pp. 257–261, Aug. 2002, doi: 10.1016/S0042-207X(02)00151-3.
[184] F.-S. Li, J.-J. Sun, and C. L. Chien, "^{57} Fe Mossbauer study of metastable 304 stainless steel film with BCC structure," *J. Phys. Condens. Matter*, vol. 7, no. 9, pp. 1921–1931, Feb. 1995, doi: 10.1088/0953-8984/7/9/016.
[185] X. Zhang, A. Misra, R. K. Schulze, C. J. Wetteland, H. Wang, and M. Nastasi, "Critical factors that determine face-centered cubic to body-centered cubic phase transformation in sputter-deposited austenitic stainless steel films," *J. Mater. Res.*, vol. 19, no. 6, pp. 1696–1702, Jun. 2004, doi: 10.1557/JMR.2004.0215.
[186] S. R. Kappaganthu and Y. Sun, "Formation of an MN-type cubic nitride phase in reactively sputtered stainless steel-nitrogen films," *J. Cryst. Growth*, vol. 267, no. 1, pp. 385–393, Jun. 2004, doi: 10.1016/j.jcrysgro.2004.03.066.
[187] N. Kaplan, H. Köçkar, A. Karpuz, H. Kuru, and M. Uçkun, "Ternary FeCrNi martensitic thin films sputtered on a flexible substrate from a single AISI 304 austenitic stainless steel source: Effect of deposition rate on structural and magnetic properties," *J. Magn. Magn. Mater.*, vol. 476, pp. 597–603, Apr. 2019, doi: 10.1016/j.jmmm.2018.12.094.
[188] M. V. F. Schroeder, A. A. C. Recco, and C. M. Garzón, "Tailoring the phase fractions by tuning the pulse frequency in stainless steel films obtained from an 316L target by pulsed-DC magnetron sputtering," *Mater. Lett.*, vol. 230, pp. 20–23, Nov. 2018, doi: 10.1016/j.matlet.2018.07.063.
[189] C. M. Garzón, G. A. Vergara, and A. A. C. Recco, "The effects of constrained atomic partitioning among FCC and BCC phases on nitrogen absorption in films that are reactively magnetron-sputtered from an 316L target," *Mater. Lett.*, vol. 206, pp. 34–38, Nov. 2017, doi: 10.1016/j.matlet.2017.06.074.
[190] K. L. Dahm and P. A. Dearnley, "On the nature, properties and wear response of s-phase (nitrogen-alloyed stainless steel) coatings on AISI 316L," *Proc. Inst. Mech. Eng. Part J. Mater. Des. Appl.*, vol. 214, no. 4, pp. 181–198, Oct. 2000, doi: 10.1177/146442070021400401.
[191] H. Buscail, S. El Messki, F. Riffard, S. Perrier, R. Cueff, and C. Issartel, "Role of molybdenum on the AISI 316L oxidation at 900 °C," *J. Mater. Sci.*, vol. 43, no. 21, pp. 6960–6966, Nov. 2008, doi: 10.1007/s10853-008-2965-7.
[192] A. J. Sedriks, "Corrosion resistance of austenitic Fe-Cr-Ni-Mo alloys in marine environments," *Int. Met. Rev.*, vol. 27, no. 1, pp. 321–353, Jan. 1982, doi: 10.1179/imr.1982.27.1.321.
[193] S. Malavasi, A. Oueldennaoua, M. Foos, and C. Frantz, "Metastable amorphous and crystalline (α,σ) phase in physical vapor deposited Fe–(Cr)–Ni–(C) deposits," *J. Vac. Sci. Technol. A*, vol. 5, no. 4, pp. 1888–1891, Jul. 1987, doi: 10.1116/1.574479.
[194] S. D. Dahlgren, "Equilibrium Phases in 304L Stainless Steel Obtained by Sputter-Deposition," *Metall. Trans.*, p. 5.
[195] A. Bourjot, M. Foos, and C. Frantz, "Basic properties of sputtered 310 stainless steel-nitrogen coatings," *Surf. Coat. Technol.*, vol. 43–44, pp. 533–542, Dec. 1990, doi: 10.1016/0257-8972(90)90104-K.
[196] A. Darbeïda, A. Saker, A. Billard, and J. von Stebut, "Optimization of the surface mechanical strength of AISI 316L physically vapour deposited nitrogen-doped coatings on

AISI 316L substrates," *Surf. Coat. Technol.*, vol. 60, no. 1, pp. 434–440, Oct. 1993, doi: 10.1016/0257-8972(93)90127-A.
[197] B. A. Shedden, F. N. Kaul, M. Samandi, and B. Window, "The role of energetic neutrals in reactive magnetron sputtering of nitrogen-doped austenitic stainless steel coatings," *Surf. Coat. Technol.*, vol. 97, no. 1, pp. 102–108, Dec. 1997, doi: 10.1016/S0257-8972(97)00138-2.
[198] J. Moon, H.-Y. Ha, and T.-H. Lee, "Corrosion behavior in high heat input welded heat-affected zone of Ni-free high-nitrogen Fe–18Cr–10Mn–N austenitic stainless steel," *Mater. Charact.*, vol. 82, pp. 113–119, Aug. 2013, doi: 10.1016/j.matchar.2013.05.011.
[199] P. R. Levey and A. van Bennekom, "A Mechanistic Study of the Effects of Nitrogen on the Corrosion Properties of Stainless Steels," *CORROSION*, vol. 51, no. 12, pp. 911–921, Dec. 1995, doi: 10.5006/1.3293567.
[200] "ExOne's Family of Metal 3D Printers." https://www.exone.com/en-US/3D-printing-systems/metal-3d-printers (accessed Feb. 16, 2022).
[201] Z. Chen, Z. Li, J. Li, C. Liu, C. Lao, Y. Fu, C. Liu, Y. Li, P. Wang, and L. He, "3D printing of ceramics: A review," *J. Eur. Ceram. Soc.*, vol. 39, no. 4, pp. 661–687, Apr. 2019, doi: 10.1016/j.jeurceramsoc.2018.11.013.
[202] S. Bose, A. Bhattacharjee, D. Banerjee, A. R. Boccaccini, and A. Bandyopadhyay, "Influence of random and designed porosities on 3D printed tricalcium phosphate-bioactive glass scaffolds," *Addit. Manuf.*, vol. 40, p. 101895, Apr. 2021, doi: 10.1016/j.addma.2021.101895.
[203] X. Yang, Q. Zhang, X. Li, X. Jia, X. Wei, and M. Shao, "Determination of Soil Texture by Laser Diffraction Method," *Soil Sci. Soc. Am. J.*, vol. 79, no. 6, pp. 1556–1566, Nov. 2015, doi: 10.2136/sssaj2015.04.0164.
[204] "Laser Diffraction," *Sympatec*. https://www.sympatec.com/en/particle-measurement/glossary/laser-diffraction/ (accessed Nov. 16, 2021).
[205] A. Mostafaei,
A.M. Elliott, J.E. Barnes, F. Li, W. Tan, C.L. Cramer, P. Nandwana, M. Chmielus, "Binder jet 3D printing—Process parameters, materials, properties, modeling, and challenges," *Prog. Mater. Sci.*, vol. 119, p. 100707, Jun. 2021, doi: 10.1016/j.pmatsci.2020.100707.
[206] T. D. Ngo, A. Kashani, G. Imbalzano, K. T. Q. Nguyen, and D. Hui, "Additive manufacturing (3D printing): A review of materials, methods, applications and challenges," *Compos. Part B Eng.*, vol. 143, pp. 172–196, Jun. 2018, doi: 10.1016/j.compositesb.2018.02.012.
[207] J. A. Muñiz-Lerma, A. Nommeots-Nomm, K. E. Waters, and M. Brochu, "A Comprehensive Approach to Powder Feedstock Characterization for Powder Bed Fusion Additive Manufacturing: A Case Study on AlSi7Mg," *Materials*, vol. 11, no. 12, Art. no. 12, Dec. 2018, doi: 10.3390/ma11122386.
[208] "US Patent Application for METHOD FOR MANUFACTURING SPUTTERING TARGET AND SPUTTERING TARGET Patent Application (Application #20200384598 issued December 10, 2020) - Justia Patents Search."
https://patents.justia.com/patent/20200384598 (accessed Feb. 17, 2022).
[209] J. F. Ziegler and J. P. Biersack, "The Stopping and Range of Ions in Matter," in *Treatise on Heavy-Ion Science: Volume 6: Astrophysics, Chemistry, and Condensed Matter*, D. A.

Bromley, Ed. Boston, MA: Springer US, 1985, pp. 93–129. doi: 10.1007/978-1-4615-8103-1_3.

[210] M. El Marsi, A. Guennoun, O. Elhaitamy, and A. Dezairi, "Monte Carlo simulations of MgO and complex oxide protective thin layers bombarded with noble-gas ion in plasma discharge devices," *J. Radioanal. Nucl. Chem.*, vol. 326, no. 3, pp. 1579–1588, Dec. 2020, doi: 10.1007/s10967-020-07440-x.

[211] M. Lanzetta and E. Sachs, "Improved surface finish in 3D printing using bimodal powder distribution," *Rapid Prototyp. J.*, vol. 9, no. 3, pp. 157–166, Jan. 2003, doi: 10.1108/13552540310477463.

[212] Y. Shan, J. Xu, G. Wang, X. Sun, G. Liu, J. Xu, and J. Li, "A fast pressureless sintering method for transparent AlON ceramics by using a bimodal particle size distribution powder," *Ceram. Int.*, vol. 41, no. 3, pp. 3992–3998, Apr. 2015, doi: 10.1016/j.ceramint.2014.11.084.

[213] W. Du, X. Ren, C. Ma, and Z. Pei, "Binder Jetting Additive Manufacturing of Ceramics: A Literature Review," in *Volume 14: Emerging Technologies; Materials: Genetics to Structures; Safety Engineering and Risk Analysis*, Tampa, Florida, USA, Nov. 2017, p. V014T07A006. doi: 10.1115/IMECE2017-70344.

[214] M. J. Cima, A. Lauder, S. Khanuja, and E. Sachs, "Microstructural Elements of Components Derived From 3D Printing," p. 8.

[215] K. Vallal Peruman, M. Mahendran, S. Seenithurai, R. Chokkalingam, R. K. Singh, and V. Chandrasekaran, "Internal stress dependent structural transition in ferromagnetic Ni–Mn–Ga nanoparticles prepared by ball milling," *J. Phys. Chem. Solids*, vol. 71, no. 11, pp. 1540–1544, Nov. 2010, doi: 10.1016/j.jpcs.2010.07.022.

[216] D. Y. Cong, P. Zetterström, Y.D. Wang, R. Delaplane, R. Lin Peng, X. Zhao, and L. Zuo, "Crystal structure and phase transformation in Ni53Mn25Ga22 shape memory alloy from 20Kto473K," *Appl. Phys. Lett.*, vol. 87, no. 11, p. 111906, Sep. 2005, doi: 10.1063/1.2043250.

[217] B. Tian, F. Chen, Y. Liu, and Y. F. Zheng, "Structural transition and atomic ordering of Ni49.8Mn28.5Ga21.7 ferromagnetic shape memory alloy powders prepared by ball milling," *Mater. Lett.*, vol. 62, no. 17, pp. 2851–2854, Jun. 2008, doi: 10.1016/j.matlet.2008.01.071.

[218] G. Cavazzini, F. Cugini, D. Delmonte, G. Trevisi, L. Nasi, S. Ener, D. Koch, L. Righi, M. Solzi, O. Gutfleisch, and F. Albertini, "Multifunctional Ni-Mn-Ga and Ni-Mn-Cu-Ga Heusler particles towards the nanoscale by ball-milling technique," *J. Alloys Compd.*, vol. 872, p. 159747, Aug. 2021, doi: 10.1016/j.jallcom.2021.159747.

[219] L. Righi, F. Albertini, E. Villa, A. Paoluzi, G. Calestani, V. Chernenko, S. Besseghini, C. Ritter, and F. Passaretti, "Crystal structure of 7M modulated Ni–Mn–Ga martensitic phase," *Acta Mater.*, vol. 56, no. 16, pp. 4529–4535, Sep. 2008, doi: 10.1016/j.actamat.2008.05.010.

[220] S. Glock, X. X. Zhang, N. J. Kucza, P. Müllner, and V. Michaud, "Structural, physical and damping properties of melt-spun Ni–Mn–Ga wire-epoxy composites," *Compos. Part Appl. Sci. Manuf.*, vol. 63, pp. 68–75, Aug. 2014, doi: 10.1016/j.compositesa.2014.04.005.

[221] F. Albertini, S. Besseghini, A. Paoluzi, L. Pareti, M. Pasquale, F. Passaretti, C.P. Sasso, A. Stantero, and E. Villa, "Structural, magnetic and anisotropic properties of Ni2MnGa melt-spun ribbons," *J. Magn. Magn. Mater.*, vol. 242–245, pp. 1421–1424, Apr. 2002, doi: 10.1016/S0304-8853(01)00992-1.

[222] J. Chu and Y. Bao, “Volatilization Behavior of Manganese from Molten Steel with Different Alloying Methods in Vacuum,” *Metals*, vol. 10, p. 1348, Oct. 2020, doi: 10.3390/met10101348.
[223] J.-R. Lee, T.-J. Chung, S.-H. Yang, G.-S. Hong, and K.-S. Oh, “Prevention of tapering in the tube-shaped sputtering target via initial heat treatment under external pressure,” *Ceram. Int.*, vol. 41, no. 3, Part A, pp. 3677–3683, Apr. 2015, doi: 10.1016/j.ceramint.2014.11.038.
[224] S. L. Taylor, R. N. Shah, and D. C. Dunand, “Microstructure and porosity evolution during sintering of Ni-Mn-Ga wires printed from inks containing elemental powders,” *Intermetallics*, vol. 104, pp. 113–123, Jan. 2019, doi: 10.1016/j.intermet.2018.10.024.
[225] R. K. Enneti, K. C. Prough, T. A. Wolfe, A. Klein, N. Studley, and J. L. Trasorras, “Sintering of WC-12%Co processed by binder jet 3D printing (BJ3DP) technology,” *Int. J. Refract. Met. Hard Mater.*, vol. 71, pp. 28–35, Feb. 2018, doi: 10.1016/j.ijrmhm.2017.10.023.
[226] Z. Baojun, Q. Xuanhui, and T. Ying, “Powder injection molding of WC–8%Co tungsten cemented carbide,” *Int. J. Refract. Met. Hard Mater.*, vol. 20, no. 5, pp. 389–394, Dec. 2002, doi: 10.1016/S0263-4368(02)00015-X.
[227] A. Mostafaei, A. M. Elliot, J. E. Barnes, F. Li, W. Tan, C. L. Cramer, P. Nandwana, and M. Chmielus, “Binder jet 3D printing—Process parameters, materials, properties, modeling, and challenges,” *Prog. Mater. Sci.*, vol. 119, p. 100707, Jun. 2021, doi: 10.1016/j.pmatsci.2020.100707.
[228] K. Kimes, K. Myers, A. Klein, M. Ahlfors, and M. Chmielus, Effects of HIP on Fatigue Life of Binder Jet 3D Printed 316L Stainless Steel, in Proceedings of the 2019 Additive Manufacturing with Powder Metallurgy Conference. 2019.
[229] H. M. Bui, R. Fischer, N. Szesni, M. Tonigold, K. Achterhold, F. Pfeiffer, and O. Hinrichsen “Development of a manufacturing process for Binder Jet 3D printed porous Al2O3 supports used in heterogeneous catalysis,” *Addit. Manuf.*, vol. 50, p. 102498, Feb. 2022, doi: 10.1016/j.addma.2021.102498.
[230] J. G. Bai, T. G. Lei, J. N. Calata, and G.-Q. Lu, “Control of nanosilver sintering attained through organic binder burnout,” *J. Mater. Res.*, vol. 22, no. 12, pp. 3494–3500, Dec. 2007, doi: 10.1557/JMR.2007.0440.
[231] W. D. C. Jr and D. G. Rethwisch, *Fundamentals of Materials Science and Engineering: An Integrated Approach*. John Wiley & Sons, 2012.
[232] B. Tian, F. Chen, Y. X. Tong, L. Li, and Y. F. Zheng, “Bending properties of epoxy resin matrix composites filled with Ni–Mn–Ga ferromagnetic shape memory alloy powders,” *Mater. Lett.*, vol. 63, no. 20, pp. 1729–1732, Aug. 2009, doi: 10.1016/j.matlet.2009.05.004.
[233] L. Hou, H. Tong, Y. Dai, Y. Fautrelle, R. Moreau, Z. Ren, and X. Li, “Correlation between microstructures and mechanical properties in Ni-rich Ni–Mn–Ga high-temperature shape-memory alloys,” *Mater. Sci. Technol.*, pp. 1–6, Dec. 2017, doi: 10.1080/02670836.2017.1410928.
[234] M. F. Qian, X.X. Zhang, X. Li, R.C. Zhang, P.G. Martin, J. F. Sun, L. Geng, T.B. Scott, and H.X. Peng, “Magnetocaloric effect in bamboo-grained Ni-Mn-Ga microwires over a wide working temperature interval,” *Mater. Des.*, vol. 190, p. 108557, May 2020, doi: 10.1016/j.matdes.2020.108557.

[235] Y. Luo, P. Leicht, A. Laptev, M. Fonin, U. Rudiger, M. Laufenberg, K. Samwer, "Effects of film thickness and composition on the structure and martensitic transition of epitaxial off-stoichiometric Ni–Mn–Ga magnetic shape memory films," *New J. Phys.*, vol. 13, no. 1, p. 013042, Jan. 2011, doi: 10.1088/1367-2630/13/1/013042.
[236] S. L. Taylor, R. N. Shah, and D. C. Dunand, "Ni-Mn-Ga micro-trusses via sintering of 3D-printed inks containing elemental powders," *Acta Mater.*, vol. 143, pp. 20–29, Jan. 2018, doi: 10.1016/j.actamat.2017.10.002.
[237] C. Jiang, Y. Muhammad, L. Deng, W. Wu, and H. Xu, "Composition dependence on the martensitic structures of the Mn-rich NiMnGa alloys," *Acta Mater.*, vol. 52, no. 9, pp. 2779–2785, May 2004, doi: 10.1016/j.actamat.2004.02.024.
[238] M.-W. Wu, D.-S. Liu, and Y.-H. Su, "The densification, microstructure, and electrical properties of aluminum-doped zinc oxide sputtering target for transparent conductive oxide film," *J. Eur. Ceram. Soc.*, vol. 32, no. 12, pp. 3265–3275, Sep. 2012, doi: 10.1016/j.jeurceramsoc.2012.04.030.
[239] S.-H. Chang, C.-W. Lu, and J.-K. Chen, "Study on the microstructures, electrical resistance and mechanical properties of sputtering chromium target by HP, HIP and canning–HIP processes," *Int. J. Refract. Met. Hard Mater.*, vol. 35, pp. 70–75, Nov. 2012, doi: 10.1016/j.ijrmhm.2012.04.010.
[240] D. B. Bergstrom, F. Tian, I. Petrov, J. Moser, and J. E. Greene, "Origin of compositional variations in sputter-deposited $Ti_x W_{1-x}$ diffusion barrier layers," *Appl. Phys. Lett.*, vol. 67, no. 21, pp. 3102–3104, Nov. 1995, doi: 10.1063/1.114878.
[241] R. S. Bailey, "Effects of target microstructure on aluminum alloy sputtered thin film properties," *J. Vac. Sci. Technol. Vac. Surf. Films*, vol. 10, no. 4, pp. 1701–1705, Jul. 1992, doi: 10.1116/1.577773.
[242] M. Reza, Z. Sajuri, J. Yunas, and J. Syarif, "Effect of sputtering target's grain size on the sputtering yield, particle size and coercivity (Hc) of Ni and Ni20Al thin films," *IOP Conf. Ser. Mater. Sci. Eng.*, vol. 114, p. 012116, Feb. 2016, doi: 10.1088/1757-899X/114/1/012116.
[243] "Effect of Crystal Size and Direction of Sputtering Target on Large Area Coating." https://www.aemdeposition.com/sputtering-targets-news/effect-of-crystal-size-and-direction-of-sputtering-target-on-large-area-coating.html (accessed Dec. 06, 2021).
[244] "Sputtering Target and grain size of sputtering targets - XK Ltd." https://www.xk-sputteringtarget.com/en/news_57.html (accessed Dec. 06, 2021).
[245] Y. Zhang, Q. Song, and Z. Sun, "Research on Thin Film Thickness Uniformity for Deposition of Rectangular Planar Sputtering Target," *Phys. Procedia*, vol. 32, pp. 903–913, Jan. 2012, doi: 10.1016/j.phpro.2012.03.655.
[246] C.-F. Lo, P. McDonald, D. Draper, and P. Gilman, "Influence of tungsten sputtering target density on physical vapor deposition thin film properties," *J. Electron. Mater.*, vol. 34, no. 12, pp. 1468–1473, Dec. 2005, doi: 10.1007/s11664-005-0152-z.
[247] W. Shao, R. Ma, and B. Liu, "Fabrication and properties of ZAO powder, sputtering target materials and the related films," *J. Univ. Sci. Technol. Beijing Miner. Metall. Mater.*, vol. 13, no. 4, pp. 346–349, Aug. 2006, doi: 10.1016/S1005-8850(06)60071-6.
[248] C.-F. Lo and D. Draper, "Quantitative measurement of nodule formation in W–Ti sputtering," *J. Vac. Sci. Technol. A*, vol. 16, no. 4, pp. 2418–2422, Jul. 1998, doi: 10.1116/1.581361.

[249] "Growth of Target Race Track Profile during Magnetron Sputtering." https://www.jstage.jst.go.jp/article/jvsj2/58/7/58_14-PR-097/_article/-char/ja/ (accessed Dec. 08, 2021).
[250] R. H. Wolf and A. H. Heuer, "TiNi (shape memory) films silicon for MEMS applications," *J. Microelectromechanical Syst.*, vol. 4, no. 4, pp. 206–212, Dec. 1995, doi: 10.1109/84.475547.
[251] F. Nilsén, I. F. Ituarte, M. Salmi, J. Partanen, and S.-P. Hannula, "Effect of process parameters on non-modulated Ni-Mn-Ga alloy manufactured using powder bed fusion," *Addit. Manuf.*, vol. 28, pp. 464–474, Aug. 2019, doi: 10.1016/j.addma.2019.05.029.
[252] M. Wuttig, C. Craciunescu, and J. Li, "Phase Transformations in Ferromagnetic NiMnGa Shape Memory Films," *Mater. Trans. JIM*, vol. 41, no. 8, pp. 933–937, 2000, doi: 10.2320/matertrans1989.41.933.
[253] E. A. I. Ellis, M. Chmielus, S. Han, and S. P. Baker, "Effect of sputter pressure on microstructure and properties of β-Ta thin films," *Acta Mater.*, vol. 183, pp. 504–513, Jan. 2020, doi: 10.1016/j.actamat.2019.10.056.
[254] S. Grachev, F. D. Tichelaar, and G. C. A. M. Janssen, "Stress in sputter-deposited Cr films: Influence of Ar pressure," *J. Appl. Phys.*, vol. 97, pp. 073508–073508, May 2005, doi: 10.1063/1.1876579.
[255] K. Seki, H. Kura, T. Sato, and T. Taniyama, "Size dependence of martensite transformation temperature in ferromagnetic shape memory alloy FePd," *J. Appl. Phys.*, vol. 103, no. 6, p. 063910, Mar. 2008, doi: 10.1063/1.2890143.
[256] T. Waitz, T. Antretter, F. D. Fischer, N. K. Simha, and H. P. Karnthaler, "Size effects on the martensitic phase transformation of NiTi nanograins," *J. Mech. Phys. Solids*, vol. 55, no. 2, pp. 419–444, Feb. 2007, doi: 10.1016/j.jmps.2006.06.006.
[257] M. Thomas, O. Heczko, J. Buschbeck, Y.W. Lai, J. McCord, S. Kaufman, L. Schultz, and S. Fahler, "Stray-Field-Induced Actuation of Free-Standing Magnetic Shape-Memory Films," *Adv. Mater.*, vol. 21, no. 36, pp. 3708–3711, 2009, doi: 10.1002/adma.200900469.
[258] A. Annadurai, M. Manivel Raja, K. Prabahar, A. Kumar, M. D. Kannan, and S. Jayakumar, "Stress analysis, structure and magnetic properties of sputter deposited Ni–Mn–Ga ferromagnetic shape memory thin films," *J. Magn. Magn. Mater.*, vol. 323, no. 22, pp. 2797–2801, Nov. 2011, doi: 10.1016/j.jmmm.2011.06.017.
[259] C. Li, J. Sun, G. Sun, G. Yao, and Z. Chen, "Study on ferromagnetic shape memory alloy Ni–Mn–Ga films," *Surf. Coat. Technol.*, vol. 201, no. 9, pp. 5348–5353, Feb. 2007, doi: 10.1016/j.surfcoat.2006.07.095.
[260] C. Liu, Z. Y. Gao, X. An, H. B. Wang, L. X. Gao, and W. Cai, "Surface characteristics and nanoindentation study of Ni–Mn–Ga ferromagnetic shape memory sputtered thin films," *Appl. Surf. Sci.*, vol. 254, no. 9, pp. 2861–2865, Feb. 2008, doi: 10.1016/j.apsusc.2007.10.031.
[261] E04 Committee, "Test Methods for Determining Average Grain Size," ASTM International. doi: 10.1520/E0112-10.
[262] C. Kooi, "Uniformity Characterization of Technics-c," p. 20.
[263] K.-H. Cheng, C.-H. Lai, S.-J. Lin, and J.-W. Yeh, "Structural and mechanical properties of multi-element (AlCrMoTaTiZr)Nx coatings by reactive magnetron sputtering," *Thin Solid Films*, vol. 519, no. 10, pp. 3185–3190, Mar. 2011, doi: 10.1016/j.tsf.2010.11.034.

[264] S. M. Rossnagel, I. Yang, and J. J. Cuomo, "Compositional changes during magnetron sputtering of alloys," *Thin Solid Films*, vol. 199, no. 1, pp. 59–69, Apr. 1991, doi: 10.1016/0040-6090(91)90052-Y.

[265] A. Y. Jaber, S. N. Alamri, M. S. Aida, M. Benghanem, and A. A. Abdelaziz, "Influence of substrate temperature on thermally evaporated CdS thin films properties," *J. Alloys Compd.*, vol. 529, pp. 63–68, Jul. 2012, doi: 10.1016/j.jallcom.2012.03.093.

[266] V. Bilgin, S. Kose, F. Atay, and I. Akyuz, "The effect of substrate temperature on the structural and some physical properties of ultrasonically sprayed CdS films," *Mater. Chem. Phys.*, vol. 94, no. 1, pp. 103–108, Nov. 2005, doi: 10.1016/j.matchemphys.2005.04.028.

[267] Y. S. Zou, S. L. Wang, H. Yang, K. Wang, and S. Hui, "Effect of substrate temperature on microstructure and optical properties of Ga doped ZnO films deposited by pulsed laser deposition," *Surf. Eng.*, vol. 31, no. 4, pp. 302–307, Apr. 2015, doi: 10.1179/1743294414Y.0000000440.

[268] "ImageJ, Fiji & OMERO," *Microscopist.co.uk*. http://www.microscopist.co.uk/other-information/image-j/ (accessed Mar. 03, 2022).

[269] S. Heiroth, R. Frison, J.L.M. Rupp, T. Lippert, E.J.B. Meier, E.M. Gubler, M. Dobeli, K. Conder, A. Wokaun, and L.J. Gauckler, "Crystallization and grain growth characteristics of yttria-stabilized zirconia thin films grown by pulsed laser deposition," *Solid State Ion.*, vol. 191, no. 1, pp. 12–23, Jun. 2011, doi: 10.1016/j.ssi.2011.04.002.

[270] S. Mushtaq, B. Ismail, M. Raheel, and A. Zeb, "Nickel Antimony Sulphide Thin Films for Solar Cell Application: Study of Optical Constants," *Nat. Sci.*, vol. 8, no. 2, Art. no. 2, Feb. 2016, doi: 10.4236/ns.2016.82004.

[271] R. Mariappan, V. Ponnuswamy, and M. Ragavendar, "Characterization of CdS1−xSex thin films by chemical bath deposition technique," *Optik*, vol. 123, no. 13, pp. 1196–1200, Jul. 2012, doi: 10.1016/j.ijleo.2011.07.050.

[272] L. Vergara, M. Clement, E. Iborra, A. Sanz-Hervas, J.G. Lopez, Y. Morilla, J. Sangrador, and M.A. Respaldiza, "Influence of oxygen and argon on the crystal quality and piezoelectric response of AlN sputtered thin films," *Diam. Relat. Mater.*, vol. 13, no. 4, pp. 839–842, Apr. 2004, doi: 10.1016/j.diamond.2003.10.063.

[273] L. Righi, F. Albertini, L. Pareti, A. Paoluzi, and G. Calestani, "Commensurate and incommensurate '5M' modulated crystal structures in Ni–Mn–Ga martensitic phases," *Acta Mater.*, vol. 55, no. 15, pp. 5237–5245, Sep. 2007, doi: 10.1016/j.actamat.2007.05.040.

[274] P. J. Kelly and R. D. Arnell, "Magnetron sputtering: a review of recent developments and applications," *Vacuum*, vol. 56, no. 3, pp. 159–172, Mar. 2000, doi: 10.1016/S0042-207X(99)00189-X.

[275] J. Mcinerney, *Computational Explorations in Magnetron Sputtering*. 2014.

[276] "(17) (PDF) Computational Explorations in Magnetron Sputtering." https://www.researchgate.net/publication/303920343_Computational_Explorations_in_Magnetron_Sputtering (accessed Sep. 22, 2021).

[277] S. Swann, "Film thickness distribution in magnetron sputtering," *Vacuum*, vol. 38, no. 8, pp. 791–794, Jan. 1988, doi: 10.1016/0042-207X(88)90465-4.

[278] Y. Ohtsu, T. Nakashima, R. Tanaka, and J. Schulze, "Characteristics of a rotational windmill-shaped radio frequency magnetron sputtering plasma for effective target

utilization," *Vacuum*, vol. 181, p. 109593, Nov. 2020, doi: 10.1016/j.vacuum.2020.109593.

[279] E. Arakelova, A. Khachatryan, A. Kteyan, K. Avjyan, and S. Grigoryan, "ZnO film deposition by DC magnetron sputtering: Effect of target configuration on the film properties," *Thin Solid Films*, vol. 612, pp. 407–413, Aug. 2016, doi: 10.1016/j.tsf.2016.06.030.

[280] S. Swann, "Spatial distribution of sputtered atoms from magnetron source," *J. Vac. Sci. Technol. Vac. Surf. Films*, vol. 5, no. 4, pp. 1750–1754, Jul. 1987, doi: 10.1116/1.574530.

[281] Qi-hua Fan and Hong-you Chen, "Effects of magnetic field on the target erosion in the symmetrical magnets magnetron sputtering method," *Thin Solid Films*, vol. 229, no. 2, pp. 143–145, Jun. 1993, doi: 10.1016/0040-6090(93)90356-T.

[282] S. Swann, "Magnetron sputtering," *Phys. Technol.*, vol. 19, no. 2, pp. 67–75, Mar. 1988, doi: 10.1088/0305-4624/19/2/304.

[283] T. Ide, A. Hossain, Y. Nakamura, and Y. Ohtsu, "Rotational cross-shaped magnetized radio-frequency sputtering plasma source for uniform circular target utilization," *J. Vac. Sci. Technol. Vac. Surf. Films*, vol. 35, p. 061312, Nov. 2017, doi: 10.1116/1.4999221.

[284] M. Wright and T. Beardow, "Design advances and applications of the rotatable cylindrical magnetron," *J. Vac. Sci. Technol. A*, vol. 4, no. 3, pp. 388–392, May 1986, doi: 10.1116/1.573888.

[285] T. Iseki, "Flat erosion magnetron sputtering with a moving unbalanced magnet," *Vacuum*, vol. 80, no. 7, pp. 662–666, May 2006, doi: 10.1016/j.vacuum.2005.11.019.

[286] "Binder Jetting and FDM vs Powder Bed Fusion and Injection Moulding," *Metal Additive Manufacturing*, Sep. 01, 2018. https://www.metal-am.com/articles/binder-jetting-fdm-comparison-with-powder-bed-fusion-3d-printing-injection-moulding/ (accessed Sep. 27, 2021).

[287] I. Rishmawi, M. Salarian, and M. Vlasea, "Tailoring green and sintered density of pure iron parts using binder jetting additive manufacturing," *Addit. Manuf.*, vol. 24, pp. 508–520, Dec. 2018, doi: 10.1016/j.addma.2018.10.015.

[288] Y. Jin, "Annealing twin formation mechanism," p. 213.

[289] N. Bozzolo and M. Bernacki, "Viewpoint on the Formation and Evolution of Annealing Twins During Thermomechanical Processing of FCC Metals and Alloys," *Metall. Mater. Trans. A*, vol. 51, no. 6, pp. 2665–2684, Jun. 2020, doi: 10.1007/s11661-020-05772-7.

[290] J. I. Langford and A. J. C. Wilson, "Scherrer after sixty years: A survey and some new results in the determination of crystallite size," *J. Appl. Crystallogr.*, vol. 11, no. 2, Art. no. 2, Apr. 1978, doi: 10.1107/S0021889878012844.

[291] Y.-T. Hwang, W.-H. Chung, Y.-R. Jang, and H.-S. Kim, "Intensive Plasmonic Flash Light Sintering of Copper Nanoinks Using a Band-Pass Light Filter for Highly Electrically Conductive Electrodes in Printed Electronics," *ACS Appl. Mater. Interfaces*, vol. 8, no. 13, pp. 8591–8599, Apr. 2016, doi: 10.1021/acsami.5b12516.

[292] C.-H. Joh, J.-G. Jung, and Y.-H. Kim, "Microstructure Characterization of Cu Thin Films: Effects of Sputter Deposition Conditions," *Appl. Microsc.*, vol. 29, no. 3, pp. 265–274, 1999.

[293] E. R. Shaaban, I. Kansal, S. H. Mohamed, and J. M. F. Ferreira, "Microstructural parameters and optical constants of ZnTe thin films with various thicknesses," *Phys. B Condens. Matter*, vol. 404, no. 20, pp. 3571–3576, Nov. 2009, doi: 10.1016/j.physb.2009.06.002.

[294] S. Mohd Yusuf, E. Choo, and N. Gao, "Comparison between Virgin and Recycled 316L SS and AlSi10Mg Powders Used for Laser Powder Bed Fusion Additive Manufacturing," *Metals*, vol. 10, no. 12, Art. no. 12, Dec. 2020, doi: 10.3390/met10121625.

[295] M. Dadfar, M. Fathi, F. Karimzadeh, and A. Saatchi, "Effect of TIG welding on corrosion behavior of 316L stainless steel," *Mater. Lett.*, vol. 61, pp. 2343–2346, May 2007, doi: 10.1016/j.matlet.2006.09.008.

[296] Y. Shan, Z. Zhang, X. Sun, J. Xu, Q. Qin, and J. Li, "Further experimental investigation on fast densification mechanism of bimodal powder during pressureless sintering of transparent AlON ceramics," *Ceram. Int.*, vol. 43, no. 11, pp. 8195–8201, Aug. 2017, doi: 10.1016/j.ceramint.2017.03.146.